Computational and experimental studies of bilayer peptide interactions

Kia Balali-Mood

Submitted in satisfaction of the requirements for the degree of Doctor of Philosophy

Division of Veterinary Biomedical Sciences
College of Medicine and Veterinary Medicine
The University of Edinburgh

2004

Declaration

I declare that this thesis has been composed by myself, and that the work described herein is my own unless stated otherwise. The candidate has not been registered for a degree at any other Institution throughout his period of registration at the University of Edinburgh.

This thesis is dedicated (in equal measure!) to:

My Father
Professor Mehdi Balali-Mood
For his never ending belief in my ability and the uncompromising principles that guide his life

My Mother
Professor Maryam Khordi-Mood
For all the colossal sacrifices she has made on my behalf and guiding her only son into scientific pursuits

My Sister
Ms. Beeta Balali-Mood
For her constant support and encouragement

Acknowledgements

I'd like to thank all the following people, without whom this thesis would not have been possible. First and foremost, I would like to thank my principal supervisor, Dr Jeremy Bradshaw for his wise counsel and exceptional patience over the last three years. A huge thank you goes out to my second supervisor Prof. Lindsay Sawyer for his constructive criticism and encouragement. Gratitude is extended to Dr Thad Harroun (a former postdoctoral fellow in the group) who was inspirational and spent numerous hours bestowing his wisdom upon me, in the first year of my studies. Dr Thomas Hauss at the Hahn Meitner Institut, Berlin, was another inspirational figure and amazed me with his enthusiasm for neutron diffraction. I'd also like to thank my thesis committee who in addition to my supervisors were Dr Paul Taylor and the recently departed Prof. Vladimir Buchman. I am indebted to Dr Richard Ashley for donation of lipids and the IAPP peptides, without which chapter two would not exist. Sarah Dennison was an irreplaceable figure, particularly towards the end of my studies; her help was much appreciated and will not be forgotten.

Last but certainly not least, I'd like to thank all the chaps from Biomedical Sciences FC for their scientific and footballing support and putting up with me in the heart of what was an otherwise solid defence!

Abstract

This thesis describes the combination of experimental (neutron diffraction) and computational techniques (molecular dynamics simulations) to investigate membrane peptide interactions.

The first part deals with a comparison of human and rat form of the amyloid inducing peptide islet amyloid polypeptide (IAPP). Lamellar neutron diffraction was performed and a structural comparison on the differing modes of actions of the rat and human forms of IAPP are reported.

A computational model for a di-oleoyl phosphatidylcholine (DOPC) bilayer was then constructed. Once this bilayer had been verified with experimental data (namely area per headgroup, volume per lipid, order parameter of the oleoyl chains and electron density profile) a mixed bilayer of DOPC and di-oleoyl phopshatidylglycerol (DOPG) was then constructed. The mixed bilayer was verified in the same manner.

A peptide (adenosine diphosphate ribosylation factor-1 (pARF-1)) was then inserted into the pre-equilibrated mixed bilayer. The orientation of this peptide with respect to the membrane was based on previous neutron diffraction studies, carried out by other group members. Four possible orientations had resulted from analysis of the neutron data. The four orientations of pARF-1 were then subjected to molecular dynamics simulations. The time course of these simulations was 4 ns. The simulation's trajectories were analysed for each of the four models. Particular emphasis was placed upon the positional changes of the phenylalanine label positions that were derived from

the neutron data. It was concluded that model A was the most likely orientation of pARF-1 in relation to the bilayer.

Having established the technique, and confirmed that the most likely orientation of the peptide was what was originally proposed, another peptide, the fusion peptide of simian immunodeficiency virus (SIV) was placed into a previously equilibrated DOPC bilayer. In this case, only the proposed orientation of the SIV fusion peptide in relation to the bilayer was studied utilizing molecular dynamics simulations. The results are interpreted in relation to the actions of SIV fusion peptide upon the membrane, with particular emphasis on the disruption of oleoyl chain order parameters and secondary structure of the membrane bound fusion peptide.

Table of contents

Abbreviations

Å= Ångstrom

ARF= adenosine diphosphate ribosylation factor

ARF1p= The N-terminal peptide of adenosine diphosphate ribosylation factor 1.

Aβ= Alzheimers beta protein

CD= Circular dichroism

cDNAs= Complementary Deoxy-Ribonucleic acids

CJD= Creutzfeld Jacob disease

CT= Calcitonin

d= The unit cell in a lamellar array of bilayers

DMPC= di-myristoyl phosphatidylcholine

DOPC= di-oleoyl phosphatidylcholine

DOPE-me= N-methylated di-oleoyl phosphatidylethanolamine

DOPG= di-oleoyl phosphatidylglycerol

DPPC= di-palmitoyl phosphatidylcholine

DPPS= di-palmitoyl phosphatidylserine

e= 2.71828

EDP= Electron density profile

EM= Energy minimization

EPC= Egg phosphatidylcholine

FeLV= Feline leukaemia virus

FT= Fourier transform

GAPs= GTPase activating proteins

GDP= Guanine diphosphate

GEF= Guanine exchange factor

gp= glycoprotein

GRO= *GROMACS* file format (equivalent of PDB)

GROMACS= GROningen MAchine for Chemical Simulations

GTP= Guanine triphosphate

GX= Gravimetric X-ray

GXC= Gravimetric X-ray corrected

hIAPP= Human islet amyloid polypeptide

H_{II}= Inverted hexagonal phase

HIV= Human Immunodefiecieny virus

IAPP= Islet amyloid polypeptide

IDDM= Insulin dependent diabetes mellitus

IMB= International Molecular Biology

ITP=Include Topology

LD = Langevin Dynamics

L_α= Lamellar alpha phase in bilayers

L_β= Lamellar crystalline phase in bilayers

MC= Monte Carlo

MD= Molecular dynamics

MDP= Molecular dynamics parameters

MLV=Multi lamellar vesicle

MSD= Mean square displacement

Myr= N-terminal myristoyl chain

NERPRC= New England and California regional primate research centres

NIDDM= Non-insulin dependent diabetes mellitus

nm= Nano metre(s)

NMR= Nuclear magnetic resonance

NOESY= Nuclear Overhauser enhancement spectroscopy

NPAT= System in which there are a constant no. of particles, Pressure, area per molecule and temperature.

NPT= System in which there are a constant no. of particles, Pressure and temperature.

ns= Nano seconds

NVE= System in which there are a constant no. of particles, constant volume & energy.

NVT= System in which there are a constant no. of particles, constant volume & temperature.

OPLS= Optimized Intermolecular Potential functions for Liquid hydrocarbonS

PC= Phosphatidylcholine

PDB= Protein data bank

PDPC= Palmitoyl-docosahexaenoyl phosphatidylcholine

PE= Phosphatidylethanolamine

PG= Phosphatidylglycerol

POPC= Palmitoyl-oleoyl phosphatidylcholine

POPE= Palmitoyl-oleoyl phosphatidylethanolamine

POPS= Palmitoyl-oleoyl phosphatidylserine

PS= Phosphatidylserine

ps= pico seconds

RD= Rotational diffusion

rIAPP= Rat islet amyloid polypeptide

SAS= Solvent accessible surface

SD= Standard deviation

SIV= Simian immunodeficiency syndrome

SPC/e= Extended simple point charge

SPC= Simple point charge

STO-3G= Standard orbital three gaussian

TFE= Tri-fluoro ethanol

T_H= Hexagonal phase temperature

TOP= Topology

Φ= Phi is the torsion angle between H, N,Cα and N in a polypeptide chain

Ψ= Psi is the torsion angle between N, Cα,C and H in a polypeptide chain

One and three letter code for amino acids

Amino acid	**Three letter code**	**One letter code**
Alanine	Ala	A
Arginine	Arg	R
Asparagine	Asn	N
Aspartic acid	Asp	D
Cysteine	Cys	C
Glutamic acid	Glu	E
Glutamine	Gln	Q
Glycine	Gly	G
Histidine	His	H
Isoleucine	Ile	I
Leucine	Leu	L
Lysine	Lys	K
Methionine	Met	M
Phenylalanine	Phe	F
Proline	Pro	P
Serine	Ser	S

Threonine	Thr	T
Tryptophan	Try	W
Tyrosine	Tyr	Y
Valine	Val	V

List of Figures

Chapter 1

Chapter 2

Chapter 3

Chapter 4

Chapter 5

List of tables

Chapter 1

Chapter 2

Chapter 3

Chapter 4

Chapter 5

Chapter 1

Introduction

1.1 Cell membranes and their components

A cell membrane is a semi-permeable barrier that separates the interior of every cell from its exterior environment. All living cells employ membranes in order to control their internal environment (e.g. pH, salt concentration) and to facilitate important biochemical processes (i.e. cellular metabolism). Certain types of substance such as ions, can passively diffuse (i.e. no energy is expended) through the membrane. Biomembranes are found both externally and internally in eukaryotic cells. The external membrane surrounds the whole cell whereas internal membranes envelop specific functional units (organelles) within the cell. A biological membrane is made up from three main components, namely lipids, proteins and sugars. These biomolecules are oriented with respect to each other to form the membrane structure. The universal membrane structural motif is the lipid bilayer. Associated with the lipid bilayer are proteins that have a range of specialised functions (e.g. receptors, molecular carriers and pumps). On the external side of many membranes there are networks of sugar molecules. They are partly responsible for communication with nearby cells and signalling molecules.

The first widely accepted model for a lipid bilayer was the Fluid-Mosaic model, proposed by Singer and Nicholson in the 1970s. Figure 1.1 illustrates this model. The model originally proposed by Singer and Nicholson (Singer and Nicolson, 1972) predicted lateral and rotational freedom and random distribution of molecular components in the membrane. Membranes are now considered to be a "two dimensional oriented solution of integral proteins in the viscous phospholipids

bilayer". Vereb and co-workers (Vereb *et al.,* 2003) have since refined the model of Singer and Nicholson. They have proposed that the emphasis be shifted from the fluidity to the mosaicism of the Singer-Nicholson model. Mosaicism can restrict free diffusion via one of the following methods:

1. Lipid domain structure;
2. Cytoskeletal or other cytosolic interaction;
3. Associations with other integral membrane proteins.

The latest reports describe the membrane as "a heavily compartmentalized, quasi-two dimensional structure, which is more mosaic-like than fluid" (Vereb *et al.,* 2003). Within this two-dimensional plane, diffusion, intermolecular force and extra cellular influences can dynamically generate and destroy supramolecular structures. It has been proposed that this latest model of the cell membrane be referred to as "the dynamically structured mosaic model" (Vereb *et al.,* 2003).

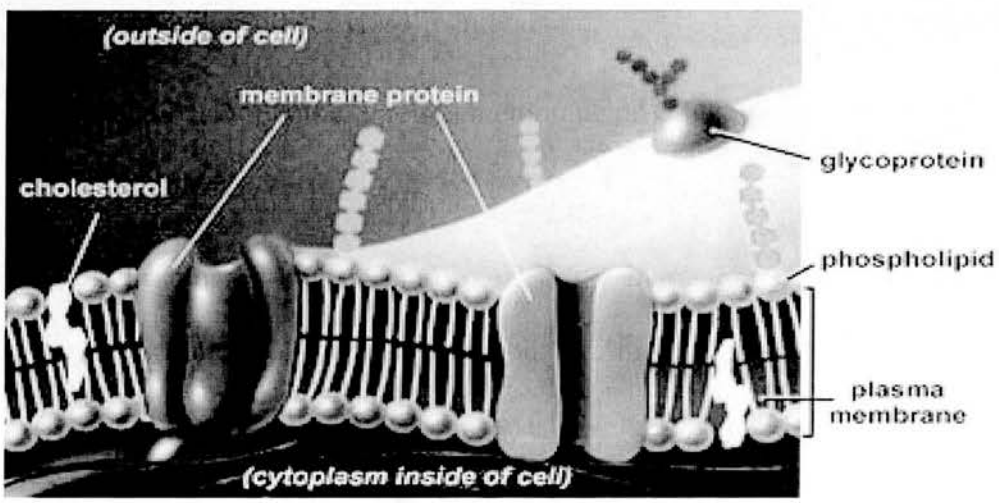

Figure 1.1. Graphical representation of a lipid bilayer.
(Source. http://www.emc.maricopa.edu/faculty/farabee/BIOBK/5_11.jpg)

The major components within a cell membrane are usually lipids (phospholipids) followed by proteins and then sugars, respectively. However, the protein component of the membrane can be greater than the lipid component. Table 1.1 displays the approximate range of composition (expressed as a percentage).

Component	Percentage present (%)
Phospholipids	40-60
Proteins	30-50
Sugars	~10

Table 1.1. Typical membrane constituents (Siegel *et al.,* 1989)

Many proteins present on the surface are receptors that are crucial to the actions of hormones, growth factors, neurotransmitters and other endogenous mediators. These receptors tend to be G-protein coupled (e.g. the muscarinic acetyl choline receptors in the mammalian nervous system), which trigger off intracellular messenger pathways within the cell. In addition, the cell membrane allows for cell to cell interaction, such as the recognition of macrophages from the immune system.

1.2 Phospholipid structure

Phospholipids are arranged in two "leaflets" within a bilayer in what can be described as a lamellar arrangement. A typical phospholipid comprises a headgroup which is *hydrophilic*, and *hydrophobic* chains, linked together by a glycerol group

(Yeagle, 1993). Figure 1.2 displays a typical phospholipid, as found within biological membranes.

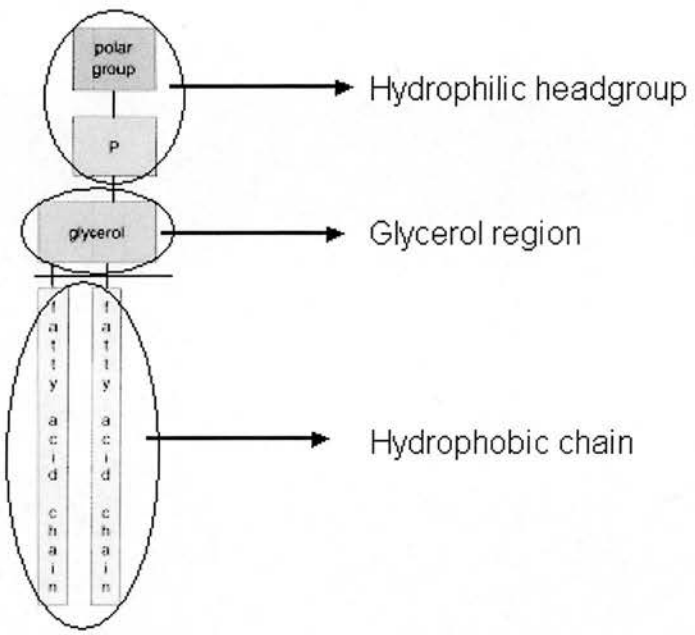

Figure 1.2. Phospholipid structure. The *hydrophilic* headgroup typically comprises two subsections. 1. A polar headgroup (e.g. choline or ethanolamine). 2. A phosphate moiety. A glycerol moiety links the headgroup to the *hydrophobic* chain region. Some bilayers contain phospholipids with either a single *hydrophobic* chain (e.g. lyso-phosphatidylcholine) or two *hydrophobic* chains (e.g. di-oleoyl phosphatidylcholine).

The bilayer is a thermodynamically stable, spontaneously arranging biological structure. The lipids within a bilayer are highly dynamic, and rotate and move in a three dimensional manner. Figure 1.3 displays a typical bilayer arrangement and various individual lipid motions that can occur.

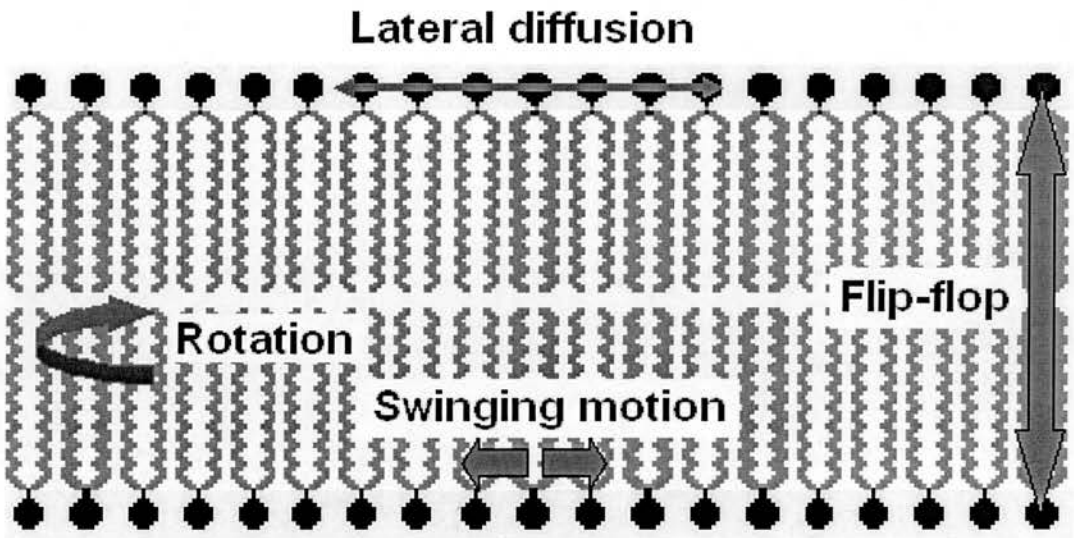

Figure 1.3. Phospholipid motions within the bilayer.

All of the motions seen in Figure 1.3 contribute to the dynamic nature of the bilayer and allow for flexibility for the bilayer to form around the cell.

1.3 Phospholipid chemistry (headgroups & chains)

The four main types of headgroups in biological membranes are as follows (Yeagle, 1993):

- Phosphatidylserine (PS)
- Phosphatidylcholine (PC)
- Phosphatidylethanolamine (PE)
- Phosphatidylglycerol (PG)

The phospholipid chains seen in nature are di-acyl, lyso, saturated (e.g. myristoyl chains) or un-saturated such as oleoyl chains. There may be one (lyso) or two (di-acyl) chains per phospholipids.

Figure 1.4a represents the chemical structures of the biologically relevant headgroups whereas Figure 1.4b represents the chemical structures of the relevant chains, respectively.

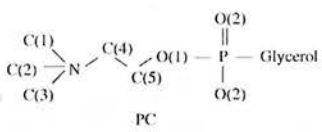

PC

Phosphatidylcholine

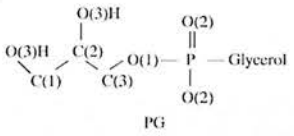

PG

Phosphatidylglycerol

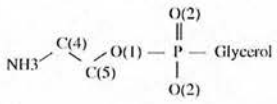

PE

Phosphatidylethanolamine

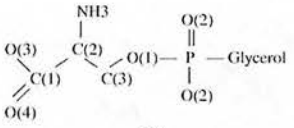

PS

Phosphatidylserine

Figure 1.4a. Chemical representation of the most biologically relevant phospholipids headgroups.

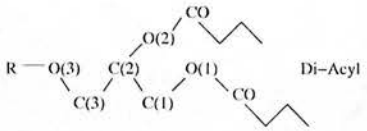

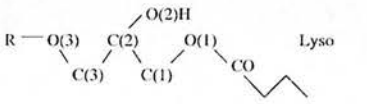

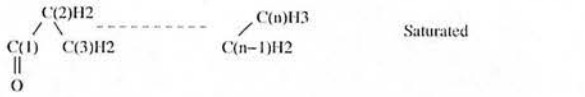

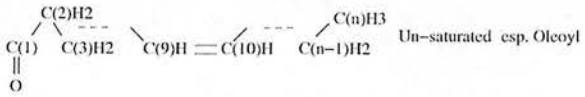

Figure 1.4b. Chemical representation of the most biologically relevant hydrocarbon chains.

Each cell type has a different composition of headgroups and chains. In eukaryotic organisms there are roughly 8 to 24 carbons in each chain. The chains tend to be in a liquid crystalline state, which in short implies a melted fluid like state.

1.4 Composition of phospholipid bilayers

Each biological membrane contains a mixture of phospholipids. An example of a membrane in which the components have been well quantified is the human erythrocyte membrane. Table 1.2 displays a distribution of lipids within a healthy human erythrocyte.

Lipid	Percentage present (%)
Phosphatidylethanolamine	22%
Phosphatidylcholine	25%
Cholesterol	25%
Phosphatidylserine	10%
Sphingomyelin	18%

Table 1.2. Lipid distribution in a typical human erythrocyte (Gennis, 1989).

The choline-containing lipids, phosphatidylcholine and sphingomyelin, are found predominantly in the outer monolayer of the bilayer. However, the aminophospholipids, comprising phosphatidylethanolamine and phosphatidylserine, are primarily located in the cytoplasmic leaflet of the membrane.

The transmembrane distribution of minor membrane lipid components was determined by reaction with lipid-specific antibodies and lipid hydrolases (Siegel *et al.,* 1989). These studies showed that about 80% of the phospholipids are localized in the cytoplasmic leaflet of the membrane.

1.5 Techniques and parameters used in the study of the bilayer

The major techniques used to study bilayers are X-ray or neutron diffraction as well as Nuclear Magnetic Resonance (NMR). Though the latter is utilised to a lesser extent compared to diffraction techniques.

There are some basic structural parameters that the structural biophysicist strives to obtain. They are area of lipid, volume of lipid, electron density profile, phosphate to phosphate distance, *d*-repeat and order parameters of the carbons located in the hydrophobic chains. The typical samples for the study of the L_α phase are multi lamellar vesicles (MLVs) (Gennis, 1989). MLVs are normally a sample of purified lipid hydrated in aqueous solution to a pre-determined concentration; they may then be deposited on a silicon wafer or other surface such as a quartz slide. Experimental studies of biological membranes focus on the biologically relevant L_α phase. A cross-section of a typical lamellar vesicle is shown in Figure 1.5.

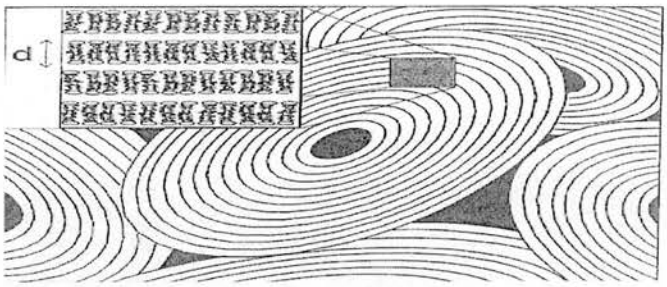

Figure 1.5. Cross-section of a lamellar vesicle. The Figure illustrates a lamellar stack of lipids within the vesicle. The symbol "*d*" represents the *d*-repeat. The *d*-repeat is the thickness of a single bilayer with a layer of water molecules and is the repeating unit of diffraction studies (modified from Nagle and Tristram-Nagle, 2000).

1.5.1 Area per lipid

The average area per lipid can be obtained by either using the gravimetric method or the electron density profile (EDP) method. An easier more cost-effective method would be the use of a Langmuir trough to obtain the area per lipid within a lipid monolayer.

1.5.1.1 The gravimetric method

The gravimetric method allows for the calculation of area per lipid without obtaining an EDP. The gravimetric X-ray (GX) method is also known as the Luzzati method (Luzzati and Spegt, 1967).

The key equation, is as follows

$$AD = 2(V_L + n_W V_W) \qquad \textbf{(1.1)}$$

Where A is the average area per lipid, D is the lamellar repeat, V_L is the average volume per lipid molecule, n_W is the number of water molecules per lipid molecule, V_W is the volume per water molecule. The major shortcoming of this method is that the gravimetrically determined value of n_w includes water molecules that go into defect regions between individual MLVs. However, the number required by the equation should only include the water molecules that are within or between lamellar arrays of bilayers. As a result this method, which has been used with a variety of lipids, over estimates the area per lipid. Rand and Parsegian formulated a modified method (GXC) to allow for a more accurate non EDP method for obtaining the area per lipid (Rand and Parsegian, 1989). They hypothesized that the defect region could be forced out by applying 10 atmospheres of osmotic pressure. The area per lipid obtained was then extrapolated to A_0 at full hydration using the following formula:

$$A = A_0 - AD_W P_{osm}/K_A \qquad \textbf{(1.2)}$$

Whereby AD_W is the water volume under osmotic pressure (P_{osm}) and K_A is the area compressibility. Using this method, the values obtained by various workers were indeed lower. Table 1.3 illustrates a range of values for area per lipid, obtained via GX, GXC and EDP methods. Further improvement was made on the GXC method, whereby a negative correction of –0.4 $Å^2$ was applied. The new value takes into account the relative bilayer fluctuations that are an integral part of a biological environment.

Method	DPPC (gel)	DPPC (L_α)	DMPC	DOPC	EPC
GX	52.3	71.2	65.2	82.0	75.6
GXC	48.6	68.1	61.7	72.1	69.5
EDP	47.9	62.9	59.7	72.2	69.4

Table 1.3. A comparison of values obtained for area per lipid ($Å^2$). Di-palmitoyl phosphatidylcholine (DPPC), di-myristoyl phosphatidylcholine (DMPC), di-oleoyl phosphatidylcholine (DOPC) and egg phosphatidylcholine (EPC) obtained from (Nagle and Tristram-Nagle, 2000).

1.5.1.2 Electron density profile (EDP) method

McIntosh and Simon first introduced this method as a method for obtaining the area per lipid (McIntosh and Simon, 1986). It was at first applied to di-palmitoyl phosphatidylcholine (DPPC). This method used the gel phase structure. Though this phase is not biologically relevant, it is very similar in terms of structural parameters to the biologically relevant L_α phase. The gel phase structure can be accurately determined using wide angle chain packing diffraction. The differences in volume and thickness are used to obtain the area per lipid in the L_α phase. This method has been applied to other phospholipids such as di-oleoyl phosphatidylcholine (DOPC) (Tristram-Nagle *et al.,* 1998), DPPC (Nagle *et al.,* 1996), di-myristoyl phosphatidylcholine (DMPC) and egg phosphatidylcholine (EPC) (Petrache *et al.,* 1998). These values are displayed in table 1.3. The values reported which were obtained by the EDP method were slightly lower than those obtained with the GXC method.

1.5.2 Volume of lipid

Measurements of lipid volume have been performed using a variety of techniques. Neutral flotation can be employed, whereby the density of the aqueous solvent is varied by mixing ^2H_2O with H_2O, combined with dilatometry which measures volume changes as a function of temperature. The density of the lipid is then given by the density of the aqueous mixture in which the bilayers neither sink nor float. However, this method is restricted to lipids that have densities which fall between ^2H_2O and H_2O (Nagle and Tristram-Nagle, 2000). Alternative methods for calculating the volume of lipid are the use of a differential vibrating tube densimeter, differential weighing or buoyant forces. In contrast to values obtained for the area of lipid, disagreement between the different methods is about 0.3% (Nagle and Tristram-Nagle, 2000). Many workers have assumed that the partial specific volume of the lipid equals that of water (i.e. 1 ml = 1 g). This has proved to be a reasonable approximation when considering the proximity of values obtained. This method is accurate and reliable for the L_α phase. However, it has been shown to be less reliable in the biologically less relevant gel phase. Table 1.4 displays values obtained for volume per lipid (V_L), from the literature. The volumes of lipid vary when the temperature of the sample is altered, this is primarily due to the alteration of energy content, which subsequently affects the packing of lipids within the unit cell.

Lipid	Temperature (°C)	$_{v}L$ (ml/g)	V_L (Å^3)
DPPC	20	0.939	1144
		0.937	1142
		0.940	1145
DPPC	50	1.011	1232
		1.009	1230
DMPC	30	0.977	1100
		0.978	1101
DOPC	30	0.999	1303
	22	0.993	1296
EPC	30	0.988	1261
	20	0.981	1252

Table 1.4. Comparison of values obtained for volume per lipid (Å^3). Di-palmitoyl phosphatidylcholine (DPPC), di-myristoyl phosphatidylcholine (DMPC), di-oleoyl phosphatidylcholine (DOPC) and egg phosphatidylcholine (EPC) obtained from (Nagle and Tristram-Nagle, 2000).

1.5.3 Order parameters of the hydrocarbon chains

The use of Nuclear Magnetic Resonance (NMR) can give a detailed picture of the phospholipid bilayer. In this spectroscopic technique, a target (e.g. bilayer stacks) is irradiated by electromagnetic radiation and radiation emitted from the target is detected (Gennis, 1989). The resonance spectrum obtained gives information about the energy states of the target atomic nucleus. When a magnetic field (B_0) is switched on, the nuclear spin interacts with the magnetic field. This results in the degenerate energy being split into different lines. The magnitude of the splitting depends on the type of atom and on the magnitude of the magnetic field. This allows for the identification of different types of atoms within the target.

There are two splittings that are of particular interest to the NMR spectroscopist. They are the chemical shift and quadrupole splitting (Gennis, 1989). Chemical shift is caused by the additional local fields due to the magnetic moments of electron shells. These local fields are anti parallel to the external field. They are described by the following equation:

$$B_{local} = B_0 - B_{induced} \qquad \textbf{(1.3)}$$

The magnetic moment of $B_{induced}$ depends on the characteristic neighbourhood of the probe nucleus. These characteristics are the bonding state of the electrons and the electron density. This allows for the identification of functional groups, such as CH_2 and CH_3 in lipid hydrocarbon chains, which have different $B_{induced}$ values.

Quadrupole splitting is caused by magnetic interactions between the nuclear spin moments of deuterium atoms and the quadrupole moments of the carbon-deuterium bonds. This splitting depends upon the orientation θ of the deuterium bond in their functional group, relative to the applied field, B_0. The following equation is used to describe the interaction:

$$B_{quadrupole} \propto \pm (1\text{-}3\cos^2\theta) \qquad \textbf{(1.4)}$$

This relation provides information about segmentational order and orientation of functional groups in macromolecules. For the measurement of the orientation of a special CH_2 group in a macromolecule, the H atoms are replaced with ^2H atoms, which possess a nuclear spin moment. Utilising the chemical shift allows for the identification of the group. Quadrupole splitting provides information on the orientation. These experiments are routinely performed in order to gain structural information on the hydrocarbon chains present in the hydrophobic core of membranes (Gennis, 1989). The values obtained for order parameters are between -0.5 and 1. A value of -0.5 refers to a bond vector which is completely parallel to the bilayer plane, a value of 1 refers to a bond vector which is completely perpendicular to the bilayer plane.

1.5.4 Meaning of structure in fluid bilayers

The projection of a fluid bilayer can be defined as the time-averaged spatial distributions of the principal structural (quasi-molecular) groups of the lipid projected onto an axis normal to the bilayer plane (Wiener and White, 1991; Wiener

and White, 1992a), as shown in Figure 1.6 for the phosphorous atom of a phosphatidylcholine molecule. This procedure would require ^{2}H labelling.

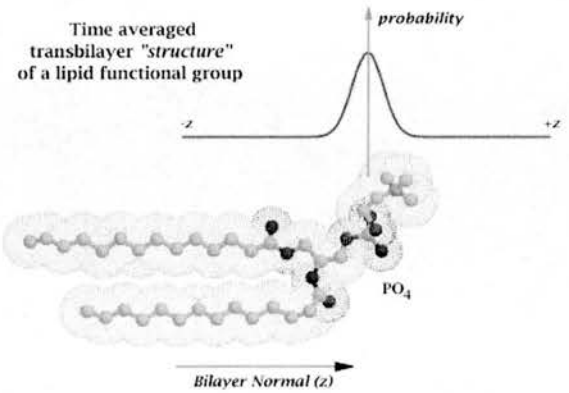

Figure 1.6. Time averaged transbilayer structure of one atom of a lipid (di-oleoyl phosphatidylcholine) (modified from Wiener and White, 1992a).

1.6 Computer simulations of pure lipids

1.6.1 Overview of the literature

As previously described, biological membranes are enormously complex in terms of both structure and dynamic properties. In order to understand membrane properties, model systems which consist of well known membrane phospholipids are studied. These models tend to utilize either molecular dynamics (MD) or Monte Carlo (MC) simulations. There have been cases cited within the literature where both MD and MC simulations have been utilised (Chiu *et al.,* 1999).

The major development in MD simulations over the past two years has been the increase in time scales of simulations. One of the first long time scale simulations of phospholipid systems was performed by Lindahl (Lindahl and Edholm, 2000). A

lipid bilayer system composed of 64 di-palmitoyl phophatidylcholine (DPPC) and 23 water molecules per lipid were simulated over 60 ns. In addition, a large bilayer composed of 1024 DPPC lipids with the same number of waters per lipid was also simulated, though for only 10ns. The relatively long time scales enabled the analysis of dynamical fluctuations, which were previously unexplored. A finite size scaling analysis of the simulations led the authors to conclude that thickness fluctuations are primarily responsible for the dependence of the simulation area per molecule on the size of the simulation box. An excellent example of the use of MD simulations in the study of bilayer assembly was the self assembly of a lipid bilayer from initially random dispersions of 64 lipids in a box with 3000 water molecules (Marrink *et al.,* 2001). This self assembly occurred in just 25 ns. For larger systems the self assembly time was slower and in the 256 DPPC system a micelle formed in addition to a separate bilayer. The relatively rapid time taken for self assembly in the 64 lipid system is probably due to the small system size, which reduces the number of molecules that need to cooperatively align in order to form a bilayer. Nevertheless, these simulations provided a unique glimpse of a critical biophysical process. The observed intermediate assembly states could also be present in larger scale events, which may include membrane fusion, exocytosis and endocytosis (Marrink *et al.,* 2001).

Feller and co-workers (Feller *et al.,* 1997a) successfully carried out MD simulations of the gel phase of DPPC. A major characteristic of this phase is the tight molecular packing and the parallel tilted hydrocarbon chains, with chain axes extending straight across both leaflets. These characteristics cause difficulties in simulation setup

which are not encountered when setting up simulations of other lamellar phases. Simulations of seven systems were carried out to examine the effect of Ewald summation as opposed to spherical cut-offs. Ewald summation and cut-offs are typical algorithms used to treat electrostatic interactions in an MD simulation. They are described in more detail in section 3.2.4.

These simulations comprehensively demonstrated that all-atom models are necessary for accurate simulation of the gel phase, as are the use of constant pressure, rather than a constant volume of the simulation box. Theoretically the use of Ewald summation is arguably the correct method for treating long-range electrostatic effects in the simulations of the gel phase. The MD simulation which used the particle mesh Ewald (PME) algorithm to treat electrostatic interactions, predicted a consistently lower area per molecule than experiment (by 1-2 $Å^2$) whereas simulations which utilised cut-offs were more accurate (within 0.1-0.2 $Å^2$). However, when experimental d-repeats of lamellar stacks of bilayers are compared, PME yields a far more realistic value.

Moore and co-workers (Moore *et al.,* 2001) carried out simulations of DPPC and DMPC bilayers with particular emphasis on the calculation of dynamical properties. Trajectories for fluid phase DMPC bilayers were analyzed to examine rotational diffusion (RD) for entire lipid molecules. Their findings revealed that whole chain rotational diffusion was slower than headgroup rotational diffusion, which in turn was slower than whole molecule diffusion. These results were significant for their

insights into the details of rotational diffusion over the 3ns of simulation time. Rotational diffusion can be described using three definitions.

1. Rotational diffusion of the P-N vector in the polar headgroup region.
2. Rotational diffusion of vectors from the top carbon to the bottom carbon for each of the two acyl chains.
3. A vector between the selected atoms on each of the acyl chains in each molecule.

The values Moore and co-workers calculated ranged from 0.04 rad^2/ns (for RD of the vector between the 8^{th} carbons on the two acyl chains) to 25 rad^2/ns for RD of the vectors from the top carbon to the bottom carbon of each of the acyl chains. The experimental value measured from POPC labelled with a fluorophore was 0.7 rad^2/ns. This was smaller than the calculated P-N RD constant, which were 2.2 rad^2/ns. The discrepancy may be due to the necessity of going beyond 3ns in the simulations to fully sample the rotational mechanisms that contribute to diffusion.

Feller and co-workers (Feller *et al.,* 1997b) utilised MD simulation trajectories to calculate nuclear Overhauser enhancement spectroscopy (NOESY) cross relaxation rates. The simulated system consisted of 72 POPC molecules, 72 ethanol molecules, and 720 waters. The simulation predictions were used in the interpretation of experimental NOESY data. Results revealed that ethanol binds to the bilayer surface. Hydrogen bonding and hydrophobic interactions stabilized the binding of ethanol.

Feller and co-workers (Feller *et al.,* 1997b) then further extended the application of MD simulations to the study of biological membranes. They used a bilayer of 72 polyunsaturated DPPC lipids and 15.1 waters per lipid. This was the first systematic combined experiment and simulation study of a lipid system consisting of one saturated chain and with a sequence of six double bonded carbons, each preceded and followed by a single bonded carbon. They used a constant pressure ensemble (1 atmosphere). The experiments and simulations revealed the effect of the very high degree of flexibility of the polyunsaturated chain. The difference in values between order parameters for this chain was within 5% of each other.

Mashl and colleagues (Mashl *et al.,* 2001) carried out an atomic level simulation of the effect of hydration on lipid bilayer structure. These studies were carried out based on experimental studies carried out by Hristova and White (Hristova and White, 1998). This study utilised five systems of 128 molecules of DOPC with a ratio of waters per lipid of 5.4:1, 11.4:1, 16:1, 23:1, and 30:1, respectively. This group demonstrated that DOPC headgroups became more parallel to the membrane surface with increasing hydration and that the dipole potential reversed direction at low hydration (particularly at a water per lipid ratio of 5.4:1). These simulations support the hypothesis that 12 waters per lipid make up the first hydration shell, consistent with an observed break point in a plot of Bragg spacing versus hydration level (Hristova and White, 1998).

Pandit and Berkowitz (Pandit and Berkowitz, 2002) were amongst the first groups that utilised counter ions in their MD simulations. They created a system using the anionic lipid DPPS which has a total negative charge of one. Sodium counter ions were used to counteract this charge. Counter ions are particularly challenging to utilize in MD simulation due to the fact that are not physically bound to any structure within the structure, careful energy minimization is necessary for a successful simulation. Pandit and Berkowitz found that hydrogen bonding between the NH^{3+} and PO_4 groups on neighbouring lipids cause DPPS bilayers to have a smaller area per molecule than DPPC. The sodium counter ions tend to coordinate with serine and phosphate oxygens on a single DPPS molecule.

More recently, MD simulations of mixed phospholipids bilayers have appeared in the literature. Huber and co-workers (Huber *et al.,* 2002) described a simulation of DPPC and POPC in equimolar ratios in the liquid crystalline state. This group used combined NMR and MD studies to solve the structure of this bilayer, the constituents of which are predominantly present in neural tissues. Balali-Mood and co-workers (Balali-Mood *et al.,* 2003) have reported an MD simulation of a mixed DOPC/ DOPG bilayer, this study is described in detail in chapter three of this thesis.

1.7 Lipid phases

The ability of a given mixture of lipids to form structurally diverse structures is called polymorphism or mesomorphism (Gennis, 1989). A well known example of mesomorphism is displayed by carbon, which can exist in crystallographically distinct phases of graphite or diamond. Lipids can exist in a number of polymorphs or phases, different examples of which can be observed when lipids are extracted from biomembranes. By studying polymorphism in isolated lipids, an understanding of the forces which are present within biomembranes and effect the organization and function of proteins and sugars can be gained. However, it should be pointed out that lipids are predominantly organized as bilayers within the living organism. Insights into the phase behaviour of lipids can aid biomedical science as a whole. For example, an understanding of the behaviour of pure lipid vesicles may be important in developing liposomal drug delivery systems.

A number of non-lamellar phases exist (Gennis, 1989). Figure 1.7 illustrates the lamellar and non-lamellar phases seen in most biologically relevant phospholipids. The main non-lamellar phases observed are the hexagonal and cubic phase (not shown in Figure 1.7).

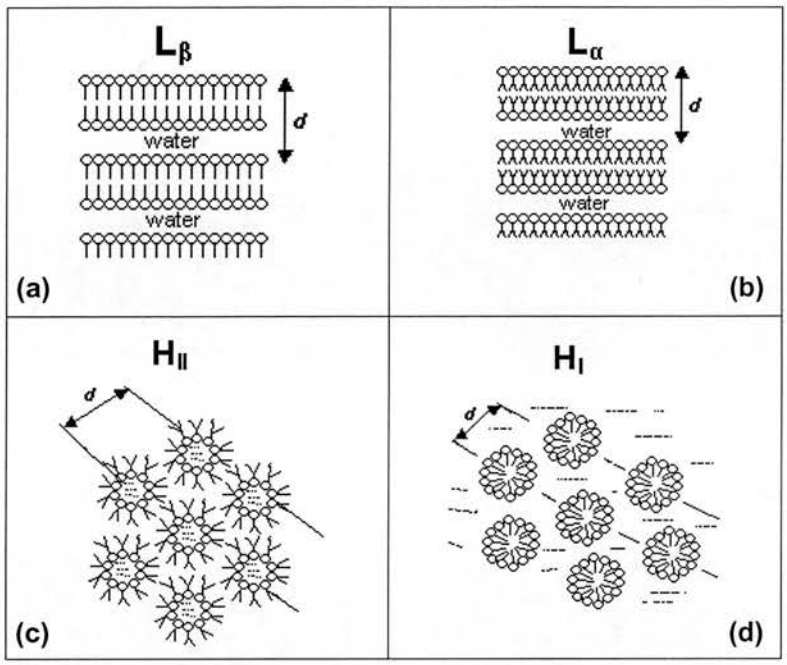

Figure 1.7. Lamellar and hexagonal phases observed in lipids. (a) the gel phase, (b) the biologically relevant L_α phase, (c) the inverted hexagonal phase and (d) the non-inverted hexagonal phase (d = d-repeat) (Modified from Gennis, 1989).

Membrane bending of bilayers can lead to the formation of non-lamellar structures. Bending of a monolayer can be characterized by the curvatures of a surface lying inside to the monolayer close to the interface between the polar heads and the hydrocarbon chains of the lipids (Figure 1.8A, dashed lines). Membrane bending of a bilayer can be described by the curvatures of the surface between the monolayers (Figure 1.8B). Surface bending can be characterized by two principal curvatures (Figure 1.8C). However, to best describe the bending, their combinations are used. This combination is referred to as the total curvature (J).

$$J = C_1 + C_2 \qquad \textbf{(1.5)}$$

Where C_1 refers to the upper monolayer and C_2 refers to the lower monolayer. Curvature for a monolayer can be explained in a simple and concise manner. If $J>0$, then the curvature is positive. In other words positive curvature occurs when the surface bends towards the polar headgroups. In the case of a bilayer, positive curvature corresponds to the bending towards the outside medium (figure 1.8B).

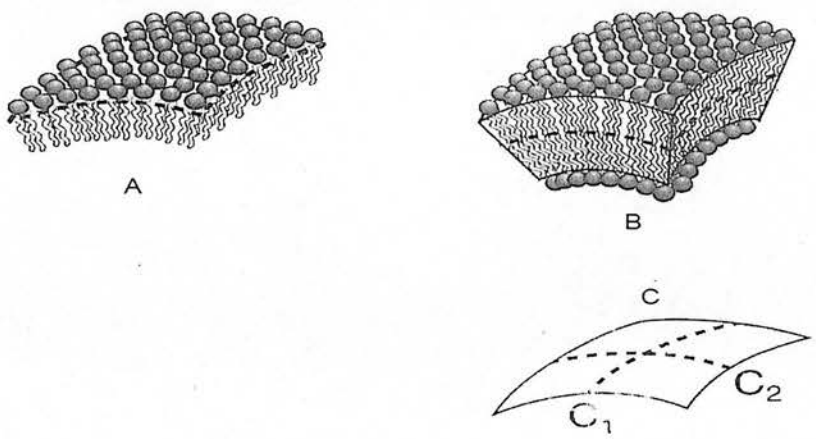

Figure 1.8. Membrane bending. A. bending of a monolayer. B. Bending of a lipid bilayer. C. Curvatures of the surface, which represent the bilayer.

One of the first reports of curvature altering phase transitions and interfacially curved lipid mesomorphs was by Luzzati and colleagues in 1968 (Luzzati *et al.,* 1968). However, it was in the 80s and 90s that a quantitative understanding of the competition of free energies that control curvature altering phase transitions was developed. This was a direct result of the rapid growth in interest in the implications of non-lamellar phases, when Cullis and colleagues began using ^{31}P NMR, as a probe of phase behaviour in lipids (Cullis and de Kruijff, 1979). Current opinion is that most biomembranes contain large lipid fractions that in isolation do not form lamellar bilayers. Nature could well have chosen biomembrane constituents that did not contain such non-lamellar prone lipids, but still have accounted for all the

physical properties of lipid bilayers in the L_α phase, that are believed to be biologically important. This led to workers questioning why non-lamellar prone lipids are so prevalent within biomembranes. This resulted in studies on the properties of lipid mixtures containing non-lamellar prone lipids and advances in the understanding of the physics of curvature altering phase transitions (Ellens *et al.*, 1989).

Non-lamellar phases can be broadly divided into two types, (hexagonal and cubic) (Yeagle, 1993). The lipids are either in an inverted or non-inverted arrangement. Another way of describing this arrangement is "water in oil" for inverted and "oil in water" for non-inverted. This terminology refers to the curvature and majority constituent of oil-water-surfactant micelles. At a high water-oil ratio the non-inverted formation is found. However, when this ratio decreases such that, the majority constituent is oil, the system often inverts and results in surfactant coated water droplets in oil (Yeagle, 1993).

1.8 Membrane active peptides

Membrane proteins account for ~25% of all genes and constitute ~50% of potential therapeutic targets. Protein crystallographers have solved thousands of proteins soluble in solution. However, only a handful of membrane proteins have been solved (e.g. bacteriorhodopsin and aquaporin). This is primarily due to the fact that membrane proteins are extremely difficult to crystallize. However, membrane active

peptides can be studied when membrane bound using diffraction techniques and NMR. Membrane active peptides can have a random coil structure, α-helical or β-strand or other secondary structure when membrane bound.

The best studied secondary structure of membrane active peptides is an amphipathic helix. An amphipathic helix may be defined as an α-helix with opposing polar (hydrophilic) and non-polar (hydrophobic) faces oriented along the long axis of the helix (Segrest *et al.,* 1974). Amphipathic helices can interact with bilayers in two orientations. The helix can lie parallel to the bilayer surface and be partially embedded within the bilayer. Hydrophilic residues remain exposed to the aqueous medium while the hydrophobic residues are facing the hydrophobic core of the bilayer. The alternative orientation is when the axis of the helix lies parallel to the bilayer normal (*z*). The helix is now membrane spanning (transmembrane). In order to adopt a transmembrane orientation without exposing the hydrophilic amino acid residues to the hydrophobic chains of the bilayer, it is necessary that the peptide aggregates into helical bundles. The resulting structure will be a "tube" with a hydrophilic core, which could have ion channel properties. Ion channel properties depend upon the the physical properties and dimensions of the helical bundles. There are many possibilities, which depend upon the number of monomers within the bundle and its relative angle of penetration to the bilayer normal. Other factors can be the presence of the known helix breaker, proline within the sequence. Neutron diffraction, complemented by the use of deuterium labelling, is a powerful experimental technique for distinguishing between two possible orientations of amphipathic helices (Bradshaw *et al.,* 1996).

Membrane active peptides can induce membrane lysis. Membrane lytic peptides are small (10-30 amino acid residues long) amphipathic molecules which are normally found in a α-helical conformation. It is proposed that these peptides act by a general mechanism which is not completely understood. These peptides can act by either coating the membrane and disrupting it by acting somewhat like a detergent and ultimately disintegrating it (the carpet mechanism) (Shai *et al.,* 2002). The alternative method proposed is the formation of transmembrane pores lined by peptides, thus starving the target cell of energy and nutrients (barrel-stave mechanism) (Zasloff, 2002).

The main class of membrane active peptides which this thesis is concerned with are the viral fusion peptides. Enveloped viruses tend to contain a viral fusion protein in a polysaccharide viral coat (Colotto *et al.,* 1996). Viral fusion proteins usually contain a highly conserved N-terminal that has been shown by mutagenesis studies to be crucial to the process of fusion, between the viral envelope and the membrane of the host cell. Small peptides (between 10-30 residues long) which are derived from the N-terminal of the larger viral fusion protein are termed fusion peptides. These peptides retain some of the membrane fusion activity of the larger viral fusion protein, albeit with slower rates and lack of a specific binding function. In addition, they insert into bilayers in an oblique manner. Brasseur and co-workers (Brasseur *et al.,* 1990) have proposed an elegant model for the action of obliquely inserting amphipathic helices acting upon bilayers. Brasseur conducted some molecular

modelling studies and proposed that the angle of insertion of the fusion peptide of SIV is ~57°. Brasseur's model predicted that the fusion peptide will insert into target membranes at an oblique angle relative to the bilayer normal (Brasseur *et al.,* 1990). The oblique angle of insertion is based on the quantification of the hydrophobic moments (Eisenberg, *et al.,* 1982), as well as the peptide being in a α-helical conformation. The contributed hydrophobic moment of each amino acid was projected perpendicular to the helical axis. According to the model, hydrophobic residues have positive values, whereas hydrophilic residues have negative values. This is an approximation. However, the hypothesis that fusion peptides form helical structures is not unreasonable as previous studies had demonstrated that fusion peptides gain helicity when membrane bound (Lear and DeGrado, 1987). Further evidence was presented that fusion peptides such as the fusion peptide of SIV, maintain a predominantly α-helical conformation, when membrane bound (Wimley and White, 1996).

In short, fusion peptides catalyse the merging of viral and endosomal leaflets (White, 1990). The process of fusion involves an orchestrated change in the structure of both the fusion peptide and in the membrane lipids. This will result in the creation of a fusion pore which could allow the passage of the viral genome into the target cytoplasm (Spruce, *et al.,* 1991). The fusion peptide of primary interest to this thesis is the fusion peptide of the Simian immunodeficiency virus (SIV), which is discussed in the proceeding section.

1.8.1 Quantification of secondary structure of a peptide

In a polypeptide the main chain N-Cα and Cα-C bonds are relatively free to rotate. These rotations are represented by the torsion angles *phi* (Φ) and *psi* (Ψ), respectively. Ramachandran (Ramachandran, 1969) used computer models of small polypeptides to systematically vary Φ and Ψ with the objective of finding stable conformations. For each conformation, the structure was examined for close contacts between atoms. Atoms were treated as hard spheres with dimensions corresponding to their van der Waals radii. Therefore, Φ and Ψ angles which cause spheres to collide correspond to sterically disallowed conformations of the polypeptide backbone.

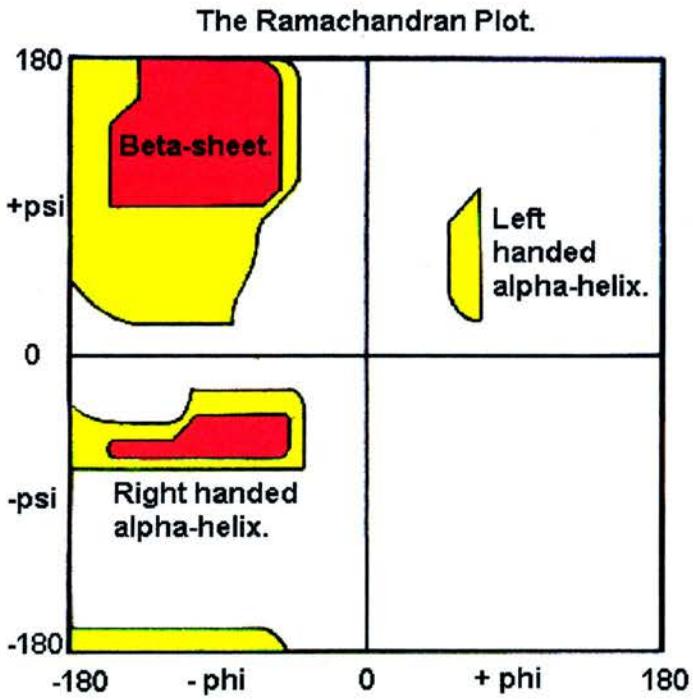

Figure 1. 9. The Ramachandran plot.
(modified from www.crystallography.bbk.ac.uk)

In the diagram above the white areas correspond to conformations where atoms in the polypeptide come closer than the sum of their van der Waals radii. These regions are sterically *disallowed* for all amino acids except glycine which is unique in that it lacks a side chain. The red regions correspond to conformations where there are no steric clashes, ie these are the allowed regions namely the alpha-helical and beta-sheet conformations. The yellow areas show the allowed regions if slightly shorter van der Waals radi are used in the calculation, i.e. the atoms are allowed to come a little (2 Å) closer together. This brings out an additional region which corresponds to the left-handed alpha-helix.

L-amino acids cannot form extended regions of left-handed helix but occasionally individual residues adopt this conformation. These residues are usually glycine but can also be asparagine or aspartate where the side chain forms a hydrogen bond with the main chain and therefore stabilises this otherwise unfavourable conformation. The 3(10) helix occurs close to the upper right of the alpha-helical region and is on the edge of allowed region indicating lower stability. Disallowed regions generally involve steric hindrance between the side chain C-β methylene group and main chain atoms. Glycine has no side chain and therefore can adopt Φ and Ψ angles in all four quadrants of the Ramachandran plot. Hence it frequently occurs in turn regions of proteins where any other residue would be sterically hindered.

1.9 Simian immunodeficiency virus (SIV)

1.9.1 The sequence and mode of action of the fusion peptide of SIV

The primary sequence of the peptide is as follows:

Gly-Val-Phe-Val-Leu-Gly-Phe-Leu-Gly-Phe-Leu-Ala

The fusion peptide region for SIV is the hydrophobic N-terminus of a transmembrane region of a viral envelope glycoprotein spike. In this case, this is the N-terminus of gp32, which itself is cleaved from gp160 (Bosch, *et al.,* 1989). Fusion assays have shown that the most active version of SIV peptide is only 12 amino acids long (the aforementioned primary sequence) (Martin, *et al.,* 1991). Recent reports include an X-ray diffraction study of SIV in multi lamellar vesicles of N-methylated di-oleoyl phopshatidylethanolamine (DOPE-me) (Harroun *et al.,* 2003). It was proposed that SIV acts upon the hydrocarbon matrix of the phospholipids (Harroun *et al.,* 2003).

Experimental studies were in agreement with Brasseur's model, such as a novel neutron diffraction study by Bradshaw and co-workers (Bradshaw *et al.,* 2000). These studies confirmed the angle of insertion, proposed by Brasseur (~57°). Furthermore, the studies gave previously undiscovered structural insights into the action of the SIV fusion peptide on a DOPC bilayer (Bradshaw *et al.,* 2000).

Whilst the majority of fusion peptides in the current literature are predominantly α-helical, there is evidence for viral fusion peptide having a β- structure. Most proteins that insert into biological membranes as β-structures do so as β-barrels. There is no "edge" with unfulfilled hydrogen bonding. The possibility of model fusion peptides aggregating as β-structures on the surface of the membrane can not be discounted. In the case of the intact fusion protein, it is difficult to see an *a priori* reason how a sufficient number of fusion proteins can cluster together such that, their fusion peptide segments associate and subsequently form a β-barrel. Nevertheless, there is evidence that the fusion peptide of HIV can form a β-structure at the amino terminus (Peisajovich *et al.,* 2000).

The degree of hydrophobicity and distribution of hydrophobic residues along the helical axis are important for fusion to occur. For example, it has been shown that changing the hydrophobicity of the fusion peptide via the addition of polar residues will result in the reduction of fusogenic activity (Bosch *et al.,* 1989). Furthermore, rearrangement of the primary sequence in order for global hydrophobicity to be maintained but alter the theoretical tilt reduced the rate of fusion. Point mutations that were intended to alter the global hydrophobicity and the optimal angle of insertion did not alter fusogenic activity (Epand *et al.,* 1994). Experiments were carried out on SIV gp160 expressed on a virus vector, which clearly demonstrated no alteration of fusogenic activity when point mutations were introduced (Epand *et al.,* 1994).

It has been suggested that the oblique insertion of the peptide will facilitate the positioning of bulky hydrophobic residues in the hydrocarbon core and smaller residues at the interface (Epand *et al.,* 1992). This orientation will locally disrupt the phospholipids in terms of hydrocarbon chain packing but not interfacially. Peptide precession around its helical axis will lead to bilayer perturbation that in turn causes the lipids to develop negative curvature strain (Gruner, 1985). This could result in the lipid molecules forming non-bilayer structures, a pre-requisite for fusion pore formation.

Promotion of negative curvature by fusion peptides is in accord with the requirement to increase the negative curvature of the contacting monolayers to form the hemifusion intermediate (Siegel, 1999). This concept can also be applied to explain the common finding that fusion peptides insert into a membrane as a tilted helix. Such an orientation is consistent with the observation that the peptide promotes negative curvature, as it would be anticipated that such an angle of insertion would have greater effect in expanding the region in the centre of the bilayer than at the membrane interface (Peisajovich *et al.,* 2003).

1.10 Overview and aims of the thesis

The primary objective of this thesis was to study the atomic details of SIV fusion peptide and its actions upon a model membrane, utilising the powerful computational

technique of MD simulation. Membrane fusion which can be induced by a fusion peptide (e.g. fusion peptide of SIV or HIV) is a fundamental biological process. Insights into the molecular mechanisms of fusion can elucidate potential therapeutic targets. To achieve this objective it was necessary to perform some experimental (neutron diffraction) and pre-requisite MD simulations.

Neutron diffraction is a structural technique that can provide details on the location of peptides embedded within synthetic membranes. The starting conditions of the SIV fusion peptide were derived from neutron diffraction data (Bradshaw *et al.,* 2000). Therefore it was logical to perform neutron diffraction experiments, to gain an appreciation of this technique. Chapter two describes a neutron diffraction study of a membrane active peptide, and comparison of structural location between the human and rat forms of this peptide.

A pre-requisite of constructing a membrane peptide simulation is the ability to carry out pure membrane simulations. Chapter three describes the construction and simulation of pure phospholipids bilayers. A customized forcefield was created and two types of bilayer were constructed. The first bilayer constructed was a single entity zwitterionic bilayer (DOPC). The second bilayer was a mixed bilayer of DOPC and DOPG (7:3 ratio). These bilayers had previously been studied using neutron diffraction by other members of the Laboratory.

To test the MD approach against experimental data, four alternative bilayer bound conformations of parallel oriented peptide were subjected to MD simulation. This demonstrated the ability of MD simulation to discriminate between unlikely conformations before moving onto oblique inserting peptides. Chapter four describes these studies.

Chapter five focuses on a long time-scale MD simulation study of the fusion peptide of SIV embedded within a pre-equilibrated DOPC bilayer. This chapter aims to provide novel information on the actions of a fusion peptide upon a bilayer. The main focus is on the order parameters of the lipid chains and the distribution of water molecules in the system. In addition, the secondary structure of the membrane bound fusion peptide is probed and discussed.

CHAPTER 2

Neutron diffraction of pre-fibrillar islet amyloid polypeptide in phospholipid bilayers

2.1 Aims of the chapter

In order to construct an accurate model for MD simulations, it is first necessary to obtain high-resolution structural data. The structural data which were used to construct the model of membrane bound SIV fusion peptide were obtained from neutron diffraction studies (Bradshaw *et al.,* 2000). Therefore, an understanding of neutron diffraction is a pre-requisite to constructing an accurate model for MD simulation.

The work described in this chapter aimed to obtain structural information regarding the location of the human and rat forms of Islet Amyloid Polypeptide (IAPP) in relation to a mixed equimolar bilayer of palmitoyl-oleyl phosphatidylethanolamine (POPE) and palmitoyl-oleyl phosphatidylserine (POPS).

The literature suggests that rat IAPP does not insert into cell membranes and forms amyloid deposits (Jaikaran and Clark, 2001). However, in stark contrast human IAPP inserts into monolayers, when studied on a Langmuir trough. Previous studies (Harroun *et al.,* 2001), had shown that human IAPP inserts into monolayers of equimolar POPE/POPS. However, to date no structural studies of membrane associated IAPP, have been performed. The studies described here will lead to information which will give previously undiscovered insights into the location of each of these peptides in relation to the bilayer as well as the distribution of water within these systems.

2.2 Diffraction studies

Our current understanding of the physics of materials is based upon knowledge of the internal arrangement of atoms or molecules within the structure in question. This knowledge is largely based upon diffraction and scattering techniques. As atoms are spaced ~2 Å apart, we employ radiation of a similar wavelength. The most widely used probes are either X-rays or neutrons, with a wavelength of 1-5 Å (Warren, 1987). In the subsequent sections, the history and properties of the neutron will be discussed. In addition, a brief comparison is made between X-rays and neutrons. The collections and subsequent analysis of data obtained from these studies are described in the proceeding sections.

2.2.1 Historical background

Neutrons have been known as building blocks in the atomic nucleus for nearly seven decades (Nobel Prize to Chadwick in 1935 for their discovery). Enrico Fermi showed in 1942 that neutrons from fission of the uranium nucleus could support a controlled chain reaction. He had earlier made the important discovery that moderated or thermal neutrons show a much greater inclination to react than fast ones do. A Nobel Prize was awarded for this discovery to Fermi among others in 1938 (Bacon, 1975). It is the special properties of slow neutrons that make them suitable for detecting the positions and movements of atoms. Even before the entry of nuclear reactors into the research arena, results from using simple neutron sources had indicated that neutron beams could be used for studying solid bodies and liquids.

These simple sources were first elucidated by Sir James Chadwick. Chadwick realised that the Joliot-Curies had produced free neutrons by the interaction of alpha particles with beryllium nuclei. However, there were many difficulties to be overcome before these possibilities could be realized (Warren, 1987). The 1994 Nobel Prize in Physics was awarded to Bertram Brockhouse and Clifford Shull for their pioneering contributions to the development of neutron scattering techniques for studies of condensed matter: for the development of the neutron diffraction and neutron spectroscopy techniques. In simple terms, they helped answer the questions of where atoms "are" and what atoms "do".

2.2.3 What is a neutron?

A neutron is an uncharged subatomic particle with mass 1,839 times that of the electron. Neutrons are stable when bound in an atomic nucleus, whilst having a mean lifetime of approximately 1000 seconds as a free particle. The neutron and the proton form nearly the entire mass of atomic nuclei, so they are both called nucleons (Bacon, 1975).

Neutrons possess a spin of 1/2. They therefore have a magnetic moment that can couple directly to spatial and temporal variations of the magnetisation of materials on an atomic scale. Unlike other forms of radiation, neutrons are ideally suited to the study of microscopic magnetism, magnetic structures and short wavelength magnetic fluctuations. The neutron is also a powerful probe for the study of soft matter (e.g. biological membranes) or condensed matter (e.g. steel). Neutron scattering gives

detailed information such as the atomic composition of condensed matter, hence playing a major role in shaping the experimental and theoretical understanding of materials ranging from magnetism and superconductivity to chemical surfaces and interfaces (Bacon, 1975).

2.2.4 Comparison of neutrons and X-rays

Neutron diffraction has significant advantages over other forms of radiation in the study of microscopic structure and dynamics as described below. 1) Neutrons are scattered from materials by interaction with the nucleus of an atom rather than the electron cloud as is the case with X-rays. This means that the scattering length (cross-section) of an atom is not strongly related to its atomic number, unlike X-rays. There is one major advantage in using neutrons to probe matter: the nuclear dependence of scattering allows isotopes of the same element to have substantially different scattering lengths for neutrons. Isotopic substitution can be used to label different parts of the molecules making up a material. This is commonly done by biophysicists, whereby selected amino acids in a peptide can be deuterated (i.e. hydrogens substituted with deuterons). 2) The neutron can probe deeper into a sample core because it is uncharged (it has an extremely small and unknown dipole moment). There are effectively no electrostatic forces to overcome. In fact approximately 98% of the primary beam passes through the sample un-deviated (Bacon, 1975). This explains the extensive shielding that is required for the beam stop in neutron diffraction instruments. 3) The radiation does not cause extensive

ionization of the sample. This is certainly not the case with X-rays, as ionizing radiation (X-rays) damages the sample within a few hours.

Having looked at the advantages of using neutrons over X-rays to study matter, the focus now changes to the advantages of X-rays over neutrons from a structural scientist's point of view. There are main disadvantages with neutron scattering compared to X-rays:

1. Neutron flux is very low compared to modern x-ray sources. At present neutron flux is the equivalent to the X-ray flux of the 1950s.
2. Large quantities of sample are required when using neutrons as a probe to study matter, which could prove to be cost inefficient. This is because of the low flux associated with neutron sources.

2.3 Background to the theory of diffraction

Max von Laue was the first scientist to discover that X-rays could be diffracted in an orderly manner from a crystal (Bragg, 1968). At this point, it is worth describing the phenomena of diffraction. Diffraction is defined as the deviation of a wave from its natural direction, when it encounters an object or medium with spatially varying transmittance (Warren, 1987).

A barrier or an aperture will cause waves to diffract. This occurs maximally when the wavelength is of a similar size to the aperture. In other words, neutrons are used to study matter as the inter-atomic spacing of structures (biological or non-biological) is similar in size to the wavelength (λ) of neutron beams. When a number of regularly spaced apertures are encountered by a wave train this will result in wave interference. When the waves are "in phase" constructive interference results. However, when waves are out of phase this gives rise to destructive interference. Figure 2.1 describes the phenomena of in phase (2.1a) and out of phase waves (2.1b).

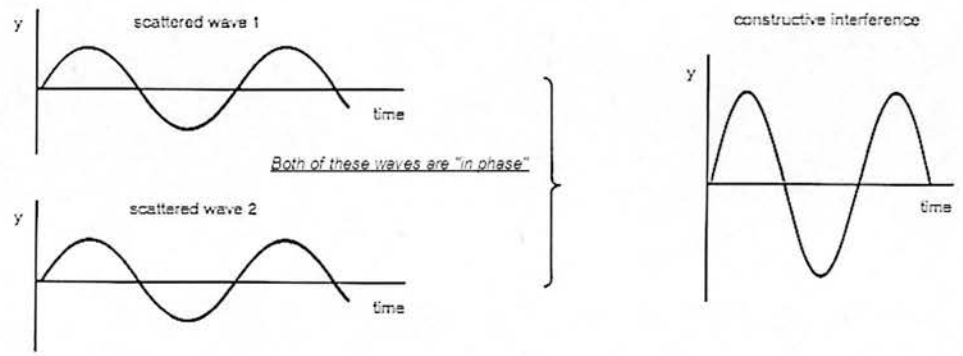

Figure 2.1a. Two waves which possess the same wavelength (λ) and are "in phase".

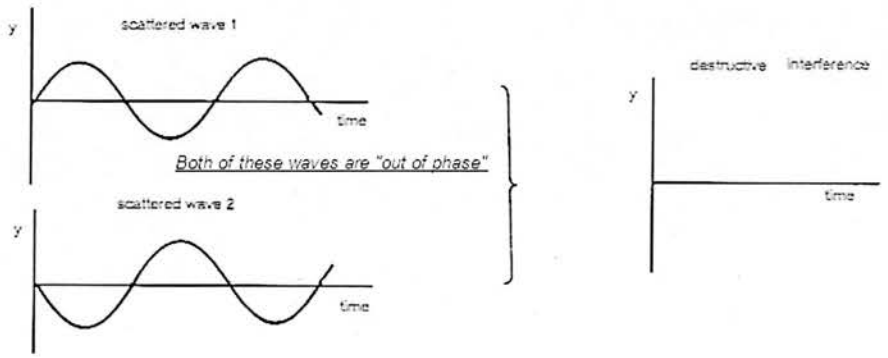

Figure 2.1b. Two waves that possess the same wavelength (λ) but are "out of phase".

2.3.1 The Bragg equation

Monochromatic beams will only diffract at discrete angles, known as the Bragg angle (equation 2.1) (Bragg, 1968). In order for the Bragg condition (equation 2.1) to be satisfied, the "waves" of neutrons (or X-rays) must be "in phase".

$$n.\lambda=2dsin\theta \quad \textbf{(2.1)}$$

Whereby n is the order of diffraction, λ is the wavelength of the neutron beam, θ is half the diffraction angle of the Bragg reflection relative to the primary beam and d is the periodicity of the lattice (also referred to as the d-repeat, in the case of a lamellar stack of lipids, the d-repeat is one bilayer together with one layer of water, usually around ~50 Å thick). There is an inverse relationship between angle and the d-repeat. This implies that large structures diffract closer to the beam stop than smaller structures. Only at the Bragg angle(s) will the path length of scattered waves equal an integral of multiples of wavelength. This results in constructive interference. Figure 2.2 displays a cartoon showing the first order of diffraction in a lipid bilayer.

2.3.2 The unit cell

The constituent atoms of phospholipid bilayers and peptides produce weak continuous scattering (also referred to as molecular transform), this cannot be measured experimentally as the signal is too weak. Therefore, the sample contains many stacks of bilayers separated by water layers, such that diffraction can be measured experimentally. The lattice (Figure 2.2) leads to amplification of the

signal. The diffracting substructure of the unit cell leads to the molecular transform. Multibilayers display a high degree of order, but only in the direction perpendicular to the bilayer surface (z).

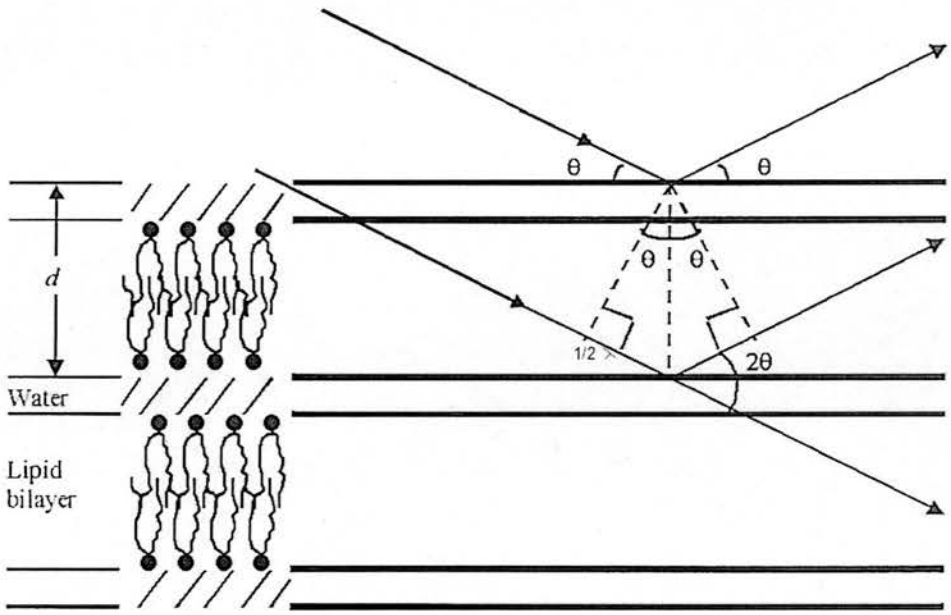

Figure 2.2. A cartoon displaying the internal structure of the unit cell (d). The first order of diffraction is shown, whereby the scattering centres are a distance (d) apart from each other.

The resulting intensity of the diffracted wave displayed in Figure 2.2, is directly related to coherent cross-section of each atom within the unit cell. When the sine of the Bragg angle is doubled, this results in a path difference of two wavelengths between the original scattering centres. There is now a new scattering centre exactly halfway between the original centres. This new scattering centre fulfils the Bragg condition and is associated with the second order diffracted wave intensity. The scattering centres are now $1/2d$ apart. This means that the resolution of the

experiment is now doubled. Higher orders of diffraction progressively increase the resolution of a neutron diffraction experiment (Warren, 1987).

2.3.3 Fourier reconstruction

Rays of light can be focused, such as those seen in light microscopy. In neutron diffraction experiments, this focusing is done by the use of the Fourier analysis (Warren, 1987).

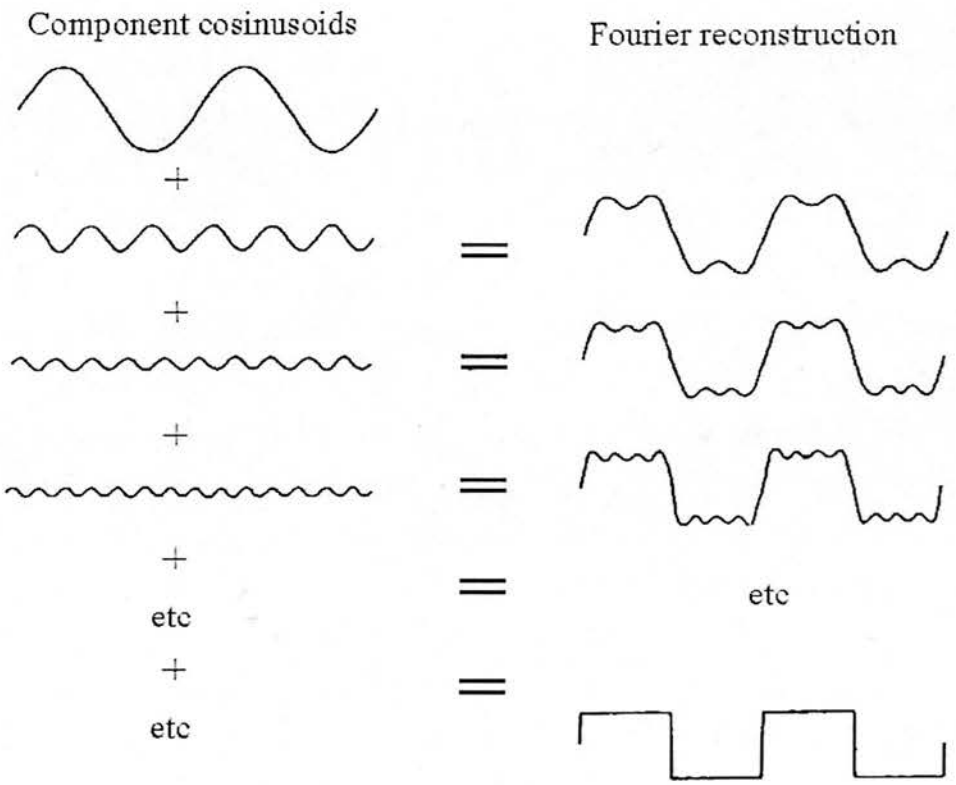

Figure 2.3. Fourier synthesis. Each of the component sinusoids can be summed to obtain the original diffracting structure. In this case, a square wave function represents a real life object of identical dimensions to the sample. The parameter of each component wave can be measured from the diffractogram (Modified from Warren, 1987).

The measured amplitudes contained within the diffractogram are the Fourier transform (FT) of the convolution of the original sample with the unit cell. The sample and diffractogram are hereby termed as FT pairs. Furthermore, the unit cell dimensions can be elucidated from the information provided in the diffractogram.

Fourier's theorem states that: "Any mathematical function can be considered as the sum of a series of sinusoidal frequency components" (Bracewell, 1989). This is illustrated by Figure 2.3. Waves can be summed together as they can be described by first order differential equations (Gough *et al.,* 1996). Hence, a square wave function can be described only if the high frequencies of components are included in the summation. Exclusion of these components will result in a under resolved structure.

The periodicity of the multi-bilayer sample allows for the use of Fourier's theorem in neutron and X-ray diffraction. The definition of a periodic structure is one that repeats over an infinite distance (or time). In reality, this is impossible but a mathematical approximation is made. The sample is a periodic structure of around 50000 unit cells. The diffraction process results in a series of delta functions at each integral multiple of the fundamental frequency (first order spatial frequency). It should be noted that each individual unit cell is a non-periodic structure. The unit cell is also referred to as *d* or the *d*-repeat. The waves that describe the unit cell are

truncated and their FT gives rise to a continuous band as opposed to discrete line functions. This is shown in Figure 2.4.

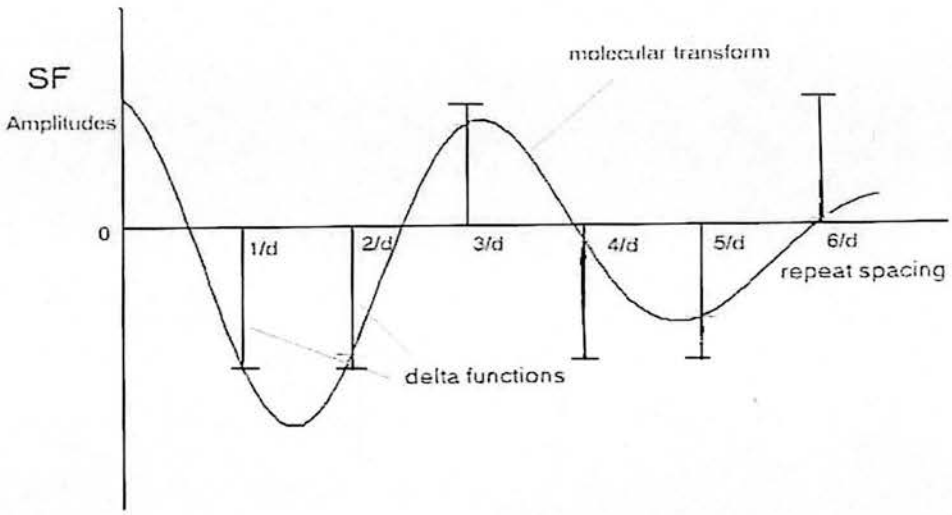

Figure 2.4. The multiplication of the lattice transform with the molecular transform. A sinc function can be utilised to fit the observed points and create a pseudo continuous transform. As can be seen delta functions should all be the same length (i.e. 1).

Multiplying the delta function at each spatial frequency with the molecular transform will give the parameters of the component wave function that will describe the bilayer profile. However, this applies to centro symmetric systems such as the bilayer/peptide system described within this chapter. In real space, each order of diffraction is representative of a cosinusoid term in a Fourier series, which describes the bilayer profile. A Fourier series is given by equation 2.2.

$$\rho(x) = \rho o + \sum_{h=1}^{h\,\max} F(h)\cos(2\pi x h / d) \qquad \textbf{(2.2)}$$

Whereby $\rho(x)$ is the mathematical function, which describes the transbilayer profile, ρo is the mean value of $\rho(x)$, $F(h)$ is the structure factor amplitude of each diffraction order and d is the d-repeat.

The unit cell is symmetric and the wave functions used in the Fourier synthesis are cosinusoids. The amplitude of the wave is known as the structure factor amplitude (Figure 2.4). The amplitude is the square root of the intensity of the diffraction spot, whereas the frequency of the wave is the spatial frequency of each diffraction spot. For periodic objects such as multi bilayer stacks of phospholipids, each frequency component is an integral of the first order frequency.

The scattering centres of the first order of diffraction are a unit cell (d) apart from each other. The spatial frequency is then $1/d$. In other words, the wavelength of the first order cosine is the same as the unit cell (d). The second order of diffraction has scattering centres at $1/2d$ apart. It follows that the frequency of the gratings are now exactly twice as many, the spatial frequency will be $2/d$ for the second order. Hence, the wavelength of the second order cosine is $1/2d$ and two complete wave cycles are observed within the unit cell.

The Fourier series describes the image of the original diffracting structure in terms of neutron scattering density parallel to the bilayer normal (z). The structure is the image of the membrane that consists of the average spatial distribution of the submolecular groups projected onto the line normal to the plane on the membrane from which the relative intergroup distances can be measured (Wiener and White, 1991). The bilayer is represented by a sum of cosinusoid waves. The peaks and troughs of the final structure represent the average distribution of the principle molecular fragments that comprise the lipid bilayer. This is illustrated in Figure 2.5, for a typical di-oleoyl phosphatidylcholine (DOPC). The neutron scattering lengths of the molecular constituents are well known therefore a real space model of the bilayer can be constructed. The bilayer profile of DOPC (66% relative humidity) has been reduced to a series of Gaussian functions that describe the average spatial projections of these principal molecular fragments (Wiener and White, 1992).

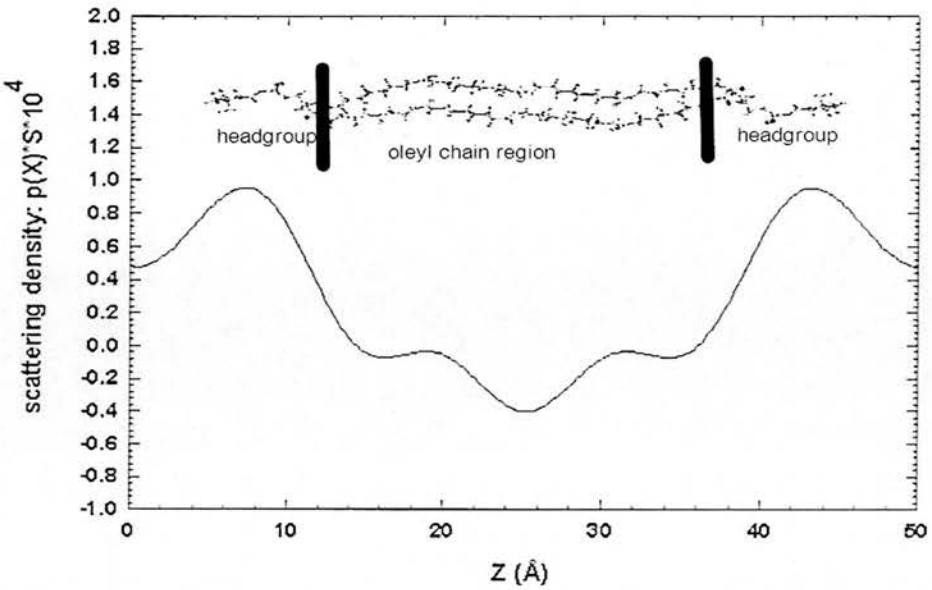

Figure 2.5. A typical neutron scattering density profile across a DOPC bilayer. The water compartments are located on either side the headgroup regions. A pair of DOPC molecules is shown to aid the interpretation of the profile. The peaks located at 8 and 42 Å respectively, are the phosphate headgroups. The trough at 25 is representative of the negative scattering of the terminal methyl groups. (Modified from Darkes and Bradshaw, 2000).

2.3.4 Phasing

The correct addition of cosinusoids is dependent upon knowledge of the phase of the wave. The phase is the relative horizontal position of each wave in the Fourier series. However, vital phase information is lost when converting from intensities to amplitudes. This problem is often referred to as the "phase problem" and applies to protein crystallography as well as neutron diffraction of stacked phospholipid bilayers. The structure factors must be accurately determined to enable the investigator to phase the data correctly.

It must be noted that the *d*-repeat of phospholipid multi-bilayers is highly susceptible to the slightest change in humidity within the sample can. This alteration in humidity will result in a change of the *d*-repeat whilst the experiment is underway. For instance, if the *d*-repeat stays constant whilst collecting the first two orders but changes when the third order is collected, then the spatial frequency of the third order will not be an integral multiple of the fundamental frequency.

Bradshaw and Darkes (Bradshaw and Darkes, 1998) have described a more accurate method of determining structure factor amplitudes, which will be described in the methods section of this chapter.

2.4 Background

A number of extra cellular proteins can misfold spontaneously and aggregate to form β-sheet rich amyloid deposits characteristic of a variety of protein misfolding diseases, most notably Alzheimer's disease and non-insulin dependent diabetes mellitus (Bucciantini *et al.,* 2002). The precise molecular basis of amyloidal diseases is unclear, strong arguments are emerging to implicate organ-specific amyloidogenic proteins, particularly oligomeric intermediates on the pathway to amyloid fibril formation, in disease pathogenesis (Walsh *et al.,* 2002).

Human islet amyloid polypeptide (hIAPP), a 37-residue peptide hormone secreted by pancreatic beta cells, often forms amyloid deposits in patients affected by NIDDM

(non-insulin dependent or type 2, maturity onset, diabetes mellitus). This chapter will describe a neutron diffraction study of the pre-fibrillar membrane bound form of IAPP, comparing the membrane activity of both the human and rat isoforms of this peptide.

2.4.1 Molecular modelling of hIAPP intermediates

Molecular forms of hIAPP can be modelled in various conformations dependent upon the number of β–sheet components present in the native monomer or folding intermediate. The conformations reported within the literature tend to be intermediates of hIAPP created during fibrillogenesis. A β–turn has been predicted at asparagine 31 (Jaikaran and Clark, 2001), which resulted in two adjacent β–strands, namely residues 24-29 and 32-37, creating an antiparallell β–sheet. The third β–strand contained in the fragment 8-20 could extend this sheet with a turn in the region 18-23, computational studies predict this turn to be at serine 20 (Higham *et al.,* 2000). A computational model which incorporated three strands (8-20, 20-29 and 30-37), with two turns predicted a structure which could form an intermolecular β –sheet, as can be observed in Figure 2.6.

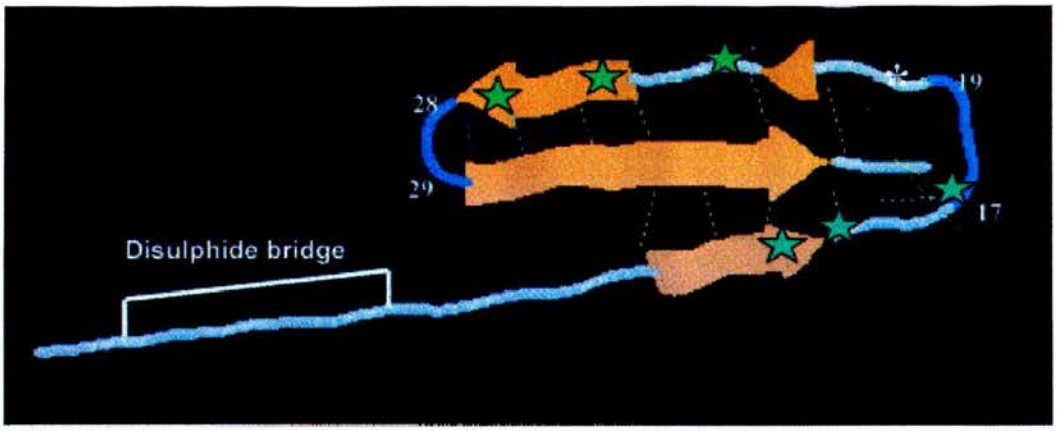

Figure 2.6. A computational model of hIAPP. The light yellow colouring represents β-strands. The blue colouring represents the turns. Dotted lines illustrate hydrogen bonds. Hydrophobic residues that are involved in hydrogen bonding between the backbones of the strands are illustrated by green stars. Serine 20 (labelled with an asterisk) is substituted with a glycine in a small subset of type 2 diabetic subjects (modified from Jaikaran and Clark, 2001).

This group depicted the first turn between amino acids 17 and 19, as a loop rather than a tight turn (Higham *et al.*, 2000). Previous experimental studies had shown that residues 22, 24, 26, 27 and 28 are critical for fibril formation (MacArthur *et al.*, 1999). This proposal was made after extensive proline substitution experiments (Moriarty and Raleigh, 1999). These residues are located in the second strand region and are predicted to localize on the outer edge of the β–sheet where they could be involved in interactions between molecules or protofilaments needed for assembly of two or more protofilaments into fibrils.

The β–sheet is predicted to be disrupted by proline substitutions (from amino acids 24-27) which results in lack of intra and intermolecular hydrogen bonding (Higham *et al.*, 2000). Furthermore, residue 28 (serine) is in the second turn of hIAPP. Zanuy and co-workers (Zanuy *et al.*, 2003) have performed a series of MD simulations with

a combination of monomers and dimers. They had used the NFGAIL sequence (residues 22-27). There was no bilayer present in their studies. However, they had reported an anti-parallel strand orientation of the simulated sequence. In addition, they reported that a mutated form of the sequence (NAGAIL), whereby a glycine residue was replaced with an alanine residue had resulted in disintegration of the molecule within 100ps of simulation. However, to date no reports of a molecular dynamics simulation involving membrane bound IAPP have been made.

2.5 Introduction

This chapter is concerned with orientated neutron diffraction from two-dimensional model membranes, that either contains islet amyloid polypeptide (IAPP) and/or an inhibitor of (IAPP) action (rifampicin). These types of experiments require the formation of highly aligned multi-bilayer stacks. A detailed explanation of sample preparation is given in the materials and methods section of this chapter.

Other members of the research group have demonstrated that an intermediate, pre-fibrillar, oligomeric form of hIAPP interacts with membranes, whereas fibrillar hIAPP (like normal, monomeric hIAPP) lacks membrane activity (Harroun *et al.,* 2001). Interestingly, the membrane activity of hIAPP could be inhibited independently of its ability to form amyloid (Harroun *et al.,* 2001), providing a further test of the idea that only the pre-fibrillar, oligomeric form of hIAPP is membrane-active, and mature fibrils are inactive. Oligomeric intermediates in the 'misfolding' process may form non-specific cation channels (Mirzabekov *et al.,*

1996), and cellular Ca^{2+}-overload could account for the toxicity of hIAPP, and explain why exposed cells die by both apoptosis and necrosis (Jaikaran and Clark, 2001).

Unlike human IAPP, rat IAPP (rIAPP) is membrane inactive (Jaikaran and Clark, 2001). Sequence variations in IAPP are strongly associated with the ability of the peptide to form amyloid, and susceptibility to NIDDM (Westermark *et al.,* 1990). Human and cat IAPP contain the internal sequence NFGAIL (Figure 2.7), and both species can form islet amyloid and develop NIDDM. The rat and mouse genes do not encode this motif, and these species do not exhibit islet amyloid or NIDDM. However, mice expressing the hIAPP transgene do develop a NIDDM-like disease (Soeller *et al.,* 1998).

Human IAPP KCNTATCATQ RLANFLVHSS NNFGAILSST NVGSNTY

Rat IAPP KCNTATCATQ RLANFLVRSS NNLG**P**VL**PP**T NVGSNTY

Figure 2.7. Sequence alignment of human IAPP (Swiss-Prot P10997) and rat IAPP (Swiss-Prot P12969). The peptides have a disulphide-bridged loop at their N-terminal end, and the NFGAIL motif, present in species susceptible to islet amyloid and NIDDM is underlined. The three prolines present in rat but not human IAPP are indicated in bold.

The membrane-active form of hIAPP is not well defined. In the present study, the membrane-associated form of hIAPP in stacked phospholipid bilayers using neutron diffraction was identified. The hypothesis that hIAPP oligomers span the bilayer was directly tested.

2.6 Materials and methods

2.6.1 Materials

hIAPP and rIAPP were obtained from Bachem (Weil am Rhein, Germany). Palmitoyl-oleoyl phosphatidylethanolamine (POPE) and palmitoyl-oleoyl phosphatidylserine (POPS) were purchased from Avanti Polar Lipids (Birmingham, AL) and rifampicin was from Fluka (Poole, UK). Tri-fluoro ethanol (TFE) and chloroform were of 99.4% and 99% purity respectively. All materials were used, without further purification or modification.

2.6.2 Sample preparation and data collection

Multibilayer stacks of phospholipids and peptides were prepared according to an established method (Darkes and Bradshaw, 2000). This involved weighing out 20 mg of a 50:50 (mol) mixture of POPE and POPS which were co-dissolved with 1% (mol) peptide in chloroform:tri-fluoro ethanol (7:3 (v/v)) and airbrushed onto a quartz glass slide to produce highly aligned multibilayers. The slides were placed under vacuum for 24 hours to remove the solvents. The slides were then mounted in sealed aluminium sample cans which were connected to computer controlled water baths and hydrated for 12 hours at 25°C to allow full equilibration and the formation of IAPP oligomers (Harroun *et al.,* 2001). The sample cans contained saturated solutions of KCl, K_2NO_3 or K_2SO_4 in $^2H_2O/H_2O$ mixtures to maintain a relative humidity of 85%, 92% or 97%, respectively, and the ^2H_2O concentration was set to 8% (v/v) in the presence of each of the three salts, and also to 20%(v/v) and 50%

(v/v) in K_2NO_3 alone. ^2H_2O at a concentration of 8% (v/v) has a net neutron-scattering density of zero, hence enabling background subtractions, without unnecessary mathematical manipulation. Diffraction data were collected for each of the five conditions, by scanning samples through $\pm 2°$ around the predicted Bragg angle for each of the first five orders of diffraction in turn.

2.6.3 Instrument setup

All experiments were performed on the V1 instrument at the Hahn Meitner Institut, Berlin. This instrument is a membrane diffractometer, designed for neutron diffraction studies with stacked bilayers.

V1 possesses a vertically focusing graphite monochromator, which results in adjustable wavelengths between 3 Å and 6 Å. Sample and detector supports are movable on aircushions, powered by liquid nitrogen. A representation of the instrument is shown in Figure 2.8. The wavelength of neutrons used in this study was 4.1852 Å and the detector to sample distance was set to 115 cm.

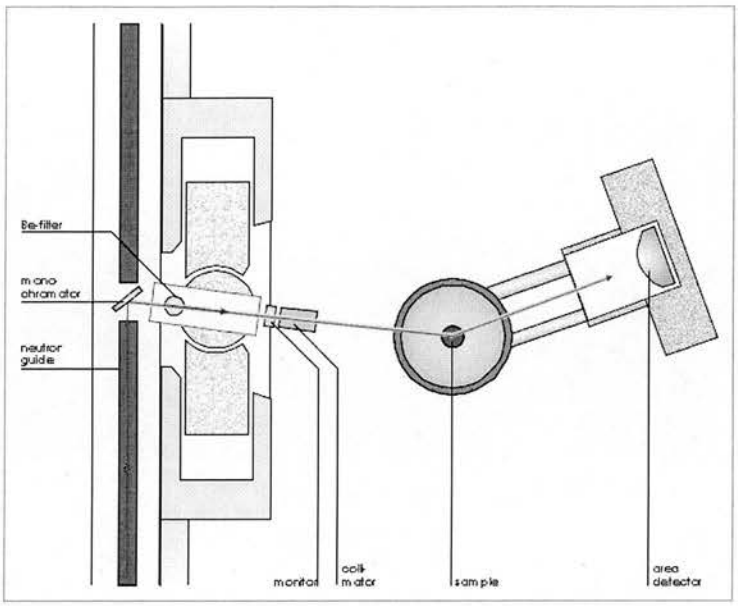

Figure 2.8. Cartoon representing the instrument setup at the V1 membrane diffractometer. The diagram was kindly provided by Dr Thomas Haußß. (Source http://www.hmi.de/bensc/instrumentation/instrumente/v1/v1-pic.html)

2.6.4 Data analysis

Monitor counts were corrected manually. Background subtractions were performed with the commercial package Peakfit™. Each peak was then fitted with Gaussians with Peakfit™. Absorption and Lorentz corrections were then applied before the intensities were square-rooted to provide structure factor amplitudes. Darkes and Bradshaw had previously demonstrated (Darkes and Bradshaw, 2000) that sets of structure factors collected at different bilayer spacings (i.e. different humidities) in 8% (v/v) ^2H_2O can be fitted to a single continuous transform, since the net neutron scattering length density of water of this isotopic composition is zero. All observed points were fitted onto a continuous transform using a least-squares minimization procedure. Sets of structure factors *F(h)* each corresponding to a *d*-repeat of *D*, were fitted against all the observed data points, including the zeroth order [*F(0)*].

The equation below must be satisfied for all observed orders of diffraction.

$$F(H) = \sum_{H=0}^{H\max} F(H) \frac{\sin(\pi Dh/d - \pi H)}{(\pi Dh/d - \pi H)} \qquad \textbf{(2.3)}$$

This formula was applied to all values obtained in three different relative humidities of 85%, 92% and 97% respectively. Analytical continuation theory (King and Worthington, 1971) predicts that all the model structure factors should lie on the same continuous transform. One of the distinct advantages in using this method is the potential increase in the accuracy of intensity measurement. Changes in *d*-repeat, which are a result of temperature or humidity fluctuations and in some cases inadequate equilibration, can result in significant differences in intensity. The indexing of each structure factor to its own spatial frequency, as opposed to assuming that they all fit onto the same reciprocal lattice, removes this source of error. Phasing the structure factors is, therefore, simple and unambiguous, and accurate sets of structure factors can be determined for subsequent use in difference subtractions (Darkes and Bradshaw, 2000).

Once the three sets of 8% ^2H_2O data had been phased for each sample, the 20% and 50% ^2H_2O data were phased to the 8% data by least-squares fitting to straight line functions, as reviewed by Duff *et al.,* (Duff *et al.,* 1994). An example of these straight line fits is shown in Figure 2.9.

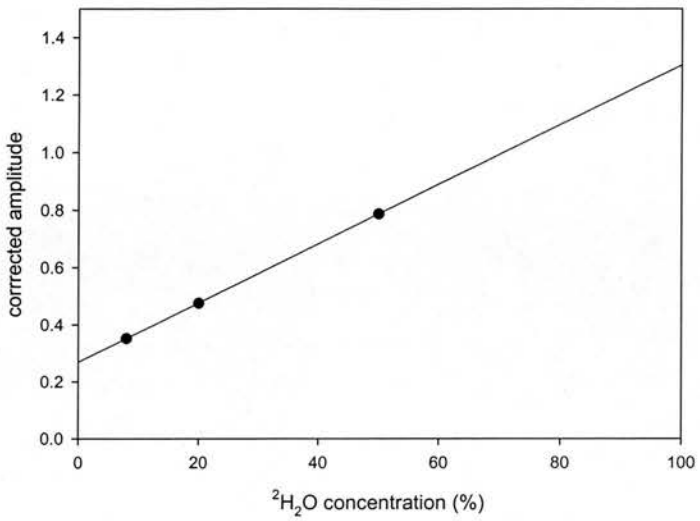

Figure 2.9. An example of straight-line fitting. The sample shown is the first order of sample containing equimolar POPE and POPS with 1% (mol) of hIAPP.

The data were then placed on a 'relative absolute' scale using the method of Jacobs and White (Jacobs and White, 1989). The relative absolute scale is based upon the absolute scattering length density $\rho(z)$ along the bilayer normal (z).

$$\rho(z) = \rho_0 + \frac{2}{d} \bullet \frac{1}{K} \sum_{h=1}^{N} F(h) \cos\left(\frac{2\pi hz}{d}\right) \qquad \textbf{(2.4)}$$

Whereby *F(h)* are the measured structure factors in arbitrary units, K is the instrument constant, d the Bragg spacing, ρ_0 the average scattering length density of the unit cell, and N the highest observed order of diffraction (five for this study). The relationship between *F(0)*, which is the zeroth order of diffraction and ρ_0 is relatively straightforward. If ρ_0 is multiplied by *d/2* then this will give the value of the zeroth order *F(0)*. *F(0)* can be determined by summing the total coherent scattering length of each atom in the unit cell. It is not possible to obtain *F(0)*

experimentally. It is noteworthy that *F(0)* changes with hydration, hence most structure factors from stacked bilayer/peptide systems do not fit onto a single continuous transform. However, an exception can be made with bilayer/peptide systems hydrated with 8% ^2H_2O. Therefore it is quite feasible to use the value of F*(0)* for all other hydrations. The fact that *F(0)* does not change removes a large source of potential error when fitting the observed points to a single continuous transform.

Equation 2.4 assumes that the volume (v) and composition of the unit cell are known. However, the volume cannot be calculated accurately, therefore the alternative approach is to use the relative absolute scale of Jacobs and White (Jacobs and White, 1989). This method describes the scattering density on a per pair of lipid molecules basis. Both sides of the equation 2.4 are multiplied by S (area per molecule), this yields the scattering density.

$$\rho^*(z) = \rho_0^* + \frac{2}{d} \bullet \frac{1}{k} \sum_{h=1}^{N} F(h) \cos\left(\frac{2\pi hz}{d}\right) \qquad \textbf{(2.5)}$$

Whereby $\rho(z)^* = \rho(z)S$, $\rho_0^* = \rho_0 S$ and $k = K/S$. Bearing in mind these definitions, the relative absolute structure factors are given by $F^*(h) = F(h)/k$.

2.7 Results and discussion

The lamellar spacings (*d*-repeats) of the samples at 92% relative humidity were determined by optimised least squares fitting to five orders of diffraction. 1% (mol) hIAPP decreased the lamellar spacing significantly from 62.09 $\pm$ 0.16 Å (mean $\pm$ SD, n = 3) to 61.51 $\pm$ 0.20 Å (mean $\pm$ SD, n = 3, $P<0.02$ by t-testing), while rIAPP increased the spacing slightly to 62.72 $\pm$ 0.57 Å (n=3, $P>0.05$). The measurements for phospholipids with 1% (mol) rifampicin were 56.96 $\pm$ 0.43 Å (mean $\pm$ SD, n = 3), and for phospholipids with 1% (mol) hIAPP and 1% (mol) rifampicin, 58.53 $\pm$ 0.27 Å (mean $\pm$ SD, n = 3). The difference in *d*-repeats between bilayers containing hIAPP and rIAPP (in the absence of rifampicin) was 1.2 Å.

The total molecular volume of hIAPP calculated from amino acid volumes in the IMB Jena Image Library (http://www.imb-jena.de) was 4680 $Å^3$. Assuming an average bilayer surface area of 72 $Å^2$ per phospholipid (Tristram-Nagle et al. 1998), the difference in *d*-repeats mentioned above equates to a volume increase of 87 $Å^3$ per pair of lipids. At 1% (mol), this equates to an extra volume of 47 $Å^3$ per lipid, or 94 $Å^3$ per pair of lipids. However, the *d*-repeats of the bilayers with hIAPP show a reduction in value and not an increase. The question then arises, as to how the additional volume of the peptide can be accommodated. It could either be by expansion of the unit cell in the *Z* direction (e.g. if the long axis of the peptide lies parallel to the bilayer), or by insertion of hIAPP between the bilayer phospholipids, or both. The significant decrease in the *d*-repeat in the presence of hIAPP was inconsistent with the first possibility. However, expansion of the unit cell in the

plane of the bilayer, (the second possibility) is invisible to lamellar diffraction methods, and is not constrained in the 'relative absolute' method used in this study. Moreover, the idea that the peptide inserted into the bilayer was consistent with the monolayer expansion seen in previous Langmuir balance measurements using the same lipids (Harroun *et al.,* 2001). We therefore investigated the possible membrane insertion of hIAPP in more detail, by examining bilayer scattering profiles. A table of neutron structure factors, for all samples is displayed in table 2.1. The neutron scattering length density profile of POPE/POPS bilayers in the absence of peptide (Figure 2.10a) differs from the "standard" profile of di-oleoyl phosphatidylcholine (DOPC) seen in Figure 2.5, most noticeably because the dip in scattering length density seen in the water region of DOPC bilayer profiles is barely visible in the POPE/POPS profile. This can be explained by the different neutron scattering lengths of the phospholipid headgroups. The total scattering length of the PC ($C_5H_{13}N$), PE (C_2H_7N) and PS ($C_3H_6O_2N$) headgroups are -0.60 x 10^{-13} cm, -0.597 x 10^{-13} cm, and 1.85 x 10^{-13} cm, respectively. When two sodium counter ions are added to the PS headgroup (0.72 x 10^{-13} cm), the extra density in the mixed lipid bilayers is readily explained.

Sample		*F(0)*	F(1)	F(2)	F(3)	F(4)	F(5)
POPE/POPS							
	0% ^2H_2O	**6.3 (±0.08)**	**12.8 (±0.05)**	**-2.2 (±0.03)**	**-1.9 (±0.02)**	**-2.6 (±0.07)**	**0.3 (±0.02)**
	8% ^2H_2O	**9.4 (±0.08)**	**17.7 (±0.04)**	**0.2 (±0.08)**	**-1.4 (±0.07)**	**-2.6 (±0.03)**	**0.3 (±0.04)**
	50% ^2H_2O	**25.7 (±0.08)**	**43.3 (±0.07)**	**13.4 (±0.07)**	**0.8 (±0.04)**	**-2.4 (±0.04)**	**0.4 (±0.09)**
POPE/POPS + 1% hIAPP							
	0% ^2H_2O	**8.2 (±0.05)**	**8.2 (±0.09)**	**-3.3 (±0.06)**	**-0.4 (±0.06)**	**-2.1 (±0.08)**	**0.4 (±0.08)**
	8% ^2H_2O	**11.5 (±0.01)**	**9.2 (±0.06)**	**-1.6 (±0.07)**	**-0.2 (±0.07)**	**-1.6 (±0.03)**	**0.4 (±0.09)**
	50% ^2H_2O	**28.6 (±0.02)**	**14.3 (±0.07)**	**7.2 (±0.00)**	**0.6 (±0.09)**	**1.2 (±0.06)**	**0.5 (±0.05)**
POPE/POPS + 1% rIAPP							
	0% ^2H_2O	**8.2 (±0.08)**	**10.2 (±0.01)**	**-0.0 (±0.05)**	**-1.7 (±0.05)**	**-0.8 (±0.08)**	**1.4 (±0.06)**
	8% ^2H_2O	**11.5 (±0.01)**	**15.2 (±0.09)**	**2.1 (±0.02)**	**-1.6 (±0.03)**	**-1.8 (±0.01)**	**1.4 (±0.01)**
	50% ^2H_2O	**28.4 (±0.03)**	**41.9 (±0.09)**	**13.5 (±0.01)**	**-1.0 (±0.01)**	**-6.6 (±0.07)**	**1.1 (±0.03)**
POPE/POPS + 1% rifampicin							
	0% ^2H_2O	**6.1 (±0.09)**	**5.7 (±0.05)**	**-3.6 (±0.03)**	**-1.3 (±0.01)**	**-2.0 (±0.03)**	**-1.5 (±0.00)**
	8% ^2H_2O	**9.4 (±0.09)**	**10.8 (±0.08)**	**-0.7 (±0.09)**	**-1.2 (±0.07)**	**-2.1 (±0.01)**	**-1.1 (±0.04)**
	50% ^2H_2O	**26.7 (±0.08)**	**37.8 (±0.03)**	**14.1 (±0.02)**	**-1.0 (±0.08)**	**-2.5 (±0.01)**	**0.7 (±0.05)**
POPE/POPS + 1% hIAPP + 1% rifampicin							
	0% ^2H_2O	**8.3 (±0.00)**	**3.4 (±0.05)**	**-5.1 (±0.07)**	**-2.4 (±0.01)**	**-1.4 (±0.03)**	**2.0 (±0.06)**
	8% ^2H_2O	**11.5 (±0.01)**	**8.7 (±0.05)**	**-2.5 (±0.08)**	**-1.8 (±0.05)**	**-1.5 (±0.08)**	**1.8 (±0.05)**
	50% ^2H_2O	**28.4 (±0.00)**	**36.5 (±0.08)**	**11.0 (±0.02)**	**1.0 (±0.06)**	**-2.3 (±0.08)**	**0.7 (±0.05)**

Table 2.1 Neutron structure factors (with standard errors). They were used to calculate the neutron scattering length density profiles shown in Figures 2.10 and 2.11. The data have been scaled using the relative absolute method (Wiener *et al.*, 1991).

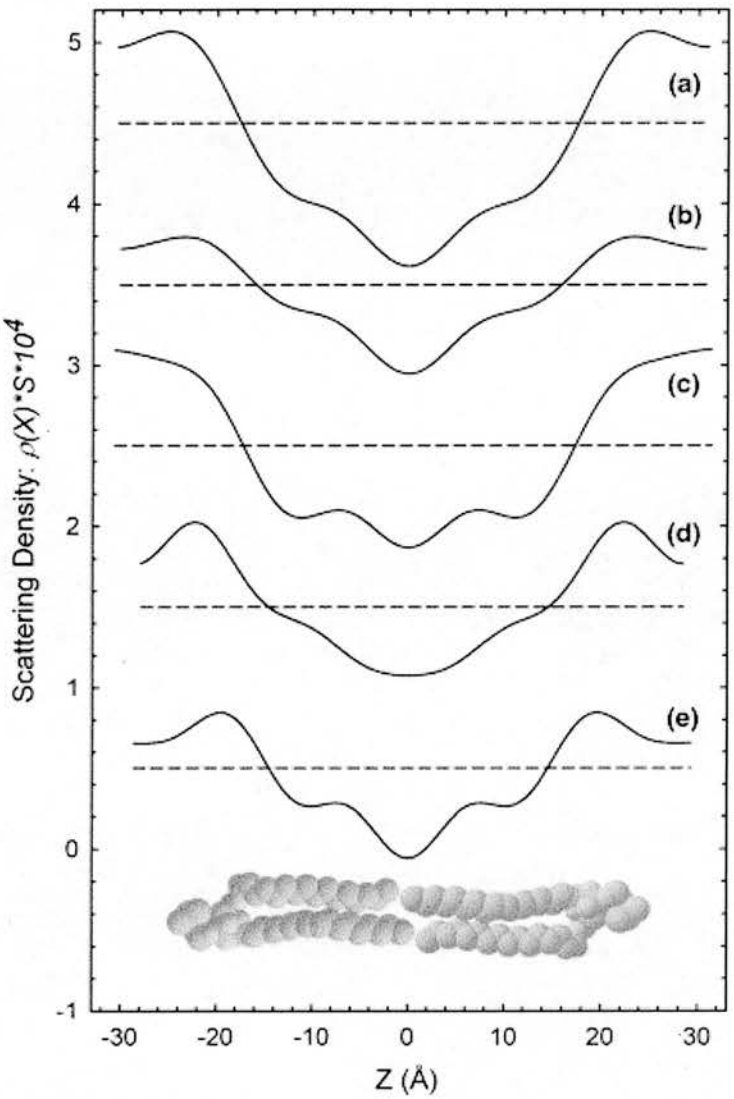

Figure 2.10. Neutron scattering length density profiles of phospholipid bilayers: (a) 50:50 (mol) mixture of POPE and POPS; (b) 50:50 (mol) mixture of POPE and POPS with 1% (mol) hIAPP; (c) 50:50 (mol) mixture of POPE and POPS with 1% (mol) rIAPP; (d) 50:50 (mol) mixture of POPE and POPS with 1% (mol) rifampicin; (e) 50:50 (mol) mixture of POPE and POPS with 1% (mol) hIAPP and 1% (mol) rifampicin hIAPP. The structure factors for bilayers hydrated with 8% ^2H_2O were used to calculate the profiles, since water of this isotopic composition has a net neutron scattering length density of zero. The profiles have been displaced vertically, for clarity.

The bilayer profile in the presence of hIAPP (Figure 2.10b) was remarkably similar to that of pure lipid bilayers. The water region was almost indistinguishable from the pure phospholipid bilayer, and any relatively slight differences were largely confined to an increase in density in the fatty-acyl region. rIAPP, on the other hand, caused major changes to the water region (Figure 2.10c). The characteristic minimum at the edges of the profile were completely absent, suggesting that the additional neutron scattering length density introduced by the peptide now filled this trough. The profile shape changes in the fatty acyl-region were consistent with lipid rearrangements rather than peptide penetration. A peptide orientated parallel to the bilayer is likely to cause greater fatty-acyl disruption than a transbilayer peptide, for two reasons: i) the parallel peptide will have contacts with a much larger number of phospholipids than a transbilayer peptide; and ii) the parallel peptide only occupies part of the full depth of the bilayer, and will create a potential void that has to be filled by the fatty-acyl chains of the surrounding lipids (Figure 2.11).

Taken together, these profiles show clear differences in the relationship of the two peptides with the lipid bilayer. rIAPP appears to reside exclusively in the water layer between the bilayers, whereas hIAPP is largely excluded from this region. This conclusion is further supported by the observation (Figure 2.10a and Figure 2.10c) that the bilayers are thinner in the presence of rIAPP, despite the overall increase in *d*-repeat. In profile (a), the two maxima in the neutron scattering length density are caused by strong neutron scattering by the phosphates and the oxygen rich (and hydrogen-poor) ester linkages of the phospholipids. Although partially obscured by

scattering from the peptide, the steep gradients up towards the corresponding region are closer together in profile (c) compared to (a).

We next examined how the inhibitor rifampicin interacted with phospholipid bilayers in the absence of peptide. Previous studies of rifampicin partitioning using derivative spectrophotometry (Rodrigues *et al.,* 2001) and ^{1}H-NMR and fluorescence energy transfer (Rodrigues *et al.,* 2003) suggested that the compound inserts deeply into the hydrophobic core of the bilayer, while remaining in contact with the polar surface. With a pK_a of 7.9, rifampicin has partial anionic character at neutral pH, and this has been correlated with a stronger interaction with zwitterionic lipids such as di-myristoyl phosphatidylcholine ($K_d = 5.09 \times 10^4$) compared to anionic lipids such as di-myristoyl phosphatidylglycerol ($K_d = 0.54 \times 10^4$) (Rodrigues *et al.,* 2003). While in broad agreement that rifampicin forms stable bilayers with anionic or zwitterionic lipids, the neutron data reveals that rifampicin induces marked structural changes in the membrane (the NMR technique used by Rodrigues (Rodrigues *et al.,* 2003) is blind to the details of bilayer structure revealed by neutron diffraction).

The bilayer profiles in Figure 2.10a and Figure 2.10d show differences in bilayer width, as revealed by the distance between the two maxima, and the bilayer thinning caused by rifampicin is reflected in the reduced *d*-repeat of the corresponding samples. These effects may be explained by "splaying" of the phospholipid headgroup regions over the top of deeply inserted rifampicin (Figure 2.11b).

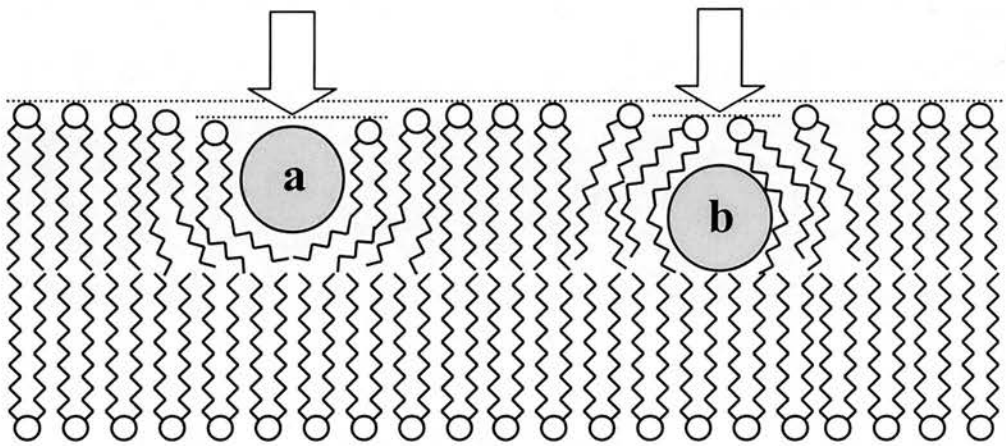

Figure 2.11. Cartoon showing possible mechanism of bilayer thinning (arrow) when (a) a peptide inserts parallel to the bilayer surface or (b) rifampicin inserts close to the terminal methyl groups. For explanation, see text.

Rodrigues also positions rifampicin close to the terminal methyls of the fatty-acyl chains (Rodrigues *et al.,* 2003), consistent with the observation that the methyl trough is broadened, as revealed by the neutron scattering length density at the centre of the bilayer. Addition of hIAPP to the bilayers in the presence of rifampicin thins the bilayer even further, yet increases the *d*-repeat by 1.5 Å. Both of these observations are consistent with location of the peptide to the water/bilayer interfacial region, strongly implying that rifampicin has prevented transbilayer insertion of the peptide.

Water distribution profiles were calculated by Fourier transformation of difference structure factor profiles obtained by least squares fitting to 8%, 20% and 50% $^{2}H_{2}O$ sample hydrations. The water profile for pure lipid bilayers, shown in Figure 2.12a

was entirely consistent with previous neutron studies of phospholipid membranes (Bradshaw *et al.,* 2000; Davies *et al.,* 1998; Bradshaw *et al.,* 1998). The single peak (split between the two ends of the profile in the Figure) represents a block of water confined between adjacent bilayers in the multi-bilayer stack. The corresponding water distribution profile for bilayers containing 1% (mol) rIAPP (Figure 2.12c) was similar. Once again, the water was confined to the outer sections of the profile, representing the inter-bilayer hydration layer. However, in the IAPP profiles (Figure 2.12b); the same amount of water was distributed very differently. Instead of being confined to the edges, it extended across the entire width of the repeating unit, including the phospholipid bilayer itself. This observation supports the proposal that hIAPP, but not rIAPP, inserts in a transbilayer orientation in the phospholipid bilayers used in this study.

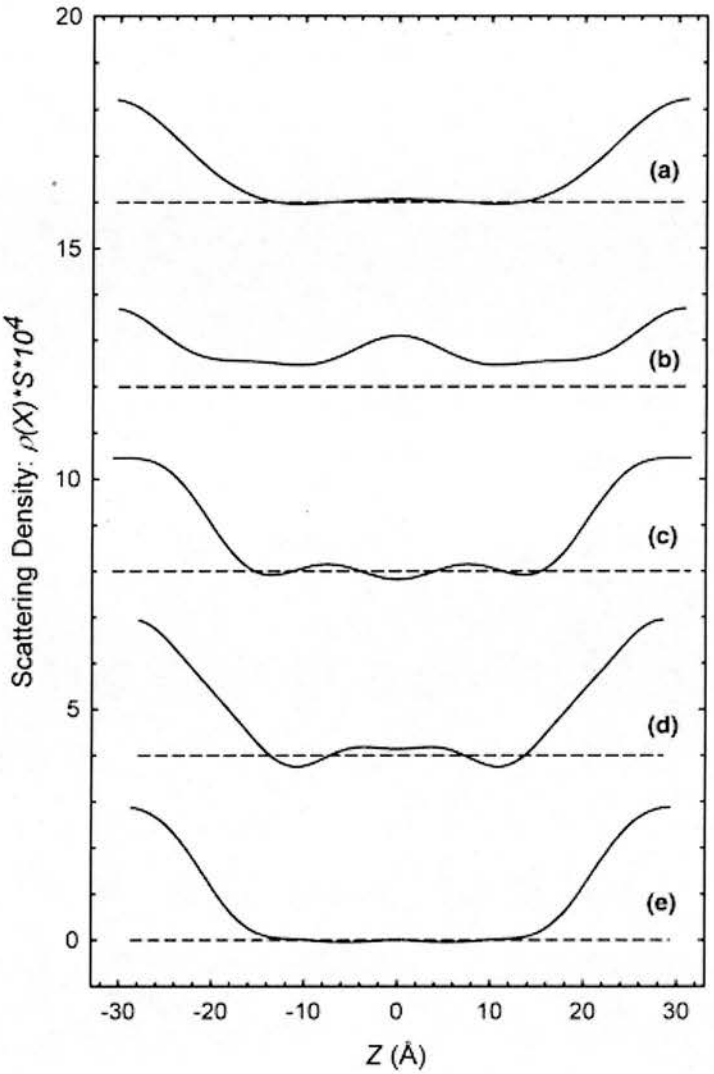

Figure 2.12. Difference profiles of the neutron scattering length density of heavy water (^2H_2O) in stacked phospholipid bilayers. (a) 50:50 (mol) mixture of POPE and POPS; (b) 50:50 (mol) mixture of POPE and POPS with 1% (mol) hIAPP; (c) 50:50 (mol) mixture of POPE and POPS with 1% (mol) rIAPP; (d) 50:50 (mol) mixture of POPE and POPS with 1% (mol) rifampicin; (e) 50:50 (mol) mixture of POPE and POPS with 1% (mol) hIAPP and 1% (mol) rifampicin hIAPP. Structure factors for bilayers hydrated in 100% H_2O were subtracted from corresponding 50% ^2H_2O structure factors and the result used to calculate the profiles shown. The profiles have been displaced vertically, for clarity.

In contrast, in POPE/POPS bilayers with 1% (mol) rifampicin (Figure 2.12d), the water was largely confined to the interbilayer region, and as previously noted; the

lipid profile differed in shape (Figure 2.12a). This confirms the suggestion that rifampicin and phospholipids form stable bilayers, but refutes the claim (Rodrigues *et al.,* 2003) that the bilayer structure remains unchanged. Of particular interest is the observation that the addition of rifampicin to bilayers containing hIAPP (Figure 2.12e) constrained the deuterons to the inter-bilayer region, in contrast to appearances in the absence of rifampicin (Figure 2.12b). However, it is known from functional studies that rifampicin prevents bilayer insertion of hIAPP, rather than blocking pre-inserted "channels" (Harroun *et al.,* 2001).

In the absence of high-resolution structural data, Harroun and co-workers have speculated that membrane-active IAPP is a misfolded, β-sheet-rich, primary nucleation element on the amyloid pathway that can insert spontaneously into membranes (Harroun *et al.,* 2001). Membrane-located IAPP may then refold to give rise to transmembrane α-helices surrounding a central ion channel or pore (Harroun *et al.,* 2001 and Mirzabekov *et al.,* 1996). In this respect, IAPP may follow the pattern displayed by calcitonin (CT), an amyloid-forming peptide that has previously been studied in detail. CT is a 32 amino acid polypeptide hormone that shows sequence and charge distribution similarities to IAPP and can adopt either α- or β-structures, depending on its environment. The former is seen in phospholipid membranes (Bradshaw, 1997), while the latter predominates in aqueous solution (Gilchrist and Bradshaw, 1993).

Using methods similar to those in the present study, Bradshaw (Bradshaw, 1997) showed that salmon CT could insert into phospholipid bilayers containing the anionic lipid phosphatidylglycerol, leading to speculation that the peptide may have ion channel properties. This was later confirmed by Stipani and colleagues (Stipani *et al.,* 2001). Human CT formed channels at the same concentration, but not as easily as salmon CT, an observation the author attributed to the reduced helical content of this form of the peptide.

The main differences between the sequences of human and rat IAPP are the replacement of the alanine at position 25, and the serines at positions 28 and 29, with proline residues. The first of these replacements disrupts the NFGAIL sequence linked to the formation of islet amyloid and susceptibility to NIDDM (Westermark *et al.,* 1990). Proline is a well-established "breaker" of both α-helix and β-sheet structures in globular proteins, because the closed loop structure of the side chain prevents the peptide backbone from adopting the Φ (phi) and Ψ (psi) angles required for either of these secondary structures. However, proline frequently occurs in the transmembrane helices of integral membrane proteins, particularly transport proteins, despite the fact that a kink is introduced wherever a proline residue interrupts a helical section.

Li and Derber (Li and Deber, 1994) resolved this apparent contradiction by postulating different rules governing structure in the hydrophobic environment of membranes, and showed that the helical propensity of proline was greatly enhanced

in the membrane-mimetic environments of both lipid micelles and organic solvents. In studies of temperature-induced conformational transitions of a single-spanning membrane protein of bacteriophage IKe, in which the proline-containing wild type protein was compared with a mutant in which proline 30 was replaced by alanine, Li and Derber (Li and Deber, 1994) showed that proline does not interfere with helix formation, but does prevent the formation of β-sheet. The intrinsic capacity of proline to disrupt β-structures has also been demonstrated by showing that prolines are excluded from transmembrane β-strands in mutagenised OmpA porins that retain the ability to assemble into a membrane-spanning β-barrel (Koebnik, 1999). Wigley and co-workers (Wigley *et al.,* 2002) have proposed that the abundance of proline in transmembrane helices can be entirely explained by the ability of the residue to block β-structures. The advantage conferred by preventing the formation of a β-sheet outweighs the entropic disadvantage in helix distortion.

2.8 Conclusion

The work described in this chapter was carried out to gain practical experience of neutron techniques. However, the results obtained have contributed to our understanding of membrane disruption induced by IAPP.

To conclude, it is instructive to consider the differences in sequence, amyloidogenicity and membrane-associated neutron scattering profiles of human and rat IAPP. Following the arguments outlined, it is tempting to suggest that rIAPP is

non-amyloidogenic because the introduction of a proline into the NFGAIL sequence prevents the peptide from adopting the β-structure necessary for amyloid fibre formation. However, this should not significantly interfere with the peptide's ability to insert into phospholipid membranes, if the membrane-active form is α-helical (like the model for CT). Previous studies, and our current neutron diffraction data, indicate that this is not so. Rats are not susceptible to NIDDM, and the neutron data suggest that rIAPP does not insert into phospholipid membranes.

This could be taken as evidence that the membrane-active form of hIAPP is not α-helical, until it is remembered that rIAPP possesses not one but three extra prolines. The disruptive effect of three prolines in close proximity (two of them consecutive residues) is likely to block the formation of both α- and β-structures by the peptide. In future work it will clearly be of interest to probe the secondary, tertiary and quaternary structure of membrane-associated hIAPP in detail. To summarize, the data obtained represent the first study of membrane-associated IAPP to use diffraction-based techniques. It has been demonstrated that oligomeric hIAPP interacts with phospholipid membranes to form transbilayer structures. rIAPP is excluded from the membrane (as predicted), and the insertion of hIAPP is inhibited by rifampicin.

2.9 Suggested future studies

The sequence-specific insertion hypothesis for IAPP proposed was confirmed by this study. Both rat and human peptides are made up of 37 residues. They differ by only six amino acids. The six amino acids HFAISS (residues 18, 23, 25, 26, 28 and 29) of hIAPP are replaced with RLPVPP in rIAAP.

To obtain further information on the location of hIAPP selected residues (e.g. 18, 23, 26 and 29) could be deuterated for future studies. The availability of four labels will allow the peptide to be orientated unambiguously in relation to the membrane (Bradshaw *et al.,* 2000). This would lead to novel information, regarding the exact location of hIAPP in the bilayer. The construction of computational models, utilizing classical molecular dynamics simulations can then be attempted, using methods similar to those described in chapters four and five respectively.

The inhibitor rifampicin was utilised in the study, and clearly inhibited the membrane insertion of hIAPP. However, this inhibitor can insert into bilayers by virtue of its own physicochemical properties. A number of reports have been made in the literature stating that the membrane diffusion of rifampicin is affected by the ratio of zwitterionic to anionic lipid present in the model membrane (Rodrigues *et al.,* 2001; Rodrigues *et al.,* 2003). Future work could look at the varying ratios of zwitterionic lipid to anionic lipid and whether this could affect the location of hIAPP with the bilayers. Other neutron diffraction studies could also utilise another inhibitor, such as Congo red.

CHAPTER 3

Molecular dynamics simulations of phospholipid bilayers

This chapter has been published in part:

Balali-Mood, K., T.A.Harroun and J.P.Bradshaw. 2003 Molecular dynamics simulation of a mixed DOPC/DOPG bilayer. *Eur Phys J E Soft Matter* 12 Suppl 1:135-140.

3.1 Introduction

3.1.1 Aims of the chapter

An important pre-requisite in construction of membrane/peptide MD simulations, is the ability to construct an accurate model of a bilayer system and subject the model bilayer system to MD simulation. The work described in this chapter aimed to construct a novel computational model of a unique biological membrane, using molecular dynamics simulations. To date, no report of a mixed DOPC/DOPG (7:3 ratio) system has been made. Neutron diffraction studies have previously been undertaken using this bilayer (Davies *et al.,* 2003).

The construction of a computational model of a mixed DOPC/DOPG membrane will provide further information of lipid properties and packing within a bilayer. Whilst the literature contains many reports on zwitterionic bilayers, there is a lack of knowledge on bilayers which contain a combination of anionic and zwitterionic lipids. This chapter aims to add to current understanding in this field. The model will be used to complement structural studies carried out by other members of the group, allowing both the visualisation of neutron and X-ray diffraction results and the verification of data produced by these MD simulations. The structural parameters (volume of lipid, area of lipid, order parameters & electron density map) generated by the MD simulation were then verified with the parameters obtained from neutron diffraction, NMR studies & combined x-ray and neutron studies respectively.

Construction of a zwitterionic phospholipid bilayer (DOPC) is also described. This bilayer was used in simulating the fusion peptide of SIV, as described in the penultimate chapter of the thesis.

3.1.2 Background to the chapter

MD simulation is rapidly becoming a popular tool that complements experimental techniques in structural biophysics, such as neutron diffraction and NMR. There are a number of computational models of bilayers available in the literature. These studies have focused on single species bilayers in particular di-palmitoyl phosphatidylcholine (DPPC), di-myristoyl phosphatidylcholine (DMPC) and di-oleoyl phosphatidylcholine (DOPC) (Aman *et al.,* 2003, Berger, et al. 1997, Chiu, et al. 1999, Feller, et al. 1997). There have been previous reports of a mixed bilayer. A bilayer of palmitoyl-docosahexaenoyl phosphatidylcholine (PDPC) and palmitoyl-oleoyl phosphatidylcholine (POPC) was studied in the liquid-crystalline (L_α) state. These studies utilised MD simulation and NMR experiments to solve the structure of the mixed PDPC/POPC bilayers. These phospholipids are found in neural tissues (Huber *et al.,* 2002). Another report made by Pandit and Berkowitz described the MD simulation of a mixed DMPC/DMPS bilayer (Pandit and Berkowitz, 2002). However, this chapter describes the first report of a mixed di-oleoyl phosphatidyl-choline (DOPC) and di-oleoyl phosphatidylglycerol (DOPG) bilayer.

3.1.3 Molecular modelling

Molecular modelling is the study of chemical structures and their molecular function utilising Information Technology. A model is a simplified way of describing a complicated system. A major feature of a good model is that it makes systems that are otherwise difficult to study, easier to analyse using a variety of quantitative approaches. Molecular modelling tools rely on our ability to extract relevant parameters from a biological system (be it a single molecule or a collection of molecules, organised in a symmetrical pattern, such as a lipid bilayer). One can then describe them in a mathematical manner, and subsequently develop computational methods that use these parameters to compute the properties of a system or predict its behaviour (Gibbs and Jambeck, 2001).

Structure analysis can be performed on static structures, or movements and interactions in the molecules. The movements & interactions can be studied with molecular simulations. There are four main types of computer simulation used in molecular modelling (Table 3.1).

Type of Simulation	Atoms
Quantum Mechanical	Yes
Classical Electromechanical	No
Stochastic	Yes
Deterministic	Yes

Table 3.1. Comparison of computational simulations.

Monte Carlo simulations are an example of a stochastic simulation. MD simulations are more involved than Monte Carlo ones and are classified under deterministic simulations. They use complex algorithms that allow for simulating non-equilibrated, dynamic systems confined within a simulation box. Molecular structures are usually represented as a collection of atoms, each of which has a defined position in three-dimensional space (Cartesian coordinates in *x, y* & *z* format).

A number of molecular dynamics and Monte Carlo simulations have been performed to replicate and/or complement data obtained from biophysical techniques such as Nuclear Magnetic Resonance (NMR), X-ray diffraction and neutron diffraction. These studies have become more popular in the late nineteen nineties coinciding with the explosion in information technology.

Computer models of biological model membranes can provide insight into molecular mechanisms of membrane protein function. Computational models of biological molecules may use Monte Carlo or Molecular Dynamics (MD) methods. A number of MD simulations of biological membranes are reported in the literature (Pandit and Berkowitz, 2002 ; Feller *et al.,* 1997 ; Tieleman *et al.,* 1997 ; Berger *et al.,* 1997). One noteworthy study combined MD and Monte Carlo simulations (Chiu *et al.,* 1999).

3.1.4 Monte Carlo simulations

The algorithms used within this type of simulation are not ideally designed or selected for a dynamic system. The atoms within the system are moved randomly, but according to probabilistic rules which lead to the generation of a representative variety of structures for given thermodynamic properties of a system (e.g. temperature & volume). This approach has been popular in the study of liquids; it has also been used in the study of proteins or lipid bilayers. However, it has recently been superceded by molecular dynamics simulations (Scott, 2002).

3.1.5 Molecular dynamics simulations

MD simulations are more complex than Monte Carlo simulations and can be classified under deterministic simulations. They use more complex algorithms that allow for simulating a non-equilibrated or dynamic system. Molecular structures are usually represented as a collection of atoms, each of which has a defined position in three dimensional space. Standard molecular simulation approaches model membranes as a collection of point masses (atoms) connected by bonds. These parameters are described in a forcefield. The parameters in a force field are generally equilibrium geometry values (lengths and angles) and force constants that describe harmonic oscillators (Rapaport, 1995). These parameters are obtained from analysis of large amounts of experimental data, or from quantum chemistry calculations on molecular fragments. In an MD simulation, atoms move according to the forces acting on them. Initially random velocities are assigned to displace the system from its equilibrium configuration (Rapaport, 1995).

3.2 Theoretical background to MD simulations

3.2.1 Basic concepts of MD simulations

MD simulations are based on classical mechanics. The simulations solve Newton's equations of motion for all atoms in a system containing a constant number of atoms. The fundamental equation of motion is:

$$m_i \frac{d^2 r_i}{dt^2} = F_i \quad i=1...N \qquad \textbf{(3. 1)}$$

Where m_i is the mass of atom number i, r_i the position of the atom in question, t the time, F_i is the total force acting upon atom i, and N (a constant number of atoms). The atoms are treated as mass points. United atoms can be used, implying that a group of atoms can be treated as a reduced unit such as a CH_2 or CH_3 group as opposed to a real chemical atom. For all MD simulations described within this thesis, a real (explicit) chemical atom was utilised. The exception is for the oleoyl chains in which methylene and methyl groups which exist in these hydrocarbon chains were treated as united atoms. The main reason for treating the aforementioned groups as united atoms was the fact that the acyl chains do not hydrogen bond. Furthermore the use of united atoms in the simulations will allow for economising on computational time.

The force (F_i) is treated conservatively. This can be expressed by the negative derivative of a potential function $V(r_1,r_2,...r_N)$, as shown in equation 3.2.

$$F_i = -\frac{\partial V}{\partial r_i} \tag{3.2}$$

MD solves these equations simultaneously, using small user specified time steps which are user-defined and can be one to five fs. The solution of these equations then results in the generation of new positions and velocities for all atoms within the system. Afterwards, new resulting forces acting upon the atoms are generated, the equations are then solved and the "loop" restarts. The output of an MD simulation is a "trajectory". This file contains the coordinates of all atoms of the system and the force acting upon them. The size of a trajectory is user defined and sampling can take place as required. The trajectories allow for the calculation of physical quantities including the area per lipid, volume per lipid and order parameters. It is with these physical quantities that the link is made between experiment and simulation. These parameters as well as the electron density plot of DOPC and DOPG are described in section 3.6 of this chapter.

3.2.2 Potentials and force fields

Having looked at the equations of motion (equations 3.1 and 3.2), it is now logical to define the potentials. In MD simulation there is always a compromise between accuracy and calculation speed. The specification of potentials is right at the heart of this compromise. Molecular and atomic physics dictates that all interatomic and intermolecular interactions must be included, in order to obtain a valid model. These

interactions must also cover the topology of the molecules within the simulated system. Therefore, intermolecular and intramolecular forces are distinguished (Rapaport, 1995). The simplified potential function, is:

$$V(r) = V_{intra}(r) + V_{inter}(r) \qquad \textbf{(3.3)}$$

3.2.2.1 Intramolecular forces

Molecules are not rigid. They have many degrees of freedom. For instance, the bonds between neighbouring atoms have a certain average equilibrium distance derived from experimental chemistry studies. However, the bonds can oscillate around that equilibrium length. They can be looked upon as spring like. The potential is therefore approximated as a harmonic oscillator, as shown in equation 3.4.

$$V_{bond}\left(r_{ij}\right) = \frac{D_{ij}^{bond}}{2}\left(r_{ij} - r_{ij}^{0}\right)^2 \qquad \textbf{(3.4)}$$

Whereby r_{ij} =| r_j-r_i |, a spring constant is D_{ij}^{bond} that depends upon the type of bond and the equilibrium length r_{ij}^{0}. Bond angles are formed between three atoms (i, j and k). The angle can also oscillate around an equilibrium value. Equation 3.5 describes this potential.

$$V_{angle}\left(\theta_{ijk}\right) = \frac{D_{ijk}^{angle}}{2}\left(\theta_{ijk} - \theta_{ijk}^{0}\right)^2 \qquad \textbf{(3.5)}$$

Whereby (θ_{ijk}) is the bond angle, θ_{ijk}^{0} the equilibrium angle and D_{ijk}^{angle} is the spring constant.

The third type of intramolecular interaction is the interaction between two atoms which have two atoms between them. These atoms taken collectively are referred to as dihedrals or torsion angles. As can be seen from Figure 3.1, the two outer atoms can rotate freely around the middle bond. The interaction is by no means straightforward hence the potential is approximated as follows:

$$V_{dihedral}(\phi_{ijkl}) = D_{ijkl}^{dihedral}(1+\cos(n\phi-\phi_0)) \qquad \textbf{(3.6)}$$

Whereby the dihedral angle is ϕ, the equilibrium angle is ϕ_0, the spring constant is $D_{ijkl}^{dihedral}$ and n is the multiplicity that determines the number of minima during a full rotation. An improved dihedral potential was proposed by Ryckaert and Belleman (Ryckaert and Belleman, 1978) which is utilised in *GROMACS*, the MD simulation package used for performing all the MD simulations described in this thesis. A graphical illustration is shown in Figure 3.1.

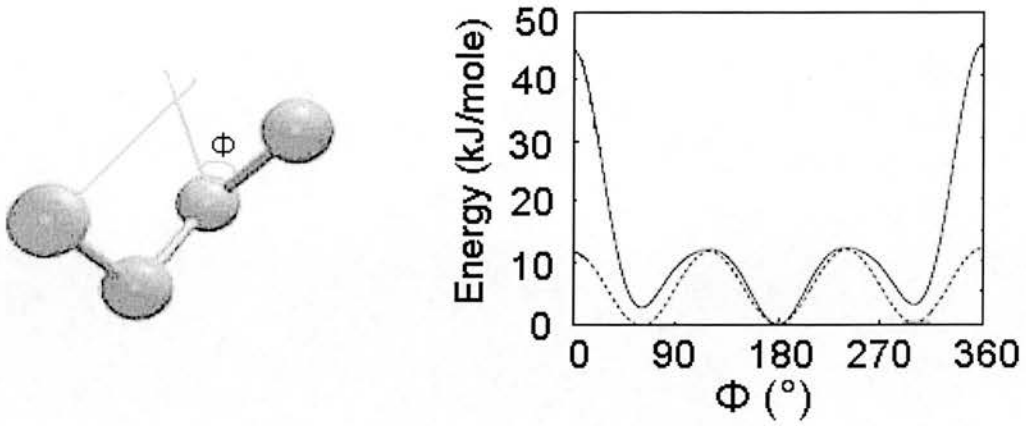

Figure 3.1. Dihedral angle (left) and plot of a typical Ryckaert Belleman dihedral potential (modified from Lindahl *et al.*, 2001).

3.2.2.2 Intermolecular forces

Compared to the bonded interactions described earlier the calculation of non-bonded interactions, requires greater computational processing power. The main reason for this is that forces between all atoms have to included and not only the forces between atoms of the same molecule. Three forces are taken into account as far as MD simulations are concerned. They are as follows:

1. Attractive van der Waals interactions, caused by induced dipole moments;
2. Repulsive forces on short distances also known as the overlap of wave functions;
3. Electrostatic interactions between charged atoms.

The first two forces are combined by a Lennard-Jones potential, as can be seen in equation 3.7.

$$V_{LJ}(r_{ij}) = \frac{C_{ij}^{12}}{r_{ij}^{12}} - \frac{C_{ij}^{6}}{r_{ij}^{6}} \quad \textbf{(3.7)}$$

The parameters C_{ij}^{12} and C_{ij}^{6} depend upon the type of atom (i or j). The third force, described above is dealt with by the Coulomb potential (equation 3.8).

$$V_{C}(r_{ij}) = \frac{q_i q_j}{4\pi\varepsilon_0 r_{ij}} \quad \textbf{(3.8)}$$

Whereby q is the atomic point charge of the atom and ε_0 is the permittivity.

All pair interactions that are negligible (i.e. $\geq$ 2 nm) are not taken into account (Lindahl *et al.*, 2001).

3.2.3 Periodic boundary conditions

Finite and infinite systems are very different, and the question of how large a relatively small system must be to yield results that resemble the behaviour of the infinite system faithfully lacks a definitive answer. MD simulations take place in a "box". It is tempting to view the box walls as rigid boundaries against which atoms collide while trying to escape from the simulation region. However, samples used for neutron and X-ray diffraction are not confined within a box. Unless the aim of an MD simulation is the study of the behaviour of atoms near walls, then walls are best eliminated.

A system that is bounded but free of physical walls can be constructed by resorting to PBC, shown schematically in a two-dimensional format in Figure 3.2.

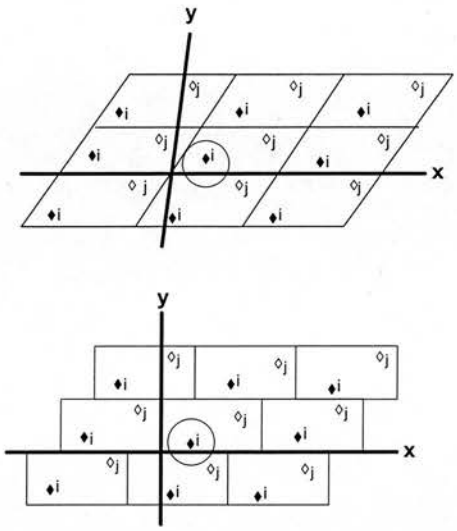

Figure 3.2. Visualization of periodic boundary conditions (PBC) in a two-dimensional format. Two atoms (*i* and *j*) are shown in the simulation boxes together with their respective periodic images.

The introduction of periodic boundaries is akin to considering an infinite space-filling array of identical copies of the simulation region. There are two consequences which arise as a result of this periodicity. The first is that an atom leaving the simulation region re-appears in the opposite face. The second is that atoms lying within a distance (r_c) of a boundary interact with atoms in an adjacent copy of the system, or equivalently with atoms near the opposite boundary. In other words, a wraparound effect occurs. An alternative way of looking at periodic boundaries is to think of mapping regions topologically onto the equivalent of a torus in four dimensions (a two-dimensional system is mapped onto a torus); then it becomes apparent that there are no physical boundaries. In this way it is possible to model systems that are effectively bounded but that are nevertheless spatially homogenous in so far as boundaries are concerned (Rapaport, 1995).

From a computational point of view; periodic boundaries are most easily handled when the dimensions are that of a rectangular prism. However, this is not an essential requirement and any space filling convex region can be used. *GROMACS*, much like other MD simulation software uses boxes which are based on crystallographic unit cells. In the case of the MD simulations described within this thesis, only triclinic boxes were used. The rationale for choosing box shapes is to enlarge the volume to surface ratio, and thus increase the maximum distance between atoms before periodic ambiguity appears (Rapaport, 1995). PBCs were used in all simulations decribed within this thesis.

3.2.4 Treatment of electrostatics and long range interactions

The total electrostatic energy of N particles and the corresponding periodic images are given by equation 3.9:

$$V = \frac{f}{2} \sum_{n_x} \sum_{n_y} \sum_{n_z}{}^{*} \sum_{i}^{N} \sum_{j}^{N} \frac{q_i q_j}{r_{ij} n} \qquad \textbf{(3.9)}$$

Whereby (n_x,n_y,n_z)=n which is the box index vector, the * indicates that terms with $i=j$ must be omitted when $(n_x,n_y,n_z) = (0,0,0)$. The distance $r_{ij}n$ is the real distance of the charges and not the minimum image when PBC is utilised.

Long-range and electrostatic interactions must be treated appropriately if the simulation is to run smoothly. The two methods of dealing with these interactions are cut-offs and Ewald summations of which the particle mesh Ewald (PME) is implemented in the *GROMACS* package (Lindahl *et al.,* 2001).

3.2.4.1 Cut-offs

Cut-offs are very straightforward, *GROMACS* simply cuts-off any electrostatic interactions occurring beyond a spherical radius, which is user defined (usually ~1.8 nm). However, cut-off restrictions do apply. For instance, the cut-off radius used to truncate non-bonded interactions must not exceed half the shortest box vector used for the grid search. The grid search is one of the software's methods for detecting long-range interactions, the other being simple search. Grid search breaks the box up into grids and searches for electrostatic and long-range interactions. Simple search performs exactly the same function except no grids are involved. If the cut-off radius used does exceed half of the smallest box vector, then more than one image will be within the cut-off distance of the force. This will lead to misinterpretation of the simulation. In short the length of each box vector must exceed the size of macromolecule in the corresponding direction and two times the cut-off radius.

3.2.4.2 Ewald summation

Ewald summation was first introduced as a method to calculate long-range interactions of the periodic images in crystals (Darden and Pedersen, 1996). The rationale is to convert the single slowly converging sum in equation 3.9 into two fast

converging terms and a constant term. Two summations are made within Ewald summation. They are the direct space sum and the reciprocal space sum. PME solves the Poisson equation over all of the simulation (reciprocal and direct) space. The Poisson equation determines the electric field at each point in space from all the charges nearby. So, instead of calculating each pair-wise electrostatic interaction (time consuming), one can quickly (by way of the Fourier transform) obtain the electric field near each atom (which is the total influence of all the pair-wise interactions), to get the force due to electrostatics. A short cut-off (~ 1nm) is used in the direct space and reciprocal sum. However, the computational cost of the reciprocal sum increases as the number of particles in the system increase. It is therefore not recommended for larger systems of the order of ~50000 atoms. It has been reported that spherical cut-offs can introduce artefacts in solutions with ions but if the cut-off radius is large enough (> 1.8 nm), this method appears to work well for lipids (Tieleman *et al.,* 1997). Hence, the initial selection of spherical cut-offs as opposed to PME for the treatment of electrostatic interactions. However, a control simulation which utilised PME to treat electrostatics was also performed. This simulation was performed only with the mixed DOPC/DOPG bilayer and not with the zwitterionic system of the DOPC bilayer. The rationale for selecting PME or cut-off is to reproduce an environment as close as possible to a biological setting. Data comparing the *d*-repeats of the different systems are presented and discussed in section 3.6 of this chapter.

3.2.5 Temperature and pressure coupling

Theoretically the information of the system's initial configuration and the equations of motion and all further configurations of the simulated system are determined microscopically. However, macroscopic properties must also be controlled collectively. These properties must be in agreement with real biological systems or else the models constructed will be of little or no value. Two macroscopic properties are of particular interest, they are temperature and pressure. In an MD simulation, these properties tend to be "coupled" to a bath (Berendsen *et al.,* 1984).

3.2.5.1 Temperature coupling

The simulations described within this thesis utilised the Berendsen method of temperature coupling. The Berendsen algorithm (Berendsen *et al.,* 1984) mimics weak coupling with first-order kinetics to an external heat bath with a user defined temperature T_0. The effect of this algorithm is that a deviation of the system temperature from T_0 is slowly corrected according to equation 3.10.

$$\frac{dT}{dt} = \frac{T_0 - T}{\tau} \qquad \textbf{(3.10)}$$

Equation 3.10 is a mathematical representation of the fact that a temperature deviation decays exponentially with a time constant of τ. This particular method of temperature coupling has the added advantage that the strength of the coupling can be controlled by the user. For example, for equilibration purposes the coupling time can be taken as ~0.01 ps, whereas for reliable equilibrium runs a value of ~0.5 ps can be used.

The heat flow into or out of the system is effected by scaling the velocities of each particle every step with a time-dependent factor λ given by equation 3.11.

$$\lambda = \left[1 + \frac{\Delta t}{\tau_T} \left\{ \frac{T_0}{T\left(t - \frac{\Delta t}{2} \right)} - 1 \right\} \right]^{1/2} \qquad \textbf{(3.11)}$$

The parameter τ_T is close to, but not exactly equal to the time constant τ of the temperature coupling (equation 3.10). Equation 3.12 describes the time constant τ.

$$\tau = 2C_v \tau_T / N_{df} k \qquad \textbf{(3.12)}$$

Whereby C_v is the total heat capacity of the system, k is the Boltzmann's constant and N_{df} is the total number of degrees of freedom. The reason $\tau \neq \tau_T$ is that the kinetic energy caused by scaling the velocities is partly redistributed between kinetic and potential energy and therefore the change in temperature is less than the scaling energy. When the term "temperature coupling time constant" is used it refers to the parameter τ_T. This type of temperature coupling has been utilised for various membrane protein simulations (Sansom *et al.,* 2002; Law *et al.,* 2003; Tieleman *et al.,* 1999).

3.2.5.2 Pressure coupling

Just as the system is coupled to a temperature bath, it can also be coupled to a "pressure bath". The Berendsen algorithm (Berendsen *et al.,* 1984) for pressure coupling was chosen which scales coordinates and box vectors at each time step with a matrix μ. This results in a first-order kinetic relaxation of the pressure towards a given reference pressure P_0. Equation 3.13 describes this type of pressure coupling:

$$\frac{dP}{dt} = \frac{P_0 - P}{\tau_p} \tag{3.13}$$

Whereby τ_p is the pressure coupling time constant and P is the actual pressure of the system. The scaling matrix is given by equation 3.14.

$$\mu_{ij} = \delta_{ij} - \frac{\Delta t}{3\tau_p}\beta_{ij}\left\{P_{0ij} - P_{ij}(t)\right\} \tag{3.14}$$

On this instance β is isothermal compressibility of the system. In most cases the scaling matrix will be diagonal with equal elements on the diagonal, the value of which is generally not known. However, it is sufficient to take a rough estimate because the value of β only influences the non-critical time constant of the pressure relaxation without affecting the average pressure itself.

3.2.6 Integration algorithm

Once *GROMACS* has calculated the forces, the next step is to update the configuration of all atomic positions and velocities. This is done by integrating the

acceleration $\frac{d^2 r_i}{dt^2}$ shown in equation 3.1. Time in an MD simulation is not continuous, hence it follows that a suitable integration algorithm is required. The integration algorithm utilised in *GROMACS* is the leap frog algorithm, which is shown schematically in Figure 3.3. This algorithm is obtained using a second order approximation of Taylor's expansion.

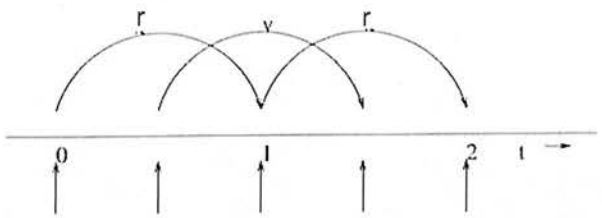

Figure 3.3. The leap-frog integration method. The algorithm is referred to as leap-frog as *r* and *v* are leaping like frogs over each others backs.

$$r_i(t+\Delta t) \approx r_i(t) + \Delta t\, v_i(t+\Delta t/2) \qquad (3.15)$$

$$v_i(t+\Delta t/2) \approx v_i(t-\Delta t/2) + \frac{\Delta t}{m_i} F_i \qquad (3.16)$$

Whereby r_i is the position of the atom(s), m_i the mass of atom number (i), Δt is the difference in time and F_i is the force acting on atom i. A timestep of 2 fs is routinely used in MD simulations. This timestep results in a more accurate simulation when compared to experimental results (Tieleman *et al.,* 1997)

3.2.7 Energy minimization (EM)

Energy minimization (EM) is a pre-requisite step before MD simulation. EM is used in order to decrease the potential energy of a system and nullify any bad contacts in the starting configuration. It is frequently used by MD simulators and can be sub-divided into two categories. They are steepest descent and conjugate gradient. Steepest descent might not be the most efficient algorithm but it is robust and easy to implement. Conjugate gradient on the other hand is initially slower than steepest descent. However, conjugate gradient becomes more efficient nearer the energy minimum. All EM used prior to the commencement of MD simulations described within this thesis were of the steepest descent category. The steepest descent can be mathematically described as follows: A vector (r) is defined as the vector of all 3 atomic coordinates. Initially a maximum displacement (h_0) must be given by the user (e.g. 0.01 nm). First of all the forces (F) and potential energy of the system are calculated. All new positions are then calculated as described by equation 3.17:

$$\bar{r}_{n+1} = \bar{r}_n + \frac{\bar{F}_n}{\max(|\bar{F}_n|)}\bar{h}_n \qquad \textbf{(3.17)}$$

Whereby h_n is the maximum displacement and $\bar{F}_n$ is the force which is also referred to as the negative gradient of the potential V. The notation max refers to the largest absolute values of the force components. The forces and energy are now once again computed for the new positions such that if ($V_{n+1} < V_n$) the new positions are accepted and $h_{n+1}=1.2h_n$, accordingly if ($V_{n+1} \geq V_n$) then the new positions are rejected and $h_n=0.2h_n$. The algorithm stops when either a user specified number of

force evaluations have been performed or when the maximum of the absolute values of the force (gradient) components is smaller than a user specified value ε. The user should bear in mind that force truncations produces some noise in the energy evaluation, the stopping criterion should not be made too tight to avoid endless iterations. A reasonable value for f can be estimated from the root mean square force of a harmonic oscillator (Berendsen *et al.,* 1995). The relationship is expressed in equation 3.18:

$$f = 2\pi v\sqrt{2mkT} \qquad \textbf{(3.18)}$$

Whereby v is the oscillator frequency, m the reduced mass, k is the Boltzmann's constant and T is temperature.

The rationale behind using steepest descent as opposed to conjugate gradient is as follows: model biological systems are dynamic and regardless of energy minimization procedures an MD simulation equilibration period of ~200 ps are required for most systems. The purpose of steepest descent was merely to produce a starting system which was stable enough for the real equilibration to take place. This equilibration can take the form of an NVT (constant number of particles, constant volume and constant temperature) MD simulation. Therefore there was no real need to reach the energy minimum such as could be achieved with conjugate gradient. This is summarized in Figure 3.4.

THE GLOBAL MD ALGORITHM

1. Input initial conditions

Potential interaction (V) as a function of atom positions

Positions (r) of all atoms in the system

Velocities (v) of all atoms in the system

⇩

Repeat steps 2, 3 and 4

2. Compute forces

The force of on any atom

$$F_i = -\frac{\partial V}{\partial r_i}$$

is computed by calculating the force between non-bonded atom pairs:

$$F_i = \Sigma_j F_{ij}$$

plus the forces due to bonded interactions (which may depend on 1, 2, 3 or 4 atoms), plus restraining and/or external forces.

The potential and kinetic energies and the pressure tensor are computed.

⇩

3. Update configuration

The movement of the atoms is simulated by numerically solving

Newton's equation of motion

$$\frac{d^2 r_i}{dt^2} = \frac{F_i}{m_i}$$

or

$$\frac{dr_i}{dt} = v_i \quad \frac{dv_i}{dt} = \frac{F_i}{m_i}$$

⇩

4. if required: Output step

write positions, velocities, energies, temperature, pressure, etc.

Figure 3.4. The global MD algorithm utilised within *GROMACS* (Berendsen *et al.*, 1995).

3.2.8 The limitations of MD simulations.

All models have their limitations. To this extent, computational models of a biological environment are no different. Approximations are made when constructing a computational model of a biological membrane utilising MD simulations, they are as follows:

1. MD simulations utilize classical mechanics. However, the space dimensions and system temperatures used in membrane protein simulations justify this approximation.

2. Forcefields are conservative and depend purely upon the positions of the atoms and not on their velocities.

3. Forcefields are pair additive. In other words, only pairwise interactions are taken into account for the calculation of intermolecular forces.

4. Long-range interactions are either cut-off or are treated using PME. Both methods are approximations.

5. Periodic boundary conditions are an approximation used primarily to avoid edge and surface effects. These effects are a direct result of forces and velocities within the system. In general, the bigger the system the smaller the error generated. In an experimental situation (e.g. neutron or X-ray diffraction) bilayers are arranged in a lamellar stack on the z axis. However, computationally this arrangement is expensive therefore PBC is utilised to create a virtual lamellar stack. Furthermore, PBC conditions ensure that the bilayer does not rotate away from the initial configuration.

3.3 Method

3.3.1 Forcefields

GROMACS software is primarily designed for MD simulation of biologically active/relevant proteins, although it is commonly used for lipids bilayers as well. The forcefield used in the MD simulations presented here was a modified explicit hydrogen forcefield included in *GROMACS* (ffgmx2_lipid) (Lindahl *et al.,* 2001). DOPC and DOPG were divided into headgroup and chain regions. The majority of MD simulations reported in the literature have utilised implicit hydrogens, primarily to save on computational time. There have been reports of explicit hydrogens in DMPC and DMPS phospholipid simulations. The main reason why explicit hydrogens were used in this study was to investigate hydrogen bonding between a peptide and the bilayers that have been generated by MD simulation. Figures 3.5 and 3.6 display the two dimensional chemical structure of DOPC and DOPG respectively.

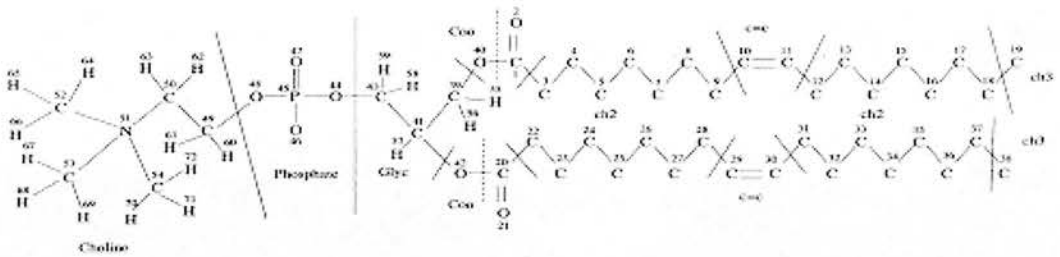

Figure 3.5. The two dimensional chemical structure of a DOPC molecule with explicit hydrogens. The headgroup contains explicit hydrogens. The explicit hydrogens are present primarily for future simulations with peptides that have been previously studied via neutron diffraction by other group members. The dashed lines indicate the borders between the headgroup and hydrocarbon chains. The solid lines divide up the molecule in precisely the same manner as in the experimental studies of Wiener and white (Wiener & White 1991; Wiener & White 1992). The headgroup region compromises choline, phosphate and glyceryl moieties. One group is shared between the glyc (glycerol) and chain regions (COO); the left-most oxygen atom is part of the headgroup, while the oxygen and the carbon are part of the chain region. The other specific groupings in the chain region are CH_2, CH_3 and C=C respectively.

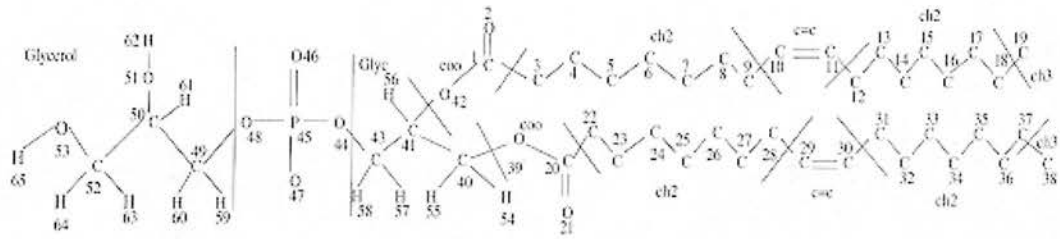

Figure 3.6. The two dimensional chemical structure of a DOPG molecule with explicit hydrogens. The headgroup contains explicit hydrogens. The explicit hydrogens are present primarily for future simulations with peptides that have been previously studied via neutron diffraction by other group members. The solid lines divide up the molecule in a similar manner as in the experimental studies of Wiener and white (Wiener & White 1991; Wiener & White 1992) for DOPC. The headgroup region compromises glyceryl and phosphate moieties. One group is shared between the glyceryl moiety and chain regions (COO); the left-most oxygen atom is part of the headgroup, while the oxygen and the carbon are part of the chain region. The other specific groupings in the chain region are CH_2, CH_3 and C=C respectively.

Nineteen unique subgroups were identified in the headgroup and chains respectively (see Figure 3.7). The locations of these subgroups were as follows: Group one (PO4) is found in all headgroups containing phosphate moieties. Group two (NC4) is found specifically in the choline moiety of phosphatidylcholine headgroups. Group three (NCH3) is found in the amide groups of both phosphatidylethanolamine and phosphatidylcholine headgroups. Group four (OP1) is a single bonded phosphorus atom bound to an oxygen atom and is found in all headgroups containing phosphate moieties. Group five (OP2) is a double bonded phosphorus atom bound to an oxygen atom and is found in all headgroups containing phosphate moieties. Group six (OCP) is commonly found within the connecting carbon to phosphate region of a phospholipid headgroup. Group seven (OCH) is found in a phosphatidylglycerol headgroup. Group eight (OCC) attaches an acyl chain to a backbone glycerol in all phospholipid headgroups. Group nine (OC1) is found in the terminating region of the phophatidylserine headgroup. Group ten (OC2) is also found on the terminating region of a phophatidylserine headgroup. Group eleven (CCCHH) is observed in a saturated lipid chain such as myristoyl. Group twelve (CCCHN) is found connecting the second carbon in a phosphatidylserine to its surrounding atoms. Group thirteen (CCCHO) is seen in a backbone glycerol region as well as in a phosphatidylglycerol headgroup. Group fourteen (CCOHH) is observed in the glycerol backbone of all phospholipids. Group fifteen (CCNHH) is the connecting carbon in a CH_2 group which attaches to a nitrogen and carbon atom in a phosphatidylcholine headgroup. Group sixteen (CNHHH) attaches a carbon (from a methyl group) onto nitrogen in phosphatidylcholine headgroups. Group seventeen (CCHHH) is a carbon attaching itself onto a terminal methyl group in any of the selected lipid chains. Group

eighteen (COOC) is commonly seen in acyl chains as the connecting carbon between an oxygen atom in the glycerol moiety (single bond) and the second carbon in an acyl chain. Group nineteen (CCCH) is the double bond seen between carbons nine and ten in an oleoyl chain. The lipid groupings were then cross-referenced against the twenty basic amino acids and DNA. Table 3.2 displays the location of the equivalent middle atom of these lipid groupings in the twenty basic amino acids and DNA. Forcefields for the bonded intramolecular forces for both DNA and proteins were present in *GROMACS*. Having cross referenced the lipid groupings with the DNA and protein forcefields, a customized forcefield was created manually. Forcefields for the non-bonded intermolecular forces of phospholipid groupings are available (Berger *et al.,* 1997) and were therefore utilised in all MD simulations described within this thesis.

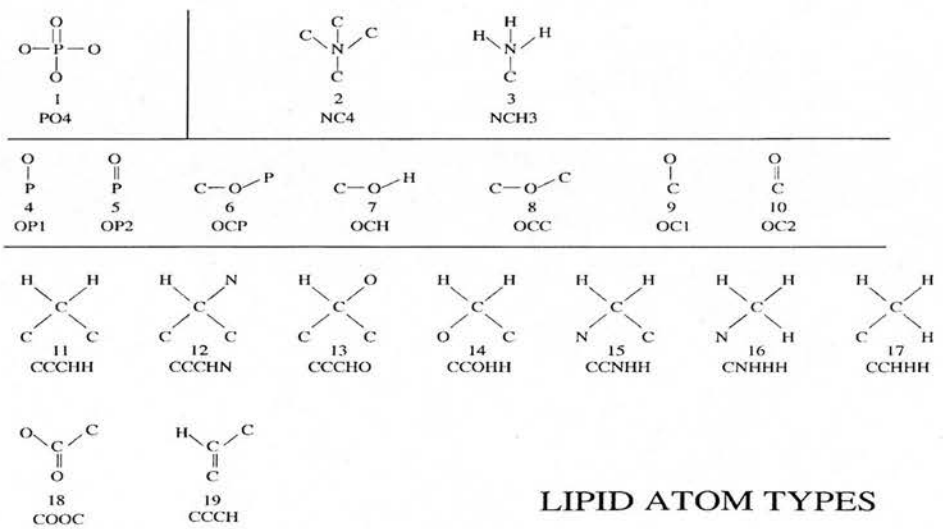

Figure 3.7. The unique sub structures that are present within the selected phospholipid headgroups and chains. These groups were then cross-referenced with the matching unique structure present within the twenty basic amino acids and DNA such that the bond lengths, energies, bond angles, forces and torsion angles (dihedrals) can be approximated from the original *GROMACS* explicit hydrogen forcefield (ffgmx2).

Lipid Number	Lipid Type	Peptide/DNA Cross reference
1	**PO4**	P -2' deoxy X 5' phosphoric acid
2	**NC4**	No exact match, used Proline N
3	**NCH3**	ASP-Nδ2; LYS-Nζ; GLN-Nε2; ARG-η2
4	**OP1**	O1 – 2' deoxy X 5' phosphoric acid
5	**OP2**	O2 – 2' deoxy X 5' phosphoric acid
6	**OCP**	O5 – 2' deoxy X 5' phosphoric acid
7	**OCH**	SER-Oγ, ASP, GLU, THR-Oγ, TYR-Oη
8	**OCC**	O4 – 2' deoxy X 5' phosphoric acid
9	**OC1**	ASP; GLU
10	**OC2**	ASN-Oδ; GLN-Oε
11	**CCCHH**	Cβ-Most AA; ILE-Cγ1; LYS-Cγ,δ; GLU-Cγ
12	**CCCHN**	Cα, except GLY& PRO
13	**CCCHO**	THR-Cβ
14	**CCOHH**	SER-Cβ
15	**CCNHH**	LYS-Cε
16	**CNHHH**	No exact match, used CCHHH
17	**CCHHH**	ALA-Cβ; VAL-Cγ; LEU-Cδ; ILE-Cδ; THR-Cγ
18	**COOC**	GLU-Cδ; TYR-Cζ
19	**CCCH**	No exact match, used Cδ & ε of TRP& PHE

Table 3.2. Cross referencing the location of the selected lipid groupings in the twenty basic amino acids and DNA.

3.3.2 File formats in *GROMACS*

In order to run a basic simulation in the *GROMACS* package, the following input files are mandatory: A coordinate file (*.pdb or *.gro which is the *GROMACS* equivalent of pdb), topology files and a linking path (*.itp & *.top) and a run parameter file (*.mdp). Figure 3.8 illustrates a typical MD simulation run with *GROMACS.*

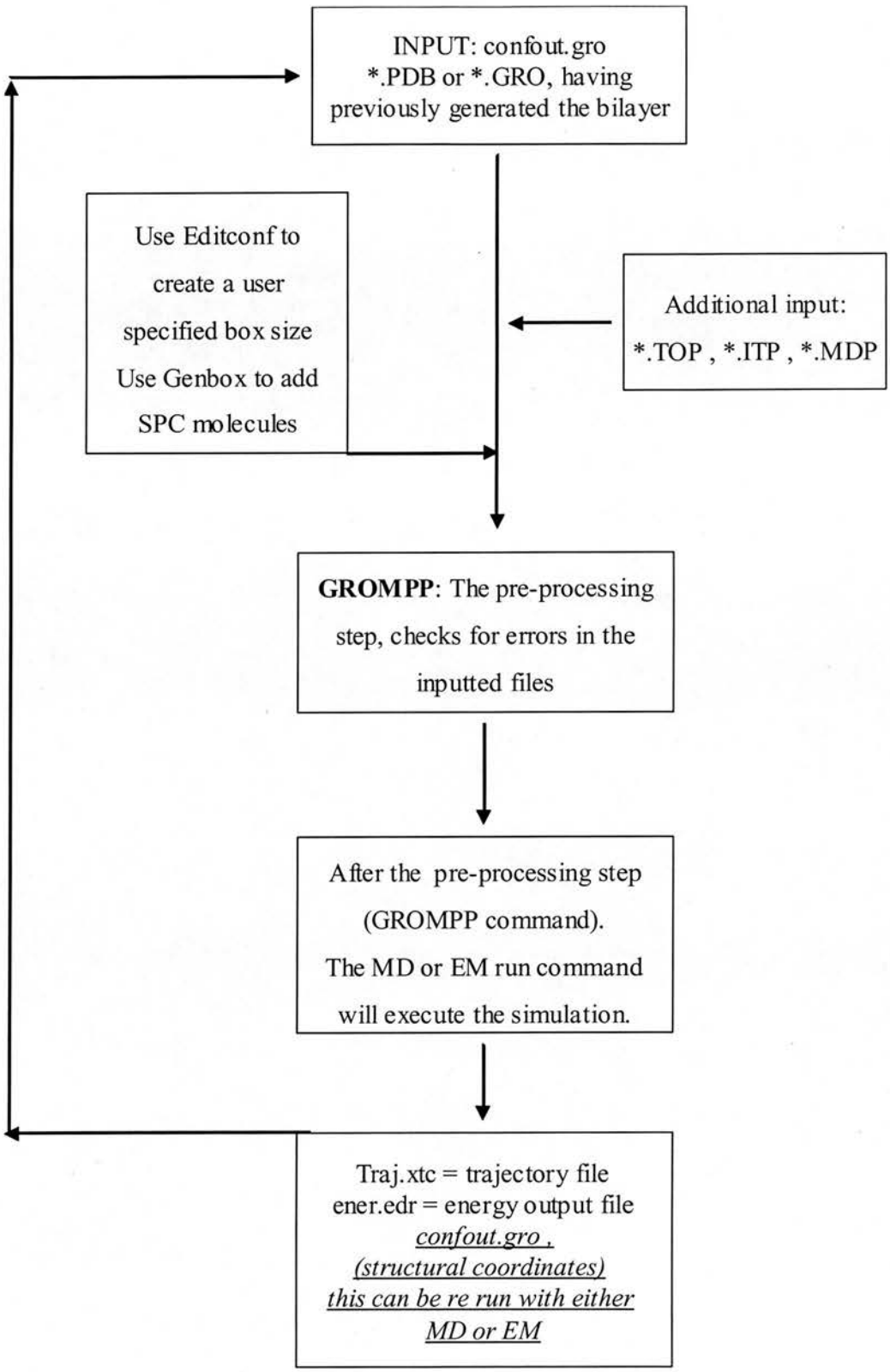

Figure 3.8. Flowchart depicting how a typical simulation runs on *GROMACS*

3.3.3 System generation

Method A

A mixed DOPC/DOPG bilayer was constructed with explicit hydrogens in the phospholipid headgroups (see Figures 3.5 and 3.6). The complete topologies of the molecules were described in the form of bonds, angles and dihedrals (torsion angles). Atomic point charges for both PC and PG headgroups were generated by *HyperChem 5.0* (Hypercube Inc., Waterloo, Canada) using the STO-3G set as used in previous studies of DMPC and DPPC (Berger *et al.,* 1997; Feller *et al.,* 1997). The bilayer was constructed by taking a previously customized PDB file of each molecule and arranging them, using *Sybyl 6.7* (Tripos Inc. St Louis MO), in a row of ten molecules with a ratio of 7 DOPC to 3 DOPG. Seven rows of ten lipid molecules were generated and the DOPG molecules were arranged in such a way that they were not in close contact with each other. This arrangement is representative of a biological environment whereby the zwitterionic PC headgroups will be interspersed with the anionic PG headgroup. The monolayer of 70 lipid molecules was then copied and rotated in order to create a bilayer of 140 lipid molecules, comprising 98 DOPC and 42 DOPG molecules. For the construction of the DOPC bilayer a pre-customized PDB of a DOPC molecule was taken and replicated in a row of eight. The rows of eight were then replicated eight times, in order to form a monolayer of 64 or 128 lipids. The monolayer was then replicated and rotated such that a bilayer was produced (128 or 256 lipids).

Method B

Two monolayers were constructed, one of 70 DOPC molecules and one of 70 DOPG molecules, by replicating each lipid in an array of ten molecules by seven molecules. The two monolayers were then superimposed and either the DOPC or the DOPG molecule at each site was deleted to leave a single molecule in that position. In order to replicate the conditions of the neutron measurements, a random number generator was used to select the type of molecule for deletion at each site, to give a final ratio of 7 DOPC to 3 DOPG molecules. The composite monolayer of 70 lipid molecules was then duplicated and rotated to form a 140-lipid bilayer (a programme written by Dr Bradshaw was used to generate the bilayer on this occasion).

3.3.4 Atomic point charges

Atomic point charges are routinely included in all MD simulations. GROMACS has the capability to generate charges for proteins. However, this facility does not exist for phospholipids. Therefore this was performed using another software package. Table 3.3 represents the atomic point charges calculated using *HyperChem*. The sto-3G data set was utilised as used in other bilayer MD simulations. To save on computational time charges were intentionally not calculated for atom number 7-19 and 26-38 for both DOPC and DOPG respectively. This is quite valid and has been recommended by other workers (Berger *et al.,* 1997; Heller and Schaefer, 1993).

1	2	3	4	5	6	7	8
Atom no.	Atom charge	Atom no.	Atom charge	Atom no.	Atom charge	Atom no.	Atom Charge
1	0.27	54	0.017	1	0.269	54	-0.082
2	-0.263	55	0.07	2	-0.236	55	0.062
3	-0.004	56	0.063	3	0.008	56	0.342
4	0.05	57	0.051	4	0.023	57	0.05
5	0.565	58	0.062	5	-0.061	58	0.051
6	-0.0295	59	0.07	6	0.00001	59	0.052
7 till 19	no charge	60	0.053	7 till 19	no charge	60	0.048
20	0.184	61	0.041	20	0.231	61	0.051
21	-0.365	62	0.168	21	-0.188	62	0.101
22	-0.136	63	0.038	22	0.002	63	0.101
23	-0.062	64	0.083	23	0.028	64	0.114
24	-0.032	65	0.175	24	0.038	65	0.138
25	-0.0295			25	0.00001	66	0.104
26 till 38	no charge			26 till 38	no charge	67	0.138
39	-0.269			39	0.025	68	0.104
40	-0.135			40	-0.23	69	0.114
41	0.023			41	0.042	70	0.107
42	-0.106			42	-0.253	71	0.114
43	-0.016			43	-0.035	72	0.114
44	-0.464			44	-0.348		
45	1.34			45	0.768		
46	-0.741			46	-0.671		
47	-0.635			47	-0.501		
48	-0.47			48	-0.358		
49	-0.021			49	-0.037		
50	0.066			50	-0.017		
51	-0.318			51	-0.156		
52	0.005			52	-0.083		
53	-0.298			53	-0.083		

Table 3.3. Atomic point charges of DOPC and DOPG. Columns 1-4 of the table correspond to DOPG (Figure 3.6), columns 5-8 correspond to DOPC (Figure 3.5). The numbering corresponds to the Figures of both DOPC and DOPG, respectively.

3.3.5 Method and run parameters for the mixed bilayer

The MD computer package *GROMACS* (Lindahl, et al. 2001) version 3.1.4 was used to centre the bilayers in a triclinic box, and a total of 2815 SPC (Simple Point Charge) (Berendsen *et al.,* 1995) water molecules were added to either side of the

bilayers. The ratio of water molecules per lipid (20.1:1) was chosen to replicate the conditions used in neutron diffraction experiments, using the same ratio of DOPC:DOPG and those quoted in the literature (Tieleman *et al.,* 1997). There is another type of water molecule used in MD simulations of biological systems, which is derived from the original SPC. Simple Point extended Charge (SPC/e) possesses a lower free energy (-26.7 $kJ.mol^{-1}$). SPC was selected, primarily due to the fact the free energy of SPC (-24.3 $kJ.mol^{-1}$) is closer to the actual experimental value (Tieleman *et al.,* 1997). The *GROMACS* programme *genion* was used to add 42 sodium counter ions to the mixed bilayers. In short, the programme replaces SPC water molecules with Na^+ counter-ions necessary to counter balance the total negative charge (-1 ve) of the DOPG molecule. The programme replaces an SPC molecule with Na^+, if the SPC molecule is in an electrostatically favourable position for a counter-ion.

Energy minimization (EM) by the "steepest descent" method was used to remove bad contacts and reduce the potential energy of the systems. The systems were then subjected to a 20 ps MD simulation utilising the NVT (constant number of particles, constant volume and constant temperature) ensemble (18315 atoms/particles, volume of 800 nm^3 & temperature of 300 K). Tieleman and co-workers have proposed running a hydrated bilayer system with an initial NVT system before proceeding to another ensemble (Tieleman *et al.,* 1997). The rationale behind such a protocol is to allow the SPC molecules to equilibrate naturally within the system, without the SPC molecules being pressurised into the bilayer. The system was then subjected to another MD simulation using the NPT (18315 atoms/particles, pressure of 1 bar &

temperature of 300 K) ensemble over a 3500 ps period. Temperature and pressure (Berendsen *et al.,* 1984) were coupled individually to the three groupings in both DOPC (DPC=headgroup, OLA=*sn-1* chain, OLB=*sn-2* chain) and DOPG (DPG=headgroup, OLC=*sn-1* chain, OLD=*sn-2* chain) molecules and SPC using the Berendsen algorithm, as implemented in *GROMACS.* A time constant of 5 ps was set for each group. For both the NVT and subsequent NPT pressure was set at 1 bar. The pressure asserted on the box was of an isotropic nature. A time constant for pressure coupling was also set at 5 ps. In the NPT ensemble the pressure coupling was isotropic. Coupling groups on an individual basis allows for greater stability during an MD run.

Order parameters were measured after 3500 ps of an NPT ensemble MD run for both the DOPC and the mixed DOPC/DOPG bilayer. The time step for all parts of the MD and EM simulations were 2 fs. This time step was used in a number of previous bilayer simulations (Berger *et al.,* 1997; Feller *et al.,* 1997a; Heller and Schaefer, 1993; Feller *et al.,* 1997b).

3.3.6 Method and run parameters for the DOPC bilayer

The methods used for the DOPC bilayer were exactly the same as those used for the mixed bilayer except that the PME algorithm was not use to treat electrostatics (explained in the proceeding section). The DOPC bilayers were composed of 256 molecules (18432 atoms) and 128 molecules (9216 atoms), repectively. No counterions were present in either system. The 256 molecules system contained

5632 SPC molecules (a water per lipid ratio of 22:1), whereas the 128 molecule system contained 2816 SPC molecules (the same water per lipid ratio of 22:1). These water per lipid ratios are based on the neutron diffraction studies (Bradshaw *et al.*, 2000).

3.4 Verification of method

The simulation was verified by comparing **four** parameters obtained from the MD simulation with the experimental values. They were as follows:

3.4.1 Area per lipid molecule

The area occupied by each lipid molecule was obtained by multiplying the X and Y dimensions of the box and dividing by the number of lipid molecules present in each leaflet (70 for the mixed bilayer system and 64 and 128 for the DOPC bilayers) (Feller *et al.,* 1997a). The area per lipid can be measured experimentally by Langmuir techniques.

$$\text{Area per lipid} = X.Y/70 \qquad \textbf{(3.17)}$$

3.4.2 Volume per lipid molecule

The volume of each lipid molecule within a bilayer system can be determined using diffraction techniques. It provides another independent parameter by which a computer simulated structure may be compared to experimental observations. The method employed for calculating the volume of lipid (Chiu *et al.,* 1999), is given by the following simple equation:

$$V_L = A.D/2 - (N_w.V_w) \qquad \textbf{(3.18)}$$

Whereby A = area per lipid, D = height of the simulation box (Z dimension), N_w = number of waters per lipid molecule, V_w = volume per water.

3.4.3 Order parameters

The ordering of hydrocarbon tails has been studied by NMR spectroscopists, who use the term "order parameter" to describe the average orientation of each section of an acyl chain. The order parameter is derived from the quadrupole splitting of NMR spectra and is determined by selective deuteration of successive carbons of the acyl chains.

The order parameter tensor S_z, which is defined as:

$$S_z = \frac{3}{2}\left\langle \cos^2 \theta_z \right\rangle - \frac{1}{2} \qquad \textbf{(3.19)}$$

Whereby θ_z is the angle between the z-axis of the simulation box and the molecular axis under consideration (in this case z, as this is the axis of the bilayer normal). The molecular axis under considersation is defined as the vector from C_{n-1} to C_{n+1}, when C is defined as a specific carbon in the oleoyl chains.

Order parameters are calculated for each atom of the hydrocarbon chain, other than the terminal methyl group and the first carbon in the chain. These order parameters can be calculated by *GROMACS*, using the g_order command. However, the resulting index file must be modified to include 3 consecutive carbon atoms. The order parameter will then be calculated for the middle carbon. It is necessary to define the previous carbon atom (i) and the subsequent carbon atom (j) in order for GROMACS to calculate the order parameter.

3.4.4 Electron density map

The electron density map of a protein may be obtained by X-ray crystallography. If, as in the case of bilayers, a crystal structure is not available, other methods may be used. Weiner and White (Wiener and White, 1991; Wiener and White, 1992a; Wiener and White, 1992b) have produced a comprehensive electron density map of a fluid DOPC bilayer by the combined use of X-ray and neutron diffraction. Their approach divided the DOPC molecule into eight individual groups, the ninth group being the water layer. Six of these Gaussian distributions are readily comparable to the MD results obtained. The electron density distributions for these groups were used as a comparator for the DOPC groups within the MD simulated DOPC/DOPG bilayer. Since the fatty acid tails of the PG molecules are also oleoyl chains, the electron density distributions of this part of the bilayer are not expected to differ significantly from the Weiner and White results. Some neutron diffraction data on mixed DOPC/DOPG bilayers is available from previous studies (Bradshaw, 1997; Davies *et al.,* 2003).

3.5 Results and discussion

3.5.1 Volume, area of lipid and the *d*-repeat

	Values from DOPC (4 separate sets of EM + MD runs)	**Values from DOPC/DOPG** (One set of EM + MD runs)	**Values from DOPC MD simulation** Chiu *et al.*, 1999	**Experimental values** Tristam-Nagle *et al.*, 1998 (DOPC only)
Area per lipid ($Å^2$)	69.9 ± 1.1	73.1	71.0 ± 1	72.2
Vol. per lipid ($Å^3$)	1294 ± 8.4	1309	1288 ± 10	1303
***d*-repeat (Å)**	5.76 ± 0.11	5.94	N/A	5.2
***d*-repeat (Å)$^+$**	N/A	5.54	N/A	5.2

Table 3.4. Comparison of calculated and experimental values for area and volume of lipid. The columns contain values obtained from our MD simulations of DOPC bilayers (1st column); values obtained from our MD simulations of DOPC/DOPG bilayers, experimental values obtained for DOPC (Tristram-Nagle *et al.,* 1998) and calculated values for DOPC bilayers from Chiu *et al.,* 1999. The *d*-repeats obtained using PME were to treat electrostatics were in closer agreement with experimental data. $^+$Denotes value obtained with the PME algorithm.

Chiu and co-workers (1999) have performed a combined Monte Carlo and MD study on an explicit 128-molecule DOPC bilayer. Prior to running the mixed DOPC/DOPG bilayer MD simulation, a 128-molecule DOPC bilayer was constructed in a similar manner to the mixed bilayer, using cut-offs to treat the electrostatic interactions. It was then subjected to a combined EM (Steepest Descent method) and an NPT MD run. The values obtained compare favourably with those obtained by Chiu *et al.,* Langmuir trough and neutron diffraction techniques were used to obtain the area and volume of DOPC respectively (Tristram-Nagle *et al.,*

1998). Figure 3.9 shows a snapshot of an equilibrated DOPC bilayer after 3.5ns of MD simulation.

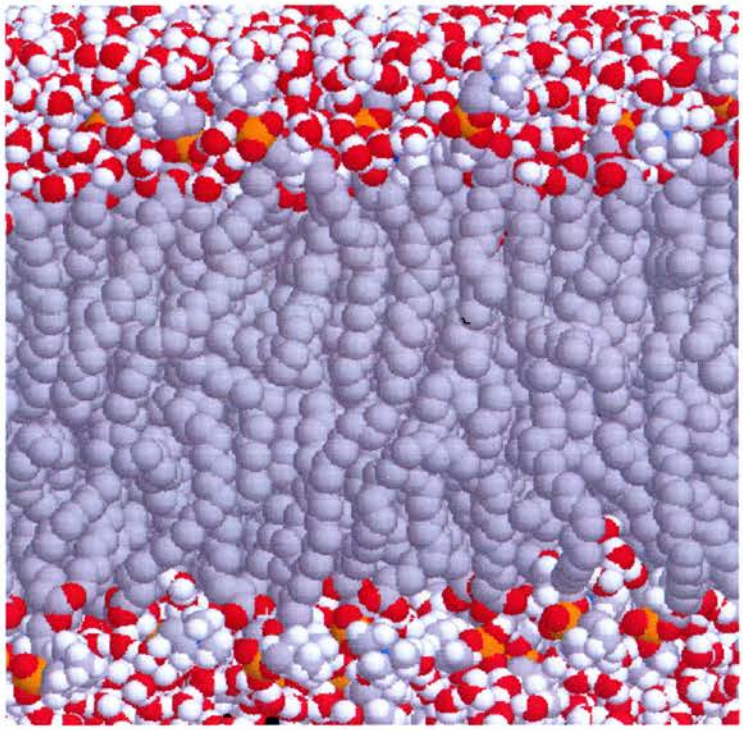

Figure 3.9. A side on snapshot (*Z* dimension) of an equilibrated bilayer of pure DOPC. The water molecules are a red oxygen atom bonded to two white hydrogens. The orange ball is representative of the phosphate atom in a PC headgroup.

3.5.2 Order parameters

Figure 3.10 is a plot of the deuterium order parameters obtained for a pure DOPC bilayer from a 3500ps MD simulation using the NPT ensemble. OLA and OLB correspond to *sn*1 and *sn*2 chains in the DOPC molecule respectively. Figure 3.11 is a plot of the order parameters obtained for the mixed DOPC/DOPG bilayer after 3500ps of MD simulation.

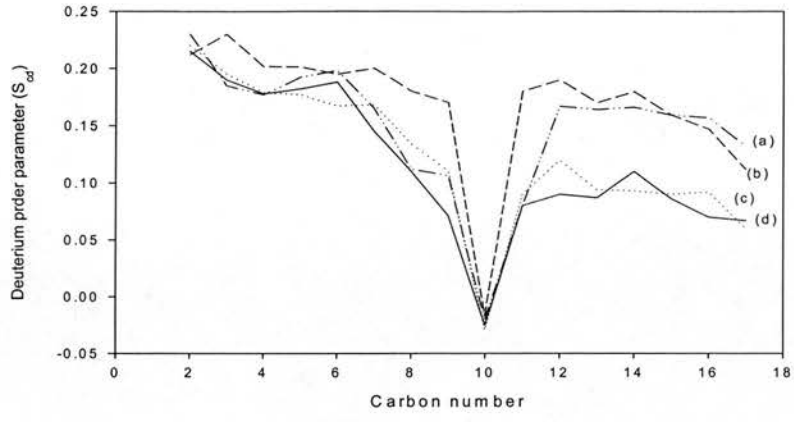

Figure 3.10. A plot of the deuterium order parameters obtained for the oleoyl chains of DOPC (OLA (a) and OLB (b)), after 3500ps of MD simulation and comparison with those of Chiu and co-workers ((c) and (d)) (Chiu *et al.*, 1999).

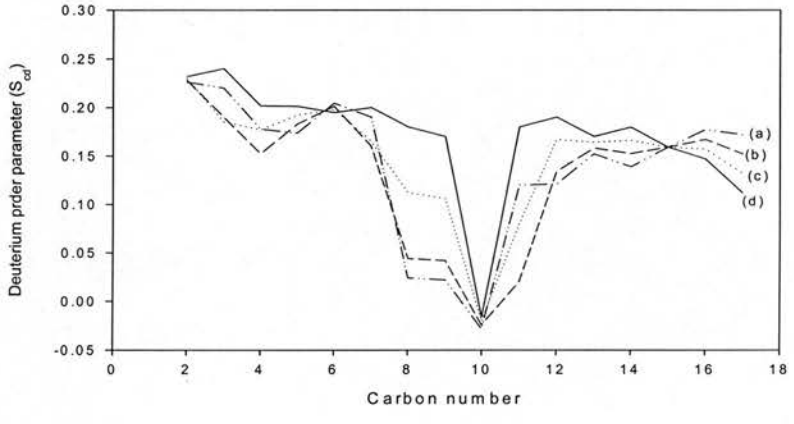

Figure 3.11. A plot of the deuterium order parameters for the oleoyl chain carbons of DOPC and DOPG in a mixed bilayer, obtained from a 3500ps MD simulation. OLA and OLB ((a) and (b)) correspond to *sn*1 and *sn*2 chains in the DOPC molecule respectively. OLC and OLD ((c) and (d)) correspond to *sn*1 and *sn*2 chains in the DOPG molecule respectively.

3.5.3 Electron density map

Figure 3.12 shows the calculated electron density distributions of the structural groups of DOPC and DOPG in a mixed bilayer. The calculated electron density profiles compare favourably with the experimental values of Wiener and White (Wiener & White, 1992), whose structural groupings have been used as a basis for the ones shown in the Figure. The electron density map was obtained over a 3.5ns equilibration run.

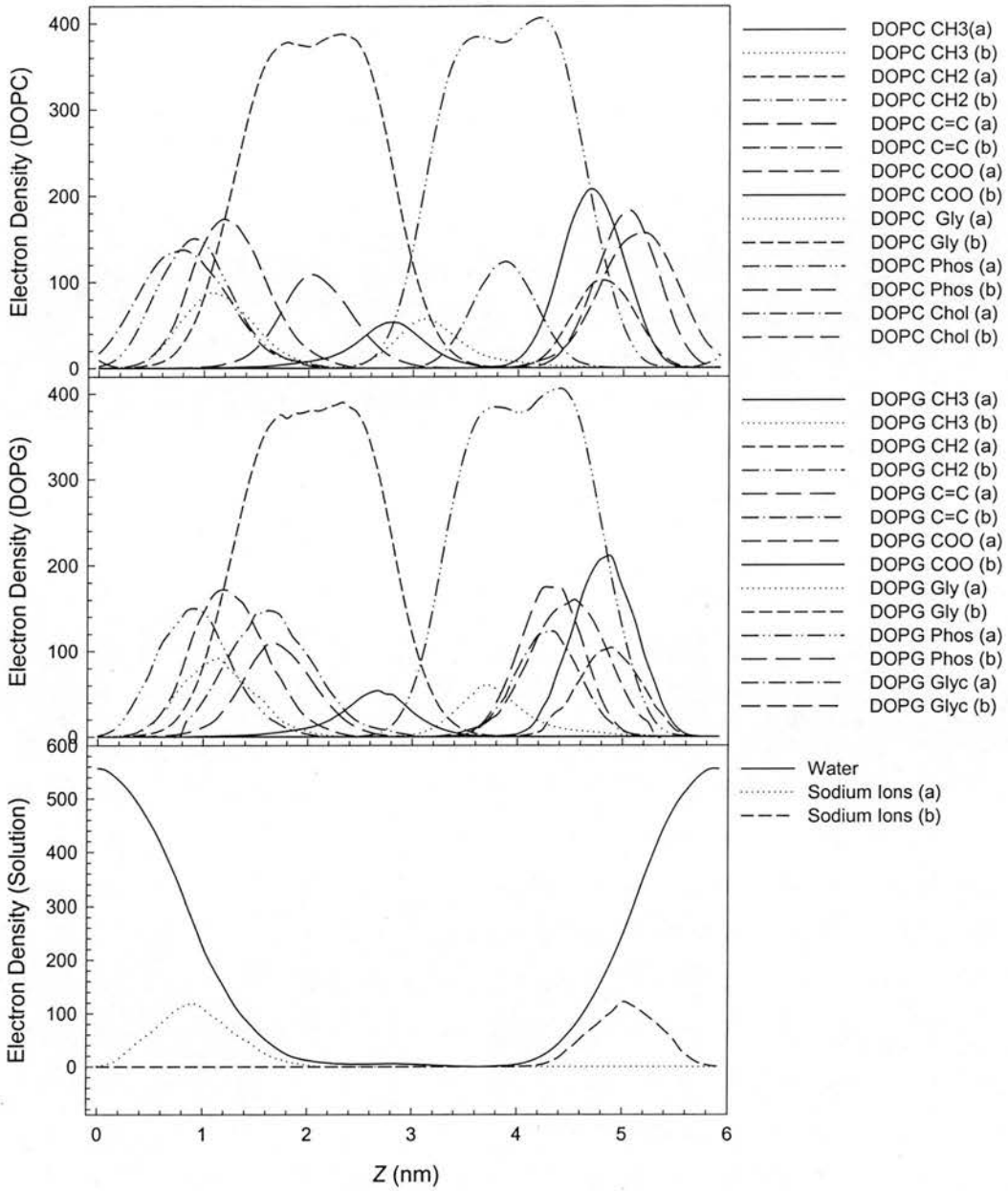

Figure 3. 12. Electron density distributions of the structural groups of DOPC and DOPG in a mixed bilayer. The groupings are based on those of Weiner and White; the calculated electron densities compare favourably with the experimental values. For breakdown of the comparison, see Table 3.4.

A snapshot of an equilibrated mixed bilayer of DOPC/DOPG is shown in Figure 3.13 for illustration purposes the water molecules are not in spacefill display mode, unlike the rest of the Figure. The blue balls are the Na+ counter ions.

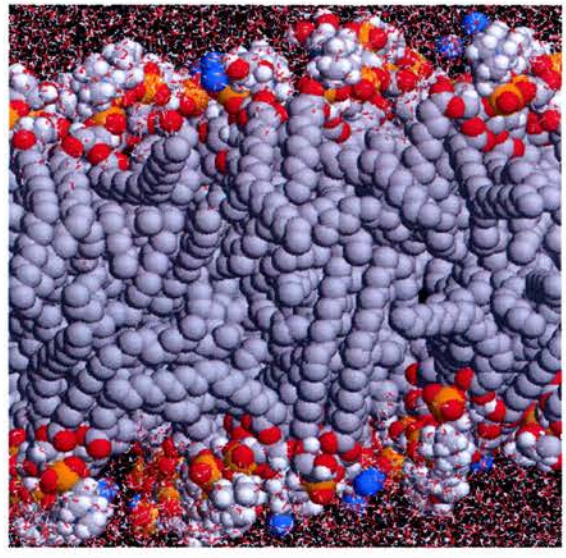

Figure 3.13. Displays a side on snapshot (*Z* dimension) of an equilibrated mixed bilayer of DOPC/DOPG after 3.5 ns of simulation. The blue balls represent the Na^+ counter ions. The PC headgroups contain orange spheres which represent the phosphate atoms. Water molecules are shown at either side of the bilayer.

	CH3	C=C	COO	Gly	PO_4	Chol
From Wiener and White, 1992						
Position	0.0 nm	0.8 nm	1.6 nm	1.9 nm	2.0 nm	2.2 nm
Half Width	0.3 nm	0.4 nm	0.3 nm	0.2 nm	0.3 nm	0.3 nm
From this study						
Position	0.2 nm	0.9 nm	1.8 nm	1.9 nm	2.0 nm	2.2 nm
Half Width	0.4 nm	0.4 nm	0.4 nm	0.4 nm	0.4 nm	0.5 nm

Table 3.5. A comparison of the electron densities of the molecular components of DOPC in a mixed DOPC/DOPG bilayer MD simulation with experimentally determined values for DOPC (Wiener and White, 1992). Gaussian distributions were fitted to the electron density profiles describing the distribution of the electrons of the different groups throughout a 3.5 ns MD simulation. The position (defined as the distance from the centre of the bilayer) and the half width (defined as half peak width at half-maximum height) are shown for all molecular groups whose electron distributions approximate to a Gaussian distribution. The midpoint of the bilayer was defined by measuring the phosphate to phosphate distance between each leaflet then dividing by two.

A number of MD simulations have been performed on explicit phospholipid bilayers. These studies have tended to use the NPT protocol, with its constant Number of particles, Pressure and Temperature. Tieleman and co-workers (Tieleman *et al.,* 1997) and Lindahl and Edholm (Lindahl and Edholm, 2000) who studied DPPC and DMPC respectively, had modified their system to include a constant area per molecule (NPAT). Tieleman (Tieleman *et al.,* 1998) then went on to develop constant surface tension by using the Berendsen semi-isotropic pressure-coupling algorithm (Berendsen *et al.,* 1984), in which the surface tension in the x and y directions are equal. However, there was no need to utilise the NPAT system. However, the mixed lipid system was initially run for 20 ps as an NVT ensemble. The system was then run as an NPT ensemble for 3480 ps. The pressure asserted on the box allowed the box vectors to adjust in all three dimensions, such that the final area and volume of lipid was effectively constant after 2500 ps. The temperature used in most lipid simulations is in the range of 300-330 K. The temperature selected for the simulation was 300 K; this being the temperature in which the neutron diffraction studies on a mixed DOPC/DOPG bilayer was performed.

The potential energy of the DOPC system (comprising of 128 lipid molecules) were -8.5 $x10^5 \pm 2 \times 10^4$ $kJ.mol^{-1}$. The method involved the use of EM and MD simulations, both of which were performed with *GROMACS.* However, the use of a stochastic simulation, such as a Monte Carlo simulation may have been more effective in reducing the potential energy of our mixed bilayer system. Once

equilibrated, the potential energy of the mixed DOPC/DOPG system was -9.4 x10^6 ± 1.0 x 10^4 kJ.mol^{-1}. The combined equilibration and simulation times for the bilayers were approximately 3.5 ns for the mixed DOPC/DOPG bilayer and 3.5ns for the pure DOPC bilayer, which corresponded to 29.5 processor days on a dual Athlon processor PC. A slightly lower *d*-repeat was observed when using the PME algorithm to treat the electrostatic interactions, in the case of the mixed bilayer. The d-repeat was closer to the experimental values obtained in experimental studies by other group members (Davies *et al.,* 2003), when treating electrostatic interactions with the particle mesh Ewald (PME) algorithm as opposed to spherical cut-offs. However, this algorithm is not recommended for use on zwitterionic systems such as DOPC (Scott, 2002). Order parameters obtained for the pure DOPC system were in excellent agreement with previously reported data. However, it is interesting to note that the order parameters of the latter carbons were not as close to the values reported by Chiu and co-workers (Chiu *et al.,* 1999). The differences in methodology could be attributed to the differences observed.

3.6 Conclusion

To conclude, the simulations were verified by comparing a DOPC simulation with three experimental parameters and a mixed bilayer of DOPC/DOPG with four parameters. The results demonstrate that the simulations gave rise to parameters that are within 5% of experimentally determined values of area & volume of lipid, respectively (Table 3.4). The electron density map for DOPC demonstrates a realistic electron distribution throughout the bilayer and closely follows the

experimental results of Wiener and White (table 3.5). The same approach was then used to model a mixed bilayer system for which there are no comparable experimental data. To the best of knowledge, no experimental studies have been performed to obtain the electron density map of DOPG. However, it is realistic to compare six of the groupings from the experimental obtained from Wiener and White's work (table 3.5). The table clearly demonstrates the excellent agreement between the common groupings between DOPC and DOPG. The construction of the mixed bilayer represents novel and original work, as this type of bilayer has not been previously reported in the literature. Furthermore, the proceeding chapter will discuss computational studies to test the methods of using neutron diffraction data as a starting point for membrane peptide simulations using the mixed DOPC/DOPG bilayer.

3.7 Suggested future studies

A widely acclaimed experimental electron density map of DOPC is available (Wiener and White, 1992b). However, no experimental electron density map is currently available for di-oleyl phosphatidylglycerol (DOPG). The construction of an experimental electron density plot of DOPG, utilising a combination of X-ray and neutron diffraction would be very useful for future studies. Further computational investigations could focus on the hydrogen bonding that can occur between the phospholipids in the bilayer. In addition, the differing levels of hydration can also be investigated and the effect on the verification parameters could be compared, as

this has not been attempted in bilayers composed of a mixture of zwitterionic and anionic phospholipids.

CHAPTER 4

Membrane peptide simulations using experimentally determined starting conditions

4.1 General Introduction

4.1.1 Aims of the chapter

The previous chapter described the construction of and validation of bilayer structures. The models were verified using experimental data, which included neutron diffraction data. The next step before constructing and simulating a membrane bound model of the fusion peptide of SIV, was to test the proposed methodology of using neutron data to construct a starting membrane bound conformation of a peptide. The most logical method for testing the methodology was to use a small peptide, which had been studied using neutron diffraction (Davies *et al.,* 2003).

Four membrane bound conformations of this peptide arose from the analysis of neutron data (Davies *et al.,* 2003). The main aim of this current study was to see if molecular modelling techniques could be used to discriminate more rigorously between the possibilities and unambiguously determine the biologically correct structure of ARF1p in a biological membrane model.

This chapter will describe an analysis of the four possible membrane bound conformations of N-terminal peptide of human adenosine diphosphate ribosylation factor-1 (ARF1p) by molecular dynamics simulations. The aim of these simulations was to determine which of the four possible structures was the most likely. In otherwords, membrane bound ARF1p is used as a model system to test the method of

using neutron data as a starting point for membrane peptide simulations. Confirming which of the four possible conformations is most likely is of utmost importance, particularly as the proceeding chapter will focus on MD simulation of the most likely conformation of the fusion peptide of SIV in a DOPC bilayer. Therefore all conformations of ARF1p were subjected to MD simulation in a bilayer environment to either confirm or discount the proposed conformation. In short, this chapter aims to demonstrate the importance of utilising experimental data in setting up membrane peptide simulations.

4.1.2 Starting conditions of MD simulations

Molecular dynamics (MD) simulations have been used to provide information about numerous biological molecules, including phospholipid membranes and membrane proteins (Berger *et al.,* 1997; Feller *et al.,* 1997a; Mashl *et al.,* 2001; Moore *et al.,* 2001; Scott 2002 ;Balali-Mood *et al.,* 2003). They have been successfully applied to investigations of ion channels and membrane-lytic peptides (Sansom *et al.,* 1998; Tieleman *et al.,* 1998; Tieleman *et al.,* 1999; Randa *et al.,* 2001). The major difficulty encountered when constructing a membrane and protein system for study by simulation is in the assembly of the starting structure. The peptide must be placed accurately within the bilayer/water simulation box before simulations can begin (Basyn *et al.,* 2003). Since the total system can be very large, simulation times tend to be relatively short. As a result, there is generally not enough simulation time available for whole body equilibration and rearrangement of the system so that the protein finds its appropriate place in the bilayer. There are several possible

approaches to overcome this problem. Firstly, some simplifications can be made, such as mean field approximations of the lipid environment (Basyn *et al.,* 2001), or solvent (Kessel *et al.,* 2001; Bechor and Ben-Tal, 2001). Alternatively, Monte Carlo simulations can be used to advance the equilibration of the system more rapidly (Chiu *et al.,* 1999) although this was in a pure lipid system. In this chapter, the use of better initial conditions from experimental observations is explored.

For a standard simulation of a single, simple protein in solvent, little more than the initial secondary structure must be known beforehand. In the course of the simulation, there may be rapid changes of secondary structure, but the simulation box is isotropic, and the molecule does not have, nor require, a preferred orientation in the Cartesian coordinates. For simulations of large proteins with multiple domains, the proper tertiary structure must also be considered. Such simulations usually start from the atomic configuration determined by X-ray crystallography (Ferrand *et al.,* 1993). Once again, the simulation is most likely to be isotropic. Additional techniques such as NMR or solution scattering can be used to determine those initial conditions. Currently, determination of the relevant initial conditions for the placement of the protein relative to a membrane relies mostly on theoretical considerations (Basyn *et al.,* 2001).

4.1.3 Background to the chapter

Other members of the group have previously reported neutron diffraction measurements that were carried out in order to elucidate the bilayer location and

orientation of the membrane bound N-terminal peptide of human adenosine diphosphate ribosylation factor-1 (ARF1p) in a mixed bilayer containing di-oleoyl phosphatidylcholine (DOPC) and di-oleoyl phosphatidylglycerol (DOPG) in a 7:3 molar ratio (Davies *et al.,* 2003). This study had used specific deuteration at the three phenylalanine residues of the peptide. Neutron diffraction combined with the difference method analysis, enabled the determination of two important parameters for each label. The first parameter was the depth of each of the three residues in the bilayer to a resolution of better than 1 Å. Secondly, the diffraction data showed the time-averaged amplitude of the fluctuations of the same residues. Combined with a model of the secondary structure, there were two mathematically possible orientations of the peptide with respect to the membrane. Bradshaw and co-workers (Bradshaw *et al.,* 2000) have proposed that at least four deuterated labels are normally required in order to orient a peptide unambiguously and result in a single fitted model, because it is possible to fit any three points to a plane making it impossible to distinguish between two orientations of the peptide. Two other possible solutions arose as a result of uncertainty regarding the exact structure of the peptide, which may be completely α-helical, or partially α-helical, as in the crystal structure of the intact protein (Amor *et al.,* 1994). Faced with these four possibilities, thermodynamic arguments were used, such as the location of hydrophobic and hydrophilic residues, to discriminate between them and propose what is considered to be the most likely structure.

4.1.4 ADP-ribosylation factor 1 (ARF1)

The peptide under study was the N-terminal sequence of adenosine diphosphate ribosylation factor-1 (ARF1), which was placed in a mixed lipid bilayer containing DOPC and DOPG. ARFs are a family of intracellular G proteins that are activated by certain cell-signaling cascades (Spang, 2002). Full length ARFs are approximately 20 kD in size (Amor *et al.,* 1994) and at least six isoforms have been identified. ARF1 is of particular biomedical interest as structural and biochemical studies of the GTP binding and hydrolysis cycle have provided clues about the potential mechanisms of action of intracellular messengers such as phosphatidylinositol, phosphatidic acid and diacylglycerol (Randazzo *et al.,* 2000). To accomplish this, they combine the characteristic GDP/GTP switch with a unique membrane/cytoplasm switch. Membrane binding is also crucial to the normal biological regulation of ARFs by their guanine exchange factor (GEF) proteins and GTPase activating proteins (GAPs) (Menetrey *et al.,* 2000).

A number of crystal structures have been published for the soluble, inactive forms of ARF proteins. However, little is known about the active, membrane bound structures of ARF, the details of which are crucial to our under-standing of how these proteins function both as molecular switches and bio-timers in cells. Membrane binding is a necessary precursor to the large structural reorganizations of the core and switch regions of ARF1 (Goldberg, 1999). The highly conserved N-terminal domain primarily controls the membrane binding of ARF1 (Franco *et al.,* 1993), and is assumed to be an amphipathic helix lying approximately parallel to the membrane

surface. The helical region seen within the N-terminal domain of ARF1 crystal structure may elongate upon membrane association (Amor *et al.,* 1994). Changes in the length of the helix, and thus the connecting flexible linker region, could affect the molecular reorganization of the core and switch regions of ARF1. Differences in the length of the flexible linker regions of ARF1 and ARF6 may contribute to the differences seen in the switch regions of these two ARF isoforms, which are thought to play an important physiological role in endocytotic pathways (Menetrey *et al.,* 2000). To understand this role as a reversible membrane anchor, it would be necessary to know the precise depth and orientation of the N-terminal peptide domain within a lipid bilayer. The neutron diffraction studies previously performed addressed the question of the precise depth of the peptide in a membrane. However, the literature (Roth, 1999) has pinpointed that ARF1 activation is by the myristoyl chain attached to the N-terminus of the peptide. To this end, further neutron studies utilizing a peptide with a myristoyl chain are required for a definitive answer to the question of the depth the myristoylated peptide within a membrane.

In the previous experimental study carried out by other group members, circular dichroism (CD) was used to indicate the secondary structure for the models (Davies *et al.,* 2003). The first model was taken directly from the published crystal structure of the full ARF1 protein. This model had similar helical content to that measured with CD. The second model was derived from the first, by adjusting the Φ and Ψ angles into a fully α-helical conformation. Since, from the neutron data alone, each of these two models of secondary structure has two alternative orientations relative to the membrane, four possibilities were left to choose from. Based on a consideration

of the location of hydrophobic and hydroΦlic residues on the peptide it can be argued that only one of these conformations is likely to be correct.

4.2 Methods

4.2.1 Determination of secondary structure models

The sequence of ARF1p used in the neutron and CD experiments was:

Gly-Asn-Ile-Phe-Ala-Asn-Leu-Phe-Lys-Gly-Leu-Phe-Gly-Lys-Lys

(SWISSPROT #P32889). The N-terminus of the peptide was capped with an acetyl group, whereas the C-terminus (q = -1) and the three lysine residues (q = +1) were charged. Full atomic coordinates and simulation topology for the peptide in the same Cartesian coordinate system as the bilayer were determined from the neutron diffraction experiments. Atomic point charges for the peptide(s) were automatically assigned by *GROMACS* (Lindahl *et al.,* 2001).

The diffraction data yields three Gaussian functions. These Gaussian functions relate to the deuteration of three different amino acids. They represent the time-averaged locations of the hydrogens on the three phenylalanine residues (Phe-4, Phe-8 and Phe-12). Each Gaussian has two important parameters. The first is the centre of the Gaussian, which is the location of the residue, measured from the centre of the bilayer. The second is the full width at half maximum height, which is the time-averaged displacement fluctuation of that residue. The area under each Gaussian function is simply the scattering length density of the ^{2}H/H substituted label, and can

be used as a means of scaling the data. Together, these parameters describe the time-averaged location of the labelled residues. The four structural models that satisfy the experimental data were as follows:

Model A: The atomic coordinates of model A were taken from the N-terminal domain of the crystal structure of ARF1 (Amor *et al.,* 1994) and oriented to fit the data. In this model, the backbone of the peptide lies at an angle of less than 5° to the bilayer surface. From a thermodynamic standpoint, this model would seem to be quite feasible because the hydrophobic surface of the peptide is oriented towards the core of the membrane. A snapshot of model A, after 3.9 ns of MD simulation is shown in Figure 4.2.

Model B: Although the structure of the peptide is the same as model A, its orientation with respect to the membrane is effectively inverted, meaning that the hydrophobic surface of model B faces away from the membrane. This orientation appears to be less favorable from a thermodynamic point of view. For example, Ile-3 was unexpectedly exposed to the aqueous environment. A snapshot of model B is shown after 3.9 ns of simulation in Figure 4.3.

Model C: The structure of this peptide was obtained by energy minimization of model A, while the Φ and Ψ angles were constrained into a α-helix. Although the relative orientation of the hydrophobic and hydrophilic residues appears to be favorable, this particular orientation lifts leucine residues 7 and 11 out of the bilayer.

It should be noted that idealised α-helices could not be positioned to fit the neutron data. A snapshot of model C, after 500 ps of MD simulation is shown in Figure in 4.4.

Model D: The peptide structure is similar to model C, but the orientation of the peptide has been reversed. Lysines 14 and 15 were pushed further into the bilayer than would be deemed physically or chemically realistic. A snapshot of model D after 500 ps of MD simulation is shown in Figure 4.5.

4.2.2 Construction of the bilayer

The pre-requisite for peptide-membrane simulations is a fully equilibrated bilayer. An equilibrated mixed DOPC/DOPG bilayer has been built and successfully simulated (Balali-Mood *et al.,* 2003), as was described in the previous chapter.

4.2.3 Placement of the peptide in the bilayer

Each peptide model was superimposed on the equilibrated membrane, centered in x and y in the simulation box. The location and angle of the peptide in the z direction was set using the Phe positions as determined from the neutron data. Bad contacts between atoms were detected, and all molecules (SPC, DOPC & DOPG) identified as significantly overlapping the peptide co-ordinates were removed manually. Finally, the molecules and atoms were renumbered. To balance the system charge, a Cl^- ion was placed near each of the three lysine residues of the peptide, and a Na^+ ion

was placed near the negatively charged C-terminus of ARF, using the *genion* programmein *GROMACS*. Table 4.1 summarizes the molecular content of the four models. The entire system was then subjected to EM (steepest descent method) prior to an NVT (constant volume of 275000 $Å^3$, constant temperature of 300 K) ensemble simulation for 20 ps. The NVT simulation was performed in order for the water molecules in the system to become re equilibrated after the disruption to the system. Table 4.1 also shows the number of molecules in each system simulated. The numbers of water molecules (SPC) per lipid and the PC:PG ratio was only slightly altered from the original plain bilayer.

Configuration	No. of DOPC lipids	No. of DOPG lipids	No. of SPC molecules	No. of Na^+ counter ions
model (A)	95 (46)	41 (20)	2745	41
model (B)	92 (43)	40 (19)	2650	40
model (C)	93 (44)	40 (19)	2681	40
model (D)	91 (42)	39 (18)	2598	39

Table 4.1. The number of lipids and SPC solvent molecules in each model. The molecules deleted were in direct atomic conflict with ARF1p. The original mixed bilayer contained 98 DOPC molecules, 42 DOPG molecules, 42 Na^+ counterions and 2815 SPC molecules, respectively. As can be observed, the ratios of DOPC:DOPG were not significantly altered; the original ratio of waters (SPC) per lipid molecule (20.1:1) was altered by <1%. The Figures in parentheses relate to the total number of lipids in the top monolayer where the peptide was placed.

Each of the four systems was then run with an NPT ensemble using PME to treat electrostatic and long-range interactions. All NPT simulations were run at 300 K and isotropic 1 bar pressure, with coupling constants of 5 and 1 ps, for pressure and

temperature, respectively. All simulations were for 4000 ps each, at the rate of about 80 ps per processor-day.

4.3 Results and discussion

4.3.1 Label positions and width

A useful criterion in assessing the validity of each of the simulated models is how closely the positions of the three phenylalanine labels agree with the experimentally determined values calculated from the neutron data. Table 4.2 illustrates the positions of each of the labelled residues in all four models, during the last ns of the simulation, and compares it with the values obtained from the neutron data. The position of each label is shown in Figure 4.1. As in neutron data, the locations are expressed as the distance from the centre of the bilayer. It has previously been proposed that model A was most likely to be the biologically correct conformation (Davies *et al.,* 2003). This proposal is supported by the label positions in model A, which have remained within 1% of the positions calculated from the neutron data, throughout the 4 ns of the simulation. Model C showed values which were close to experimental values, although not as close as those observed in model A. However, models B and D had values that have deviated from the initial positions and are clearly no longer in agreement with experimental data.

	Phe4		Phe8		Phe12	
	Position	Width	Position	Width	Position	Width
Model A	18.0	4.0	17.0	4.4	21.9	5
Model B	13.0	3.8	11.8	4.0	9.0	4.2
Model C	19.8	3.2	18.0	3.4	24.0	3.5
Model D	7.8	3.0	10.0	3.6	12.0	2.8
Experiment	17.99(2)	5.83(3)	16.68(4)	6.64(4)	22.06(6)	5.88(8)

Table 4.2. The position and width of the three phenylalanine residues of ARF1p, deuterium labelled in the neutron study (Davies *et al.,* 2003). The table provides a comparison between experimental data previously published and two of the simulated models. Both of these models were in the correct hydrophobic/hydrophilic orientation. The position of each label site is expressed as the distance from the centre of the bilayer. The width of each label site is calculated at 1/e of the full height of the gaussian in both experimental and simulation studies.

Table 4.2 also displays the peak widths obtained from the four simulated models. The width of the labelled residues was previously calculated from the neutron data. The width of the label position was narrower in all four of the simulated configurations than the neutron experiments. However, this is to be expected, since the neutron data represent the average of 4.9×10^{19} molecules of ARF1p embedded in a lamellar stack of bilayers, as opposed to the simulation systems whereby only one peptide was present. Nevertheless, we can see that, model A displays values closest to experimental values.

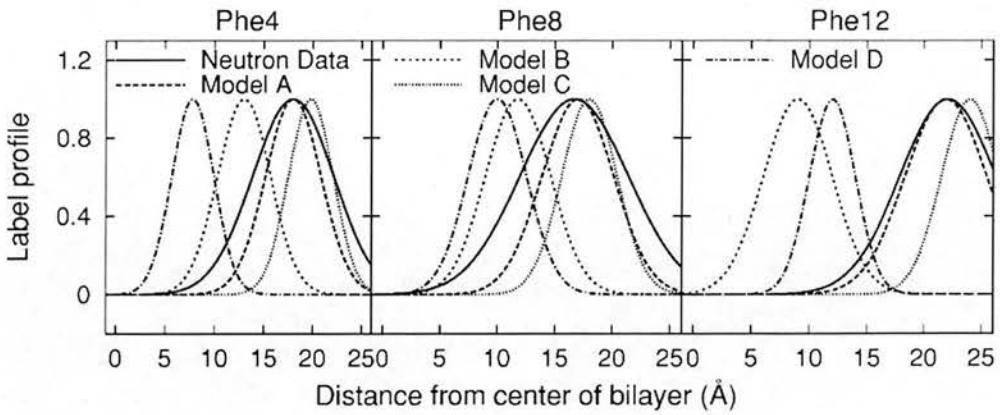

Figure 4.1. A schematic representation of the label positions at the end of the MD simulations. Comparison is shown between each of the four simulated model, as well as experimental data (Davies *et al.,* 2003). (This Figure was kindly produced by Dr Thad Harroun).

The amplitude of the fast fluctuation motion of the phenylalanine residues is indicated in the widths of the peaks in table 4.2. For model A, the simulation matches the neutron data well, while for models C, B and D, there were greater deviations from the starting positions. This suggests that the simulations reproduced the local environment of those residues of model A accurately. Conformation A had a mean square displacement (MSD) of 0.40 nm^2 conformation C (Figure 4.4) a MSD of 0.50 nm^2, conformation B a MSD of 0.64 nm^2 and conformation D a MSD of 0.78 nm^2. Perhaps not surprisingly models B (Figure 4.3) and D (Figure 4.5) had higher average MSD values; this was primarily due to the fact that both models were not placed in the correct hydrophobic orientation, resulting in less stable structures when compared to models A and C. In addition, the label positions deviated from experimental values (in both models B and D) within the 20 ps NVT simulation of

the peptide, as well as the first 50 ps of the 4000 ps NPT run. Figure 4.2 shows a snapshot of model A after 3.9 ns of simulation time (NPT ensemble).

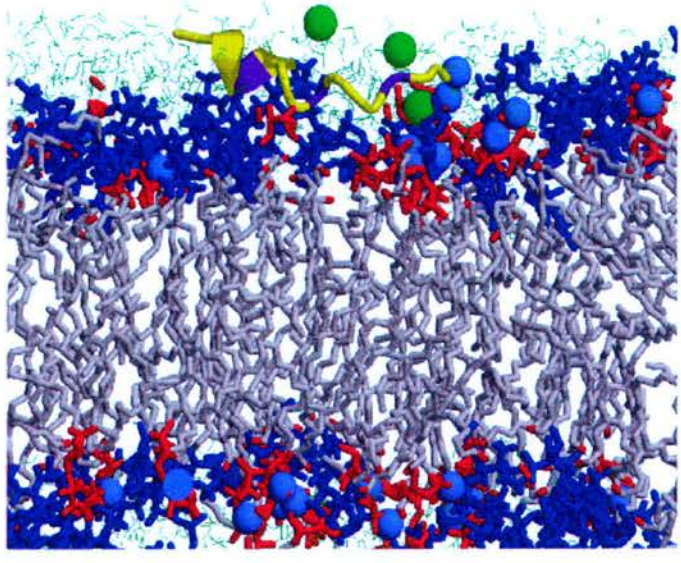

Figure 4.2. A snapshot of AFR1p in a mixed DOPC/DOPG bilayer (model A) after 3.9 ns of MD simulation with an NPT ensemble.

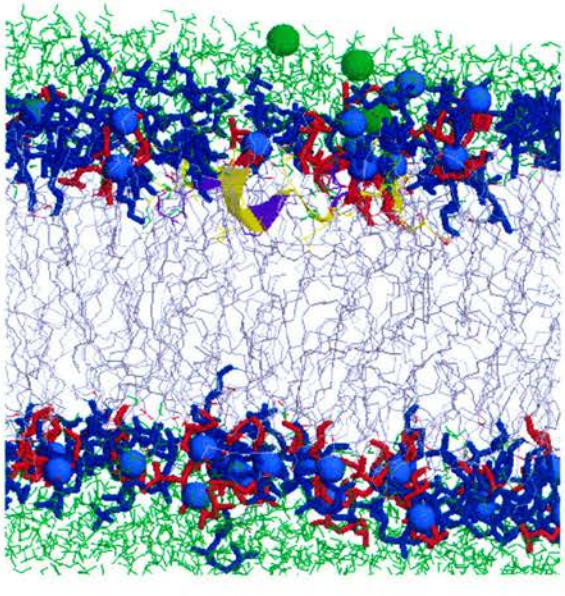

Figure 4.3. A snapshot of AFR1p in a mixed DOPC/DOPG bilayer (model B) after 3.9 ns of MD simulation with an NPT ensemble.

The ARF1p peptide models did not shift significantly during the simulations in model A. Table 4.2 illustrates the time-averaged position of the hydrogens of the three phenylalanine residues, both from simulation and from the neutron data. The whole body displacement of the peptide in the *z* direction was negligible for model A, as the position of each phenylalanine remained close to its experimentally measured position during the simulation. However, the peptides in models C, B and D did "ride" down from their initial conditions. Furthermore, the peptide axes did not tilt more than 1° from its initial angle in model A. However, models B, C and D reduced their tilt by 4°, 5° and 8°, respectively.

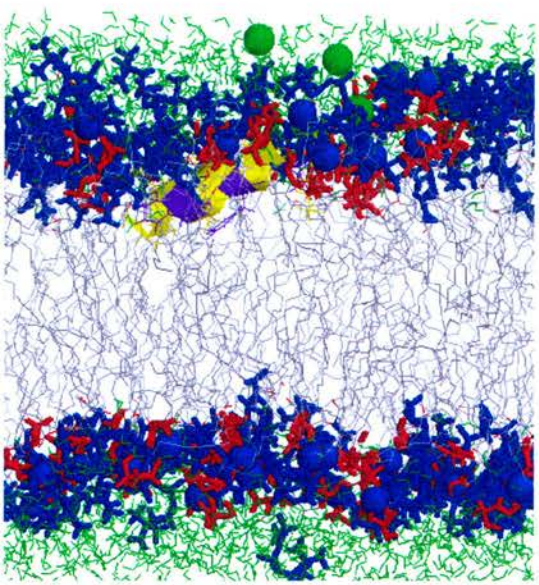

Figure 4.4. A snapshot of AFR1p in a mixed DOPC/DOPG bilayer (model C) after 500 ps of MD simulation with an NPT ensemble.

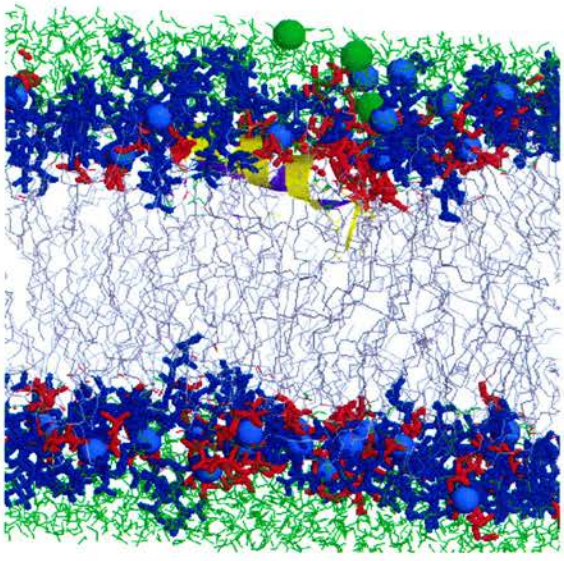

Figure 4.5. A snapshot of AFR1p in a mixed DOPC/DOPG bilayer (model D) after 500 ps of MD simulation with an NPT ensemble.

4.3.2 System energy

Figure 4.6 (upper panel) displays the total energies (the sum of kinetic and potential energies of the system) of the four systems. Each of the models reached a near equilibrium energy after only 10 ps of an NVT simulation. Furthermore, the energy fluctuations were never larger than 2000 kJ/mol. The total energy of the mixed bilayer before the insertion of ARF is shown in Figure 4.6 for comparison. All the kinetic energies of the four models were within 1% of each other, reflecting the fact that they all contained a similar number of atoms.

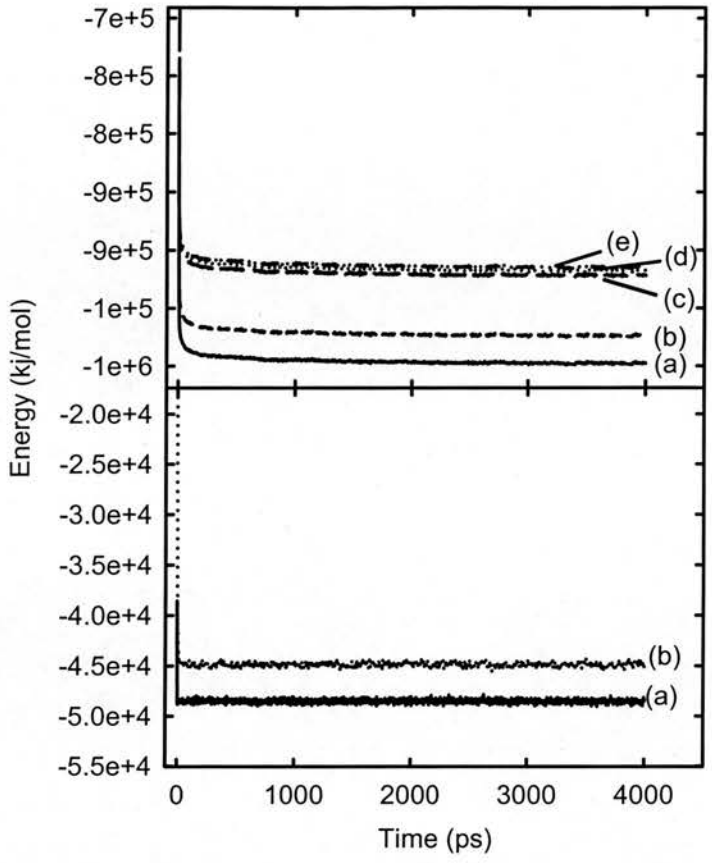

Figure 4.6. (upper panel) Total energies of the simulated systems: (a) model A, which as can be observed had the lowest total system energy; (b) model C; (c) model B; (d) model D. For the purpose of comparison (e) represents the system energy of a mixed bilayer without ARF. (lower panel) Total energies of ARF1p in SPC: (a) the total energy of the crystal structure of ARF as utilised in models A and B; (b) the total energy of the fully helical structure utilised in models C and D.

Model A is the most energetically favorable conformation. The mean total energy of model A was -9.87×10^5 kJ/mol. Conformations C, B and D had mean total energies of -9.58×10^5, -9.21×10^5 and -9.16×10^5 kJ/mol, respectively. The differences in

energy are almost certainly due to the energetically unfavorable conditions in which the peptide was placed in models B, C, and D. In an earlier paper (Davies *et al.*, 2003), it was reported that the hydrophobic moment of models B and D was unfavorably oriented, with the hydrophobic face of the peptide upward, towards the water. These models are expected, therefore, to have a higher potential energy than A and C (hydrophobic face down). Conformation D has such a large tilt (20°), that it is expected to cause the most disruption to the system, as the C-terminus has inserted into the hydrophobic oleoyl chains of the bilayer. Thus it was not surprising to find it had the largest total energy. The order in which we find the system energies, clearly demonstrate the effect of hydrophobicity on the binding of the peptide to the membrane.

For comparison, the peptides were placed in a water solvent box and were subjected to MD simulation. The α-helical structure of ARF (models C and D) in water possessed a slightly higher total energy than the crystal structure (models A and B). Figure 4.6 (lower panel) shows the total energies of the two different ARF structures. Importantly, the energy of the combined system for models A and C were less than the combined energy of the separate simulations.

4.3.3 Hydrogen bonding

The hydrogen bonding between the peptide and the bilayer was monitored during the course of all four simulations. *GROMACS* was used to calculate the maximum number of possible hydrogen bonds and identified 30 donors and 38 acceptors within the peptide. The internal hydrogen bonds within models A (crystal structure) and C (initial α-helix) were monitored throughout the 4000 ps of simulation time and are shown in Figure 4.7.

Model A had the highest intermolecular hydrogen bonding, with an average of 34 bonds, throughout the course of the simulation. This Figure comprises 21 peptide-SPC and 13 peptide-phospholipid bonds, 9 of which were with the PC headgroups. All amino acid residues apart from the first residues glycine (Gly-1) and asparagine (Asn-2) were involved in hydrogen bonding with PC headgroups. Four amino acids hydrogen bonded with PG headgroups: Asn-2 and all three lysine residues.

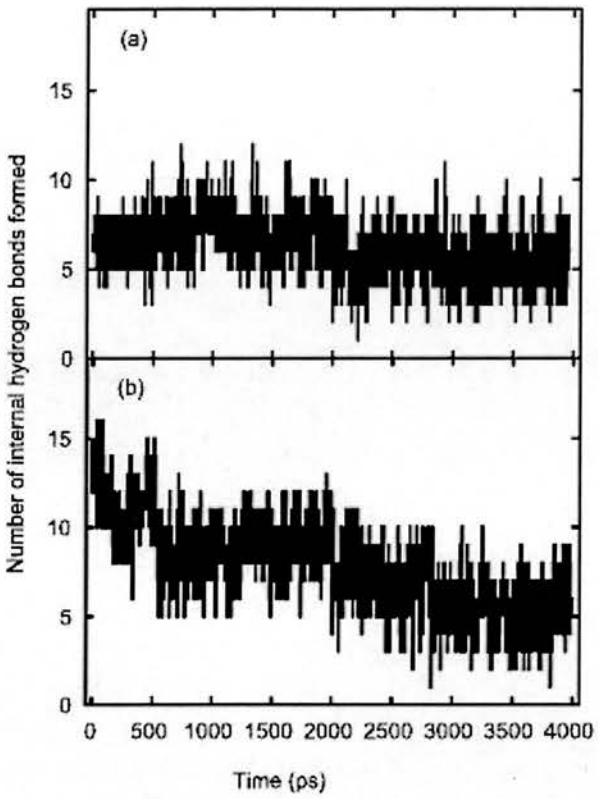

Figure 4.7. Total internal hydrogen bonding within ARF1p: (a) the stable hydrogen bonding pattern of the crystal structure of model A. There are no major fluctuations observed within this model. (b) The initial α-helical structure of model C. The initial hydrogen bonding pattern within this model was typical of a α-helix. However, as the simulation progresses, the number of hydrogen bonds were reduced to values closely associated with model A.

The next highest number of hydrogen bonds was found in model C, with an average of 29, which breaks down as 24 peptide-SPC and 7 peptide-phospholipid bonds. Much of the difference between these two models is accounted for by the fact that the C-terminal lysines did not form hydrogen bonds in model C. This conformation of the peptide produced a slightly higher number of hydrogen bonds with the solvent in comparison to model A. This was due to the higher solvent accessible surface (SAS) of model C. A comparison of SAS, between models A and C, is shown in Figure 4.8.

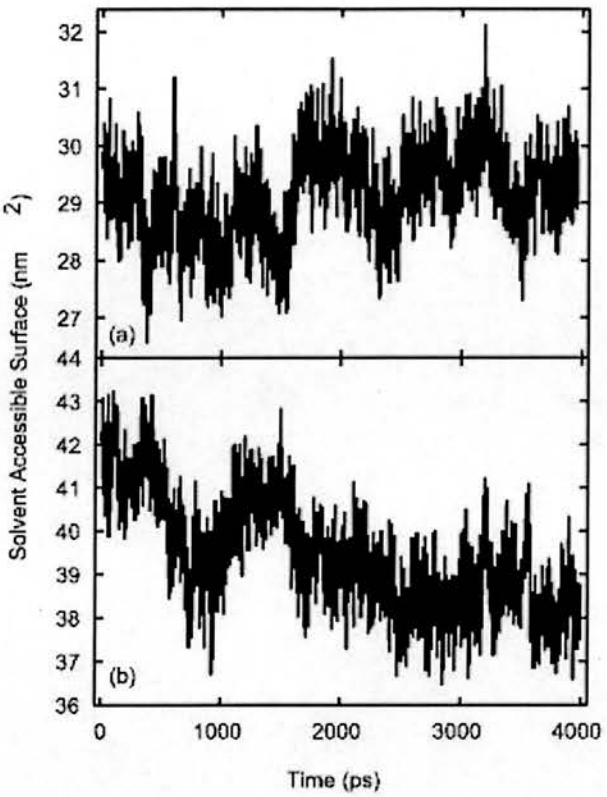

Figure 4.8. Solvent Accessible Surface (SAS) of models A and C. (a) model A which, due to a partially helical structure, had a lower SAS than model C. However, as can be seen the fluctuations of SAS were lowest in model A. (b) The SAS of model C. Initially the SAS of model C was higher, primarily due to the peptide's helical conformation. As the simulation progressed, the SAS of model C was reduced, due to a decrease in helical content.

As expected, models B and D both of which have the amphipathic peptide inverted, have far fewer hydrogen bonds, 18 for model B and 15 for model D. Model B contained only 4 hydrogen bonds between the peptide and lipids. These hydrogen bonds were formed between PC headgroups and asparagines (Asn-2), lysine (Lys-9) and phenylalanine (Phe-12), respectively. In addition Lys-9, which formed a hydrogen bond with the PC headgroup, also formed a hydrogen bond with a PG headgroup. This conformation of the peptide only formed 14 stable hydrogen bonds with the solvent (SPC) present in the system.

At this point, it was appropriate to discard models B and D as the data presented so far has clearly demonstrated that neither conformation is in the biologically correct orientation. Taking into consideration the changes in label positions of the phenylalanine residues, the higher values observed in average MSD, total energy of the respective systems, as well as a significantly lower number of hydrogen bonds seen in these two models, no further analysis of these simulated systems can be justified. The common feature in these models was the incorrect hydrophobic orientation. Therefore the remainder of this chapter will only focus on models A and C.

4.3.4 Structural changes

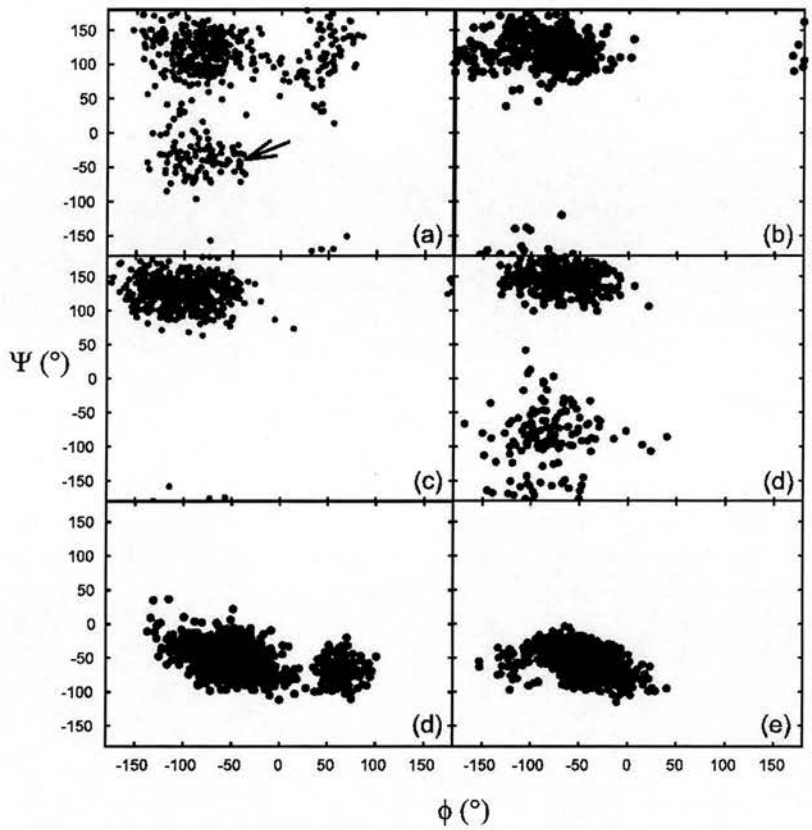

Figure 4.9. Ramachandran plot of selected amino acid residues in models A and C. (a) The penultimate lysine residue in model C, between 0 and 1 ns of simulation. This residue was initially helical (arrow), but rapidly developed a non-helical conformation. (b) The same residue between 3-4 ns of simulation. There is no indication of helicity within this time frame. (c) The penultimate residue (Lys-13) in model A between 0 and 1 ns. As can be observed no helicity is present in the starting structure. (d) The same residue between 3 and 4 ns of simulation. The conformation is still predominantly non helical, although there are minor fluctuations in Φ/Ψ these are still outside the α-helical region of the Ramachandran plot. (d) A complete 0-4 ns Ramachandran plot of a residue from the α-helical region of the peptide (Ile-3) in model C. The conformation remains predominantly helical throughout the 4 ns simulation period. (e) The corresponding isoleucine residue in model A, which also maintains its predominantly helical conformation throughout the 4 ns of simulation.

4.3.5 Helical content

Φ and Ψ angles of selected residues were analysed, as illustrated in the Ramachandran plot in Figure 4.9. The main difference between models A and C was the extent of the helical region. In model A, the helix terminates before the last 3 residues. Ramachandran plots for individual residues of models A and C (examples shown in Figure 4.9) demonstrate that these three residues retain a predominantly non-helical structure in model A throughout the simulation. In contrast, however, the corresponding residues in model C unwind during the simulation to a non-helical conformation, despite having a helical structure to start with. An example amino acid residue taken from the helical region of the peptide (Ile-3) demonstrates that the helical conformation of this section of the peptide is maintained through the four nanoseconds of MD simulation. In other words, model C rapidly reverted to a structure closely approximating that of model A, in the last 3.5 ns of the simulation.

4.3.6 Effects on the bilayer

The bilayer was not significantly altered by the presence of the peptide. The area per lipid and volume per lipid (determined from the undisturbed monolayer opposite the peptide) were 74 $Å^2$ and 1312 $Å^3$ respectively. These values compare favorably with previously reported values, as shown in the previous chapter (3.7.3). The values were within 1% of the previously published values for a plain mixed bilayer. Figure 4.10 shows that the lipid order parameter did not change significantly between the plain bilayer and the peptide/bilayer system. These results show that the cavity

introduced by the deletion of lipids in close contact with the peptide did not disrupt the overall integrity of the bilayer structure.

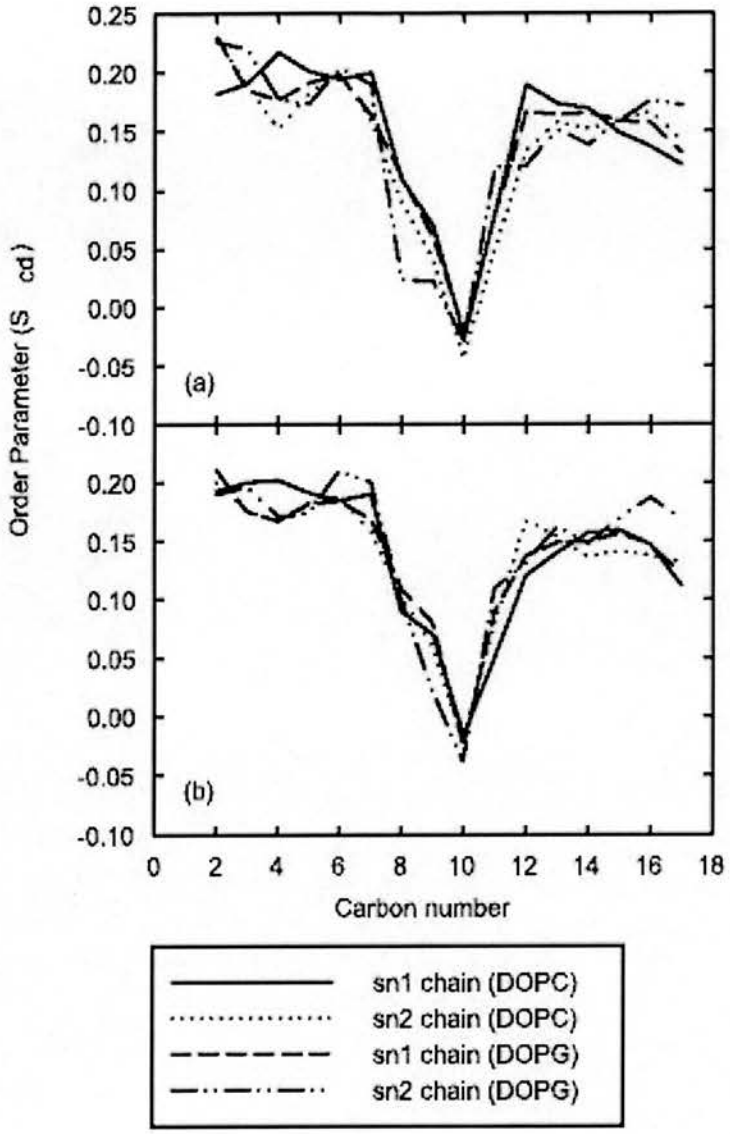

Figure 4.10. Order parameters of oleoyl chains in model A. (a) The deuterium order parameters calculated for the top leaflet of the membrane, which contained ARF. (b) The lower leaflet, which was unperturbed from the pre-equilibrated bilayer. As can be seen, no significant changes in order parameters occurred as a result of peptide insertion.

4.4 Conclusion

Although tremendous advances have been made in molecular dynamics simulations of proteins and lipid bilayers, typically such simulations are qualified by uncertainties in the initial conditions. Reaching both energetic and structural equilibrium in such large systems poses a difficult computational problem. Without data to support the choice of initial conditions, only a small number of possible initial states can be reasonably tested. The need for combining experimental techniques, which provide data on the Ångstrom length or picosecond time scales, with MD simulations is clear (Kamath and Wong, 2002). The neutron diffraction data (Davies *et al.,* 2003) provided directly verifiable length scale data, not previously used in such simulations.

The difficulty is compounded when one considers that for the enormous variety of bilayer simulations with different sizes, ensembles and force fields, nearly all simulations of pure bilayers yield reasonable results (Scott, 2002). This is most likely due to the fact that all force fields contain atomic interaction parameters that mimic the hydrophobic effect quite well. When combined with the confinement of the simulation box it is perhaps not surprising that the structural integrity of the bilayer is maintained, at least over short simulation times.

We can see a related problem in the simulations of models B and D; although obviously incorrect in comparison to models A and C, they reached an equilibrium

state very quickly and showed no signs of further change in 4 ns of simulation time. Had we not known at the beginning that A and C were, mutually exclusive choices based on the data, (B and D were mathematically optional orientations), there was no *a priori* reason to reject the simulations of B and D. This is directly relevant to simulations that study proteins at membrane interfaces. Such simulations may not yield clues as to whether there are better orientations of the protein within the membrane. One can argue that transmembrane helices or ion channels studied using MD might not fall into this category as the protein in question spans the membrane, hence the depth of the protein in relation to the membrane is no longer an issue.

In this chapter, it has been demonstrated that the information gained from structural experiments can be used to generate starting structures for explicit atomic level studies with molecular dynamics simulations. To conclude, this chapter has shown that MD simulation is a powerful tool for exploring neutron diffraction data to atomic resolution. However, the starting position of a peptide in relation to a membrane is crucial to the interpretation of the data. The analysis and comparison of the four models lead to the confirmation of the originally proposed choice of model A, as the correct conformation of ARF1p in relation to the bilayer. This confirmation then allows for the MD simulation of the most likely conformation of the SIV fusion peptide in a DOPC bilayer, which is described in the proceeding chapter.

4.5 Suggested future work

The results from this chapter have clearly demonstrated that the originally proposed model (A) was the most likely conformation. This finding will allow for a long time scale simulation of the fusion peptide of SIV in a pre-equilibrated DOPC bilayer, without the necessity of testing all four conformations which arose as a result of the neutron studies. However, further experimental work could investigate the effect of myristoylation on membrane activity. Furthermore, the protonation states of the labelled residues can be calculated, although this will require extensive computational work.

CHAPTER 5

Molecular dynamics simulations of the fusion peptide of SIV in a DOPC bilayer

5.1 General Introduction

5.1.1 Aims of chapter five

The chapter aims to present a detailed MD study of a peptide in a pre-equilibrated bilayer of DOPC, the initial conditions of which were derived from previously reported neutron diffraction studies (Bradshaw *et al.,* 2000). In contrast to the preceding chapter only the most likely conformation, as predicted by neutron diffraction, was studied. The preceding chapter showed that labels will move within 1-2 ns, if the starting conditions are wrong. In this study the labels do not move, even after 100 ns of simulation.

No previous MD simulations of the fusion peptide of SIV embedded in a DOPC bilayer have been undertaken. The simulations provide explicit atomic detail of the structure and dynamics of the peptide and the lipid hydrocarbon chains. Hydrogen bonding in the system was analysed and interpreted accordingly. Particular emphasis is placed upon the modification of oleoyl chain order parameters and the secondary structure of the membrane bound peptide. This information contributes knowledge to current understanding of the action of fusion peptides on lipid bilayers.

5.1.2 Curvature modulation induced by fusion peptides

Fusion peptides were described in the introduction section of this thesis (1.9.1). A common property of a number of fusion peptides is that they lower the hexagonal phase temperature (T_H) of phosphatidylethanolamine. This indicated that the peptide induced negative curvature (Epand *et al.,* 1998). This property is well correlated with conditions which lead to biomembrane fusion. For instance, there is a direct correlation between the fusion activity of SIV mutants and the ability of its fusion peptides to lower T_H (Colotto *et al.,* 1996; Epand *et al.,* 1994).

5.2 MD simulations of fusion peptides

A number of MD simulations have been performed on fusion peptides embedded within pre-equilibrated bilayers. Vaccaro and co-workers (Vaccaro *et al.,* 2004) performed MD simulations of the 20 amino acid residue fusion peptide of the influenza haemagglutin (strain X34) in a POPC bilayer. They compared mutants and evaluated their fusogenic activity. They reported reduced order parameters of the palmitoyl and oleoyl lipid chains. The most significant reduction in order parameter was observed in the oleoyl chains, with the original fusion peptide sequence and to a lesser extent with the mutant sequences.

Huang and co-workers (Huang *et al.,* 2004) were another group to report such a study. They had used a DMPC bilayer and placed a 20 amino acid fusion peptide of

influenza haemagglutin (strain X31) within the bilayer. Their simulations revealed that the peptide adopted a kinked conformation. The findings were in agreement with the NMR structures of a closely related peptide in detergent micelles (strain X33). The peptide was located at the amphipathic interface between the headgroups and hydrocarbon chains of the phospholipids. In addition, they reported that the average hydrophobic thickness of the lipid phase close to the N-terminus is reduced in comparison with the average hydrophobic thickness of a pure DMPC bilayer. Aliste and co-workers (Aliste *et al.,* 2003) have reported simulations of two pentapeptides, ACE-WLXLL (with X=Arg or LYS and ACE= capped N-terminus). Embedded within a DOPC bilayer, a salt bridge had formed within the peptide and had penetrated the bilayer. It has been speculated that this sequence is important in the fusion mechanism (Aliste *et al.,* 2003). Kamath and Wong (Kamath and Wong, 2002) performed extensive MD simulations of the gp41 fusion domain of HIV. They reported a reduction in area and volume per lipid induced by the peptide and two mutant forms in a POPE bilayer. Furthermore, their simulations showed that the peptide remains a predominantly helical conformation when membrane bound (Kamath and Wong, 2002).

To date, no MD simulations have been performed which report on the fusion peptide of SIV. Furthermore, no MD simulation reported within the literature has utilised experimentally determined starting conditions. In the previous chapter, it was shown that experimentally determined starting conditions play a key role in the final outcome of a simulation. This chapter describes an atomic level investigation into the actions of a fusion peptide upon a pre-equilibrated bilayer of DOPC. The fusion

peptide was not capped at either the N or C terminus. The rationale for not capping the peptide was simply to adhere to experimental conditions whereby the peptide was not capped in the neutron diffraction study (Bradshaw *et al.,* 2000).

5.3 Placement of the peptide in the bilayer

The peptide was superimposed on the equilibrated membrane, centered in x and y in the simulation box. The location of the peptide in the z direction was determined from the neutron data, as previously discussed. Bad contacts between atoms were detected, and all molecules (SPC and DOPC) identified as significantly overlapping the peptide co-ordinates were removed manually. Finally, the molecules and atoms were renumbered. The entire system was then subjected to EM (steepest descent method) prior to an NVT (32001 atoms, 480000 $Å^3$, constant temperature of 300 K) ensemble simulation for 20ps. The NVT simulation was performed in order for the water molecules in the system to become re equilibrated after the disruption to the system. The system disruption was not significant as only eight lipids were deleted (8x72=576 atoms). In addition only fifty water molecules were removed (50x3=150 atoms). The NPT simulation ran for 100000ps.

5.4 Method and simulation parameters

The DOPC bilayer was constructed by taking a previously customized PDB file of a DOPC molecule and replicating it to form a monolayer of 128 lipids, using *Sybyl 6.7.* The monolayer was then rotated to form a bilayer of 256 lipids. For a full description of construction and equilibration, please see chapter 3 (section 3.3.3).

The complete topologies of the molecules were described in the form of bonds, angles and dihedrals (torsion angles). Atomic point charges for DOPC molecules were generated by *HyperChem 5.0* (Hypercube Inc., Waterloo, Canada) using the STO-3G set as used in previous studies of DMPC and DPPC (Berger *et al.,* 1997; Feller *et al.,* 1997a). A complete set of these charges can be seen in chapter 3 (table 3.3).

The use of Ewald summations in zwitterionic systems (i.e. a DOPC bilayer) can potentially induce unwanted periodicities, leading to errors no less significant than those which result when the interaction is simply 'switched off' for interatomic distances beyond some spherical cut-off. For smaller simulation boxes, the effect will be more severe (Scott, 2002). The electrostatic interactions within the spherical cut-off were summed directly and the remaining part of the system was treated using an analytical solution of Poisson's equation implemented by *GROMACS.*

It has been reported that spherical cut-offs can introduce artefacts in solutions with ions but if the cut-off radius is large enough (> 1.8 nm), this method appears to work well for zwitterionic lipids (Tieleman *et al.,* 1997). Hence, the selection of spherical cut-offs as opposed to PME for the treatment of electrostatic interactions.

GROMACS allows for temperature and pressure coupling using the Berendsen temperature and pressure coupling algorithm. In the case of temperature coupling, all molecules (DOPC, SIV and SPC) were coupled individually to a bath with a temperature of 300 K. A time constant of 5 ps was set for each group. This time constant was used for both the NVT (32001 atoms, 480000 $Å^3$ and 300 K) and subsequent NPT (32001 atoms, 300 K and pressure of 1 bar). The pressure asserted on the box was of an isotropic nature. A time constant for pressure coupling was also set at 5 ps. In the NPT ensemble the pressure coupling was isotropic. Coupling groups on an individual basis allows for greater stability during an MD run. Furthermore, PBC was utilised in all directions as in previously reported MD simulations. The NVT simulation lasted for only 20 ps and was intended as a further equilibration measure after EM.

The time steps of the MD and EM simulations was 2 fs. This time step was used in a number of previous bilayer simulations (Berger *et al.,* 1997; Feller *et al.,* 1997).

5.5 Results and discussion

5.5.1 Deuterated labels and average mean square displacement of the peptide

This simulation, as those described in the previous chapter, was based upon experimental conditions. The location of deuterated labels and their deviation after the 100 ns simulation are presented in table 5.1. The positions of the labels are relative to the bilayer normal (z) and are in excellent agreement with the experimental deuterated labels obtained from neutron diffraction studies (Bradshaw *et al.*, 2000).

Data type	Parameter	Valine 2	Leucine 8	Leucine 11
Experimental	Position	19.9 ± 1.2 Å	18.6 ± 0.5 Å	16.5 ± 0.2 Å
(neutron diffraction)	Width	7.14 ± 2.6 Å	4.6 ± 0.5 Å	8.9 ± 0.6 Å
Simulation (0-10 ns)	Position	20.0 Å	18.5 Å	16.6 Å
(molecular dynamics)	Width	6.3 Å	4.4 Å	6.4 Å
Simulation (90-100 ns)	Position	20.2 Å	18.7 Å	16.8 Å
(molecular dynamics)	Width	6.1 Å	4.2 Å	6.2 Å

Table 5.1. Label positions from experimental data (neutron diffraction) and simulation. As can be seen, there was only minor fluctuations observed in the label positions, when comparing the first 10ns to the final 10 ns of simulation. The position of each label is expressed as the distance from the centre of the bilayer. The width is the full width at 1/e height.

The deviations seen in the width (table 5.1) can be readily explained by the fact that in neutron diffraction samples a lamellar stack of DOPC bilayers (~50000) with peptide embedded in each bilayer. However, only one peptide is studied in the MD simulation, hence the width obtained in the simulation will be of reduced value when compared to the neutron diffraction data.

An important consideration in bilayer/peptide MD simulations is the deviation of a peptide from its starting position, to this end the average mean square displacement (MSD) of the peptide was obtained throughout the 100 ns of NPT simulation. The average MSD of the peptide was comparatively low (Figure 5.1).

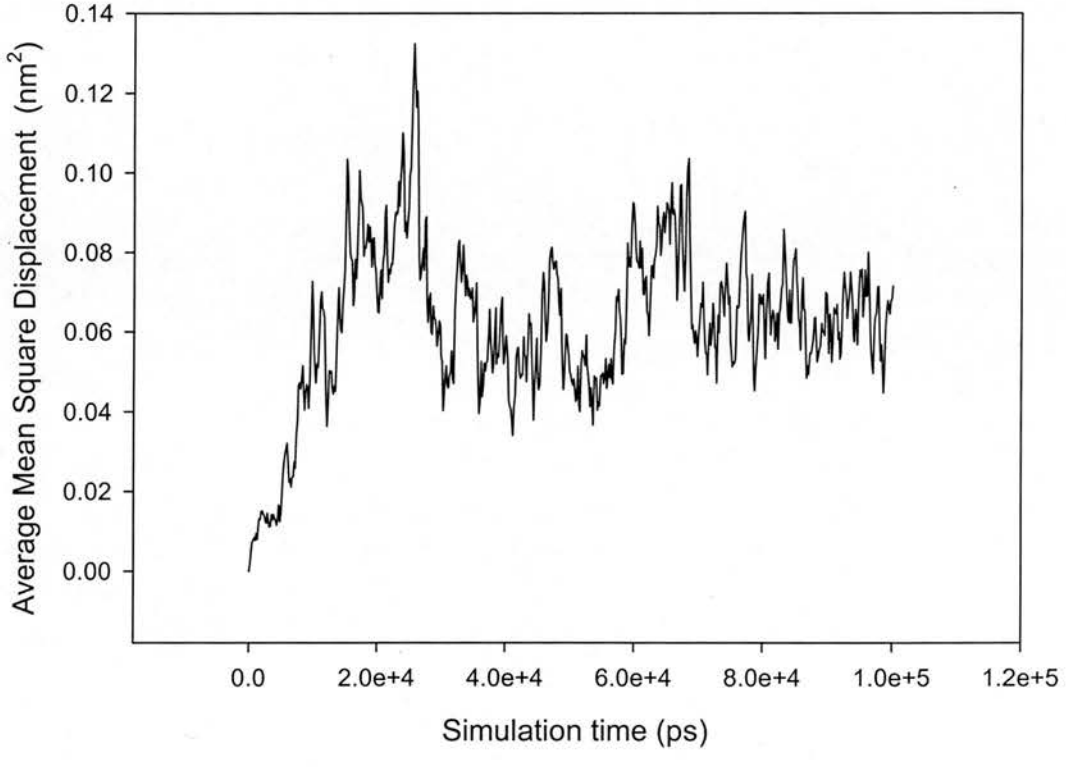

Figure 5.1. The average mean square displacement of the fusion peptide of SIV embedded within a DOPC bilayer (from the starting position).

As can be observed from Figure 5.1, the average MSD of the peptide increases at 20 ns. However, the average MSD then re stabilises over the next 40 ns of simulation. The average MSD of the peptide is particularly stable throughout the final 20ns of simulation.

5.5.2 Hydrogen bonding

One of the many features of MD simulation analysis is the ability to extract information concerning hydrogen bonding. The focus in this section is the hydrogen bonding which occurs between the peptide and other components of the system. The hydrogen bonding in this study can be broken down into the hydrogen bonding between the peptide and the phospholipid headgroups (Figure 5.2), the peptide and the solvent SPC (Figure 5.3) and the peptide and the oleoyl chains (Figure 5.4).

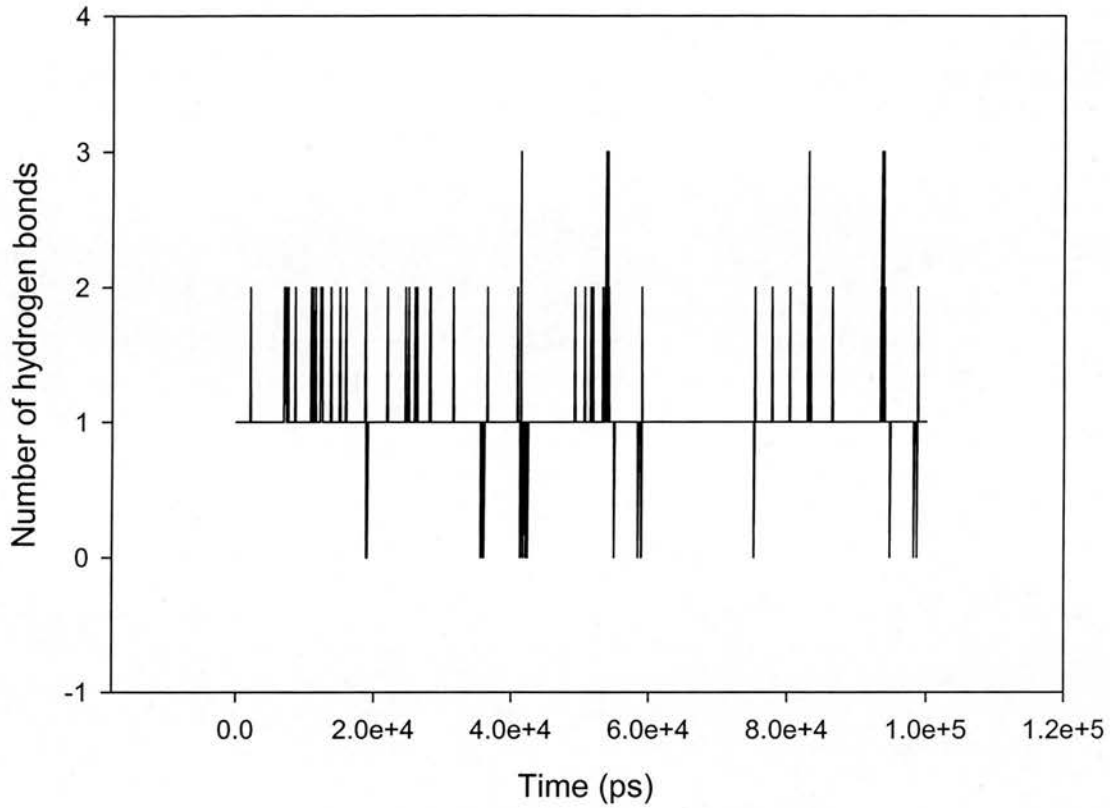

Figure 5.2. Number of hydrogen bonds formed between the phosphatidylcholine headgroups and the fusion peptide of SIV in the simulated system.

Hydrogen bonding between the peptide and phosphatidylcholine headgroups was minimal compared to those of ARF1p and the mixed bilayer. This can be explained readily as ARF1p lies perpendicular to the bilayer normal (z). However, the fusion peptide of SIV inserts obliquely at an angle of 55° relative to the bilayer normal, resulting in lower hydrogen bonding when compared to that reported in the previous chapter. The hydrogen bonding occurred between the residues eight, ten and eleven of the peptide. These residues were leucine, phenylalanine and the penultimate leucine residue, respectively.

Due to the oblique insertion of the peptide, hydrogen bonding was detected between the peptide and the oleoyl chains (Figure 5.3). Phenylalanine (residue three) was the amino acid which was involved on this instance.

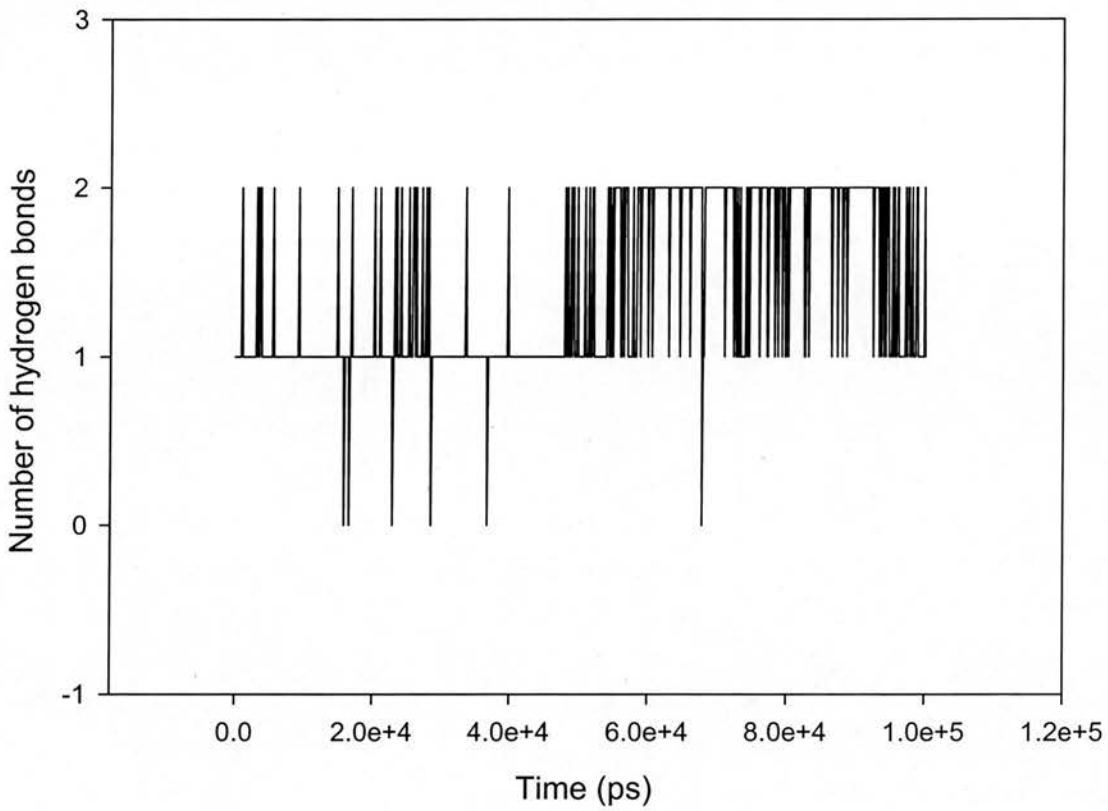

Figure 5.3. Total number of hydrogen bonds formed between SIV and the oxygens of the oleoyl chains in a DOPC bilayer.

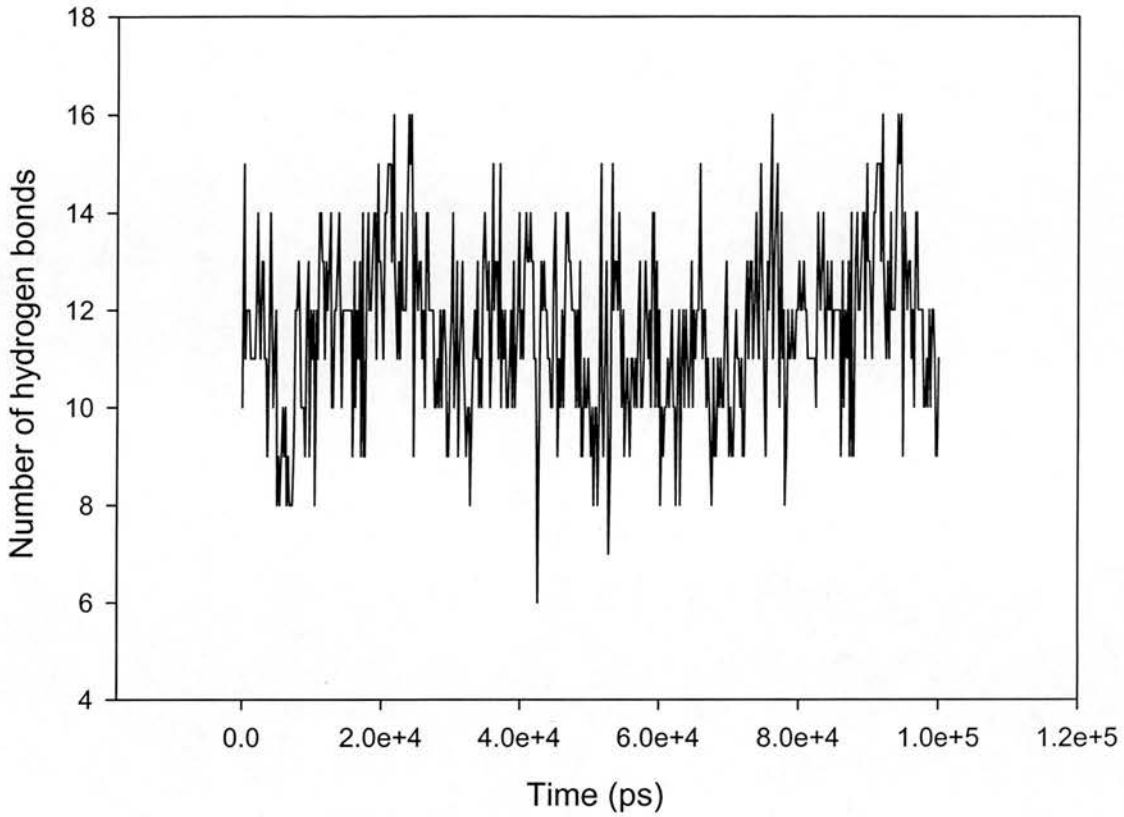

Figure 5.4. Number of hydrogen bonds formed between SIV and solvent water (SPC) molecules over 100ns of MD simulation, in the simulated system.

Figure 5.4 shows a plot of hydrogen bonds formed between the peptide and the water molecules (SPC). The lower number of hydrogen bonds when compared to ARF1p is mainly due to the lower number of polar residues present in the SIV fusion peptide. Furthermore, the oblique angle of insertion of the peptide into the hydrophobic core of the bilayer, results in less solvent peptide hydrogen bonding. All amino acid residues, with the exception of the first two residues (glycine and valine) were involved in hydrogen bonding between the solvent molecules and peptide.

5.5.3 Angle of Insertion

Brasseur and co-workers (Brasseur *et al.,* 1990) had previously proposed an angle of insertion of 57° for the fusion peptide of SIV, which they had assumed to be α-helical. Bradshaw and co-workers confirmed the findings of Brasseur *et al.,* by a novel neutron diffraction study to be 55° for the fusion peptide of SIV relative to the bilayer normal (*z*). Some fluctuation is observed as would be expected of a small peptide embedded in a DOPC bilayer and subjected to MD simulation. The fluctuations were in line with previously reported angles of insertion (Kamath and Wong, 2002).

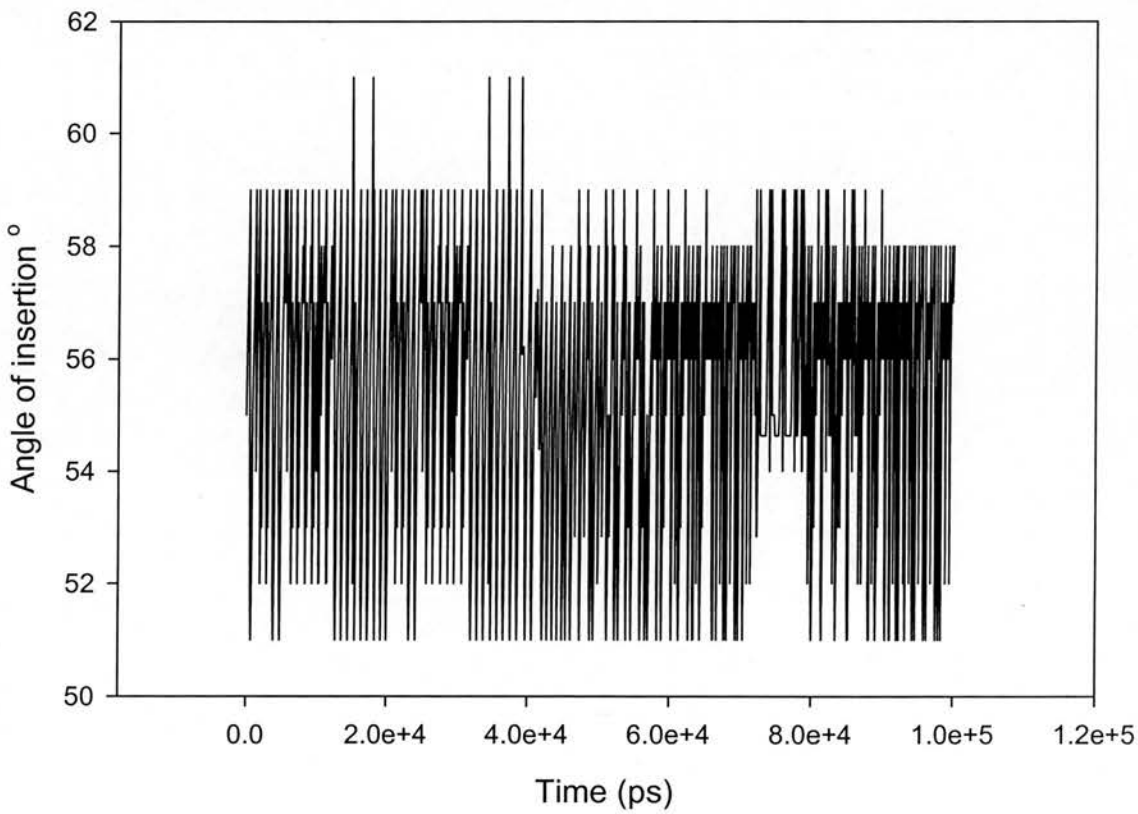

Figure 5.5. Angle of insertion of the fusion peptide of SIV relative to the bilayer normal (*z*) in a DOPC bilayer, over 100ns of simulation.

The fluctuations observed in the angle of insertion decrease towards the second half of the simulation. The decrease is probably due to the fact that the system is energetically more stable in the latter half of the simulation.

5.5.4 Order parameters

Order parameters of the oleoyl chains have been discussed in chapter 1 (1.5.3). In addition, order parameters of the oleoyl chains of an intact DOPC bilayer were presented in chapter three (3.6.3). The fusion peptide of SIV has been proposed to act via disruption to the hydrocarbon core of the membrane (Harroun *et al.,* 2003). Therefore it was logical to obtain order parameters from both the peptide containing leaflet and the non peptide containing leaflet. In previous chapters, the order parameters have been expressed collectively, as the average mean for the whole leaflet. To attain a deeper understanding of the effect of fusion peptide action upon the hydrocarbon core of the bilayer (i.e. the lipid chains), individual order parameters are presented in this chapter. Using a programme written by Dr Bradshaw, the nearest lipid to the peptide was identified in the upper leaflet. In addition, the corresponding (mirror image) lipid molecule was then identified in the lower leaflet. Using this program, a lipid was identified that was next to the initially selected DOPC molecule. In other words, a radius of 8.5 Å was selected (as the average area per lipid in the DOPC bilayer was 72.2 $Å^2$), between each lipid. A left handed direction (in the x axis) was selected for both the upper and lower leaflets when choosing all lipids. Once the lipids were selected, the *GROMACS* analysis

programme *g_order* was used to calculate the individual order parameters. The data were then divided into order parameters of the lower and upper leaflets and *sn-1 /sn-2* chains. The data is presented in Figures 5.6-5.9.

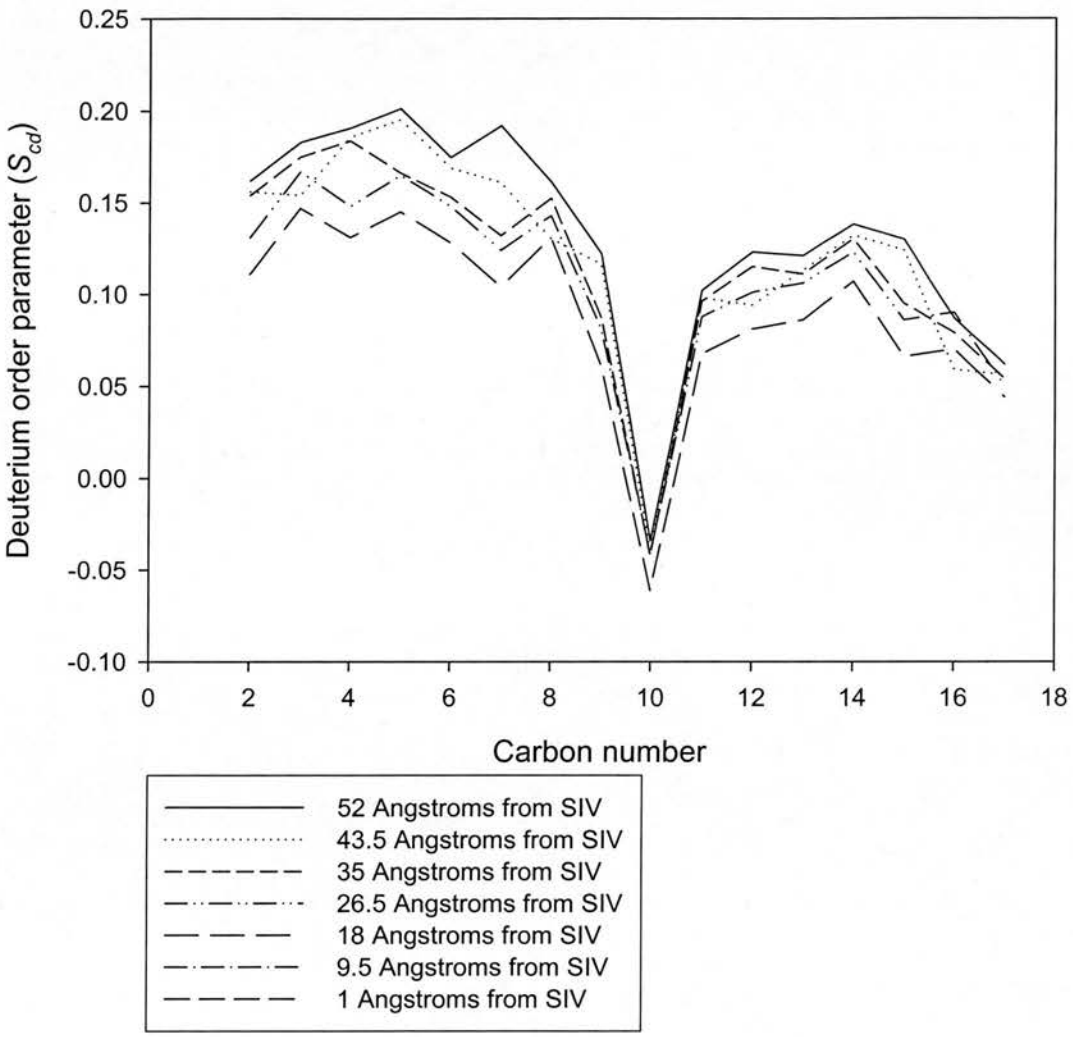

Figure 5.6. Order parameters of selected individual *sn-1* chains of the lipids in the upper leaflet. (see text for explanation).

A reduction in order parameters was observed in the leaflet containing the fusion peptide. The pattern observed was as follows:

When the peptide was within 1 Å of the oleoyl chains, the most dramatic decrease in order parameters was observed. In addition, a more significant reduction is seen in the carbons 10-17 (i.e. carbons nearer the centre of the bilayer), when compared with carbons 1-10. This is probably due to the fact that the peptide penetrates deep into the hydrophobic core of the bilayer, thereby having the greatest effect on the order parameters of carbons nearer the hydrophobic core.

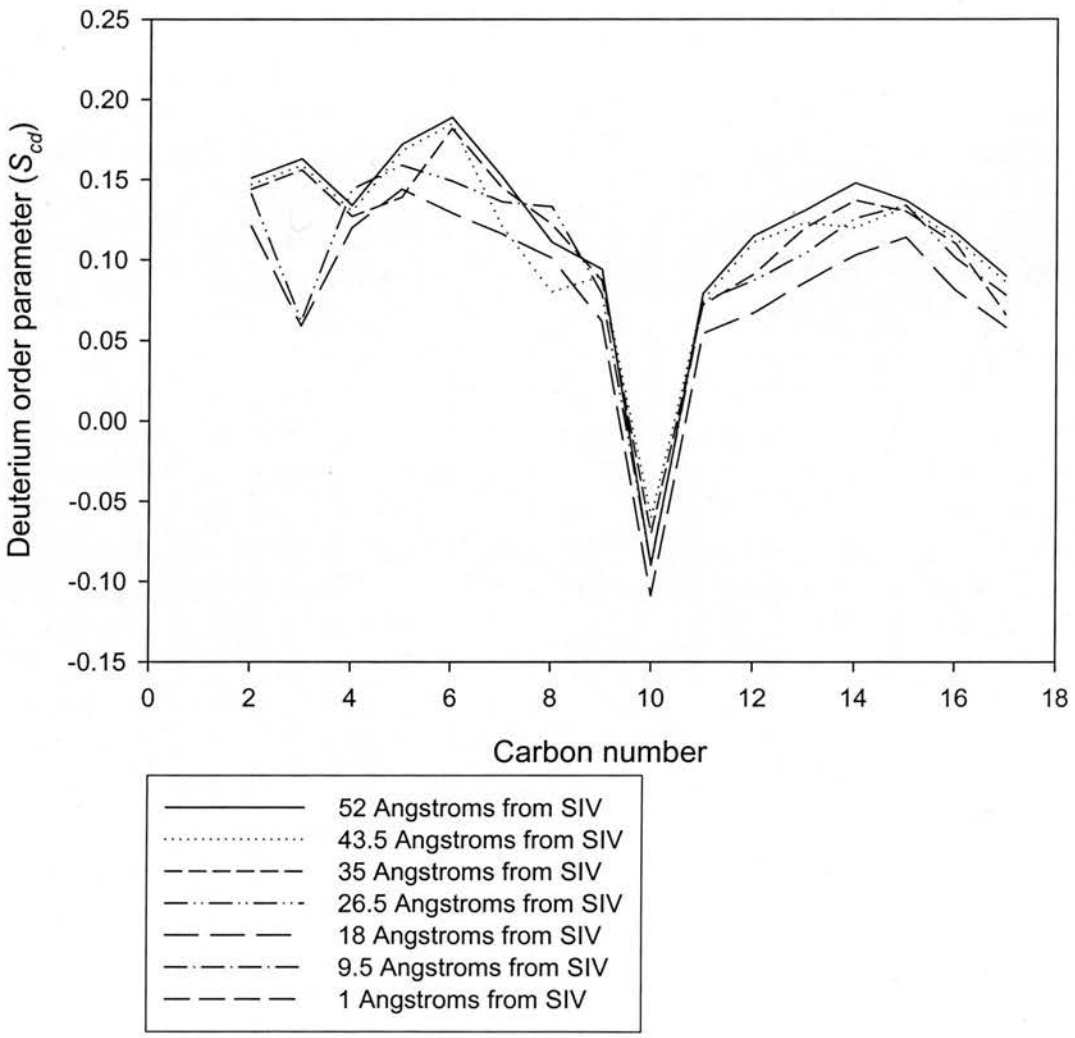

Figure 5.7. Order parameters of selected individual *sn-2* chains of the lipids in the upper leaflet (see text for explanation).

The *sn-2* chains also displayed a reduction in the order parameters, confirming the hypothesis proposed by Harroun and co-workers (Harroun *et al.,* 2003) that SIV fusion peptide acts by disrupting the hydrophobic core of the membrane. Once again, order parameters are reduced when compared to values of an unperturbed DOPC bilayer (section 3.7.3). The reduction in order parameter observed in the *sn-2* chains follows a similar pattern to that of the *sn-1* chains. However, the reduction in order parameter is not as significant in the latter carbons (10-17) as that observed with the *sn-1* chain.

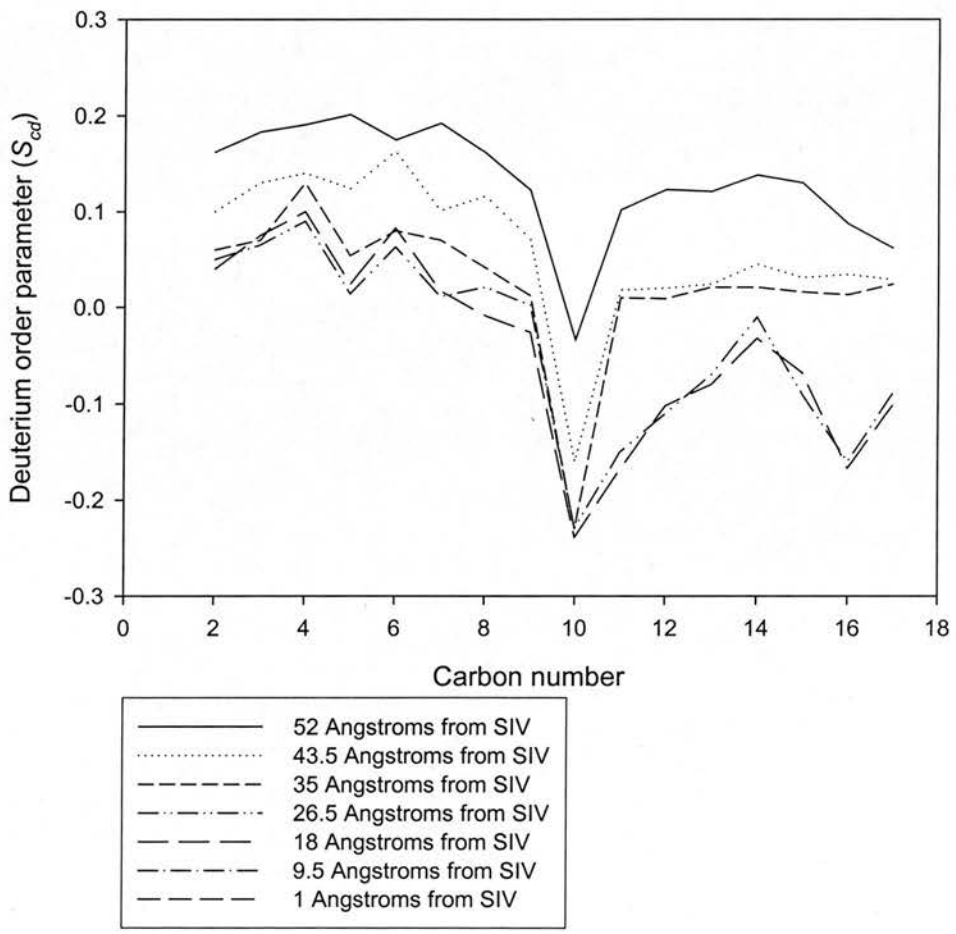

Figure 5.8. Order parameters of selected *sn-1* chains of the lipids in the lower leaflet (see text for explanation).

A reduction of order parameter is observed in the opposing leaflet as well. Interestingly, a greater reduction in order parameters is observed in the leaflet opposite to where the peptide was placed. The literature cites experimental NMR studies (Koenig *et al.,* 1999) whereby a reduction in order parameter has been reported in Stearoyl-oleoyl phosphatidylserine bilayers which contained the gp41 domain of HIV. In addition, an MD simulation study (Vaccaro *et al.,* 2004), has reported a reduction in order parameter in DMPC bilayers which contained the influenza haemagglutinin fusion peptide. However, this group had reported a slightly higher decrease in order parameter in the peptide containing leaflet. The observation that a greater reduction in order parameters occurs in the non peptide containing leaflet has not been reported before for any other fusion peptide. From an intuitive point of view, one would expect the leaflet containing the peptide to be most disrupted. However, the data presented here clearly demonstrates that the most significant reduction in the order parameters is in the non peptide containing leaflet.

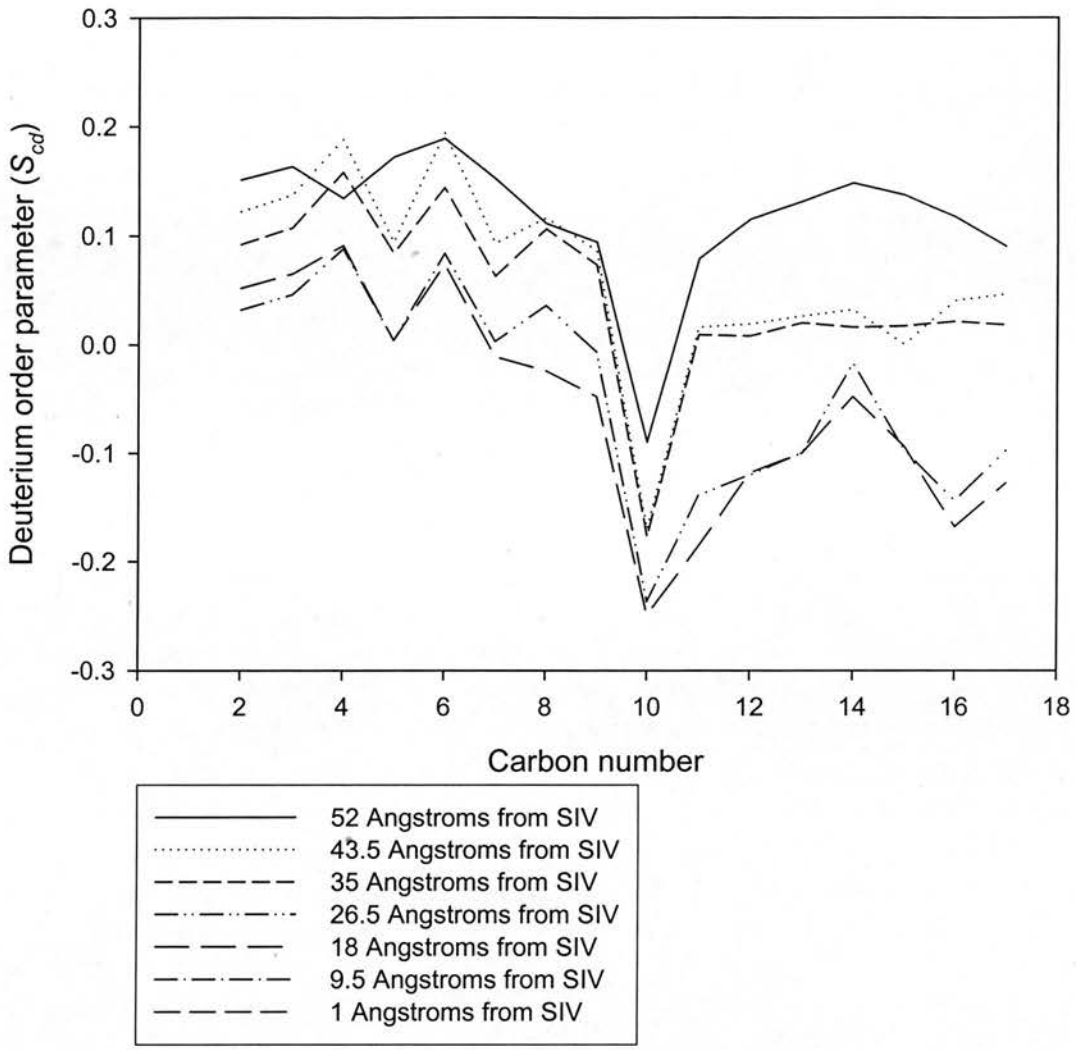

Figure 5.9. Order parameters of selected *sn-2* chains of the lipids in the lower leaflet (see text for explanation).

The selected *sn-2* chains of the lower leaflet show a dramatic decrease in order parameter. The pattern closely follows that of the *sn-1* chain. There is no directly proportional relationship between order parameter and close proximity to the peptide. If the oleoyl chains are within 10 Å of the peptide, a dramatic reduction in order parameter is observed (particularly carbons 10-17). As stated in section 1.5.3, a value of -0.5 refers to a bond vector which is completely parallel to the bilayer plane

(*z*). On the other hand a value of 1 refers to a bond vector which is completely perpendicular to the bilayer plane (*z*). Therefore, from the results obtained it can be deduced that the fusion peptide of SIV causes the oleoyl chains of the DOPC molecule to become more parallel to the bilayer plane particularly those in the non peptide containing leaflet and the latter carbons (10-17) of the oleoyl chain.

5.5.5 Secondary structure of the fusion peptide of SIV

A previous computational (MD simulation) study (Kamath and Wong, 2002) had demonstrated that the membrane bound secondary structure of the gp41 fusion peptide of HIV was α-helical. Experimental studies using Fourier transform infra red (Martin *et al.,* 1991) had shown that the fusion peptide of SIV was α-helical when associated with DOPC. However, Ramachandran analysis of the following residues of the peptide have revealed otherwise. A full Ramachandran plot of the full peptide is presented in Figure 5.10. The initial starting membrane bound conformation of the peptide was a right handed α-helix. However, the Ramachandran plot of the peptide clearly shows random coil and β-strand structures present in the peptide. Throughout the 100ns simulation the peptide is a right handed α-helical conformation for only 40% of simulation time. The ψ and Φ angles of residues 2-11 of this twelve residue peptide were then plotted on an individual basis and are shown in Figures 5.11-5.20.

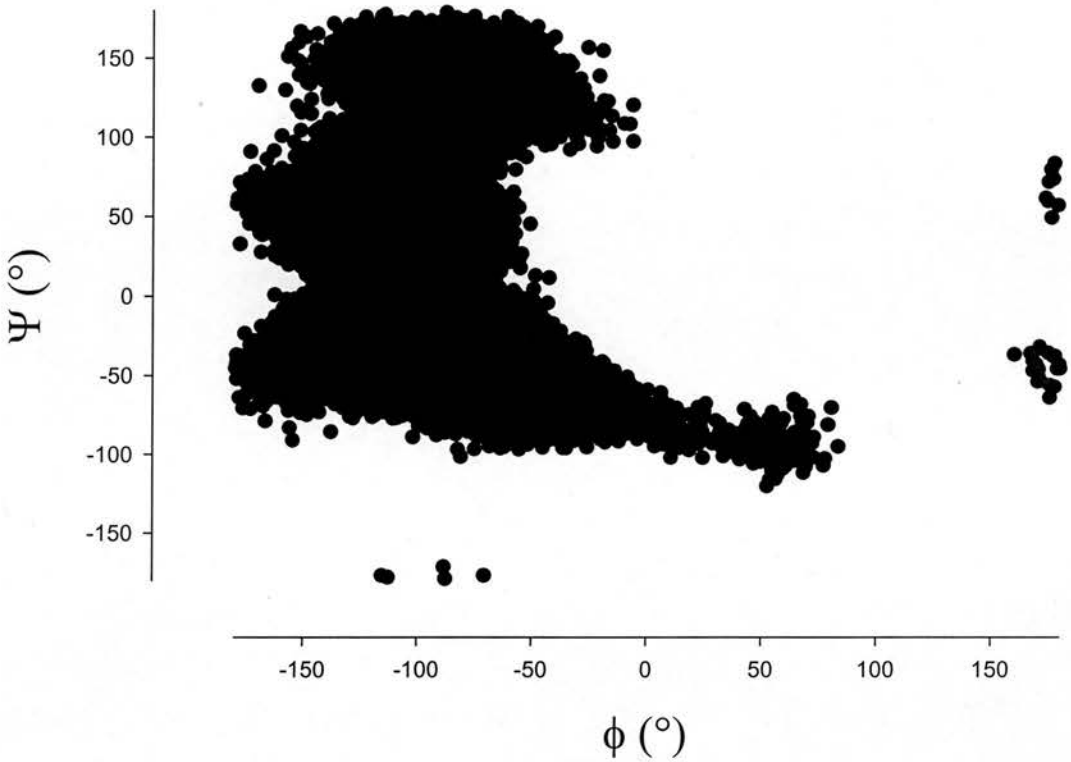

Figure 5.10. Full Ramachandran plot of the whole fusion peptide of SIV (over 100 ns of MD simulation), when inserting obliquely at angle of 55° ± 4.5° (from the bilayer normal) into a DOPC bilayer.

The Ramachandran plot above presents clear evidence that the fusion peptide of SIV is not in a fully helical conformation when membrane bound to a DOPC bilayer. The peptide remains in a pre-dominantly helical conformation in the first 10 ns of simulation. Therefore it was decided that the Φ and Ψ angles of the final 90 ns of residues 2-11 of the 12 residue fusion peptide will be plotted in the form of Ramachandran plots.

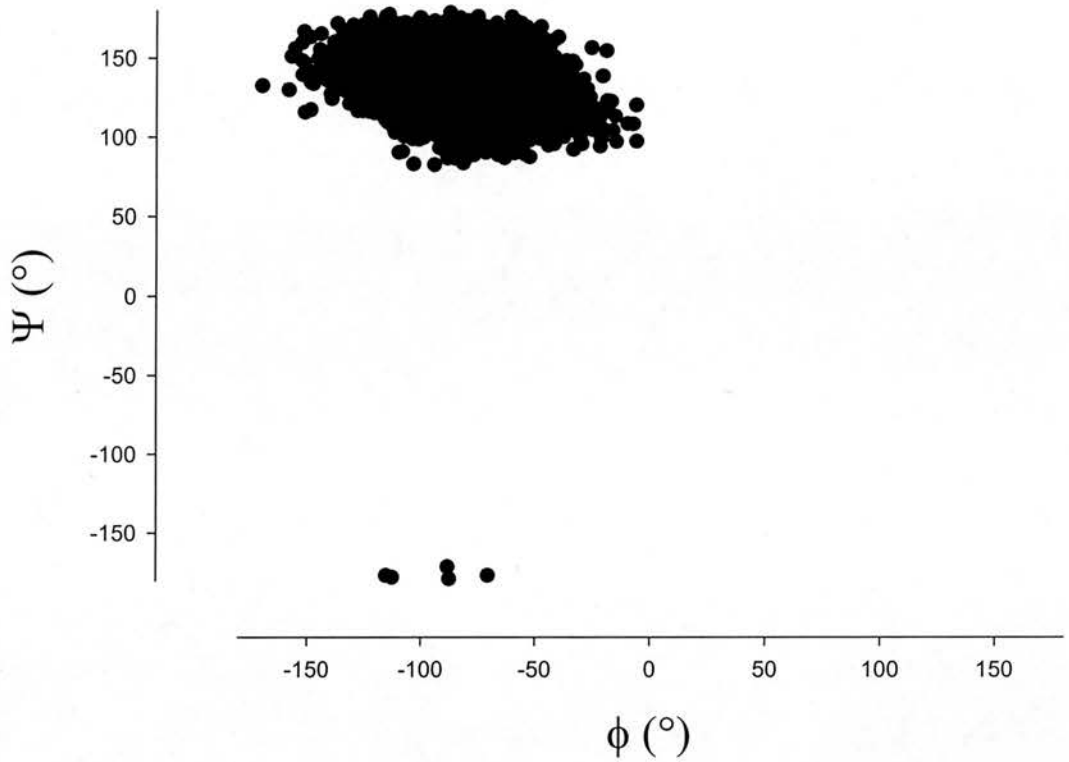

Figure 5.11 Ramachandran plot of the second residue of the SIV fusion peptide over the final 90ns of simulation.

The second residue of the peptide (Val) was in a primarily β–strand conformation (Figure 5.11).

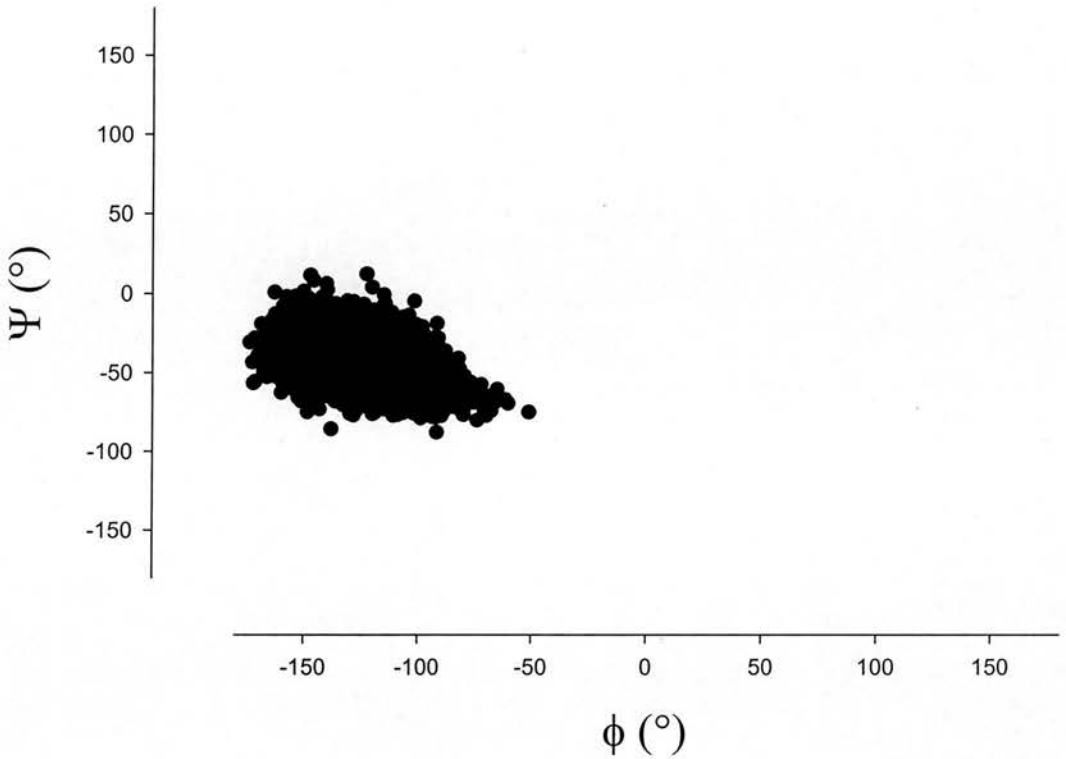

Figure 5.12 Ramachandran plot of the third residue of the SIV fusion peptide over the final 90ns of simulation.

The third residue of the peptide (Phe) is in a pre-dominantly right handed α-helical helical conformation.

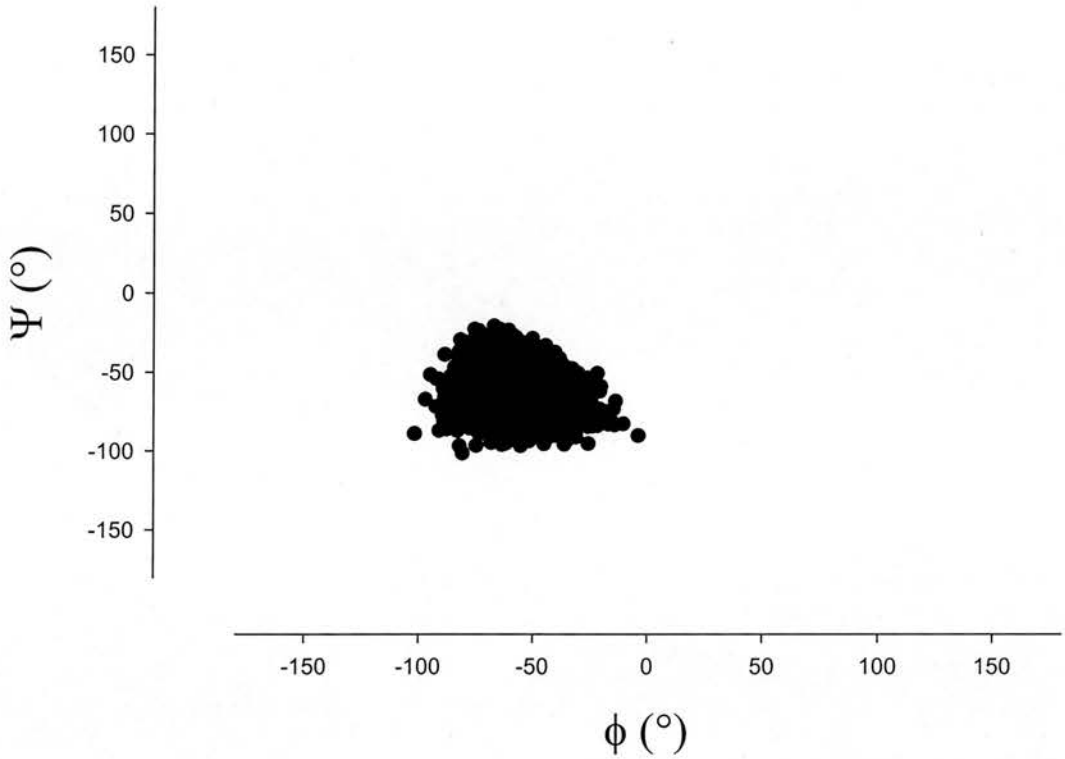

Figure 5.13 Ramachandran plot of the fourth residue of the SIV fusion peptide over the final 90ns of simulation.

The fourth residue of the peptide (Val) is in a pre-dominantly right handed α-helical conformation.

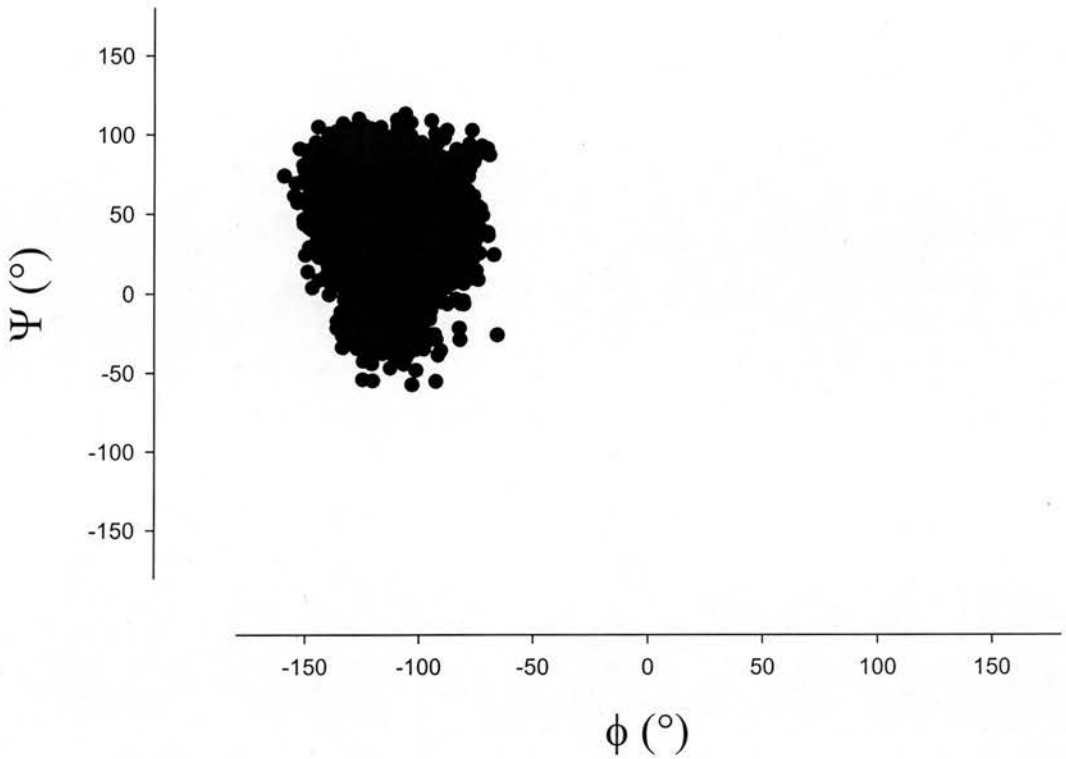

Figure 5.14 Ramachandran plot of the fifth residue of the SIV fusion peptide over the final 90ns of simulation.

The fifth residue of this peptide (Leu) is switching conformation from a right handed α–helical conformation to a β–strand conformation.

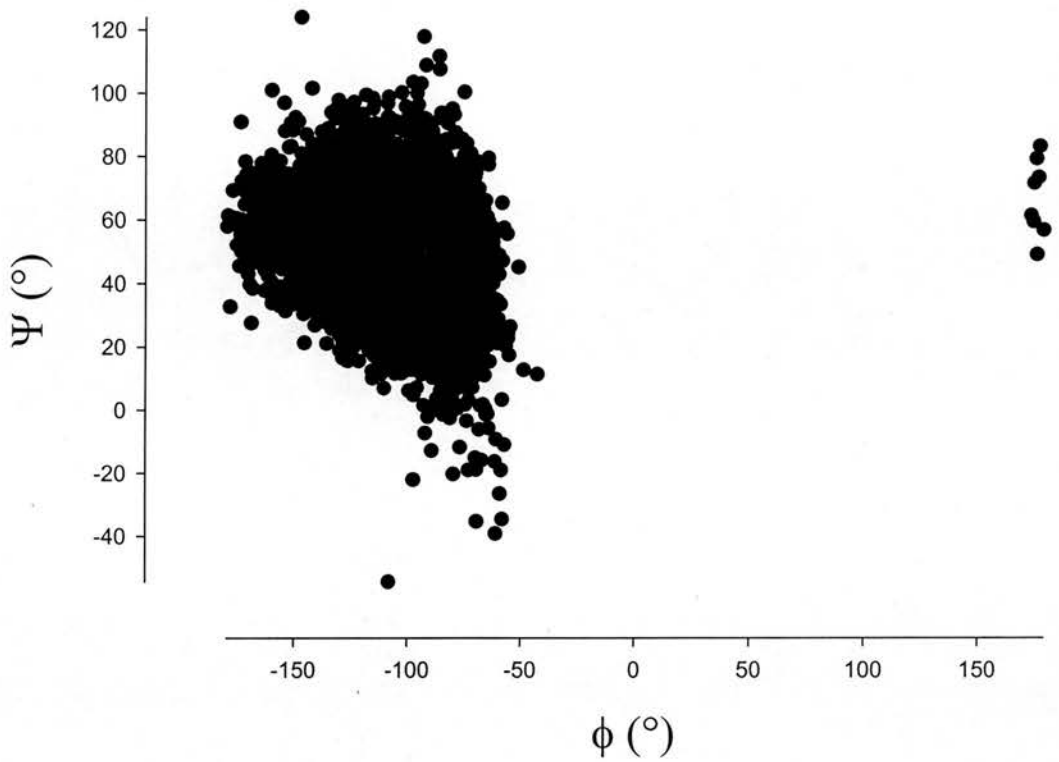

Figure 5.15 Ramachandran plot of the sixth residue of the SIV fusion peptide over the final 90ns of simulation.

The sixth residue of the peptide (Gly) is in a pre-dominantly β–strand conformation.

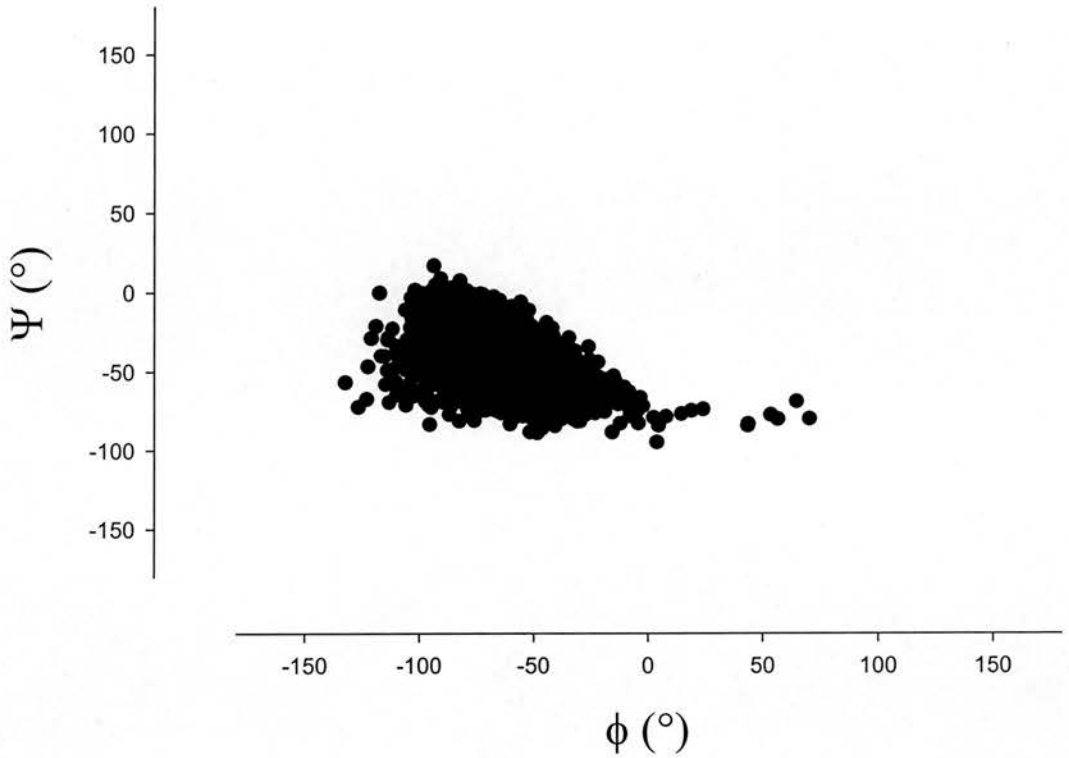

Figure 5.16 Ramachandran plot of the seventh residue of the SIV fusion peptide over the final 90ns of simulation.

The seventh residue of the peptide (Phe) is in a pre-dominantly right handed α–helical conformation for virtually all of the final 90ns of MD simulation.

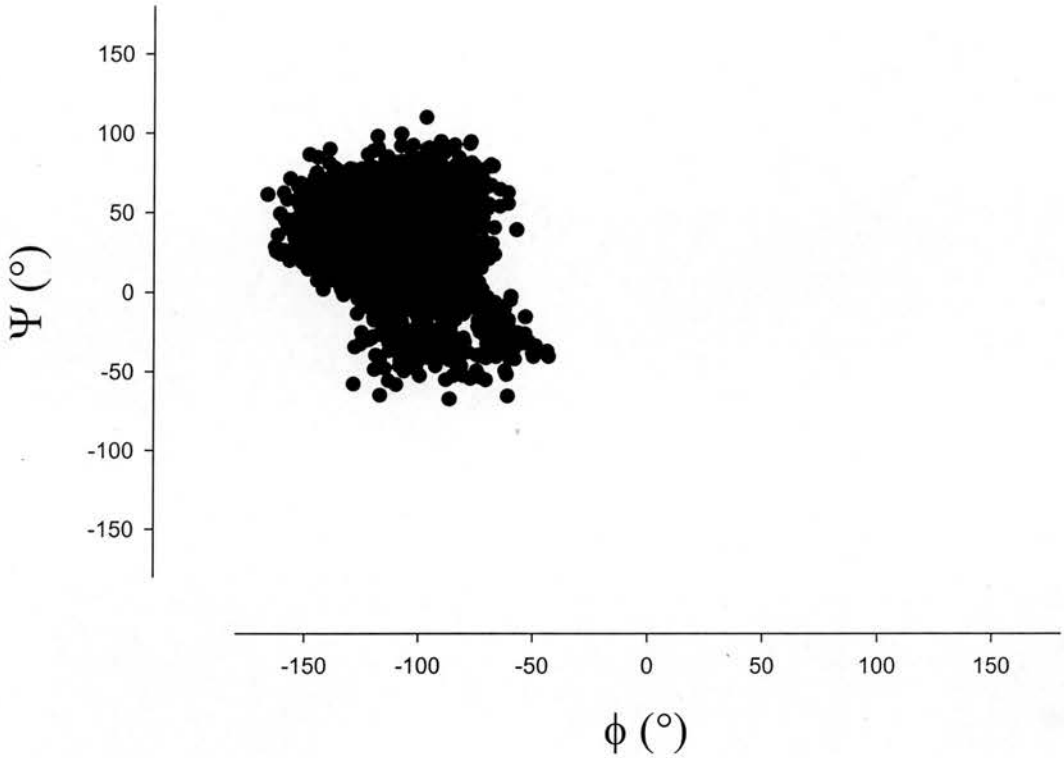

Figure 5.17 Ramachandran plot of the eighth residue of the SIV fusion peptide over the final 90ns of simulation.

The eighth residue (Leu) of the membrane bound peptide was in a random coil and a β–strand conformation. A very small amount of helical conformation was observed at any point in the final 90 ns with this particular residue.

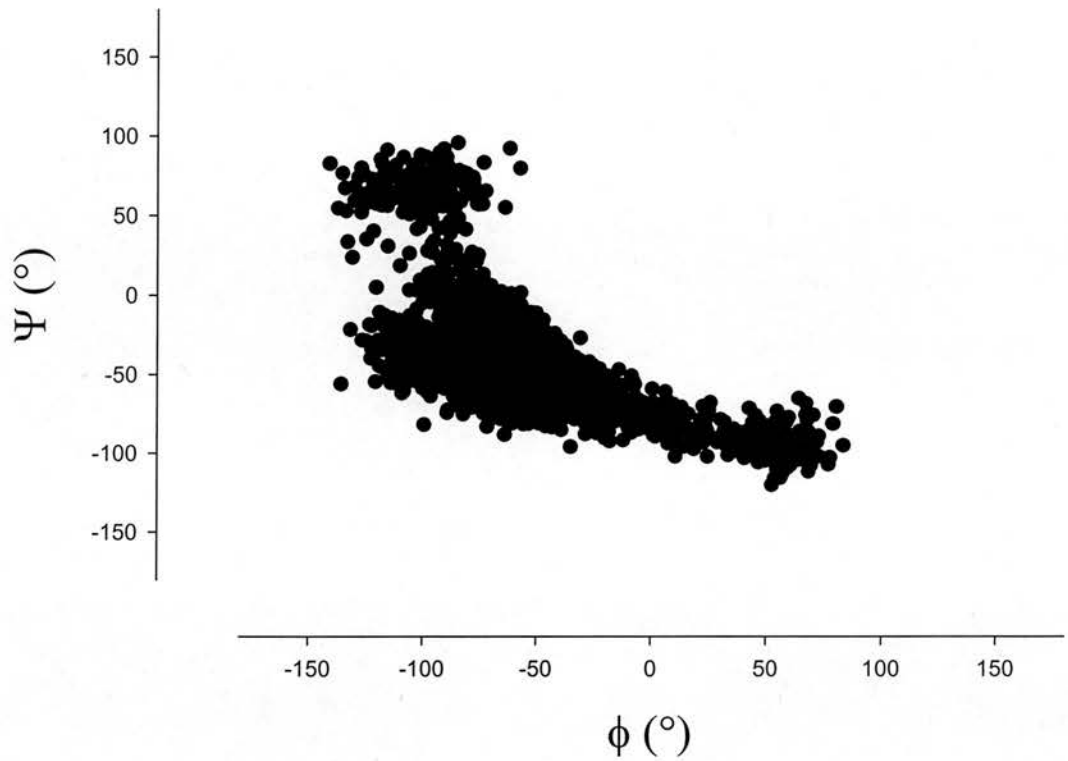

Figure 5.18 Ramachandran plot of the ninth residue of the SIV fusion peptide over the final 90ns of simulation.

The ninth residue (Gly) of the peptide was in a pre-dominantly α–helical conformation. However, as can be observed from the Ramachandran plot, evidence of random coil is also observed.

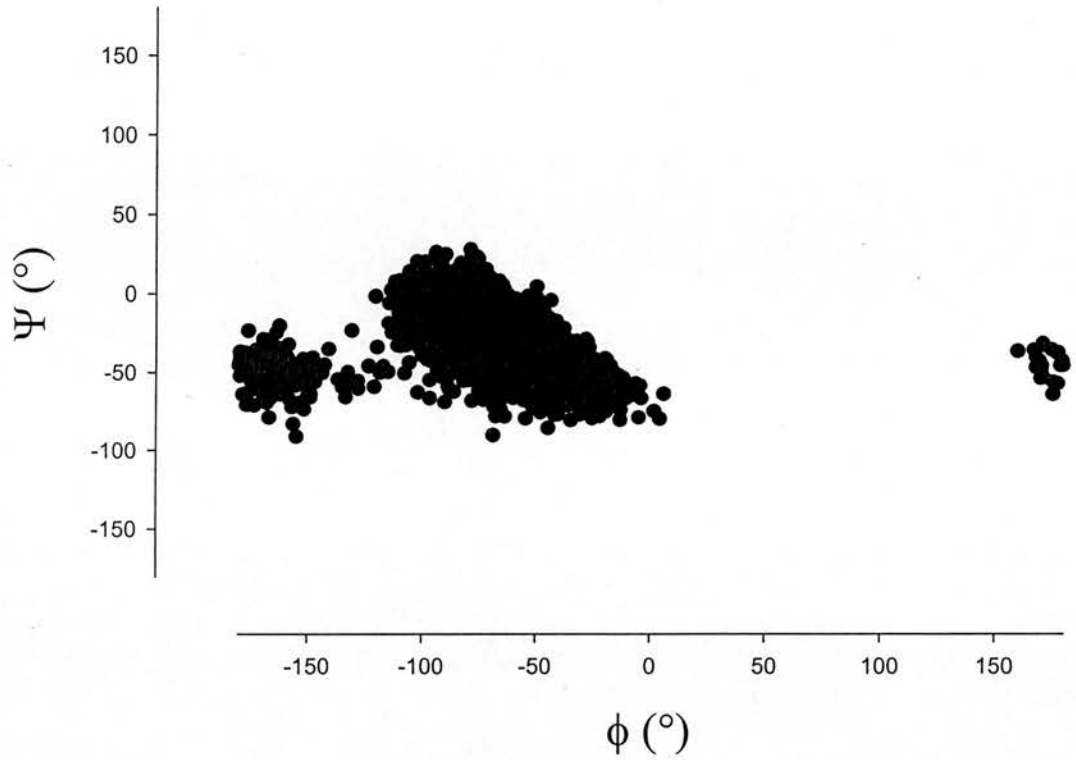

Figure 5.19 Ramachandran plot of the tenth residue of the SIV fusion peptide over the final 90ns of simulation

The tenth residue (Phe) of the peptide is switching between a random coil and a α-helical conformation. The membrane bound structure of the fusion peptide of SIV, was initially proposed to be fully α-helical by Fourier transform infra red (Martin *et al.,* 1991). Brasseur (Brasseur *et al.,* 1990) was amongst the first group of workers to propose that fusion peptides are α-helical and insert obliquely into the bilayer plane. The second proposal was confirmed by both the experimental study conducted by Bradshaw and colleagues (Bradshaw *et al.,* 2000) and the MD simulation study, described in this chapter. However, the first proposal has been shown to be inaccurate and has not stood the test of time. The data presented here, clearly show that only ~50% of the peptide is in a α-helical conformation when membrane bound

to a DOPC bilayer. It should be noted that it would not have been possible to probe the secondary membrane bound structure of this fusion peptide without the availability of the neutron diffraction data (Bradshaw *et al.,* 2000).

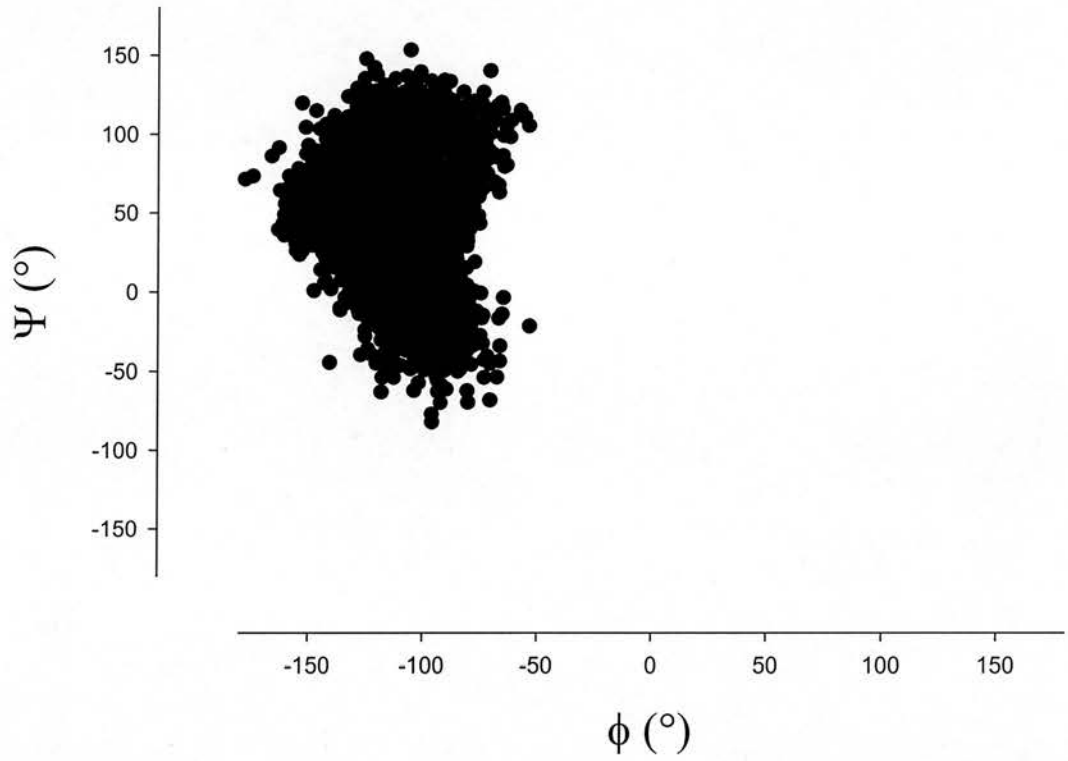

Figure 5.20 Ramachandran plot of the eleventh residue of the SIV fusion peptide over the final 90ns of simulation

The eleventh residue (Leu) which was subjected to the Ramachandran plot was the eleventh residue of the peptide. This leucine residue exhibited no significant α-helical content in the latter parts of the simulation and was in a partial random coil and partial β–strand conformation.

Epand (Epand, 2003) had discussed fusion peptides that were not in a α-helical conformation when membrane bound. However, the fusion peptide of SIV (sequence GVFVLGFLGFLA), much like the gp41 fusion peptide (sequence AVGIGALFLGFLGAAG), was thought to be α-helical when membrane bound. Furthermore, FTIR experiments showed that the fusion peptide of SIV is pre-dominantly α-helical when associated with DOPC (Martin et al., 1990). Bradshaw and co-workers (Bradshaw et al., 2000) have suggested that this may not be the case, as their neutron data would be more easily fitted to a random secondary structure and not a pre-dominantly α-helical structure. The simulations clearly demonstrate that no more than 40% of the peptide remained alpha helical throughout the simulation. These findings further enhance the theory (Epand, 2003) that fusion peptides are not necessarily in a α-helical conformation when membrane bound. Furthermore, fusion peptides do not necessarily require a α-helical conformation to exert their actions upon the membrane.

5.5.6 Area and volume of lipid

	Area of Lipid ($Å^2$)	Volume of Lipid ($Å^3$)	*d*-repeat (Å)
Pure DOPC	70 ± 1.1	1294 ± 8.4	5.9
Lower Leaflet	68	1284	5.6
Upper Leaflet	65	1281	5.6

Table 5.2. Comparison of area and volume of lipid and the *d*-repeat between a pure DOPC bilayer and a DOPC bilayer containing fusion peptide

There was no significant change in area or volume of lipid. This is hardly unexpected as the peptide is relatively small and despite the angle of insertion is unlikely to cause huge disruption to the system by way of changing the area and or volume of lipid. The *d*-repeat was reduced compared to that of a pure DOPC bilayer. This could be an indication of membrane thinning, which will be discussed in the next section.

5.5.7 Area and Water distribution

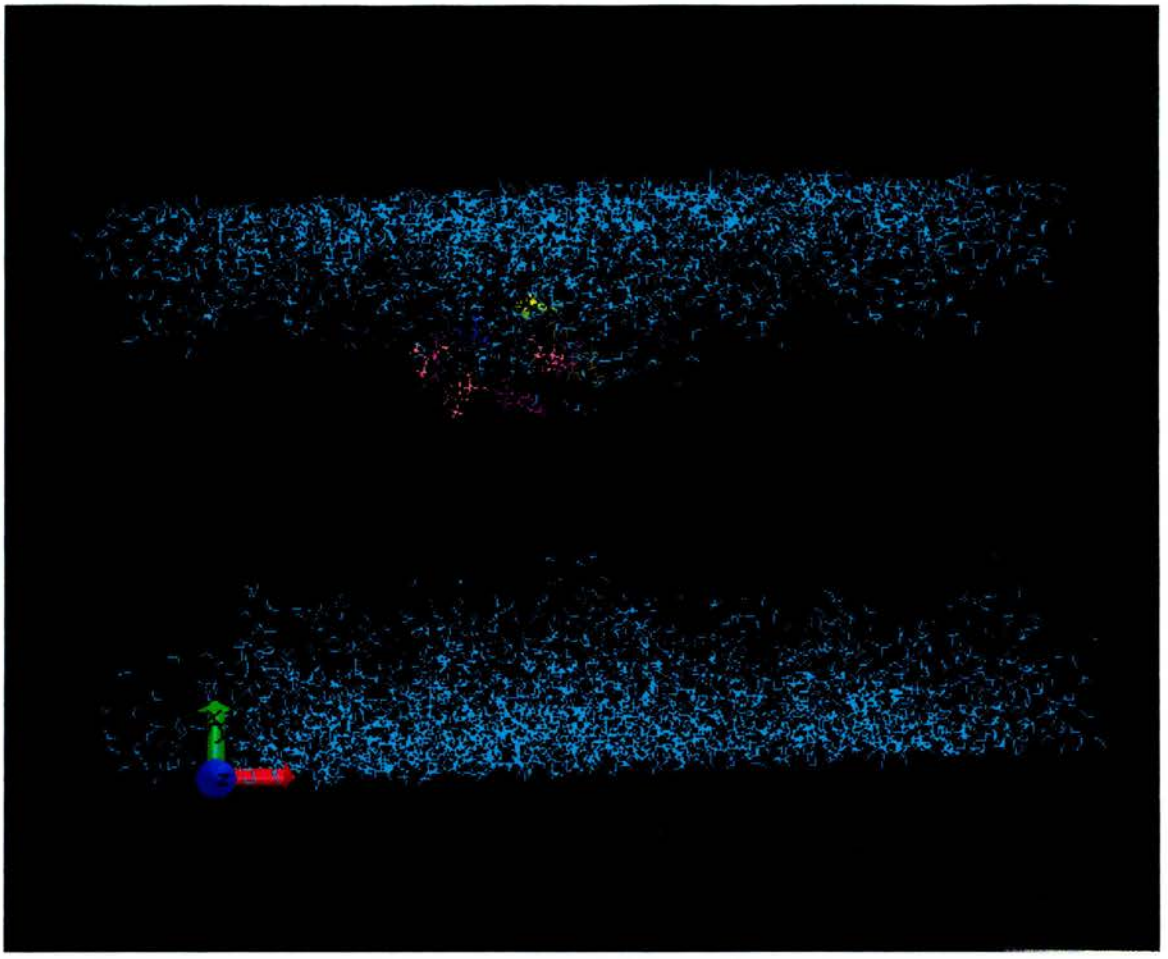

Figure 5.21 distribution of water. The penetration of water molecules into the hydrophobic core is of particular interest, as it could be taken as an indication of membrane thinning.

The process of fusion may involve membrane thinning. One indication of membrane thinning is the penetration of water into the hydrophobic core of the membrane. Figure 5.21 displays a snapshot of the system (bilayer deleted for clarity) with the water molecules penetrating the hydrophobic core. Figure 5.22 displays a snapshot of the peptide embedded in the DOPC bilayer. Waters are removed for clarity.

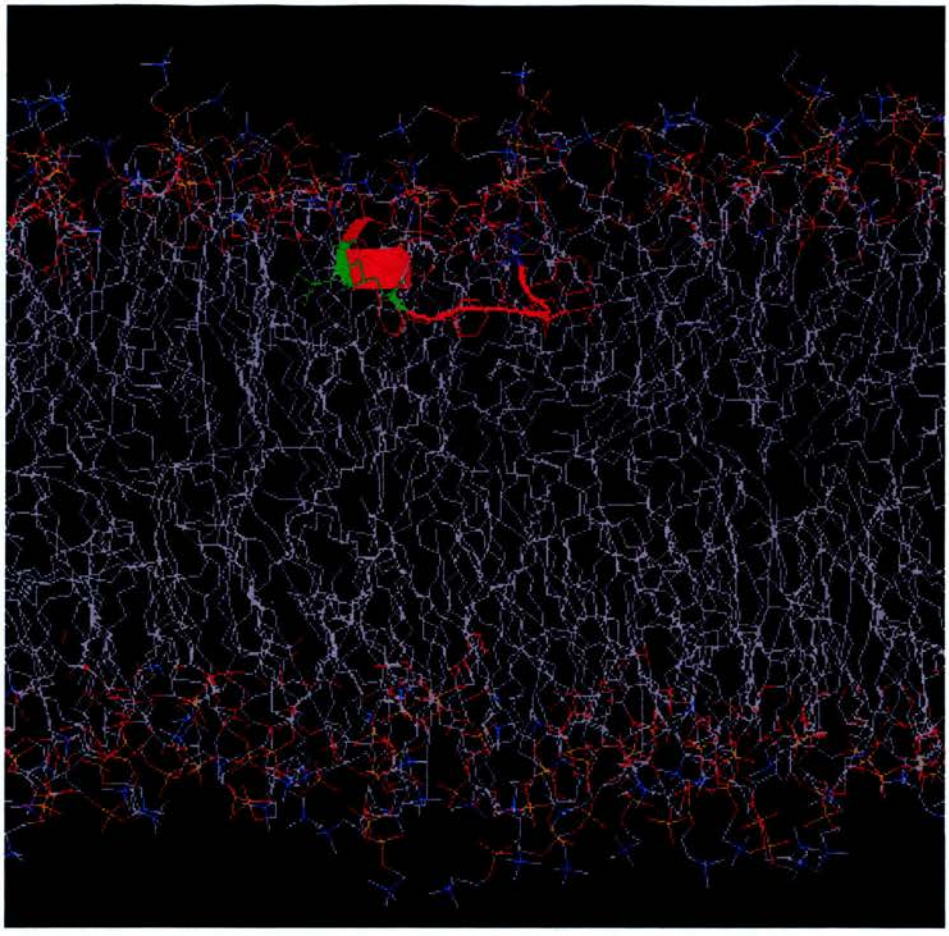

Figure 5.22. A snapshot of the SIV fusion peptide embedded within the DOPC bilayer. The peptide is shown in red. The green colouring represents the leucines 8 and 11. The blue colouring represents valine 2. These residues were deuterated in the neutron diffraction study. The snapshot was taken after 99 ns of MD simulation.

Synthetic viral fusion peptides utilised in experimental studies are less effective in accelerating membrane fusion compared with the intact fusion protein. It is not surprising that small peptide (<25 residues) can not reproduce all of the functions of an intact protein. There are two main factors that are likely to contribute to greater activity of the intact protein. Firstly, the viral fusion protein forms stable multimers which tend to self-associate in membranes to form higher order complexes (Markovic *et al.*, 2001; Hernandez *et al.*, 1996). Hence, the fusion peptide segment

does not function as an isolated unit, but is rather assembled into an organized complex in which several fusion peptide segments can act in a coordinated fashion.

Secondly, some regions outside the fusion peptide may also participate in accelerating the fusion process (Peisajovich *et al.,* 2003). Evidence has been presented for a role of the transmembrane segment and the cytoplasmic tail of the fusion protein of a number of fusion proteins (Epand *et al.,* 1998).

Isolated fusion peptides promote contents leakage of vesicles (Lear and DeGrado, 1987), but true fusion can be measured accurately using lipid mixing. In order for the mixing of aqueous contents to be measured, the rate of formation of a fusion pore has to be more rapid than the rate of leakage. However, an agent which can destabilize membranes will inevitably induce leakage. Many intact viruses induce haemolysis and it has been reported that influenza virus causes the lysis of liposomes (Epand, 2003). It is therefore not surprising that a small fragment of the viral fusion protein, i.e. the fusion peptide, can cause sufficient leakage to prevent measurement of aqueous content mixing. To summarize, the use of synthetic fusion peptides to study the membrane fusion process using diffraction techniques is quite valid and could provide insights into the fusion mechanism.

5.6 Conclusion

This chapter has shown that the fusion peptide of SIV maintains its starting position within the bilayer to within 5% over a 100ns MD simulation, emphasizing the importance of starting conditions which utilise experimental data. Hydrogen bonding was observed between the peptide, water molecules and both headgroups and the oxygen atom present in oleoyl chains. The order parameters of the oleoyl chains were significantly reduced, particularly in the lower leaflet. The reduction of order parameters was observed in both the upper (peptide containing) and lower leaflet (no peptide), experimental studies have reported a reduction in order parameters in previous experimental (Koenig *et al.,* 1999) and computational (Vaccaro *et al.,* 2004) studies. However, no specification was made regarding the differences between the upper and the lower leaflet.

Membrane thinning occurred and was demonstrated by the distribution of the water molecules. The helical content of the peptide was significantly reduced and β-strand structures were observed. Furthermore, random coil structures were seen in the individual Ramachandran plots of residues 2-11.

To summarize, this chapter has described a long time scale simulation of a fusion peptide embedded within a DOPC bilayer. The major findings were the reduction in order parameters, particularly in the lower leaflet (no peptide). Evidence of membrane thinning was detected, via the distribution of water. Furthermore, the peptide was thought to be α-helical when membrane bound (Bradshaw *et al.,* 200).

However, the simulation and subsequent Ramachandran analysis have clearly demonstrated decreased helical content.

5.7 Suggested future studies

This chapter focused on a long time scale MD simulation of the fusion peptide of SIV in a pre-equilibrated bilayer of DOPC. The previous chapter, verified that the proposed most likely conformation of ARF1p was indeed the correct orientation of the peptide in relation to the bilayer. Therefore, the simulation undertaken in this chapter used the most likely conformation. This allowed for the maximum usage of computational processing power, resulting in a trajectory of 100ns. The simulation parameters were in excellent agreement with experimental data. Furthermore, the simulation demonstrated evidence of membrane thinning. To date, membrane thinning induced by this peptide has not been demonstrated in an MD simulation. Fusion peptides such as the fusion peptide of SIV are said to act by lowering the hexagonal phase transition temperature of membranes (T_H). A combined experimental and computational investigation into the effects of the fusion peptide of SIV in a membrane which is in the inverted hexagonal phase (H_{II}) will add knowledge to the field and open up broad possibilities for therapeutic intervention. A pre-requisite measure would be to obtain neutron diffraction data to construct a computational model of a phospholipid in an H_{II} phase. The non-lamellar lipid, N-methylated di-oleyl phosphatidylethanolamine (DOPE-me) would be a prime candidate for this sort of investigation. After neutron diffraction studies to determine the location of the fusion peptide of SIV in the H_{II} phase, utilising deuterated labels,

the construction of a computational model of a membrane in the H_{II} phase can then be undertaken. The model will provide novel insights into the actions of fusion peptides. To conclude, other fusion peptides such as the fusion peptide of the feline leukaemia virus (FeLV) can be embedded within the bilayer, providing experimental data is available to accommodate a starting conformation.

Chapter 6

Conclusions

6 General conclusions

The most important finding of this thesis is that computational techniques such as MD simulations can be very effective in investigating peptide membrane interactions, when the starting conditions of the model(s) are based on experimental data. MD simulations can give explicit atomic level insights into bilayer peptide interactions, providing the orientation of the peptide to be embedded in the bilayer can be adjusted appropriately. In the case of smaller peptides (<40 residues) the correct orientation is of utmost importance in an MD simulation. However, this is not as important for larger transmembrane helices.

Neutron diffraction has provided detailed information on bilayer peptide systems. It can be used to study the membrane activity of two different isoforms of a peptide. For instance, the comparison of human and rat isoforms of IAPP, as was described in chapter two. However, neutron diffraction is more routinely used to identify the location of a peptide, when membrane bound. This is performed by deuterating specific amino acids in the peptide sequence. Ideally four residues should be deuterated so the peptide can be orientated unambiguously. This is not always the case, as previous studies have used only three deuterated labels (Bradshaw *et al.,* 2000: Davies *et al.,* 2003).

Neutron diffraction studies can give rise to a number of possible conformations. A preferred conformation can be proposed as a result of uncertainty over the membrane

bound secondary structure and thermodynamic arguments. However, neutron diffraction can not give atomic level insights into the intricate details of the peptide in relation to the bilayer. The powerful computational technique of MD simulations was therefore utilised to further explore neutron diffraction data.

Chapter three described the background to MD simulations, as well as construction and simulation of pure DOPC bilayers and mixed DOPC/DOPG bilayers. This was an important pre-requisite to performing bilayer peptide simulations. Chapter four described work which was intended to test the proposed methodology of setting up bilayer peptide simulations using neutron diffraction data as a starting point. The neutron data led to four possible conformations of membrane bound ARF1p. These conformations were placed in the mixed DOPC/DOPG bilayer, which was used in the experimental measurements and subjected to MD simulation. The hypothesis proposed was that model A was the most likely conformation. The analysis of the four systems, lead to the hypothesis being accepted.

Chapter five described a long time-scale MD simulation of the fusion peptide of SIV in a DOPC bilayer. The pre-requisite steps for this study were performed in the preceding chapters. This chapter gave novel atomic level insights into the actions of a fusion peptide upon a bilayer. The experimental data of the neutron measurements were in excellent agreement with the simulation parameters. The hydrocarbon core of the bilayer was closely investigated and lipid chain order parameters were found to be reduced. A significant reduction in order parameter was observed in the non-

peptide containing (lower) leaflet. Previous experimental (Koenig *et al.,* 1999) and computational studies (Vaccaro *et al.,* 2004) have reported a reduction of order parameters in the lipid chains when studying the fusion peptides of HIV (gp42) and the haemagglutin influenza fusion peptide. However, no reports of fusion peptide induced order parameter reduction in the non-peptide containing leaflet of a bilayer have been made.

Understanding the action of fusion peptides can lead to novel targets for therapeutic intervention for both human (e.g. HIV) and veterinary diseases (e.g. feline leukaemia). To this extent, this thesis has provided novel atomic level insights into the action of the SIV fusion peptide upon a bilayer. This was achieved by using a combined experimental and computational approach. This opens up the possibility of studying a number of membrane-active peptides in atomic resolution. One possibility could be studying the actions of SIV upon phospholipids in the H_{II} phase. In order to achieve this, neutron measurements must be made on the H_{II} phase of a non-lamellar lipid (e.g. DOPE-me). The measurements can then be used to construct a starting unit cell of the H_{II} phase. The next step would be to repeat the procedure but use a fusion peptide, such as the fusion peptides of SIV and FeLV.

To conclude, this thesis has bridged the gap between simulation and experimentation. A combination of experimental and computational techniques is without doubt a powerful combination for investigating biophysical phenomena.

7 References

Aliste, M. P., J. L. MacCallum, and D. P. Tieleman. 2003. Molecular dynamics simulations of pentapeptides at interfaces: salt bridge and cation-pi interactions. *Biochemistry.* 42:8976-8987.

Aman, K., E. Lindahl, O. Edholm, P. Hakansson, and P. O. Westlund. 2003. Structure and dynamics of interfacial water in an L-alpha phase lipid bilayer from molecular dynamics simulations. *Biophys. J.* 84:102-115.

Amor, J. C., D. H. Harrison, R. A. Kahn, and D. Ringe. 1994. Structure of the human ADP-ribosylation factor 1 complexed with GDP. *Nature.* 372:704-708.

Antonny, B., D. Beraud, P. Chardin, and M. Chabre. 1997. N-terminal hydrophobic residues of the G-protein ADP-ribosylation factor-1 insert into membrane phospholipids upon GDP to GTP exchange. *Biochemistry.* 36:4675-4684.

Bacon, G. E. 1975. Neutron diffraction (third edition). *Oxford University Press,Oxford, pp.* 48-50.

Balali-Mood, K., T. A. Harroun, and J. P. Bradshaw. 2003. Molecular dynamics simulation of a mixed DOPC/DOPG bilayer. *Eur. Phys. J. E. Soft Matter.* 12(1):135-140.

Basyn, F., B. Charloteaux, A. Thomas, and R. Brasseur. 2001. Prediction of membrane protein orientation in lipid bilayers: a theoretical approach. *J. Mol. Graph Mod.* 20:235-244.

Basyn, F., B. Spies, O. Bouffioux, A. Thomas, and R. Brasseur. 2003. Insertion of X-ray structures of proteins in membranes. *J. Mol. Graph Mod.* 22:11-21.

Bechor, D., and N. Ben-Tal. 2001. Implicit solvent model studies of the interactions of the influenza hemagglutinin fusion peptide with lipid bilayers. *Biophys. J.* 80:643-655.

Berendsen, H. J. C., D. van der Spoel, and R. Vandrunen. 1995. *GROMACS* - A message-passing parallel molecular-dynamics implementation. *Comp. Phys. Commun.* 91:43-56.

Berendsen, H. J. C., J. P. M. Postma, W. F. van Gunsteren, A. Dinola, and J. R. Haak. 1984. Molecular-dynamics with coupling to an external bath. *J. Chem. Phys.* 81:3684-3690.

Berger, O., O. Edholm, and F. Jahnig. 1997. Molecular dynamics simulations of a fluid bilayer of di-palmitoyl phosphatidylcholine at full hydration, constant pressure, and constant temperature. *Biophys. J.* 72:2002-2013.

Bosch, M. L., P. L. Earl, K. Fargnoli, S. Picciafuoco, F. Giombini, F. Woong-Staal, and G. Franchini. 1989. Identification of the fusion peptide of primate Immunodeficiency Viruses. *Science.* 244:694-697.

Bracewell, R. N. 1989. The Fourier Transform. *Sc. Am.* 260(6):86-95.

Bradshaw, J. P. 1997. Phosphatydylglycerol promotes bilayer insertion of salmon calcitonin. *Biophys. J.* 72:2180-2186.

Bradshaw, J. P., M. J. Darkes, T. A. Harroun, J. Katsaras, and R. M. Epand. 2000. Oblique membrane insertion of viral fusion peptide probed by neutron diffraction. *Biochemistry.* 39:6581-6585.

Bradshaw, J. P., M. J. M. Darkes, and S. M. A. Davies. 1998. Improved accuracy and phasing of lamellar neutron diffraction data by real-time swelling series method. *Physica B: Condensed Matter.* 241-243:1115-1121.

Bradshaw, J.P., K.C. Duff, P.J. Gilchrist, and A.M. Saxena. 1996. Neutron diffraction studies of amphipathic helices in phospholipids bilayers. *Basic Life Sci.* 64:191-202.

Bragg, L. 1968. X-ray crystallography. *Sc. Am.* 219:58-70.

Brasseur, R., M. Vandenbranden, B. Cornet, and J. M. Ruysschaert. 1990. Orientation into the lipid bilayer of an asymmetric amphipathic helical peptide located at the N-terminus of viral fusion proteins. *Biochim. Biophys. Act*a. 1029:267-273.

Bucciantini, M., E. Giannoni, F. Chiti, F. Baroni, L. Formigli, J. S. Zurdo, N. Taddei, G. Ramponi, C. M. Dobson, and M. Stefani. 2002. Inherent toxicity of aggregates implies a common mechanism for protein misfolding diseases. *Nature.* 416:507-511.

Chiu, S.W., E. Jakobsson, S. Subramaniam, and H. L. Scott. 1999. Combined monte carlo and molecular dynamics simulation of fully hydrated di-oleoyl and palmitoyl-oleoyl phosphatidylcholine lipid bilayers. *Biophys. J.* 77:2462-2469.

Colotto, A., I. Martin, J. M. Ruysschaert, A. Sen, S. W. Hui, and R. M. Epand. 1996. Structural study of the interaction between the SIV fusion peptide and model membranes. *Biochemistry.* 35:980-989.

Cullis, P. R., and B. de Kruijff. 1979. Lipid polymorphism and the functional roles of lipids in biological membranes. *Biochim. Biophys. Acta.* 559:399-420.

Darden, T., and L. Pedersen. 1996. Use of fast Ewald summation in molecular dynamics simulations. *Abstracts of Papers of the American Chemical Society.* 212:6-10.

Darkes, M. J., and J. P. Bradshaw. 2000. Real-time swelling-series method improves the accuracy of lamellar neutron-diffraction data. *Acta Crystallogr. D. Biol. Crystallogr.* 56(1):48-54.

Davies, S. M. A., M. J. M. Darkes, and J. P. Bradshaw. 1998. A neutron study of the feline leukemia virus fusion peptide: Implications for biological fusion. *Physica B.* 241-243:1148-1151.

Davies, S. M., T. A. Harroun, T. Hauss, S. M. Kelly, and J. P. Bradshaw. 2003. The membrane bound N-terminal domain of human adenosine diphosphate ribosylation factor-1 (ARF1). *FEBS Lett.* 548:119-124.

Dimitriadis, G., E. Crowne, A. Clark, and D. B. Dunger. 1998. Islet amyloid polypeptide decreases the effects of insulinlike growth factor-I on glucose transport and glycogen synthesis in skeletal muscle. *Int. J. Biochem. Cell Biol.* 30:1039-1046.

Duff, K. C., P. J. Gilchrist, A. M. Saxena, and J. P. Bradshaw. 1994. Neutron diffraction reveals the site of amantidine blockade in the influenza A M2 ion channel. *Virol.* 202:287-293.

Eisenberg, D., R. M. Weiss, and T. C. Terwilliger. 1982. The helical hydrophobic moment: a measure of the amphilicity of a helix. *Nature.* 299:371-374.

Ellens, H., D. P. Siegel, D. Alford, P. L. Yeagle, L. Boni, L. J. Lis, P. J. Quinn, and J. Bentz. 1989. Membrane fusion and inverted phases. *Biochemistry.* 28:3692-3703.

Epand, R. F., M. R. Infante, T. D. Flanagan, and R. M. Epand. 1998. Properties of lipoamino acids incorporated into membrane bilayers. *Biochim. Biophys. Acta.* 1373:67-75.

Epand, R. M. 2003. Fusion peptides and the mechanism of viral fusion. *Biochim. Biophys. Acta.* 1614(1):116-121.

Feller, S .E., D. Yin, R. W. Pastor, and A. D. MacKerell. 1997a. Molecular dynamics simulation of unsaturated lipid bilayers at low hydration: parameterization and comparison with diffraction studies. *Biophys. J.* 73:2269-2279.

Feller, S. E., R. M. Venable, and R. W. Pastor. 1997b. Computer simulation of a DPPC phospholipid bilayer: Structural changes as a function of molecular surface area. *Langmuir.* 13:6555-6561.

Ferrand, M., G. Zaccai, M. Nina, J. C. Smith, C. Etchebest, and B. Roux. 1993. Structure and dynamics of bacteriorhodopsin. Comparison of simulation and experiment. *FEBS Lett.* 327:256-260.

Forrest, L. R., A. Kukol, I. T. Arkin, D. P. Tieleman, and M. S. P. Sansom. 2000. Exploring models of the influenza A M2 channel: MD simulations in a phospholipid bilayer. *Biophys. J.* 78:55-69.

Franco, M., P. Chardin, M. Chabre, and S. Paris. 1993. Myristoylation is not required for GTP-dependent binding of ADP-ribosylation factor ARF1 to phospholipids. *J. Biol. Chem.* 268:24531-24534.

Franco, M., P. Chardin, M. Chabre, and S. Paris. 1995. Myristoylation of ADP-ribosylation factor 1 facilitates nucleotide exchange at physiological Mg^{2+} levels. *J. Biol. Chem.* 270:1337-1341.

Gennis, R. B. 1989. *Biomembranes: Molecular Structure and Function*. Springer-Verlag, New York.

Gibbs, C., and P. Jambeck. 2001. *Developing Bioinformatics Computer Skills*. O'Reilly & Associates, Inc. Sebastopol, CA 95472, U.S.A.

Gilchrist, P. J., and J. P. Bradshaw. 1993. Amyloid formation by salmon calcitonin. *Biochim. Biophys. Acta.* 1182:111-114.

Goldberg, J. 1999. Structural and functional analysis of the ARF1-ARFGAP complex reveals a role for coatomer in GTP hydrolysis. *Cell.* 96:893-902.

Gough, W., J. P. G. Richards, and R. P. Williams. 1996. *Vibrations and Waves*. Prentice Hall, London.

Gruner, S. M. 1985. Intrinsic curvature hypothesis for biomembrane lipid composition: A role for nonbilayer lipids. *Proc. Natl. Acad. Sci. USA.* 82:3665-3669.

Harroun, T. A., J. P. Bradshaw, and R. H. Ashley. 2001. Inhibitors can arrest the membrane activity of human islet amyloid polypeptide independently of amyloid formation. *FEBS Lett.* 507:200-204.

Harroun, T. A., K. Balali-Mood, I. Gourlay, and J. P. Bradshaw. 2003. The fusion peptide of simian immunodeficiency virus and the phase behaviour of N-methylated dioleoylphosphatidylethanolamine. *Biochim. Biophys. Acta.* 1617:62-68.

Heller, H., and Schaefer, M. 1993. Molecular Dynamics Simulation of a bilayer of 200 lipids in the gel and in the liquid -crystal phase. *J. Phys. Chem.* 97:8343-8360.

Helms, J. B., D. J. Palmer, and J. E. Rothman. 1993. Two distinct populations of ARF bound to Golgi membranes. *J. Cell Biol.* 121:751-760.

Higham, C. E., R. L. Hull, L. Lawrie, K. I. J. Shennan, J. F. Morris, N. P. Birch, K. Docherty, and A. Clark. 2000. Processing of synthetic pro-islet amyloid polypeptide (proIAPP) 'amylin' by recombinant prohormone convertase enzymes, PC2 and PC3, *in vitro*. *Eur. J. Biochem.* 267:4998-5004.

Hristova, K., and S. H. White. 1998. Determination of the hydrocarbon core structure of fluid dioleoylphosphocholine (DOPC) bilayers by x-ray diffraction using specific bromination of the double-bonds: effect of hydration. *Biophys. J.* 74:2419-2433.

Huang, Q., C. L. Chen, and A. Hermann. 2004. Bilayer conformation of fusion peptide of influenza virus haemagglutinin:a molecular dynamics simulation study. *Biophys. J.* 87(1): 14-22.

Huber, T., K. Rajamoorthi, V. F. Kurze, K. Beyer, and M. F. Brown. 2002. Structure of docosahexaenoic acid-containing phospholipid bilayers as studied by $^{(2)}$H NMR and molecular dynamics simulations. *J. Am. Chem. Soc.* 124:298-309.

Jacobs, R. E. and S. H. White. 1989. The nature of the hydophobic binding of small peptides at the bilayer interface: implications for the insertion of transbilayer helices. *Biochemistry.* 28:3421-3437.

Jaikaran, E. T. A. S., and A. Clark. 2001. Islet amyloid and type 2 diabetes: from molecular misfolding to islet pathophysiology. *Biochim. Biophys. Acta.* 1537:179-203.

Jaikaran, E. T. A. S., M. R. Nilsson, and A. Clark. 2004. Pancreatic beta-cell granule peptides form heteromolecular complexes which inhibit islet amyloid polypeptide fibril formation. *Biochem. J.* 377:709-716.

Kamath, S., and T. C .Wong. 2002. Membrane structure of the human immunodeficiency virus gp41 fusion domain by molecular dynamics simulation. *Biophys. J.* 83:135-143.

Kessel, A., B. Musafia, and N. Ben-Tal. 2001. Continuum solvent model studies of the interactions of an anticonvulsant drug with a lipid bilayer. *Biophys. J.* 80: 2536-2545.

King, G. I., and C. R. Worthington. 1971. Analytic continuations as a method of phase determination. *Phys. Lett.* 35:259-260.

King, G. I., R. E. Jacobs, and S. H. White. 1985. Hexane dissolved in dioleoyllecithin has a partial molar volume of approximately zero. *Biochemistry.* 24:4637-4645.

Koebnik, R. 1999. Membrane assembly of the *Escherichia coli* outer membrane protein OmpA: Exploring sequence constraints on transmembrane beta-strands. *J. Mol. Biol.* 285:1801-1810.

Koenig, B. W., J. A. Ferretti, and K. Gawrisch. 1999. Site-specific deuterium order parameters and membrane bound behaviour of a peptide fragment from the intracellular domain of HIV-1 gp41. *Biochemistry*. 38:6327-6334.

Law, R. J., D. P. Tieleman, and M. S. Sansom. 2003. Pores formed by the nicotinic receptor m2delta Peptide: a molecular dynamics simulation study. *Biophys. J.* 84:14-27.

Lear, J. D., and W. F. DeGrado. 1987. Membrane binding and conformational properties of peptides representing the NH_2 terminus of influenza HA-2. *J. Biol. Chem.* 262:6500-6505.

Li, S. C., and C. M. Deber. 1994. A measure of helical propensity for amino-acids in membrane environments. *Nat. Struct. Biol.* 1:368-373.

Lindahl, E., and O. Edholm. 2000. Mesoscopic undulations and thickness fluctuations in lipid bilayers from molecular dynamics simulations. *Biophys. J.* 79:426-433.

Lindahl, E., Hess, B., and van der Spoel D. 2001. GROMACS 3.0: A package for molecular simulations and trajectory analysis. *J. Mol. Model.* 7: 306-317.

Lindstrom, T., A. Leckstrom, P. Westermark, and H. J. Arnqvist. 1997. Effect of insulin treatment on circulating islet amyloid polypeptide in patients with NIDDM 490. *Diabetic Medicine.* 14:472-476.

Luzzati, V., and P. A. Spegt. 1967. Polymorphism of lipids. *Nature.* 215:701-704.

Luzzati, V., T. Gulik-Krzywicki, and A. Tardieu. 1968. Polymorphism of Lecithins. *Nature.* 218:1031-1034.

MacArthur, D. L. A., E. J. P. de Koning, J. S. Verbeek, J. E. Morris, and A. Clark. 1999. Amyloid fibril formation is progressive and correlates with beta-cell secretion in transgenic mouse isolated islets. *Diabetologia.* 42:1219-1227.

Makin, O. S., and L. C. Serpell. 2004. Structural characterisation of islet amyloid polypeptide fibrils. *J. Mol. Biol.* 335:1279-1288.

Marrink, S. J., E. Lindahl, O. Edholm, and A. E. Mark. 2001. Simulation of the spontaneous aggregation of phospholipids into bilayers. *J. Am. Chem. Soc.* 123:8638-8639.

Martin, I., F. Defrise-Quertain, V. Mandieau, N. M. Nielsen, T. Saermark, A. Burny, R. Brasseur, J. M. Ruysschaert, and M. Vandenbranden. 1991. Fusogenic activity of SIV (Simian Immunodeficiency Virus) peptides located in the gp32 NH_2 terminal domain. *B. B. R. C.* 175:872-879.

Mashl, R. J., H. L.Scott, S. Subramaniam, and E. Jakobsson. 2001. Molecular simulation of dioleoylphosphatidylcholine lipid bilayers at differing levels of hydration. *Biophys. J.* 81:3005-3015.

McIntosh, T. J., and S.A. Simon. 1986. Hydration force and bilayer deformation - a re-evaluation. *Biochemistry.* 25:4058-4066.

Menetrey, J., E. Macia, S. Pasqualato, M. Franco, and J. Cherfils. 2000. Structure of Arf6-GDP suggests a basis for guanine nucleotide exchange factors specificity. *Nature Structural Biol.* 7:466-469.

Mirzabekov,T.A., M.C.Lin, and B.L.Kagan. 1996. Pore formation by the cytotoxic islet amyloid peptide amylin. *J. Biol. Chem.* 271:1988-1992.

Moore, P.B., C. F. Lopez, and M. L. Klien. 2001. Dynamical properties of a hydrated lipid bilayer from a multi nanosecond molecular dynamics simulation. *Biophys. J.* 81:2484-2494.

Moriarty, D. F., and D. P. Raleigh. 1999. Effects of sequential proline substitutions on amyloid formation by human amylin (20-29). *Biochemistry.* 38:1811-1818.

Nagle, J. F., and S. Tristram-Nagle. 2000. Structure of lipid bilayers. *Biochim. Biophys. Acta.* 1469:159-195.

Nagle, J. F., R. Zhang, S. Tristram-Nagle, W. Sun, H. I. Petrache, and R. M. Suter. 1996. X-ray structure determination of fully hydrated L_α phase di-palmitoyl phosphatidylcholine bilayers. *Biophys. J.* 70:1419-1431.

Pandit, S. A., and M. L. Berkowitz. 2002. Molecular dynamics simulation of a di-palmitoyl phosphatidylserine bilayer with Na^+ counterions. *Biophys. J.* 82:1818-1827.

Peisajovich, S. G., L. Blank, R. F. Epand, R. M. Epand, and Y. Shai. 2003. On the interaction between gp41 and membranes: the immunodominant loop stabilizes gp41 helical hairpin conformation. *J. Mol. Biol.* 326:1489-1501.

Petrache, H. I., S. Tristram-Nagle, and J. F. Nagle. 1998. Fluid phase structure of EPC and DMPC bilayers. *Chem.Phys. Lipids.* 95:83-94.

Ramachandran, G.N. 1968. Need for nonplanar peptide units in polypeptide chains. *Biopolymers.* 10:1494-1496.

Rand, R. P., and V. A. Parsegian. 1989. Hydration forces between phospholipid-bilayers. *Biochim. Biophys. Acta.* 988:351-376.

Randa, H. S., L. R. Forrest, G. A. Voth, and M. S. P., Sansom. 2001. Molecular dynamics of synthetic leucine-serine ion channels in a phospholipid membrane. *Biophys. J.* 77:2400-2410.

Randazzo, P. A., Z. Nie, K. Miura, and V. W. Hsu. 2000. Molecular aspects of the cellular activities of ADP-ribosylation factors. *Sci STKE.* 2000:59-64.

Rapaport, D.C. 2001. *The art of molecular dynamic simulation.* Cambridge University Press, Cambridge, U.K.

Rodrigues, C., P. Gameiro, M. Prieto, and B. de Castro. 2003. Interaction of rifampicin and isoniazid with large unilamellar liposomes: spectroscopic location studies. *Biochim. Biophys. Acta.* 1620:151-159.

Rodrigues, C., P. Gameiro, S. Reis, J. L. F. C. Lima, and B. de Castro. 2001. Spectrophotometric determination of drug partition coefficients in dimyristoyl-L-alpha-phosphatidylcholine/water: a comparative study using phase separation and liposome suspensions. *Anal. Chim. Acta.* 428:103-109.

Roth, M. G. 1999. Lipid regulators of membrane traffic through the Golgi complex. *Trends Cell Biol.* 9:174-179.

Ryckaert, J. P. and A. Bellemans. 1978. Molecular dynamics of liquid alkanes. *Faraday Discuss.* 66:95-106.

Sansom, M. S., D. P. Tieleman, L. R. Forrest, and H. J. Berendsen. 1998. Molecular dynamics simulations of membranes with embedded proteins and peptides: porin, alamethicin and influenza virus M2. *Biochem. Soc. Trans.* 26:438-443.

Sansom, M. S., P. Bond, O. Beckstein, P. C. Biggin, J. Faraldo-Gomez, R. J. Law, G. Patargias, and D. P. Tieleman. 2002. Water in ion channels and pores-simulation studies. *Novartis. Found. Symp.* 245:66-78.

Scott, H. L. 2002. Modeling the lipid component of membranes. *Curr. Opin. Struct. Biol.* 12:495-502.

Segrest, J.P., R.L. Jackson, J.D. Morrisett, and A.M. Gotto. 1974. A molecular theory of lipid-protein interactions in the plasma lipoproteins. *FEBS Lett.* 38(3):247-258.

Shacklett, B. L., C. J. Weber, K. E. Shaw, E. M. Keddie, M. B. Gardner, P. Sonigo, and P. A. Luciw. 2000. The intracytoplasmic domain of the Env transmembrane protein is a locus for attenuation of simian immunodeficiency virus SIVmac in rhesus macaques. *J. Virol.* 74:5836-5844.

Shai, Y. 2002. Mode of action of membrane active antimicrobial peptides. *Biopolymers.* 66(4):236-248.

Siegel, D. P., J. L. Banschbach, D. Alford, H. Ellens, L. J. Lis, P. J. Quinn, P. L. Yeagle, and J. Bentz. 1989. Physiological levels of diacylglycerols in phospholipid membranes induce membrane fusion and stabilize inverted phases. *Biochemistry.* 28:3703-3709.

Singer, S. J., and G. L. Nicolson. 1972. The fluid mosaic model of the structure of cell membranes. *Science.* 175:720-731.

Soeller, W. C., J. Janson, S. E. Hart, J. C. Parker, M. D. Carty, R. W. Stevenson, D. K. Kreutter, and P. C. Butler. 1998. Islet amyloid-associated diabetes in obese A(vy)/a mice expressing human islet amyloid polypeptide. *Diabetes*. 47:743-750.

Spang, A. 2002. ARF1 regulatory factors and COPI vesicle formation. *Cur. Opin. Cell. Bio.* 14:423-427.

Spruce, A. E., A. Iwata, and W. Almers. 1991. The first milliseconds of the pore formed by a fusogenic viral envelope protein during membrane fusion. *Proc. Natl. Acad. Sci. USA.* 88:3623-3627.

Stipani, V., E. Gallucci, S. Micelli, V. Picciarelli, and R. Benz. 2001. Channel formation by salmon and human calcitonin in black lipid membranes. *Biophys. J.* 81:3332-3338.

Tabata, H., J. Hirayama, R. Sowa, H. Furuta, T. Negoro, T. Sanke, and K. Nanjo. 1992. Islet amyloid polypeptide (IAPP amylin) causes insulin resistance in perfused rat hindlimb muscle. *Diabetes Res. Clin. Prac.* 15:57-62.

Tieleman, D. P., H. J. C., Berendsen, and M. S. P. Sansom. 1999. Surface binding of alamethicin stabilizes its helical structure: molecular dynamics simulations. *Biophys. J.* 76, 3186-3191.

Tieleman, D. P., J. Breed, H. J. Berendsen, and M. S. Sansom. 1998. Alamethicin channels in a membrane: molecular dynamics simulations. *Faraday Discuss.* 111:209-223.

Tieleman, D. P., L. R. Forrest, M. S. P. Sansom, and H. J. C. Berendsen. 1998. Lipid properties and the orientation of aromatic residues in OmpF, influenza M2 and alamethicin systems: molecular dynamics simulations. *Biochemistry*. 37:17554-17561.

Tieleman, D. P., M. S. Sansom, and H. J. Berendsen. 1999. Alamethicin helices in a bilayer and in solution: molecular dynamics simulations. *Biophys. J.* 76:40-49.

Tieleman, D. P., S. J. Marrink, and H. J. Berendsen. 1997. A computer perspective of membranes: molecular dynamics studies of lipid bilayer systems. *Biochim. Biophys. Acta.* 1331:235-270.

Tristram-Nagle, S., H. I. Petrache, and J. F. Nagle. 1998. Structure and interactions of fully hydrated dioleoylphosphatidylcholine bilayers. *Biophys. J.* 75:917-925.

Vaccaro, L., K. Cross, J. Kleinjung, S., Strauss, D., Thomas, and F., Fraternali. 2004. Plasticity of Influenza haemagglutinin fusion peptides and the interaction with lipid bilayers. *Biophys. J.* In press.

Vereb, G., J. Szollosi, J. Matko, P. Nagy, T. Farkas, L. Vigh, L. Matyus, T. A. Waldmann, and S. Damjanovich. 2003. Dynamic, yet structured: The cell membrane three decades after the Singer-Nicolson model. *Proc. Natl. Acad. Sci. USA.* 100:8053-8058.

Walsh, D. T., R. M. Montero, L. G. Bresciani, A. Y. T. Jen, P. D. Leclercq, D. Saunders, A. N. El Amir, L. Gbadamoshi, S. M. Gentleman, and L. S. Jen. 2002. Amyloid-beta peptide is toxic to neurons in vivo via indirect mechanisms. *Neurobiol. Dis.* 10:20-27.

Warren, R. C. 1987. *Physics and the architecture of Cell Membranes*. Adam Hilger, Bristol.

Westermark, P., U. Engstrom, K. H. Johnson, G. T. Westermark, and C. Betsholtz. 1990. Islet amyloid polypeptide - pinpointing amino-acid-residues linked to amyloid fibril formation. *Proc. Natl. Acad. Sci. USA*. 87:5036-5040.

White, J. M. 1990. Viral and cellular membrane fusion peptides. *Annu. Rev. Physiol.* 52:675-697.

Wiener, M. C., and S. H. White. 1991. Fluid bilayer structure determination by the combined use of x-ray and neutron diffaction. II. "Composition-space" refinement method. *Biophys. J.* 59:174-185.

Wiener, M. C., and S. H. White. 1992a. Structure of a fluid dioleoylphosphatidylcholine bilayer determined by joint refinement of x-ray and neutron diffraction data: III. Complete structure. *Biophys. J.* 61:434-447.

Wiener, M. C., and S. H. White. 1992b. Structure of a fluid dioleoylphosphatidylcholine bilayer determined by joint refinement of x-ray and

neutron diffraction data: II. Distribution and packing of terminal methyl groups. *Biophys. J.* 61:428-433.

Wiener, M. C., G. I. King, and S. H. White. 1991. Structure of a fluid dioleoylphosphatidylcholine bilayer determined by joint refinement of x-ray and neutron diffraction data. I. Scaling of neutron data and the distribution of double bonds and water. *Biophys. J.* 60:568-576.

Wigley, W. C., M. J. Corboy, T. D. Cutler, P. H. Thibodeau, J. Oldan, M. G. Lee, J. Rizo, J. F. Hunt, and P. J. Thomas. 2002. A protein sequence that can encode native structure by disfavoring alternate conformations. *Nat. Struc. Biol.* 9:381-388.

Wimley, W. C. and S. H. White. 1996. Experimentally determined hydrophobicity scale for proteins at membrane interfaces. *Nat. Struc. Biol.* 3:842-848.

Yeagle, P. 1993. *The membranes of cells*. Academic Press, San Diego.

Zanuy, D., B. Y. Ma, and R. Nussinov. 2003. Short peptide amyloid organization: Stabilities and conformations of the islet amyloid peptide NFGAIL. *Biophys. J.* 84:1884-1894.

Zasloff, M. 2002. Antimicrobial peptides of multicellular organisms. *Nature.* 415 (6870):389-395.

Appendix: Publications arising from research conducted during the course of this Ph.D.

Eur. Phys. J. E **12**, s01 (2003) 031
Digital Object Identifier (DOI) 10.1140/epjed/e2003-01-031-3

EPJ E direct
electronic only

Molecular dynamics simulations of a mixed DOPC/DOPG bilayer

K. Balali-Mood[1,a], T.A. Harroun[2,b], and J.P. Bradshaw[3,c]

[1] Preclinical Veterinary Sciences, R(D)SVS, College of Medicine and Veterinary Medicine, University of Edinburgh, Summerhall, Edinburgh EH9 1QH, UK
[2] National Research Council, Neutron Program for Materials Research, Chalk River Laboratories, Chalk River, Ontario K0J 1J0, Canada
[3] Preclinical Veterinary Sciences, R(D)SVS, College of Medicine & Veterinary Medicine, University of Edinburgh, Summerhall, Edinburgh EH9 1QH, UK

Received January, 2003
Published online November 5, 2003

Abstract. We have constructed a mixed dioleoylphosphatidylcholine (DOPC) and dioleoylphosphatidylglycerol bilayer (DOPG) bilayer utilizing MD simulations. The aim was to develop an explicit molecular model of biological membranes as a complementary technique to neutron diffraction studies that are well established within the group. A monolayer was constructed by taking a previously customised PDB file of each molecule and arranging them in a seven rows of ten molecules and duplicated and rotated to form a bilayer. The 140-molecule bilayer contained 98 DOPC molecules and 42 DOPG molecules, in a 7:3 ratio in favour of DOPC. Sodium counter ions were placed near the phosphate moiety of DOPG to counteract the negative charge of DOPG. This was representative of the lipid ratio in a sample used for neutron diffraction. The MD package *GROMACS* was used for confining the bilayer in a triclinic box, adding Simple Polar Charge water molecules, energy minimization (EM). The bilayer/solvent system was subjected to EM using the steepest descent method to nullify bad contacts and reduce the potential energy of the system. Subsequent MD simulation using an initial NVT (constant number of particles, volume and temperature) for a 20 ps MD run followed by a NPT (constant number of particles, pressure and temperature) was performed. Structural parameters including volume of lipid, area of lipid, order parameter of the fatty acyl carbons and electron density profiles generated by the MD simulation were verified with values obtained from experimental data of DOPC, as there are no comparable experimental data available for the mixed bilayer.

PACS. 31.15.Qg Molecular dynamics and other numerical methods – 81.16.Fg Supramolecular and biochemical assembly – 83.85.Hf X-ray and neutron scattering – 87.16.Dg Membranes, bilayers, and vesicles

1 Introduction

Computer models of biological model membranes provide insight into molecular mechanisms of membrane protein function. Computational models of biological molecules may use Monte Carlo or Molecular Dynamics (MD) methods. MD simulations are more involved than Monte Carlo ones and are classified under deterministic simulations. They use complex algorithms that allow for simulating a non-equilibrated, dynamic systems confined within a simulation box. Molecular structures are usually represented as a collection of atoms, each of which has a defined position in three-dimensional space (Cartesian co-ordinates in x, y & z format).

The parameters in a force field are generally equilibrium geometry values (lengths and angles) and force constants that describe harmonic oscillators. These parameters are obtained from analysis of large amounts of experimental data, or from quantum chemistry calculations on molecular fragments. In an MD simulation, atoms move according to the forces acting on them. Initially random velocities are assigned to displace the system from its equilibrium configuration.

MD simulations are rapidly becoming popular tools that complement experimental techniques in structural biophysics, such as neutron diffraction and NMR. There are a number of computational models of bilayers available in the literature. These studies have focused on single species bilayers in particular dipalmitoylphosphatidylcholine (DPPC), dimyristoylphosphatidylcholine (DMPC) and dioleoylphosphatidylcholine (DOPC) [1,2,3,4,5,6]. There have been previous reports of a mixed bilayer. A bilayer of 1-Palmitoyl-2-docosahexaenoyl-sn-glycero-3-phosphocholine (PDPC) and 1-palmitoyl-2-oleoyl-sn-glycero-3-phosphocholine (POPC), was studied in the

[a] e-mail: Kia.Balali-Mood@ed.ac.uk
[b] e-mail: thad.harroun@nrc.gc.ca
[c] e-mail: j.bradshaw@ed.ac.uk

liquid-crystalline (L(α)) state. These studies utilised MD simulation and NMR experiments to solve the structure of the mixed PDPC/POPC bilayers that are present in neural tissues [7]. However, to the best of our knowledge this is the first report of a mixed dioleoylphosphatidylcholine (DOPC) and dioleoylphosphatidylglycerol bilayer (DOPG) bilayer. Our aim was to develop an explicit atomic level computational model of a biological membrane utilising Molecular Dynamics Simulations. The model will be used to complement structural studies carried out by our group, allowing both the visualisation of neutron and X-ray diffraction results and the mutual verification of data produced by all these techniques. The structural parameters (volume of lipid, area of lipid, order parameters and electron density map) generated by the MD simulation were verified with the parameters obtained from neutron diffraction, NMR studies & combined X-ray and neutron studies respectively.

A recurring theme underlying our work on molecular interactions within biological membranes is confinement. The peptides that we study partition into the steep hydrophobic gradient at the bilayer surface, confining both their location and their secondary structure. It is of great interest to determine how this confinement influences their dynamics. Secondly, the stacked bilayer samples of the type used in our neutron and X-ray experiments are characterised by narrow water layers separating adjacent bilayers. The consequences of this confinement on the dynamics of the water and its knock-on effects on the phospholipids has long been a matter for discussion [8]. Part of the rationale behind replicating our neutron samples in MD simulations is to investigate this confinement. The next step in our MD work will be to look at the effects of the confinement on the peptides introduced into the water layers of our systems.

2 Method

2.1 System generation

A mixed DOPC/DOPG bilayer was constructed with explicit hydrogens in the phospholipid headgroups (see Fig. 1). The complete topologies of the molecules were described in the form of bonds, angles and dihedrals (torsion angles). Atomic point charges for both PC and PG headgroups were generated by *HyperChem 5.0* (Hypercube Inc., Waterloo, Canada) using the STO-3G set as used in previous studies of DMPC and DPPC [2,4]. The bilayer was constructed by taking a previously customized PDB file of each molecule and arranging them, using *Sybyl 6.7* (Tripos Inc. St Louis MO), in a row of ten molecules with a ratio of 7 DOPC to 3 DOPG. Seven rows of ten lipid molecules were generated and the DOPG molecules were arranged in such a way that they were not in close contact with each other. This arrangement is representative of a biological environment whereby the zwitterionic PC headgroups will be interspersed with the anionic PG headgroup. The monolayer of 70 lipid molecules was then copied and rotated in order to create a bilayer of 140 lipid

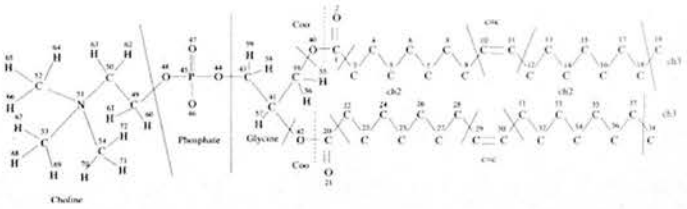

Fig. 1. Illustrates the two dimensional chemical structure of a DOPC molecule with explicit hydrogens. The headgroup contains explicit hydrogens. The explicit hydrogens are present primarily for future simulations with peptides that have been previously studied via neutron diffraction by other group members. The dashed lines indicate the borders between the headgroup and hydrocarbon chains. The solid lines divide up the molecule in precisely the same manner as in the experimental studies of Wiener and white [17,18]. The headgroup region compromises choline, phosphate and glycine groups. One group is shared between the glycine and chain regions (Coo); the leftmost oxygen atom is part of the headgroup, while the oxygen and the carbon are part of the chain region. The other specific groupings in the chain region are ch2, ch3 and c=c respectively.

molecules, comprising 98 DOPC and 42 DOPG molecules, and 42 sodium counter ions.

The molecular dynamics computer package *GROMACS* [9] version 3.1.4 was used to centre the bilayer in a triclinic box, and a total of 2815 SPC (Simple Point Charge [10]) water molecules were added to either side of the bilayer. The ratio of water molecules per lipid (20.1:1) was chosen to replicate the conditions used in neutron diffraction experiments, using the same ratio of DOPC:DOPG and those quoted in the literature [11]. There is another type of water molecule used in MD simulations of biological systems, which is derived from the original SPC. Simple Point Charge extended (SPC/e) possesses a lower free energy (–26.7 kJ.mol^{-1}). SPC was selected, primarily due to the fact the free energy of SPC (-24.3 kJ.mol^{-1}) is closer to the actual experimental value. Energy minimization (EM) by the "steepest descent" method was used to remove bad contacts and reduce the potential energy of the system. The system was then subjected to a 20 ps MD simulation utilising the NVT (18315 atoms/particles, volume of 800 nm^3 & temperature of 300 K) ensemble. Tieleman and co-workers have proposed running a hydrated bilayer system with an initial NVT system before proceeding to another ensemble [11]. The rationale behind such a protocol is to allow the SPC molecules to equilibrate naturally within the system, without the SPC molecules being pressurised into the bilayer. The system was then subjected to another MD simulation using the NPT (18315 atoms/particles, pressure of 1 bar & temperature of 300 K) ensemble over a 3500 ps period. Temperature and pressure were coupled individually to the three groupings in both DOPC (DPC=headgroup, OLA=sn-1 chain, OLB=sn-2 chain) and DOPG (DPG=headgroup, OLC=sn-1 chain, OLD=sn-2 chain) molecules and SPC using the Berendsen algorithm implemented in *GROMACS*. Order parameters were measured after 400 ps of an NPT ensemble MD run.

2.1.1 Forcefield

GROMACS software is primarily designed for MD simulation of biologically active/relevant proteins, although is commonly used for lipids bilayers as well. The forcefield used in the MD simulations presented here was a modified explicit hydrogen forcefield included in *GROMACS* (ffgmx2_lipid) [9]. DOPC and DOPG were divided into headgroup and chain regions. Nineteen unique subgroups were identified in the headgroup and chains respectively. These groups were then cross-referenced with the matching unique structure present within the twenty basic amino acids so that the bond lengths, energies, bond angles, forces and torsion angles (dihedrals) can be approximated from the original *GROMACS* explicit hydrogen forcefield (ffgmx2).

The majority of MD simulations reported in the literature have utilised implicit hydrogens, primarily to save on computational time. There have been reports of explicit hydrogens in DMPC and DMPS phospholipid simulations. The main reason why we use explicit hydrogens is to investigate hydrogen bonding between a peptide and the bilayers we have generated by MD simulation.

2.2 Run parameters

2.2.1 Periodic boundary conditions

A system that is bounded but free of physical walls can be constructed by resorting to periodic boundary conditions (PBC). Introducing PBC is equivalent to considering an infinite space-filling array of identical arrays of the simulation region. There are two consequences of this periodicity. Firstly, an atom leaves the simulation region through a particular bounding face immediately re-enters the region through the opposite face. The second consequence is that atoms lying within a distance of a boundary interact with atoms in an adjacent copy of the system. PBC is frequently used in bilayer MD simulations. PBC has been a standard run parameter in MD simulations involving biological systems and in particular bilayers [1,2]. In addition, PBC also creates a stack of bilayers in the lamellar phase, which is representative of the multibilayer stacks used in neutron and X-ray diffraction measurements.

2.2.2 Cut-off and treatment of electrostatics

Most MD simulations use either simple spherical cut-offs whereby an electrostatic interaction is cut off beyond the van der Waals radius (in our case 1.8 nm). The alternative is to use the Particle Mesh Ewald (PME) algorithm developed by Tom Darden [12,13] to improve the performance of the reciprocal sum. PME solves the Poisson equation over all of the simulation space. The Poisson equation determines the electric field at each point in space from all the charges nearby. So, instead of calculating each pairwise electrostatic interaction (time consuming), we can quickly (by way of the Fourier transform) just figure the electric field near each atom (which is the total influence of all the pair-wise interactions), to get the force due to electrostatics.

For the simulation of fluid phases of phospholipids, in which molecules are by definition more disordered and liquid-like than in the gel phase, the situation is less clear. The use of Ewald summations in zwitterionic systems in disordered phases can potentially induce unwanted periodicities, leading to errors no less significant than those which result when the interaction is simply 'switched off' for interatomic distances beyond some spherical cutoff. For smaller simulation boxes such is in the current setup, the effect will be more severe [15]. The electrostatic interactions within the spherical cut-off were summed directly and the remaining part of the system was treated using an analytical solution of Poisson's equation.

It has been reported that Spherical cutoffs can introduce artefacts in solutions with ions but if the cutoff radius is large enough (>1.8 nm), this method appears to work well for lipids [11]. Hence, the selection of spherical cutoffs as opposed to PME for the treatment of electrostatic interactions.

2.2.3 Temperature & pressure coupling & time step

GROMACS allows for temperature and pressure coupling using the Berendsen temperature and pressure coupling algorithm. In the case of temperature coupling, all molecules (DOPC, DOPG and SPC) were coupled individually to a bath with a temperature of 300 K. A time constant of 5 ps was set for each group. For both the NPT and subsequent NPAT Pressure was set at 1 bar. The pressure asserted on the box was of an isotropic nature. A time constant for pressure coupling was also set at 5 ps. In the NPT ensemble the pressure coupling was isotropic. Coupling groups on an individual basis allows for greater stability during an MD run.

The time step for all parts of the MD and EM simulations were 2 fs. This time step was used in a number of previous bilayer simulations [2,4].

2.3 Verification of method

The simulation was verified by comparing **four** parameters obtained from the MD simulation with the experimental values. They were as follows.

2.3.1 Area per lipid molecule

The area occupied by each lipid molecule was obtained by multiplying the X and Y dimensions of the box and dividing by the number of lipid molecules present in each leaflet (70 in this instance) [4]. The area per lipid can be measured experimentally by Langmuir techniques

$$\text{Area per lipid} = X.Y/70. \quad (1)$$

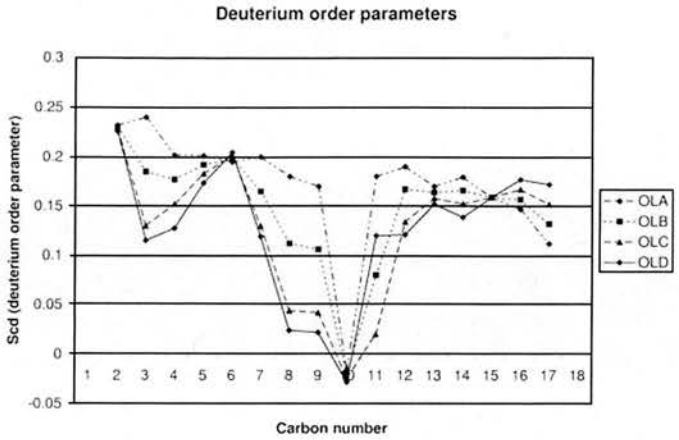

Fig. 2. A plot of the deuterium order parameters for the fatty acyl carbons of DOPC and DOPG in a mixed bilayer, obtained from a 400 ps MD simulation. OLA and OLB correspond to $sn1$ and $sn2$ chains in the DOPC molecule respectively. OLC and OLD correspond to $sn1$ and $sn2$ chains in the DOPG molecule respectively.

2.3.2 Volume per lipid molecule

The volume of each lipid molecule within a bilayer system can be determined using diffraction techniques. It provides another independent parameter by which a computer simulated structure may be compared to experimental observations. The method employed for calculating the volume of lipid [16], is given by the following simple equation:

$$V_L = AD/2 - (N_w V_w) \tag{2}$$

A = area per lipid, D = height of the simulation box (Z dimension), N_w = number of waters per lipid molecule, V_w = volume per water.

2.3.3 Order parameters

The ordering of hydrocarbon tails has been studied by NMR spectroscopists, who use the term "order parameter" to describe the average orientation of each section of an acyl chain. The order parameter is derived from the quadrupole splitting of NMR spectra and is determined by selective deuteration of successive carbons of the acyl chains.

The order parameter tensor S, which is defined as:

$$S_{ij} = \frac{\langle 3\cos(\theta_i)\cos(\theta_j) - \delta a_{ij}\rangle}{2} \tag{3}$$

$i, j = (x, y, z)$.

Order parameters are calculated for each atom of the hydrocarbon chain, other than the terminal methyl group and the first carbon in the chain [17]. These order parameters can be calculated by *GROMACS*, using the *g_order* command. However, the resulting index file must be modified to include 3 consecutive carbon atoms. The order parameter will then be calculated for the middle carbon.

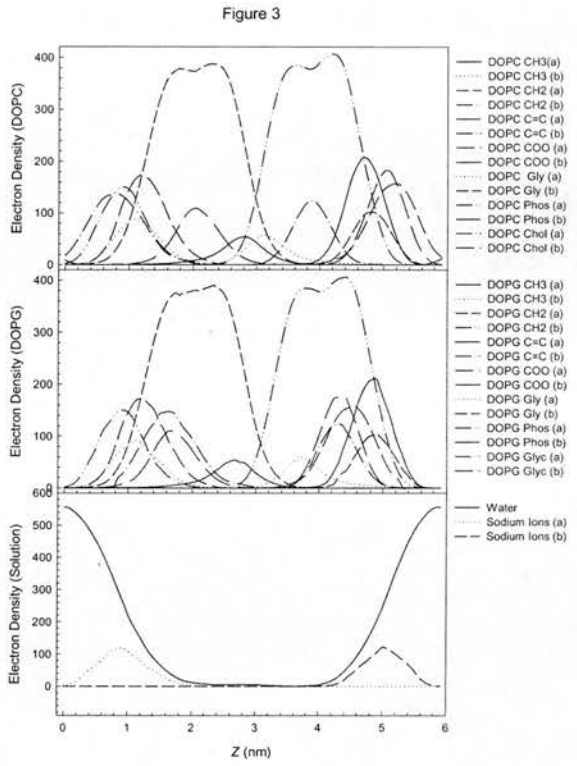

Fig. 3. Electron density distributions of the structural groups of DOPC and DOPG in a mixed bilayer. The groupings are based on those of Weiner and White [5]; the calculated electron densities compare favourably with the experimental values. For breakdown of the comparison, see Table 2.

It is necessary to define the previous carbon atom (i) and the subsequent carbon atom (j) in order for *GROMACS* to calculate the order parameter.

2.3.4 Electron density map

The electron density map of a protein may be obtained by X-ray crystallography. If a crystal structure is not available, other methods may be used. Weiner and White [18,19,20,21,22,23] have produced a comprehensive electron density map of a DOPC bilayer by the combined use of X-ray and neutron diffraction. Their approach divided the DOPC molecule into eight individual groups, the ninth group being the water layer. Six of these Gaussian distributions are readily comparable to our MD results. We have, therefore, used the electron density distributions for these groups as a comparator for the DOPC groups within our MD simulated DOPC/DOPG bilayer. Since the fatty acid tails of the PG molecules are also oleoyl chains, the electron density distributions of this part of the bilayer are not expected to differ greatly from the Weiner and White results. Some neutron diffraction data

Table 1. Comparison of calculated and experimental values for area and volume of lipid. The columns contain values obtained from our MD simulations of DOPC bilayers (1st column), values obtained from our MD simulations of DOPC/DOPG bilayers, experimental values obtained for DOPC obtained by Nagle and Wiener [26] and calculated values for DOPC bilayers from Chiu [3].

	Values from DOPC (4 separate sets of EM + MD runs)	Values from DOPC/DOPG (One set of EM + MD runs)	Values from DOPC MD simulation [3]	Experimental values [25]
Area per lipid (Å^2)	69.9 ± 1.1	73.1	71.0 ± 1	72.2
Vol. per lipid (Å^3)	1294 ± 8.4	1309	1288 ± 10	1303

on mixed DOPC/DOPC bilayers is available from previous studies [24,25].

3 Results

3.1 Volume/area of lipid

Chiu and co-workers have performed a combined Monte Carlo and Molecular dynamics study on an explicit 128-molecule DOPC bilayer. Prior to running the mixed DOPC/DOPG bilayer MD run, a 128-molecule DOPC bilayer was constructed, in a similar manner to the mixed bilayer. It was then subjected to a combined EM (Steepest Descent method) and an NPT MD run. The values obtained compare favourably with those obtained by Chiu *et al.* Langmuir trough and Neutron diffraction techniques were used to obtain the area and volume of DOPC respectively. These studies were performed by Nagle and co-workers [26].

3.2 Order parameters

Figure 2 is a plot of the deuterium order parameters obtained from a 400 ps MD simulation using the NPT ensemble. OLA and OLB correspond to *sn*1 and *sn*2 chains in the DOPC molecule respectively. OLC and OLD correspond to *sn*1 and *sn*2 chains in the DOPG molecule respectively.

3.3 Electron density map

Figure 3 shows the calculated electron density distributions of the structural groups of DOPC and DOPG in a mixed bilayer. The calculated electron density profiles compare favourably with the experimental values of Weiner and White [18], whose structural groupings have been used as a basis for the ones shown in the figure. The electron density map was obtained over a 3.5 ns equilibration run

4 Discussion

A number of MD simulations have been performed on explicit phospholipid bilayers. These studies have tended to use the NPT protocol, with its constant Number of particles, Pressure and Temperature. Tieleman [27] and Lindahl [9], who studied DPPC and DMPC respectively, had modified their system to include a constant area per molecule (NPAT). Tieleman [28] then went on to develop constant surface tension by using the Berendsen semi-isotropic pressure-coupling algorithm [29], in which the surface tension in the x and y directions are equal. Our system was initially run for 20 ps as an NVT ensemble. The type of water molecule used was Simple Point Charge (SPC), for the reasons explained in the methods section. SPC has been used by a number of previous simulations [27,30]. The system was then run as an NPT ensemble for 3480 ps. The pressure asserted on the box allowed the box vectors to adjust in all three dimensions, such that the final area and volume of lipid was effectively constant after 2500 ps. The temperature used in most lipid simulations is in the range of 300–330 K. The temperature selected for the simulation was 300 K, this being the temperature in which the neutron diffraction studies on a mixed DOPC/DOPG were performed.

The potential energies of our DOPC system (comprising of 128 lipid molecules) were $-8.5 \times 10^5 \pm 2.0 \times 10^4$ kJ mol^{-1}.Our method involved the use of EM and MD simulations, both of which were performed with *GROMACS*. However, the use of a stochastic simulation, such as a Monte Carlo simulation may have been more effective in reducing the potential energy of our mixed bilayer system. Once equilibrated, the potential energy of our mixed DOPC/DOPG system was $-9.4\times10^6\pm1.0\times10^4$ kJ mol^{-1}. The combined equilibration and simulation times for our bilayers were approximately 3.5 ns, which corresponded to 29.5 processor days on our dual Athlon processor PC.

To conclude, our approach was verified by comparing a DOPC simulation with four experimental parameters. Our results demonstrate that we have obtained parameters that are within 5% of experimentally determined values of area & volume of lipid, respectively (Tab. 1). The electron density map demonstrates a realistic electron distribution throughout the bilayer and closely follows the experimental results of Wiener and White (Tab. 2). The same approach was then used to model a mixed bilayer system for which there are no comparable experimental data. To the best of our knowledge, no experimental studies have been performed to obtain the electron density map of DOPG. However, it is realistic to compare six of the groupings from the experimental obtained from

Table 2. A comparison of the electron densities of the molecular components of DOPC in a mixed DOPC/DOPG bilayer MD simulation with experimentally determined values for DOPC [17]. Gaussian distributions were fitted to the electron density profiles describing the distribution of the electrons of the different groups throughout a 3.5 ns MD simulation. The position (defined as the distance from the centre of the bilayer) and the half width (defined as half peak width at half maximum height) are shown for all molecular groups whose electron distributions approximate to a Gaussian distribution.

	CH3	C=C	COO	Gly	PO_4	Chol
From reference [22]						
Position	0.0 nm	0.8 nm	1.6 nm	1.9 nm	2.0 nm	2.2 nm
Half Width	0.3 nm	0.4 nm	0.3 nm	0.2 nm	0.3 nm	0.3 nm
From this study						
Position	0.2 nm	0.9 nm	1.8 nm	1.9 nm	2.0 nm	2.2 nm
Half Width	0.4 nm	0.4 nm	0.4 nm	0.4 nm	0.4 nm	0.5 nm

Wiener and White's work (Tab. 2). Planned future computational studies will include an explicit MD simulation of peptide bilayer interactions, complementing previous neutron and X-ray diffraction studies by other members of the laboratory.

References

1. K. Aman, E. Lindahl, O. Edholm, P. Hakansson, P.O. Westlund, Biophys. J. **84**, 102 (2003)
2. O. Berger, O. Edholm, F. Jahnig, Biophys. J. **72**, 2002 (1997)
3. S.W. Chiu, E. Jakobsson, S. Subramaniam, H.L. Scott, Biophys. J. **77**, 2462 (1999)
4. S.E. Feller, D. Yin, R.W. Pastor, A.D. MacKerell Jr., Biophys. J. **73**, 2269 (1997)
5. H. Heller, M. Schaefer, J. Phys. Chem. **97**, 8343 (1993)
6. E. Lindahl, O. Edholm, Biophys. J. **79**, 426 (2000)
7. T. Huber, K. Rajamoorthi, V.F. Kurze, K. Beyer, M.F. Brown, J. Am. Chem. Soc. **124**, 298 (2002)
8. G. Pabst, J. Katsaras, V.A. Raghunathan, M. Rappolt, Langmuir **19**, 1716 (2003)
9. E. Lindahl, B. Hess, D. van der Spoel, J. Mol. Modell. **7**, 306 (2001)
10. H.J.C. Berendsen, J.P.M. Postma, *Intermolecular Forces* (Reidel, Dordrecht, The Netherlands, 1981)
11. D.P. Tieleman, S.J. Marrink, H.J. Berendsen, Biochim. Biophys. Acta **1331**, 235 (1997)
12. M.S. Sansom, D.P. Tieleman, L.R. Forrest, H.J. Berendsen, Biochem. Soc. Trans. **26**, 438 (1998)
13. T. Darden, D. York, L.J. Pedersen, J. Chem. Phys. **98**, 10089 (1993)
14. U. Essmann, L. Perera, M.L. Berkowitz, T. Darden, H. Lee, L.G. Pedersen, J. Chem. Phys. **103**, 8577 (1995)
15. H.L. Scott, Curr. Opin. Struct. Biol. **12**, 495 (2002)
16. S.W. Chiu, E. Jakobsson, S. Subramaniam, Biophys. J. **76**, 1929 (1999)
17. S. Bernèche, M. Nina, B. Roux, Biophys. J. **75**, 1603 (1998)
18. M.C. Weiner, S.H. White, Biophys. J. **59**, 162 (1991)
19. M.C. Weiner, G.I. King, S.H. White, Biophys. J. **62**, 2762 (1991)
20. K. Hristova, S.H. White, Biophys. J. **74**, 2419 (1998)
21. G.I. King, S.H. White, Biophys. J. **49**, 1047 (1986)
22. M.C. Wiener, G.I. King, S.H. White, Biophys. J. **60**, 568 (1991)
23. M.C. Wiener, S.H. White, Biophys. J. **61**, 434 (1992)
24. J.P. Bradshaw, Biophys. J. **72**, 2180 (1997)
25. J.P. Bradshaw, S.M.A. Davies, T. Hauß, Biophys. J. **75**, 889 (1998)
26. J.F. Nagle, M.C. Weiner, BBA **942**, 1 (1988)
27. D.P. Tieleman, H.J.C. Berendsen, M.S.P. Sansom, Biophys. J. **76**, 3186 (1999)
28. D.P. Tieleman, L.R. Forrest, M.S. Sansom, H.J. Berendsen, Biochemistry **37**, 17554 (1998)
29. H.J.C. Berendsen, D. van der Spoel, R. van Drunen, Comput. Phys. Commun. **91**, 43 (1995)
30. D.P. Tielman, Biophys. J. **76**, 40 (2002)

Available online at www.sciencedirect.com
SCIENCE DIRECT®
Biochimica et Biophysica Acta 1617 (2003) 62–68
BIOCHIMICA ET BIOPHYSICA ACTA
BBA
www.bba-direct.com

The fusion peptide of simian immunodeficiency virus and the phase behaviour of *N*-methylated dioleoylphosphatidylethanolamine

Thad A. Harroun[1], Kia Balali-Mood, Ian Gourlay, Jeremy P. Bradshaw*

Department of Preclinical Veterinary Sciences, Royal (Dick) School of Veterinary Studies, University of Edinburgh, Summerhall, Edinburgh, EH9 1QH Scotland, UK

Received 13 May 2003; received in revised form 20 August 2003; accepted 11 September 2003

Abstract

Temperature-scan X-ray scattering was used to study the effect of the fusion peptide of simian immunodeficiency virus (SIV) on the lipid polymorphism of *N*-methylated dioleoylphosphatidylethanolamine (DOPE-Me), in the presence and absence of one or both of the fusion inhibitors carbobenzoxy-D-phenylalanine-L-phenylalanine-glycine and 1-lauroyl-2-hydroxy-*sn*-glycero-3-phosphocholine (LPC). Using X-ray diffraction at stations 2.1 and 8.2 of the Synchrotron Radiation Source at Daresbury Laboratory, UK, the structure of multilamellar vesicles (MLVs) was probed as the temperature was raised from 20 to 90 °C. The results are compared to those of similar studies, reported earlier, that used the fusion peptide of feline leukaemia virus (FeLV) which, at 28 amino acid residues in length, is considerably longer than the SIV peptide (12 amino acid residues). We interpret the results within the framework of current understanding of membrane fusion, and demonstrate how observed lipid polymorphism might describe the fusion process.

Keywords: Small angle X-ray diffraction; Biomembrane fusion; Inhibitor; Lamellar phase; Cubic phase; Hexagonal phase

1. Introduction

The fusion of phospholipid bilayers is an integral part of a number of biological processes, including mitosis, exocytosis, spermatozoid–egg fusion and viral infection [1]. However, the molecular rearrangements of the lipids and the precise kinetic events involved are still uncertain. This is largely because the fusion event is transient and involves only local, isolated patches of lipid. It is clear that biomembrane fusion is a protein-regulated event [2,3]. In order to introduce their infective nuclear material into a host cell, enveloped virus particles use membrane fusion, catalysed by specialised, extra-membranous glycoprotein 'spike', of which the best known is hemagglutinin of the influenza A virus. Viral fusion proteins usually contain a highly conserved N-terminal region that has been shown to be crucial to the process of fusion between the viral envelope and a membrane of the host cell during the infection process. Short peptides (10 to 30 residues long) of corresponding sequence, termed *fusion peptides*, retain much of the membrane fusion activity of the larger protein, albeit with slower rates and lack of a specific binding function. They have enabled research on membrane fusion mechanisms to focus on the fundamental interactions between peptide and phospholipid, in isolation from membrane proteins, and their added levels of complexity.

The precise molecular events that occur during peptide-induced membrane fusion are still unclear. The membrane

Abbreviations: CBZ-D-FFG, carbobenzoxy-D-phenylalanine-L-phenylalanine-glycine; d_H, lattice repeat distance (hexagonal phase phospholipid); d_L, lattice repeat distance (lamellar phase phospholipid); d_Q, lattice repeat distance (cubic phase phospholipid); DOPC, dioleoylphosphatidylcholine; DOPE, dioleoylphosphatidylethanolamine; DOPE-Me, *N*-methylated dioleoylphosphatidylethanolamine; EDTA, ethylenediaminetetra-acetic acid; FeLV, feline leukaemia virus; H, hexagonal phase; L, lamellar phase; LPC, 1-lauroyl-2-hydroxy-*sn*-glycero-3-phosphocholine; MLV, multilamellar vesicle; p15EK, fusion peptide from spike protein p15E of FeLV; PIPES1,4-piperazinediethanesulfonic acid; Q, cubic phase; q, $2\pi/d$; SAXS, small angle X-ray scattering; SIV, simian immunodeficiency virus; T_H, temperature at which hexagonal phase is first observed; T_Q, temperature at which cubic phase is first observed

* Corresponding author. Tel.: +44-131-650-6139; fax: +44-131-650-6576.

E-mail address: j.bradshaw@ed.ac.uk (J.P. Bradshaw).

[1] Current address: National Research Council, Neutron Program for Materials Research, Chalk River Laboratories, Chalk River, Ontario, Canada K0J 1J0.

0005-2736/$ - see front matter © 2003 Elsevier B.V. All rights reserved.
doi:10.1016/j.bbamem.2003.09.003

leaflets, composed of phospholipid molecules, must rearrange into highly curved intermediates prior to fusion pore development [4,5]. These intermediates can also be induced by fusion peptides. It has been demonstrated that peptides that lower the bilayer (L_α)-to-inverted hexagonal (H_{II}) phase-transition temperature in model membranes can also promote membrane fusion through this kind of bilayer destabilization [6]. It is recognised that a large fraction of the lipids of many biological membranes form the H_{II} phase when purified and hydrated under physiological conditions [7]. These lipids have been termed *nonbilayer lipids* in contrast to the *bilayer lipids* that form lamellar structures under the same conditions. It has been suggested that, although membranes are bilayers most of the time, the high concentration of nonbilayer lipids has functional significance in allowing the membranes to form transient nonbilayer structures because vital processes, including fusion, would be topologically impossible with intact bilayers.

A concept that has proved very useful in the attempts to understand fusion peptide activity has been *monolayer curvature strain*. Indeed, it has been proposed that this property is homeostatically controlled in living biomembranes [8]. Current models of fusion peptide function are usually based upon their effect on the monolayer curvature strain of the membranes involved in the fusion process. The peptides are thought to destabilise lamellar bilayers by increasing the hydrophobic volume of a monolayer, relative to the volume of the solvated polar groups [9].

Highly curved lipid mesomorphs, similar to those involved in the fusion process, recently were directly observed for the first time with diphytanoyl-phosphocholine lipids, however, under non-physiological, dehydrated conditions [10]. Similar structures are suspected to occur during the L_α-to-Q_{II} (inverted cubic) phase transition and the L_α-to-H_{II} phase transition [11]. The ability of a number of agents to promote fusion appears to be correlated to their ability to lower the L_α-to-H_{II}-transition temperature (T_H) [12–14]. Similarly, some fusion inhibitors raise T_H [15]. Although the Q_{II} and the H_{II} phases, which are kinetically stable, are unlikely to exist at the site of a developing fusion pore, knowledge about the topology of the interface as these phases begin to form has clear implications for our understanding of biological fusion mechanisms.

This paper describes a continuation of the work previously reported [16,17] in which we have used temperature-scan X-ray scattering to study the effect of the fusion peptide of feline leukaemia virus (FeLV) on the lipid polymorphism of *N*-methylated dioleoylphosphatidylethanolamine (DOPE-Me). In the more recent paper, we have reported how the tri-peptide carbobenzoxy-D-phenylalanine-L-phenylalanine-glycine (CBZ-D-FFG) and the lipid 1-lauroyl-2-hydroxy-*sn*-glycero-3-phosphocholine (LPC) modify the phase transition of this lipid. Here we extend the studies to a different fusion peptide, that from simian immunodeficiency virus (SIV), and discuss the findings for this peptide in the context of the model of membrane fusion presented in the earlier paper [17]. The work also related to a study of SIV peptide on phospholipid phase transitions by Colotto et al. [18], who collected X-ray diffraction data at a range of constant temperatures, ranging from 15 to 80 °C.

2. Materials and methods

2.1. Sample preparation

The fusion peptide from the GP160 protein of SIV (Macaque isolate, SWISSPROT accession number P05885, sequence GVFVLGFLGFLA), and the fusion peptide p15EK of FeLV (strain C/Sarma, SWISSPROT accession number P06752, sequence EPISLTVALMLGGLTVGGIAAGVGTGTK), were synthesised and purified by Albachem (Edinburgh, Scotland). CBZ-D-FFG was obtained from Sigma (St. Louis, MO). LPC and DOPE-Me were purchased from Avanti Polar Lipids (Alabaster, AL) and used without further purification.

Multilamellar vesicles (MLVs) were prepared by rehydrating phospholipid films as previously described [16,17]. The buffer used for rehydration was 20 mM PIPES, 1 mM EDTA, 150 mM sodium chloride and 0.3 mM sodium azide at pH 7.4. All samples had a low lipid concentration of 100 mM, equivalent to 7.57% (w/v), to ensure an excess water condition. The lipid dispersions were then subjected to five freeze–thaw cycles. Repeated freezing and thawing across the chain-melt temperature ensures that the lipid is fully hydrated regardless of the thermal history of the lipid.

2.2. Temperature-resolved X-ray diffraction

The X-ray diffraction experiments were performed at stations 2.1 and 8.2 of the Synchrotron Radiation Source at Daresbury Laboratory, UK. The experimental set-up at the two instruments was essentially identical. The X-ray wavelength was 0.154 nm. The specimen-to-detector length was approximately 1.5 m. Each sample was contained in a glass capillary tube, held in a steel block with electronic (Linkam) programmable temperature control. A thermocouple fixed to the sample chamber monitored the temperature continuously and wrote the temperature into the data files. The temperature increased in a linear fashion at a rate of 30 K/h, a rate originally chosen because the metastable cubic phase of DOPE-Me is not normally observed. Each frame of data collection lasted for 30 s. The effect of thermal radiation from X-ray beams of this kind was minimal. Aluminium foils were added to attenuate the incident beam until no loss of diffracted intensity was observed throughout the duration of a complete temperature scan.

2.3. Data analysis

The program XOTOKO [19] was used to correct for sample thickness and variations in detector response, and to

subtract the background counts. Detector response was determined by measuring a fixed source, ^{59}Fe, overnight both before and after data collection. Calibration of the *x*-axis for small angle scattering was achieved by using rat-tail collagen as a standard [20]. This calibration was repeated prior to the exposure of each new sample. The location, width and amplitude of each Bragg peak were determined by fitting Lorentzian distributions (PeakFit, SPSS Ltd.).

3. Results and discussion

Fig. 1 shows the relationship between lattice basis vector length and temperature for all observed phases of DOPE-Me with respect to temperature. Fig. 2 is a schematic summary of the phase behaviour of DOPE-Me in the presence of SIV fusion peptide and/or fusion inhibitors, as a function of temperature. Relevant data from our earlier papers [16,17] are reproduced for comparison.

3.1. SIV and FeLV

In earlier papers [16,17], we have discussed the effects of the fusion peptide from feline leukaemia virus (FeLV); with the current data, we are now able to compare the two peptides in terms of their effects upon the phase behaviour of DOPE-Me. Each of the peptides is thought to be helical in its active form [21] and Brasseur has proposed that both insert at an oblique angle into phospholipid bilayers. To date, this has only been determined experimentally for SIV [22], though a molecular dynamics study of a related fusion peptide from human immunodeficiency virus also showed oblique insertion [23]. The most striking difference between the two peptides used in this study is their length. FeLV peptide, with 28 amino acids, is considerably longer than SIV peptide, with only 12. In α-helical conformation, this corresponds to a length of 42 Å for FeLV peptide and 18 Å for SIV. Clearly, FeLV peptide may span an entire bilayer, even at a tilt, while SIV reaches across just one leaflet. This may explain why FeLV fusion peptide is always more potent than SIV, in terms of its effects on the phase behaviour of DOPE-Me.

3.1.1. Lamellar phase

Both peptides reduce the temperature of breakdown for the lamellar phase, SIV by 5 °C and FeLV by more than 10 °C. This may be a direct consequence of the peptides' length. Whereas SIV is easily incorporated in two populations in DOPC bilayers [22] and its influence is directed more towards individual monolayers, the hydrophobic length of FeLV requires a full bilayer to span, thus its influence on bilayer breakdown is more direct.

3.1.2. Hexagonal phase

The hexagonal phase is the dominant high-temperature phase for DOPE-Me both with and without FeLV. The lamellar to hexagonal transition is narrow, and in pure DOPE-Me there is a brief coexistence region. SIV, on the other hand, induces a gap between the phases where no structure is present. This brief dissolving of the lipids is perhaps expected, if we consider that SIV acts on individual leaflets, rather than the entire bilayer, making it easier to form micellization products. An important difference between the actions of the two peptides is that while FeLV peptide lowers T_H (by 6 °C), the SIV peptide raises T_H (by 10 °C). The hexagonal phase repeating structural motif is essentially a bilayer. Although FeLV partitions more easily in such a phase than actual lamellar bilayers, the direct influence of SIV on monolayers means that it is readily incorporated into non-bilayer phases, as we shall see. At 2% SIV, the hexagonal phase is eliminated altogether. However, since inverse hexagonal phase is not observed in samples cooled back to 20 °C without a fusion peptide present, it appears that SIV peptide does indeed stabilise this phase, in keeping with our previous observation that inverse hexagonal phase is closely related to the fusion process. The importance of the lamellar to hexagonal pathway in fusion will be discussed in a later section.

3.1.3. Cubic phase

Both FeLV and SIV have similar effects of lowering T_Q, SIV by 10 °C, and FeLV by as much as 20 °C. With 1% SIV, the cubic phase comes to dominate the high T regions, eventually coexisting with a lesser hexagonal phase. The cubic phase with FeLV and 2% SIV is only transient; however, the SIV-induced cubic phase is shifted 15 °C to higher T. In addition, with FeLV the cubic gives way to the hexagonal phase but with SIV the lipid loses all structure. In all cases, the cubic phase is metastable; this phase was observed in samples that had been allowed to cool back to room temperature. The only means to return the sample to pure bilayer form is to incubate the sample for at least 1 h well below the main transition of the lipid.

In terms of its effect upon T_H and T_Q, 2% SIV peptide is clearly not as potent as 1% SIV. This could be caused by aggregation of the hydrophobic peptide, as we have previously speculated for FeLV peptide [24], or it could be that the phospholipid monolayer curvature strain becomes "saturated" between 1% and 2% SIV peptide. Support for the latter comes from similar measurements in the presence of fusion inhibitors, where the 2% peptide produces a lower onset temperature than 1% peptide for the H_{II} phase in the presence of either LPC or CBZ-D-FFG. In addition, the Q_{II} phase that eventually forms in the presence of 2% SIV peptide has a smaller d_Q, and therefore a tighter Gaussian curvature, than that which forms with lower concentrations of the peptide.

3.2. CBZ-D-FFG and LPC

In our previous work on FeLV, the fusion inhibitors had a clear and pronounced opposite effect to that of the peptide itself. Both CBZ-D-FFG and LPC reversed the H_{II} promot-

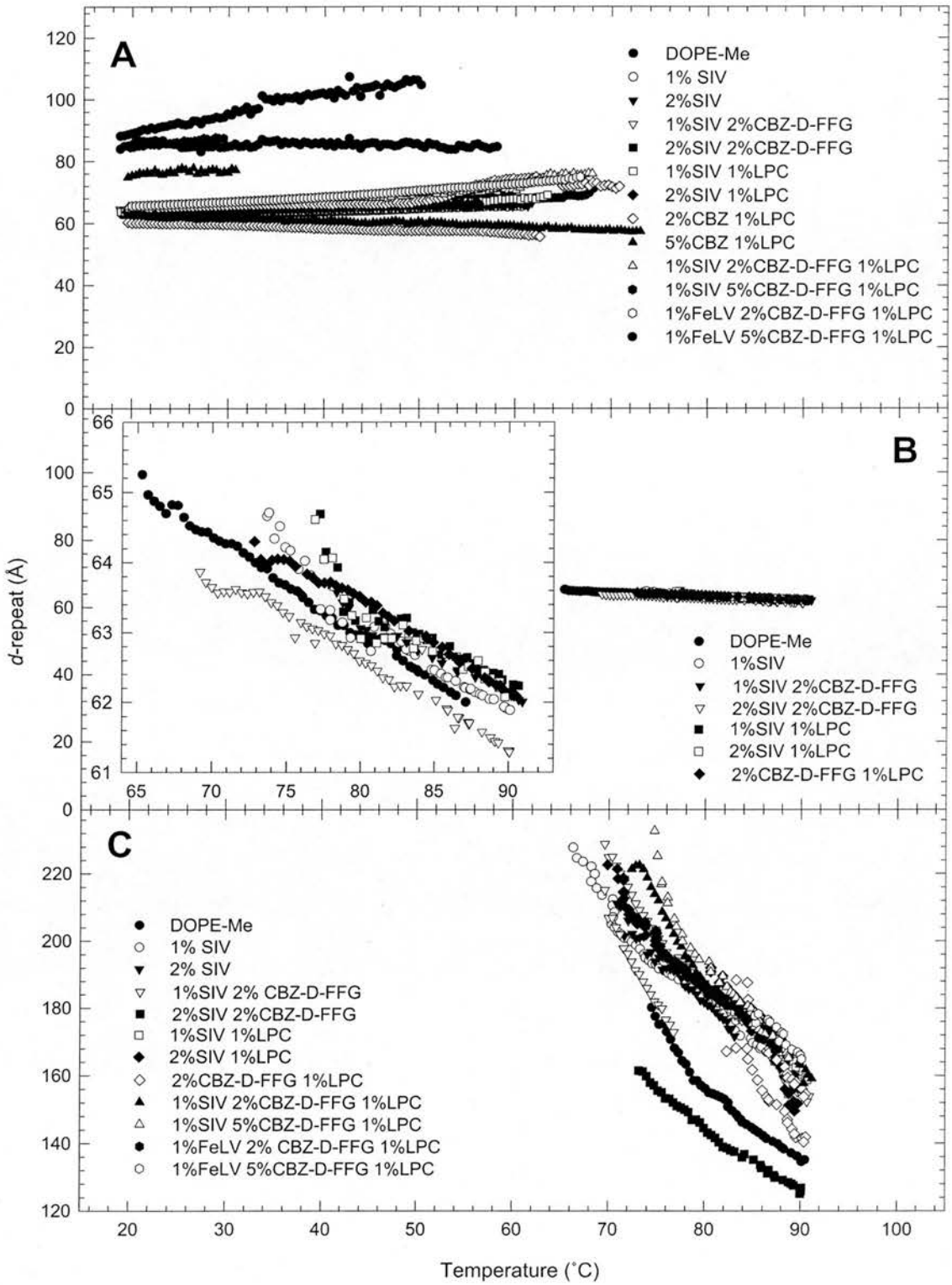

Fig. 1. The relationship of the *d*-repeat (Å) to temperature (°C) for all observed phases of DOPE-Me as determined by temperature-scan X-ray scattering at stations 2.1 and 8.2 of the Synchrotron Radiation Source at Daresbury Laboratory. (A) Lamellar; (B) inverse hexagonal (H_{II}); (C) inverse cubic (Q_{II}). For ease of comparison, the vertical scale is the same for all three panels, though displaced by 120 Å in panel C. Only alternate data points are shown, for clarity. The inset figure in panel B is an enlarged version of the H_{II} plot.

ing effects of FeLV, and promoted large *d*-spacing cubic phases, and some lamellar stability instead. With SIV, the fusion inhibitors once again counteract the peptide's effects on non-lamellar phases; however, this time, they allow for the presence of a metastable H_{II} phase along with the typical cubic phase.

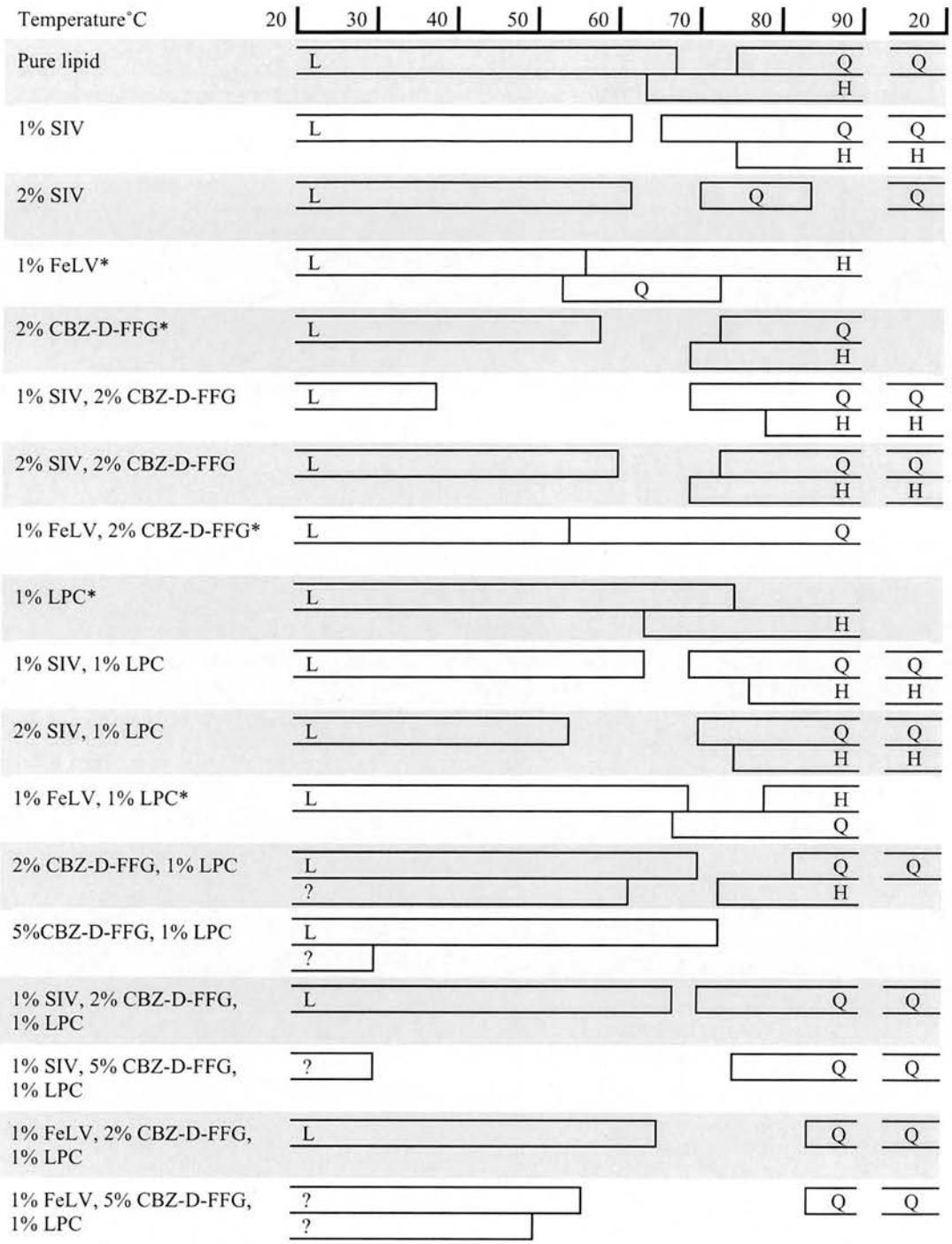

Fig. 2. Schematic summary of the phase behaviour of MLVs of DOPE-Me and DOPE-Me with fusion peptides from SIV and FeLV and/or fusion inhibitors, as a function of temperature. L, lamellar; H, inverse hexagonal; Q, inverse cubic. Data from samples indicated with an asterisk came from a previous study [17].

3.2.1. Lamellar phase

We have previously reported the micellization of the lamellar phase with as little as 2% CBZ-D-FFG. With the similar effect of SIV on the lamellar phase, it is not surprising that their combination dramatically increases the breakdown of that phase. In contrast, the lamellar stabilization properties of LPC are maintained in the presence of SIV. This disparity on the effect on lamellar bilayers between CBZ-D-FFG and LPC is shown dramatically when they are combined. In only the dilute samples of CBZ-D-FFG and LPC were lamellar phases identifiable. In all cases of 5% CBZ-D-FFG with LPC, a single diffraction peak at large d-spacing (70 Å) was seen, precluding the identification of the phase. The addition of FeLV or SIV restored the lamellar phase.

Considered from another perspective, the mystery phase seen in the CBZ-D-FFG/LPC combination samples is seen

with the addition of LPC to otherwise protein-solubilised lipids. LPC forms type I (headgroup exposed) tightly curved micelles, thus we might conclude the peptide (SIV and/or CBZ-D-FFG)-dissolved lipids are type II, where the lipid acyl-chain that might be exposed to the water is protected by the peptides. In combination, LPC is structure-stabilizing by offsetting the preference for SIV and CBZ-D-FFG for the hydrocarbon core of a curved monolayer. The large *d*-spacing of the mystery phase may then be explained as a swollen lamellar phase, where the peptides have been sequestered into the centre of the bilayer, increasing its fluctuations, and in turn its overall *d*-spacing.

3.2.2. Hexagonal and cubic phases

Both fusion inhibitors have nearly the same effect on the formation of the hexagonal and cubic phases in the presence of SIV. For 1% SIV, T_H and T_Q are slightly raised by the inhibitor. For 2% SIV the H_{II} phase is restored, and T_H is slightly lower than in 1% SIV. The Q phase is no longer transient, and T_Q is even slightly higher than in 1% SIV. When combined, CBZ-D-FFG and LPC drive the lipids to a Q phase that is highly metastable at elevated temperatures. This Q phase overcomes any effects of the SIV and FeLV peptides, although FeLV is clearly more potent as the onset of the Q phase is delayed by 10 °C. The similarity of effects on the non-lamellar phases, despite the profound differences on the lamellar phase, is significant. The stable non-lamellar phase outwith the normal fusion pathway is a cubic phase with *d*-repeat of 160–220 Å. Hexagonal phases, and presumably hexagonal and fusion precursors, are eliminated entirely.

3.3. The H_{II} phase and fusion pathways

DOPE-Me was chosen for these experiments because of its ability to monitor the effects of fusion agents on monolayer curvature strain. Our previous work with FeLV peptide and fusion inhibitors [17] has told us that there is some feature of the action of fusion peptides that is revealed by their ability to induce inverse hexagonal phases, which is quite separate from their similar ability to induce cubic phases. The lamellar–hexagonal pathway (in DOPE-Me) must share common ground with fusion pathway (in other lipids) *and* this feature must not be present in all lamellar–cubic pathways (there are many cubic phases and there many be many transition pathways). Although membrane curvature-strain clearly plays an important role in fusion, it appears that it is not the only factor involved.

A fluid monolayer is able to respond to a non-zero value of spontaneous curvature by deforming into a curved surface. In this way, the monolayer can accommodate substantial discrepancies between the cross-sectional area per lipid at the headgroup region (A_h) and the corresponding area of the fatty acyl chains (A_c). However, in a bilayer this flexibility is frustrated by the opposing tendencies of the two monolayers, as well as the entropic energy cost of water exposure in the hydrocarbon region. In a planar bilayer, the area per phospholipid molecule is assumed to be constant at all depths of the bilayer ($A_h = A_c$). Increasing temperature will tend to expand the tail region (A_c) more than the headgroups (A_h), due to the increased conformational disorder of the chains, thereby increasing the frustration [25]. This build up of frustration is energetically unfavourable and eventually the system must reduce it by rearrangement of the phospholipids into a curved phase, such as the inverted hexagonal (H_{II}) or inverse cubic (Q_{II}) phases. One way of understanding the effect of fusion peptides and inhibitors upon phospholipid phase transitions is to consider their role in increasing or reducing the frustration within bilayers, as the temperature is steadily increased.

The monolayer curvature strain hypothesis predicts that the addition of agents that affect the curvature strain (such as fusion peptides or inhibitors) should change the Gaussian curvature, at any given temperature, in those phases where such a change is possible. Agents that increase A_c relative to A_h should result in structures with a reduced radius of curvature, and those that increase A_h relative to A_c should show an increase in radius of curvature. One of the most remarkable findings of the present study is how small is the effect of fusion peptides or fusion inhibitors on the lattice repeat of the H_{II} phase in DOPE-Me. In our measurements, the change is only just above the level of experimental error. Colotto et al. [18] have reported that SIV peptide reduces d_Q by a very small amount (<0.25 Å); a mutant, non-fusogenic, analogue of the peptide had no measurable effect at all. Fig. 1 shows that, when plotted on the same vertical scale as the lamellar and cubic data, the repeat distance at any given temperature and, therefore, the radius of curvature of the H_{II} phase remain effectively unchanged, no matter which agents are present. It is only when the vertical scale is exaggerated, as in the inset panel, that small differences in d_Q appear, at a level that is close to the limits of experimental error. The presence or absence of peptides or inhibitors changes the temperature at which the onset of H_{II} phase occurs, but does not change the lattice dimensions. It could be that these agents only affect small, localised regions, and their concentration is too low to have a visible effect on d_Q. If this were true, it would be reasonable to expect to see an increase in the mosaic spread of the H_{II} samples, reflected in the width of the diffraction peaks. However, the FWHM of the first-order Bragg peaks from all H_{II} samples (with/without peptide/inhibitors) is 0.03 ± 0.02 $Å^{-1}$ (q). The peaks do not get broader with peptide or inhibitors, implying that these agents do not disrupt the inverse hexagonal structure, even in localised areas. This may explain why higher concentrations of peptide seem to be less effective in promoting H_{II} phase. It is almost as if the peptides are most effective when they induce earlier phase transitions, without modifying the actual structure formed.

In summary, we have reconfirmed our earlier hypothesis that precursors of membrane fusion are common to the lamellar to inverted hexagonal phase. The mechanism of

bilayer destabilization between the fusion peptides SIV and FeLV differs due to their folded conformational lengths; SIV acts on leaflets of lipids interacting within the hydrocarbon matrix, while FeLV prefers mixing into curved bilayers (such as the H_{II} phase). The net destabilization effect leads to fusion. When CBZ-D-FFG or LPC is added, they tend to undo curvature-strain effects and promote Q phases at higher temperatures, bypassing the intermediate structures that lead to hexagonal formation. These insights should lead us to refine theories of the mechanism of membrane fusion, such as tests for whether lipid mixing between leaflets occurs during the fusion process.

Acknowledgements

This work was supported by grants from the Wellcome Trust and the Central Laboratories of the Research Councils (CLRC). The authors wish to thank Dr. J.G. Grossmann and Dr N.J. Terrill of the Daresbury Laboratory for technical assistance.

References

[1] J.M. White, Viral and cellular membrane fusion peptides, Annu. Rev. Physiol. 52 (1990) 675–697.
[2] P.A. Bullough, F.M. Hughson, J.J. Skehel, D.C. Wiley, Structure of influenza hemagglutinin at the pH of membrane-fusion, Nature 371 (1994) 37–43.
[3] F.M. Hughson, Enveloped viruses: a common mode of membrane fusion? Curr. Biol. 7 (1997) R565–R569.
[4] D.P. Siegel, The modified stalk mechanism of lamellar/inverted phase transitions and its implications for membrane fusion, Biophys. J. 76 (1999) 291–313.
[5] A.E. Spruce, The first milliseconds of the pore formed by a fusogenic viral envelope protein during membrane fusion, Proc. Natl. Acad. Sci. U. S. A. 88 (1991) 3623–3627.
[6] R.F. Epand, I. Martin, J. Ruysschaert, R.M. Epand, Membrane orientation of the SIV fusion peptide determines its effect on bilayer stability and ability to promote membrane fusion, Biochem. Biophys. Res. Commun. 205 (1994) 1938–1943.
[7] V. Luzzati, in: D. Chapman (Ed.), Biological Membranes, vol. 1, Academic Press, NY, 1968, pp. 71–123.
[8] S.M. Gruner, Intrinsic curvature hypothesis for biomembrane lipid composition: a role for nonbilayer lipids, Proc. Natl. Acad. Sci. U. S. A. 82 (1985) 3665–3669.
[9] L.V. Chernomordik, J. Zimmerberg, Bending membranes to the task—structural intermediates in bilayer fusion, Curr. Opin. Struck. Biol. 5 (1995) 541–547.
[10] L. Yang, H.W. Huang, Observation of a membrane fusion intermediate structure, Science 297 (2002) 1877–1879.
[11] H. Ellens, D.P. Siegel, D. Alford, P.L. Yeagle, L. Boni, L.J. Lis, P.J. Quinn, J. Bentz, Membrane fusion and inverted phases. The modified stalk mechanism of lamellar/inverted phase transitions and its implications for membrane fusion, Biochemistry 28 (1989) 3692–3703.
[12] R.M. Epand, Diacylglycerols, lysolecithin, or hydrocarbons markedly alter the bilayer to hexagonal phase transition temperature of phosphatidylethanolamines, Biochemistry 24 (1985) 7092–7095.
[13] D.P. Siegel, J. Banschbach, D. Alford, H. Ellens, L.J. Lis, P.J. Quinn, P.L. Yeagle, J. Bentz, Physiological levels of diacylglycerols in phospholipid membranes induce membrane fusion and stabilize inverted phases, Biochemistry 28 (1989) 3703–3709.
[14] G. Basáñez, J.L. Nieva, E. Rivas, A. Alonso, F.M. Goñi, Diacylglycerol and the promotion of lamellar–hexagonal and lamellar–isotropic phase transition in lipids: implications for membrane fusion, Biophys. J. 70 (1996) 2299–2306.
[15] R.M. Epand, Virus replication inhibitory peptide inhibits the conversion of phospholipid bilayers to the hexagonal phase, Biosci. Rep. 6 (1986) 647–653.
[16] M.J.M. Darkes, S.M.A. Davies, J.P. Bradshaw, X-ray diffraction study on feline leukaemia virus fusion peptide and lipid polymorphism, FEBS Lett. 461 (1999) 178–182.
[17] M.J.M. Darkes, T.A. Harroun, S.M.A. Davies, J.P. Bradshaw, The effect of fusion inhibitors on the phase behaviour of *N*-methylated dioleoylphosphatidylethanolamine, Biochim. Biophys. Acta 1561 (2002) 119–128.
[18] A. Colotto, I. Martin, J.-M. Ruysschaert, A. Sen, S.W. Hui, R.M. Epand, Structural study of the interaction between the SIV fusion peptide and model membranes, Biochemistry 35 (1996) 980–989.
[19] C. Boulin, R. Kempf, M.H.J. Koch, S.M. McLaughlin, Data appraisal, evaluation and display for synchrotron radiation experiments—hardware and software, Nucl. Instrum. Methods Phys. Res. A249 (1986) 399–407.
[20] R.D.B. Fraser, T.P. MacRae, Unit cell and molecular connectivity in tendon collagen, Int. J. Biol. Macromol. 3 (1981) 193–200.
[21] R. Brasseur, M. Vandenbranden, B. Cornet, A. Burny, J.-M. Ruysschaert, Orientation into the lipid bilayer of an asymmetric amphipathic helical peptide located at the N-terminus of viral fusion proteins, Biochim. Biophys. Acta 1029 (1990) 267–273.
[22] J.P. Bradshaw, M.J.M. Darkes, T.A. Harroun, J. Katsaras, R.M. Epand, Oblique membrane-insertion of viral fusion peptide probed by neutron diffraction, Biochemistry 39 (2000) 6581–6585.
[23] S. Kamath, T.C. Wong, Membrane structure of the human immunodeficiency virus gp41 fusion domain by molecular dynamics simulation, Biophys. J. 83 (2002) 135–143.
[24] S.M.A. Davies, J.P. Bradshaw, R.M. Epand, Modulation of lipid polymorphism by the feline leukaemia virus fusion peptide: implications for the fusion mechanism, Biochemistry 37 (1998) 5720–5729.
[25] J.M. Seddon, Structure of the inverted hexagonal (H_2) phase and nonlamellar phase transitions of lipids, Biochim. Biophys. Acta 1031 (1990) 1–69.

Neutron diffraction reveals sequence-specific membrane insertion of pre-fibrillar islet amyloid polypeptide and inhibition by rifampicin

Kia Balali-Mood[a], Richard H. Ashley[b], Thomas Haußc, Jeremy P. Bradshaw[a,*]

[a] *Veterinary Biomedical Sciences, R.(D.)S.V.S., University of Edinburgh, Summerhall, Edinburgh EH9 1QH, UK*
[b] *Biomedical Sciences, University of Edinburgh Medical School, George Square, Edinburgh EH8 9XD, UK*
[c] *Hahn-Meitner-Institut, Glienicker Straße 100, D-14109 Berlin, Germany*

Received 30 August 2004; revised 8 November 2004; accepted 23 December 2004

Available online 19 January 2005

Edited by Irmgard Sinning

Abstract Human islet amyloid polypeptide (hIAPP) forms amyloid deposits in non-insulin-dependent diabetes mellitus (NIDDM). Pre-fibrillar hIAPP oligomers (in contrast to monomeric IAPP or mature fibrils) increase membrane permeability, suggesting an important role in the disease. In the first structural study of membrane-associated hIAPP, lamellar neutron diffraction shows that oligomeric hIAPP inserts into phospholipid bilayers, and extends across the membrane. Rifampicin, which inhibits hIAPP-induced membrane permeabilisation in functional studies, prevents membrane insertion. In contrast, rat IAPP (84% identical to hIAPP, but non-amyloidogenic) does not insert into bilayers. Our findings are consistent with the hypothesis that membrane-active pre-fibrillar hIAPP oligomers insert into beta cell membranes in NIDDM.

Keywords: Alzheimer's disease; Diabetes mellitus; Ion channel; Non-insulin-dependent diabetes mellitus; Phospholipid bilayer

1. Introduction

A number of extracellular proteins can misfold spontaneously and aggregate to form β-sheet rich amyloid deposits characteristic of a variety of "protein misfolding" diseases, most notably Alzheimer's disease [1,2]. While the precise molecular basis of such conditions is unclear, strong arguments are emerging to implicate organ-specific amyloidogenic proteins, particularly oligomeric intermediates on the pathway to amyloid fibril formation, in disease pathogenesis (e.g. [3]).

Human islet amyloid polypeptide (hIAPP), a 37-residue peptide hormone secreted by pancreatic beta cells, often forms amyloid deposits in patients affected by NIDDM (non-insulin dependent or type 2, maturity onset, diabetes mellitus). We recently demonstrated that an intermediate, non-fibrillar, oligomeric form of hIAPP interacts with membranes, whereas fibrillar hIAPP (like normal, monomeric hIAPP) lacks membrane activity [4]. Interestingly, the membrane activity of hIAPP could be inhibited independently of its ability to form amyloid [5]. These Langmuir balance measurements provided a further test of the idea that only the pre-fibrillar, oligomeric form of hIAPP is membrane-active, and mature fibrils are inert. Oligomeric intermediates in the 'misfolding' process may form non-specific cation channels [6], and cellular Ca^{2+}-overload could account for the toxicity of hIAPP [7], and explain why exposed cells die by both apoptosis and necrosis [4].

Unlike hIAPP, rat IAPP (rIAPP) is inert [4]. Sequence variations in IAPP are strongly associated with the ability of the peptide to form amyloid, and susceptibility to NIDDM [8,9]. Human and cat IAPP contain the internal sequence NFGAIL (Fig. 1), and both species can form islet amyloid and develop NIDDM. The rat and mouse genes do not encode this motif, and these species do not exhibit islet amyloid or NIDDM. However, mice expressing the hIAPP transgene do develop a NIDDM-like disease [10].

The membrane-active form of hIAPP is currently poorly defined. In the present study, we identified the membrane-associated form of hIAPP in stacked phospholipid bilayers using neutron diffraction. In order to mimic, as closely as possible, the experimental conditions of our previous studies [4,5] the lipid system for this work was a 50:50 mixture of palmitoyl-oleoyl phosphatidylethanolamine (POPE) and palmitoyl-oleoyl phosphatidylserine (POPS). We directly tested the hypothesis that hIAPP oligomers span the bilayer, and our findings are consistent with the idea that oligomeric hIAPP is associated with the formation of transmembrane channels. rIAPP was excluded from the membrane, as predicted, and rifampicin, an inhibitor of the membrane activity of hIAPP [5], prevents membrane insertion.

2. Materials and methods

2.1. Materials

hIAPP and rIAPP were obtained from Bachem (Weil am Rhein, Germany). POPE and POPS were purchased from Avanti Polar Lipids (Birmingham, AL) and rifampicin was from Fluka (Poole, UK). Other chemicals were of the highest purity available.

2.2. Sample preparation and data collection

Multibilayer stacks of phospholipids and peptides were prepared as described previously [11]. Briefly, 20 mg of a 50:50 (mol) mixture of POPE and POPS were co-dissolved with 1% (mol) peptide in chloroform:trifluoroethanol (7:3, v/v) and airbrushed onto a quartz glass slide to produce highly aligned stacks of some 50 000 or so bilayers. Where rifampicin was required in a sample, this was added to the lipid mixture before the peptide. The wafers were placed under vacuum for 24 h to remove the solvents before being mounted in sealed sample cans and hydrated for 12 h at 25 °C to allow full equilibration and the formation of IAPP oligomers [4,5]. The sample cans contained

*Corresponding author. Fax: +44 131 650 6139.
E-mail address: j.bradshaw@ed.ac.uk (J.P. Bradshaw).

0014-5793/$30.00
doi:10.1016/j.febslet.2004.12.085

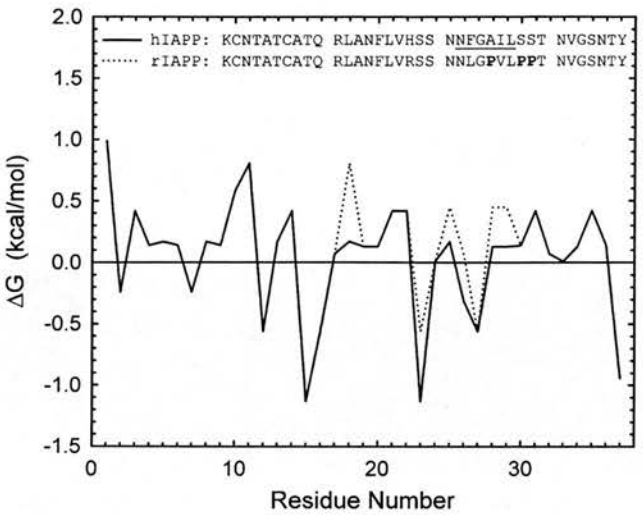

Fig. 1. Hydrophobicity plot of hIAPP (Swiss-Prot P10997) and rIAPP (Swiss-Prot P12969), using the whole residue hydrophobicity scale of Wimley and White [25]. The inset shows a sequence alignment of the two peptides. Each peptide has a disulfide-bridged loop at its N-terminal end. The NFGAIL motif, present in species susceptible to islet amyloid and NIDDM, is underlined. The three prolines present in rat but not hIAPP are indicated in bold.

saturated solutions of KCl, K_2NO_3 or K_2SO_4 in $^2H_2O/H_2O$ mixtures to maintain a relative humidity of 85%, 92% or 97%, respectively, and the ^2H_2O concentration was set to 8% (v/v) in the presence of each of the three salts, and also to 20% (v/v) and 50% (v/v) in K_2NO_3 alone. Diffraction data sets, comprising five orders of diffraction, were collected for each of the five conditions on V1 at the Berlin Neutron-Scattering Center, Hahn-Meitner-Institut, Berlin, Germany, by scanning samples through ±2° around the predicted Bragg angle for each of the first five orders of diffraction in turn.

2.3. Data analysis

After background subtraction, peak fitting and absorption and Lorentz corrections, the intensities were square-rooted to provide structure factor amplitudes. Phasing the structure factors is a two stage process. In the first, the three sets of 8% ^2H_2O structure factors are fitted to a single continuous transform, thereby fixing their phases [11]. In the second, the 8% ^2H_2O phases are used as a basis for phasing the data collected at 20% and 50% ^2H_2O by least-squares fitting to straight line functions, as described previously [12]. This two-step approach has the added advantage that an accurate set of 8% ^2H_2O structure factors can be calculated from first stage for increased accuracy in the second. The data were then placed on a 'relative absolute' scale using the method of White and co-workers [13]. In this approach, the data are placed on an absolute scale using the known neutron scattering lengths of all component molecules. However, since the x and y dimensions are not probed by lamellar diffraction methods, these two dimensions are not specified in the treatment of the data. The structure factor data, and the profiles calculated from them are, therefore, scaled to represent a single pair of lipids plus the appropriate number of water and peptide molecules. At 1% (mol) peptide, the unit cell in this study represents two lipid molecules and 0.02 molecules of peptide.

3. Results

3.1. Lamellar d-repeats

The lamellar spacings (d-repeats) of the samples at 92% relative humidity were determined by optimised least squares fitting to five orders of diffraction. 1% (mol) hIAPP decreased the lamellar spacing significantly from 62.09 ± 0.16 Å (means ± S.D., $n = 3$) to 61.51 ± 0.20 Å (means + S.D., $n = 3$, $P < 0.02$ by t-testing), while rIAPP increased the spacing slightly to 62.72 ± 0.57 Å ($n = 3$, $P > 0.05$). The measurements for phospholipids with 1% (mol) rifampicin were 56.96 ± 0.43 Å (means ± S.D., $n = 3$), and for phospholipids with 1% (mol) hIAPP and 1% (mol) rifampicin, 58.53 ± 0.27 Å (means ± S.D., $n = 3$). The difference in d-repeats between bilayers containing hIAPP and rIAPP (in the absence of rifampicin) is 1.2 Å. Assuming an average bilayer surface area of 72 $Å^2$ per phospholipid [14], this difference equates to a volume increase of 87 $Å^3$ per pair of lipids (the basis of the 'relative absolute' scaling method). The total molecular volume of IAPP calculated from amino acid volumes in the IMB Jena Image Library (http://www.imb-jena.de) is 4680 $Å^3$. At 1% (mol), this equates to an extra volume of 47 $Å^3$ per lipid, or 94 $Å^3$ per pair of lipids.

The additional volume of the peptide could be accommodated either by expansion of the unit cell in the Z-direction (e.g., if the long axis of the peptide lies parallel to the bilayer), or by insertion of hIAPP between the bilayer phospholipids, or both. The significant decrease in the d-repeat in the presence of hIAPP was inconsistent with the first possibility. However, expansion of the unit cell in the plane of the bilayer, the second possibility, is invisible to lamellar diffraction methods, and is not constrained in the '*relative* absolute' method used in this study. Moreover, the idea that the peptide inserted into the bilayer was consistent with the monolayer expansion seen in previous Langmuir balance measurements using the same lipids [5]. We therefore investigated the possible membrane insertion of hIAPP in more detail, by examining bilayer scattering profiles.

3.2. Bilayer profiles

The neutron scattering length density profile of POPE/POPS bilayers in the absence of peptide (Fig. 2(a)) differs from the "standard" profile of dioleoylphosphatidylcholine (DOPC) [11], most noticeably because the dip in scattering length density seen in the water region of DOPC bilayer profiles is barely visible in the POPE/POPS profile. This can be explained by the different neutron scattering lengths of the phospholipid headgroups. The total scattering length of the PC ($C_5H_{13}N$), PE (C_2H_7N) and PS ($C_3H_6O_2N$) headgroups are -0.60×10^{-13} cm, -0.597×10^{-13} cm and 1.85×10^{-13} cm, respectively. When two sodium counter ions are added to the PS headgroup (0.72×10^{-13} cm), the extra density in the mixed lipid bilayers is readily explained.

The bilayer profile in the presence of hIAPP (Fig. 2(b)) was remarkably similar to that of pure lipid bilayers. The total neutron scattering length per peptide molecule is 98.78×10^{-12} cm (hIAPP) or 98.51×10^{-12} cm (rIAPP). The water region was almost indistinguishable from the pure phospholipid bilayer, and any relatively slight differences were largely confined to an increase in density in the fatty-acyl region. rIAPP, on the other hand, caused major changes to the water region (Fig. 2(c)). The characteristic minimum at the edges of the profile were completely absent, suggesting that the additional neutron scattering length density introduced by the peptide now filled this trough. The profile shape changes in the fatty acyl-region were consistent with lipid rearrangements rather than peptide penetration. A peptide orientated parallel to the bilayer is likely to cause greater fatty-acyl disruption than a transbilayer peptide, for two reasons: (i) the parallel peptide will have contacts with a much larger number of phospholipids than a transbilayer peptide and (ii) the parallel peptide only occupies part

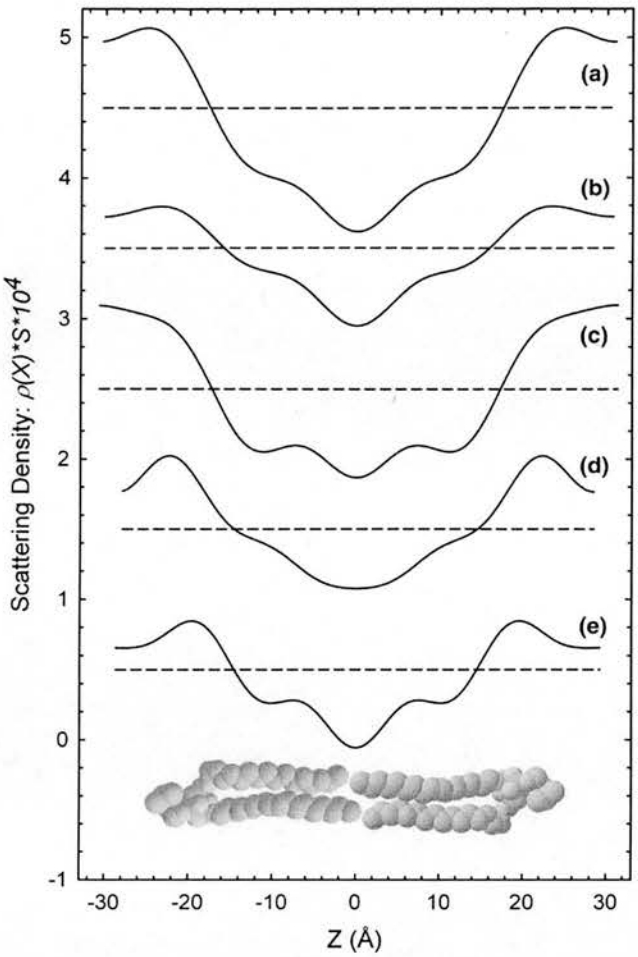

Fig. 2. Neutron scattering length density profiles of phospholipid bilayers: (a) 50:50 (mol) mixture of POPE and POPS; (b) 50:50 (mol) mixture of POPE and POPS with 1% (mol) hIAPP; (c) 50:50 (mol) mixture of POPE and POPS with 1% (mol) rIAPP; (d) 50:50 (mol) mixture of POPE and POPS with 1% (mol) rifampicin; (e) 50:50 (mol) mixture of POPE and POPS with 1% (mol) hIAPP and 1% (mol) rifampicin hIAPP. The structure factors for bilayers hydrated with 8% ^2H_2O were used to calculate the profiles, since water of this isotopic composition has a net neutron scattering length density of zero. The profiles have been displaced vertically, for clarity. A pair of lipid molecules is also shown, for orientation.

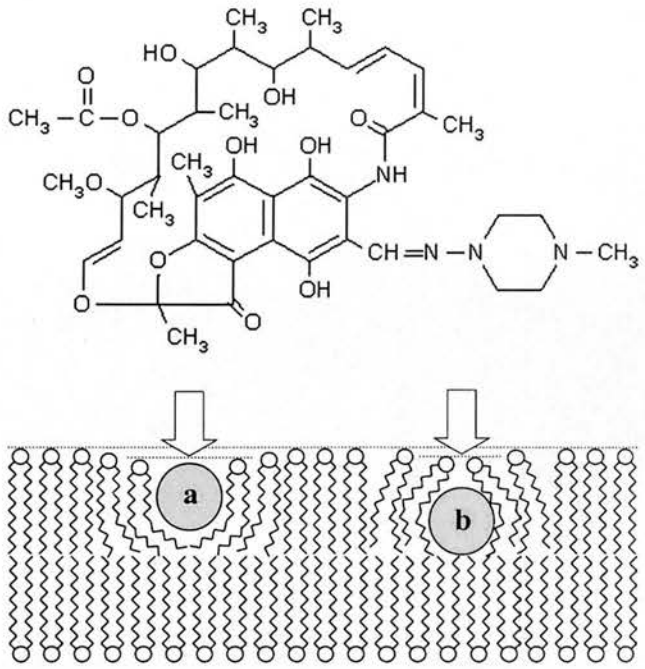

Fig. 3. Top: the structure of rifampicin. Bottom: Cartoon showing possible mechanism of bilayer thinning (arrow) when (a) a peptide inserts parallel to the bilayer surface or (b) rifampicin inserts close to the terminal methyl groups. For explanation, see text.

of the full depth of the bilayer, and will create a potential void that has to be filled by the fatty-acyl chains of the surrounding lipids (Fig. 3(a)). A similar effect has been observed in another interfacial peptide, the antimicrobial peptide protegrin-1 [15]. An alternative mechanism of bilayer thinning is based on the observation that an incorporated molecule may alter the thermal fluctuations which, in turn, can affect the inter-bilayer distance [16].

Taken together, these profiles show clear differences in the relationship of the two peptides with the lipid bilayer. rIAPP appears to reside exclusively in the water layer between the bilayers, whereas hIAPP is largely excluded from this region. This conclusion is further supported by the observation (Figs. 2(a) and (c)) that the bilayers are thinner in the presence of rIAPP, despite the overall increase in *d*-repeat. In profile (a), the two maxima in the neutron scattering length density are caused by strong neutron scattering by the phosphates and the oxygen rich (and hydrogen-poor) ester linkages of the phospholipids. Although partially obscured by scattering from the peptide, the steep gradients up towards the corresponding region are closer together in profile (c) compared to (a).

We next examined how the inhibitor rifampicin interacted with phospholipid bilayers in the absence of peptide. The total neutron scattering length per rifampicin molecule is 18.67×10^{-12} cm. Previous studies of rifampicin partitioning using derivative spectrophotometry [17] and ^1H NMR and fluorescence energy transfer [18] suggested that the compound inserts deeply into the hydrophobic core of the bilayer, while remaining in contact with the polar surface. With a pK_a of 7.9, rifampicin has partial anionic character at neutral pH, and this has been correlated with a stronger interaction with zwitterionic lipids such as di-myristoyl phosphatidylcholine ($K_d = 5.09 \times 10^4$) compared to anionic lipids such as di-myristoyl phosphatidylglycerol ($K_d = 0.54 \times 10^4$) [18]. While in broad agreement that rifampicin forms stable bilayers with anionic or zwitterionic lipids, our neutron data reveal that rifampicin induces marked structural changes in the membrane (the NMR technique used by Rodrigues [18] is blind to the details of bilayer structure revealed by neutron diffraction).

In particular, the bilayer profiles in Figs. 2(a) and (d) show differences in bilayer width, as revealed by the distance between the two maxima, and the bilayer thinning caused by rifampicin is reflected in the reduced *d*-repeat of the corresponding samples. These effects may be explained by "splaying" of the phospholipid headgroup regions over the top of deeply inserted rifampicin (Fig. 3(b)). Rodrigues also positions rifampicin close to the terminal methyls of the fatty-acyl chains [18], consistent with our observation that the methyl trough is broadened, as revealed by the neutron

scattering length density at the centre of the bilayer. Addition of hIAPP to the bilayers in the presence of rifampicin thins the bilayer even further, yet increases the *d*-repeat by 1.5 Å. Both of these observations are consistent with location of the peptide to the water/bilayer interfacial region, strongly implying that rifampicin has prevented transbilayer insertion of the peptide.

3.3. The distribution of water

Water distribution profiles were calculated by Fourier transformations of difference structure factor profiles obtained by least-squares fitting to 8%, 20% and 50% ^2H_2O sample hydrations. The water profile for pure lipid bilayers, shown in Fig. 4(a), was entirely consistent with previous neutron studies of phospholipid membranes. The single peak (split between the two ends of the profile in the figure) represents a block of water confined between adjacent bilayers in the multi-bilayer stack. The peak can be fitted (in reciprocal space) to a single pair of Gaussians, centred at 27.8(6) Å from the middle of the bilayer and 5.8(2) Å wide (full width at 1/*e* height).

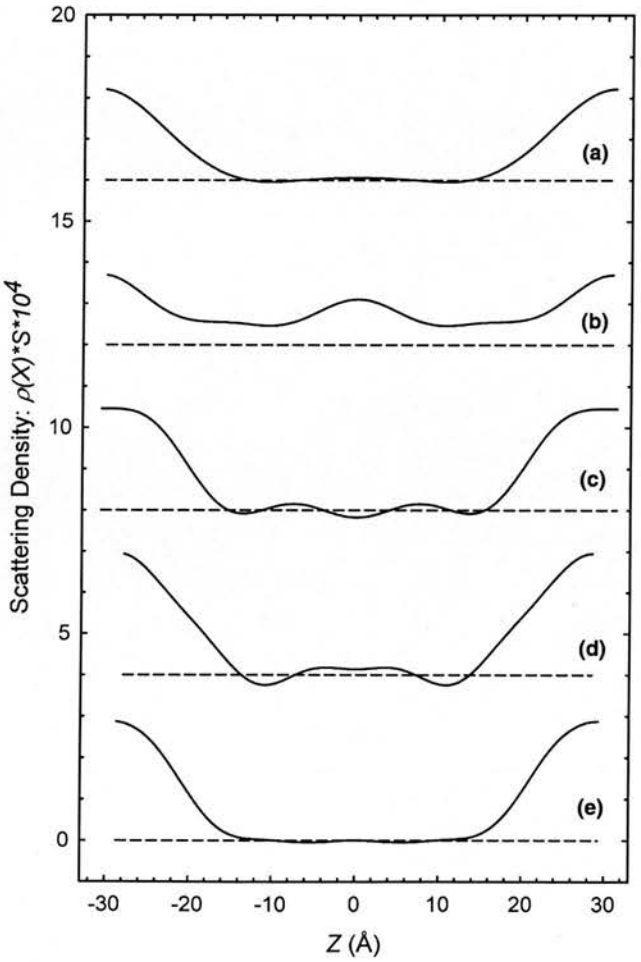

Fig. 4. Difference profiles of the neutron scattering length density of water (^2H_2O) in stacked phospholipid bilayers: (a) 50:50 (mol) mixture of POPE and POPS; (b) 50:50 (mol) mixture of POPE and POPS with 1% (mol) hIAPP; (c) 50:50 (mol) mixture of POPE and POPS with 1% (mol) rIAPP; (d) 50:50 (mol) mixture of POPE and POPS with 1% (mol) rifampicin; (e) 50:50 (mol) mixture of POPE and POPS with 1% (mol) hIAPP and 1% (mol) rifampicin hIAPP. Structure factors for bilayers hydrated in 100% H_2O were subtracted from corresponding 50% ^2H_2O structure factors and the result used to calculate the profiles shown. The profiles have been displaced vertically, for clarity.

The corresponding water distribution profile for bilayers containing 1% (mol) rIAPP (Fig. 4(c)) was similar. Once again, the water was confined to the outer sections of the profile, representing the inter-bilayer hydration layer. This block of neutron scattering length density was fitted (in reciprocal space) to a pair of Gaussians, centred 27.1(1) Å from the middle of the bilayer, and 4.2(5) Å wide. However, in the IAPP profiles (Fig. 4(b)), the same amount of water was distributed very differently. Instead of being confined to the edges, it extended across the entire width of the repeating unit, including the phospholipid bilayer itself. The area under the central portion of this curve corresponds to around 500 deuterons per peptide, comprising water and exchanged protons. This indicates the presence of channel-structures, though the neutron data do not supply any information on the number of peptides per channel. This observation supports the proposal that hIAPP, but not rIAPP, inserts in a transbilayer orientation in the phospholipid bilayers used in this study.

In contrast, in POPC/POPS bilayers with 1% (mol) rifampicin (Fig. 4(d)), the water was largely confined to the inter-bilayer region, and as previously noted, the lipid profile differed in shape (cf. Fig. 4(a)). This confirms the suggestion that rifampicin and phospholipids form stable bilayers, but refutes the claim [18] that the bilayer structure remains unchanged. Of particular interest is the observation that the addition of rifampicin to bilayers containing hIAPP (Fig. 4(e)) constrained the deuterons to the inter-bilayer region, in contrast to appearances in the absence of rifampicin (Fig. 4(b)). However, it is known from functional studies that rifampicin prevents bilayer insertion of hIAPP, rather than blocking pre-inserted "channels" [5].

4. Discussion

In the absence of high-resolution structural data, we have speculated that membrane-active IAPP is a misfolded, β-sheet-rich, primary nucleation element on the amyloid pathway that can insert spontaneously into membranes [5]. Membrane-located IAPP may then refold to give rise to transmembrane α-helices surrounding a central ion channel or pore [5,6]. In this respect, IAPP may follow the pattern displayed by calcitonin (CT), an amyloid-forming peptide that has previously been studied in detail. CT is a 32-amino acid polypeptide hormone that shows sequence and charge distribution similarities to IAPP and can adopt either α- or β-structures, depending on its environment. The former is seen in phospholipid membranes [19], while the latter predominates in aqueous solution [20]. Using methods similar to those in the present study, Bradshaw [19] showed that salmon CT could insert into phospholipid bilayers containing the anionic lipid phosphatidylglycerol, leading to speculation that the peptide may have ion-channel properties. This was later confirmed by Stipani et al. [21]. Human CT formed channels at the same concentration, but not as easily as salmon CT, an observation the authors attributed to the reduced helical content of this form of the peptide.

One possible concern is that, over the several hours of a neutron experiment, the amyloid-forming proteins may form fibrils. However, the neutron data describe highly ordered systems, that do not change over the duration of the neutron measurements. This is consistent with our previous lipid bilayer work [4] and Langmuir balance work [5] that demonstrated that the mature fibril for of IAPP is not membrane-active. Furthermore, it is simply not known whether fibrils can form from peptide that has already inserted into a membrane. The transconformational changes involved in morphing from a structure optimised for a hydrophobic membrane environment to the cross-β amyloid structure could be considerably greater than those involved in adopting the amyloid conformation from aqueous solution.

Fig. 1 shows a hydrophobicity plot for the two peptides. rIAPP is clearly less hydrophobic than hAIPP, a fact which may contribute to the latter's inability to insert into phospholipid bilayers. However, peptide insertion into bilayers also requires the formation of secondary structure and the sequence differences between the two forms of IAPP will have a significant effect on rIAPP's ability to form this structure. The main differences between the sequences of hIAPP and rIAPP are the replacement of the alanine at position 35, and the serines at positions 38 and 39, with proline residues. The first of these replacements disrupts the NFGAIL sequence linked to the formation of islet amyloid and susceptibility to NIDDM [8,9]. Proline is a well-established "breaker" of both α-helix and β-sheet structures in globular proteins, because the closed loop structure of the side chain prevents the peptide backbone from adopting the φ and ψ angles required for either of these secondary structures. However, proline frequently occurs in the transmembrane helices of integral membrane proteins, particularly transport proteins, despite the fact that a kink is introduced wherever a proline residue interrupts a helical section. Li and Derber [22] resolved this apparent contradiction by postulating different rules governing structure in the hydrophobic environment of membranes, and showed that the helical propensity of proline was greatly enhanced in the membrane-mimetic environments of both lipid micelles and organic solvents. In studies of a proline to alanine replacement in a single-spanning membrane protein of bacteriophage IKe, Li and Derber [22] showed that proline does not interfere with helix formation, but does prevent the formation of β-sheet. The intrinsic capacity of proline to disrupt β-structures has also been demonstrated by showing that prolines are excluded from transmembrane β-strands in mutagenised OmpA porins that retain the ability to assemble into a membrane-spanning β-barrel [23]. Wigley et al. [24] has proposed that the abundance of proline in transmembrane helices can be entirely explained by the ability of the residue to block β-structures. The advantage conferred by preventing the formation of a β-sheet outweighs the entropic disadvantage in helix distortion.

In this context, it is instructive to consider the differences in sequence, amyloidogenicity and membrane-associated neutron scattering profiles of hIAPP and rIAPP. Following the arguments outlined above, it is tempting to suggest that rIAPP is non-amyloidogenic because the introduction of a proline into the NFGAIL sequence prevents the peptide from adopting the β-structure necessary for amyloid fibre formation. However, this should not significantly interfere with the peptide's ability to insert into phospholipid membranes, if the membrane-active form is α-helical (like the model for CT). Previous studies, and our current neutron diffraction data, indicate that this is not so. Rats are not susceptible to "NIDDM", and the neutron data suggest that rIAPP does not insert into phospholipid membranes.

This could be taken as evidence that the membrane-active form of hIAPP is not α-helical, until it is remembered that rIAPP possesses not one but three extra prolines. The disruptive effect of three prolines in close proximity (two of them consecutive residues) is likely to block the formation of both α- and β-structures by the peptide. In the future work, it will clearly be of interest to probe the secondary, tertiary and quaternary structure of membrane-associated hIAPP in detail.

In conclusion, our data represent the first study of membrane-associated IAPP to use diffraction-based techniques. We have shown that oligomeric hIAPP interacts with phospholipid membranes to form transbilayer structures. rIAPP is excluded from the membrane (as predicted), and the insertion of hIAPP is inhibited by rifampicin.

Acknowledgements: We thank the Alzheimer's Research Trust and the University of Edinburgh Development Trust for support.

References

[1] Bucciantini, M., Giannoni, E., Chiti, F., Baroni, F., Formigli, L., Zurdo, J., Taddei, N., Ramponi, G., Dobson, C.M. and Stefani, M. (2002) Inherent toxicity of aggregates implies a common mechanism for protein misfolding diseases. Nature 416, 507–511.
[2] Ellis, R.J. and Pinheiro, T.J.T. (2002) Danger – misfolding proteins. Nature 416, 483–484.
[3] Walsh, D.M., Klyubin, I., Fadeeva, J.V., Cullen, W.K., Anwyl, R., Wolfe, M.S., Rowan, M.J. and Selkoe, D.J. (2002) Naturally secreted oligomers of amyloid beta protein potently inhibit hippocampal long-term potentiation in vivo. Nature 416, 535–539.
[4] Janson, J., Ashley, R.H., Harrison, D., McIntyre, S. and Butler, P.C. (1999) The mechanism of islet amyloid polypeptide toxicity is membrane disruption by intermediate-sized toxic amyloid particles. Diabetes 48, 491–498.
[5] Harroun, T.A., Bradshaw, J.P. and Ashley, R.H. (2001) Inhibitors can arrest the membrane activity of human islet amyloid polypeptide independently of amyloid formation. FEBS Lett. 507, 200–204.
[6] Mirzabekov, T.A., Lin, M.C. and Kagan, B.L. (1996) Pore formation by the cytotoxic islet amyloid peptide amylin. J. Biol. Chem. 271, 1988–1992.
[7] Kelly, J.W. (1998) The alternative conformations of amyloidogenic proteins and their multi-step assembly pathways. Curr. Opin. Struct. Biol. 8, 101–106.
[8] Westermark, P., Engstrom, U., Johnson, K.H., Westermark, G.T. and Betsholtz, C. (1990) Islet amyloid polypeptide – pinpointing amino-acid-residues linked to amyloid fibril formation. Proc. Natl. Acad. Sci. USA 87, 5036–5040.
[9] Tenidis, K., Waldner, M., Bernhagen, J., Fischle, W., Bergmann, M., Weber, M., Merkle, M.L., Voelter, W., Brunner, H. and Kapurniotu, A. (2000) Identification of a penta- and hexapeptide of islet amyloid polypeptide (IAPP) with amyloidogenic and cytotoxic properties. J. Mol. Biol. 295, 1055–1071.
[10] Janson, J., Soeller, W.C., Roche, P.C., Nelson, R.T., Torchia, A.J., Kreutter, D.K. and Butler, P.C. (1996) Spontaneous diabetes mellitus in transgenic mice expressing human islet amyloid polypeptide. Proc. Natl. Acad. Sci. USA 93, 7283–7288.
[11] Darkes, M.J.M. and Bradshaw, J.P. (2000) Real-time swelling series method improves the accuracy of lamellar neutron diffraction data. Acta Crystallogr. D 56, 48–54.
[12] Duff, K.C., Gilchrist, P.J., Saxena, A.M. and Bradshaw, J.P. (1994) Neutron diffraction reveals the site of amantadine

blockade in the influenza A M2 ion channel. Virology 202, 287–293.
[13] Wiener, M.C., King, G.I. and White, S.H. (1991) Structure of a fluid dioleoylphosphatidylcholine bilayer determined by joint refinement of X-ray and neutron-diffraction data. 1. scaling of neutron data and the distributions of double-bonds and water. Biophys. J. 60, 568–576.
[14] Tristram-Nagle, S., Petrache, H.I. and Nagle, J.F. (1998) Structure and interactions of fully hydrated dioleoylphosphatidylcholine bilayers. Biophys. J. 75, 917–925.
[15] Heller, W.T., Waring, A.J., Lehrer, R.I., Harroun, T.A., Weiss, T.M., Yang, L. and Huang, H.W. (2000) Membrane thinning effect of the beta-sheet antimicrobial protegrin. Biochemistry 39, 139–145.
[16] McIntosh, T.J., Magid, A.D. and Simon, S.A. (1989) Cholesterol modifies the short-range repulsive interactions between phosphatidylcholine membranes. Biochemistry 28, 17–25.
[17] Rodrigues, C., Gameiro, P., Reis, S., Lima, J.L.F.C. and Castro, B. (2001) de Derivative spectrophotometry as a tool for the determination of drug partition coefficients in water/dimyristoyl-L-α-phosphatidylglycerol (DMPG) liposomes. Biophys. Chem. 94, 97–106.
[18] Rodrigues, C., Gameiro, P., Prieto, M. and Castro, B. (2003) de Interaction of rifampicin and isoniazid with large unilamellar liposomes: spectroscopic location studies. Biophys. Biochim. Acta 1620, 151–159.
[19] Bradshaw, J.P. (1997) Phosphatidyl glycerol promotes bilayer insertion of salmon calcitonin. Biophys. J. 72, 2180–2186.
[20] Gilchrist, P.J. and Bradshaw, J.P. (1993) Amyloid formation by salmon calcitonin. Biochim. Biophys. Acta 1182, 111–114.
[21] Stipani, V., Gallucci, E., Micelli, S., Picciarelli, V. and Benz, R. (2001) Channel formation by salmon and human calcitonin in black lipid membranes. Biophys. J. 81, 3332–3338.
[22] Li, S.C. and Deber, C.M. (1994) A measure of helical propensity for amino-acids in membrane environments. Nat. Struct. Biol. 1, 368–373.
[23] Koebnik, R. (1999) Membrane assembly of the *Escherichia coli* outer membrane protein OmpA: exploring sequence constraints on transmembrane beta-strands. J. Mol. Biol. 285, 1801–1810.
[24] Wigley, W.C., Corboy, M.J., Cutler, T.D., Thibodeau, P.H., Oldan, J., Lee, M.G., Rizo, J., Hunt, J.F. and Thomas, P.J. (2002) A protein sequence that can encode native structure by disfavoring alternate conformations. Nat. Struct. Biol. 9, 381–388.
[25] Wimley, W.C. and White, S.H. (1996) Experimentally determined hydrophobicity scale for proteins at membrane interfaces. Nat. Struct. Biol. 3, 842–848.

Available online at www.sciencedirect.com

SCIENCE DIRECT

Biochimica et Biophysica Acta 1668 (2005) 138–144

BIOCHIMICA ET BIOPHYSICA ACTA BBA

http://www.elsevier.com/locate/bba

A structural study of the myristoylated N-terminus of ARF1

Thad A. Harroun[a,*], Jeremy P. Bradshaw[b], Kia Balali-Mood[b], John Katsaras[a]

[a]*National Research Council, Neutron Program for Materials Research, Chalk River Laboratories, Chalk River, ON, Canada K0J 1J0*
[b]*Preclinical Veterinary Sciences, University of Edinburgh, Summerhall, Edinburgh EH8 1QH, UK*

Received 7 October 2004; received in revised form 1 December 2004; accepted 2 December 2004
Available online 18 December 2004

Abstract

The effect of myristoylation on the 15-amino-acid peptide from the membrane-binding N-terminus of ADP ribosylation factor 1 (ARF1) was studied using neutron diffraction and circular dichroism. A previous study on the non-acylated form indicated that the peptide lies parallel to the membrane, at a shallow depth and in the vicinity of the phosphorylcholine headgroups. It was suggested that the helix does not extend past residue 12, an important consequence for the linking region of the ARF1 protein. In this paper, we show that the result of myristoylation is to increase the helical content reaching the peptide's C-terminus, resulting in the formation of a new hydrophobic face. This increased helicity may augment the entire protein's membrane-binding affinity, indicating that ARF1 effectively has two interdependent membrane-binding motifs.

Keywords: ADP ribosylation factor (ARF); Phospholipid; Neutron diffraction; Myristoylation

1. Introduction

Myristoylation is a common post-transcriptional modification of proteins that involves the covalent attachment of a saturated, fourteen-carbon fatty acid to the N-terminal glycine. Such a modification confers additional membrane-binding affinity through the lipid anchoring properties of the myristoyl chain. The utility of myristoylation is as varied as the functions of the numerous proteins that are modified in this way [1].

Adenosine diphosphate ribosylation factors (ARF) are just one type of myristoylated proteins. ARFs are a family of GTP-binding proteins, abundant and ubiquitous in eukaryotic cells. Their strongest characteristic is their regulatory behavior on different forms of membrane fusion, including vesicle formation, secretion, and endocytosis.

ARF1, in particular, is involved in the regulation of vesicle transport in the Golgi apparatus [2–5] and the activation of phospholipase D (PLD) in the process of secretion of granules from neutrophil-like cells [6]. In the inactive state, ARF1 is bound to GDP and is found soluble in the cytosol. ARF1 switches to its active form upon interaction with any number of guanine exchange factors (GEFs), with a conserved Sec7 domain [7]. ARF1 exchanges its GDP for GTP, the myristoyl chain is unfurled, and the protein binds to the Golgi membrane [8]. From there, it serves as a necessary cofactor for the regulation of the proteins involved in the packaging and coating of coat protein complex I (COPI) vesicles [9]. After the transport of the vesicle, ARF1 hydrolyses GTP under the influence of GTPase Activation Protein (GAP) and releases from the membrane, reverting back to its inactive state.

The role of the myristoyl chain in this case is not clear. Data suggests that there are two contributors to ARF1's ability to bind to membranes: the myristoyl chain and the N-terminus helix. Membrane-binding persists upon the removal of the acyl chain [10], and secretory function is restored upon the addition of non-Myr-ARF1 to ARF1 depleted cells [11]. However, ARF1 activity is considerably altered upon the removal of the N-terminus [12]. Mutant

* Corresponding author. Tel.: +1 613 584 8811x6237; fax: +1 613 584 4040.
E-mail address: Thad.Harroun@nrc.gc.ca (T.A. Harroun).

0005-2736/$ - see front matter © 2004 Elsevier B.V. All rights reserved.
doi:10.1016/j.bbamem.2004.12.003

ARF1 with 17 residues deleted from the N-terminus no longer activates PLD and inhibits coat protein recruitment in competition with the wild type ARF1 [13]. This is despite the fact that ARF1 can still bind to GTP strongly without its N-terminus.

There have been crystal structures of the non-myristoylated, inactive form of ARF1 [2] and one structure of the GTP bound form, with the 17 N-terminus amino acids deleted [14]. (For a review of ARF crystal structures, see Ref. [15]). However, not enough is known about the membrane bound structure [16]. It is thus important to determine how ARF1 acts to bring together the necessary proteins in COPI vesicle formation.

We have previously determined the location and orientation of the non-acylated form of the fifteen-amino-acid peptide from the N-terminus of human ARF1 (ARF1p) [17]. Our conclusions from that study, and subsequent analysis by molecular dynamics simulations [18,19], were that the peptide lies parallel to the plane of the membrane, among the lipid headgroups. At that time, we suggested that the amount of helix in the peptide did not extend much past Phe12. The structural characterization in that analysis was already further than any reported to date, as it was based on the determination of total secondary structure and the location in the bilayer of three labeled residues. Two recent NMR studies have attempted a similar determination of the myristoylated from of ARF1p N-terminus segment (Myr-ARF1p) in a lipid environment [20,21]. However, the efficacy of this method is somewhat questionable, because the structure was based on no more than the orientation of three individual peptide bonds with respect to the plane of the membrane. The locations in the membrane of groups or bonds were not determined, however, the conclusions regarding peptide orientation and location were similar to Davies et al. [17].

In this paper, we extend our first experiments, this time concentrating on the role that myristoylation plays on the membrane-binding properties of Myr-ARF1p. We find that the addition of the myristoyl chain increases the helical content of the peptide, resulting in a new hydrophobic face for membrane binding. This data may have important implications for explaining the previous membrane-binding data.

2. Methods

The technique of neutron lamellar diffraction with specific deuterium labeling is based on the method of Weiner and White [22] and extended by Bradshaw et al. [23]. In summary, the technique involves the one-dimensional reconstruction of the bilayer profile, normal to the plane of the membrane, using common methods of crystallography. For neutron diffraction, this results in a map of the neutron scattering length of the bilayer cross section, rather than the electron density measured by X-ray crystallography. The result is a low-resolution, time- and sample-averaged profile of the bilayer. One can then utilize the significant difference between hydrogen and deuterium in their ability to scatter neutrons, to label specific parts of the system. The difference between the scattering length density profiles of the H and D samples yields a higher resolution, time- and sample-averaged map of the location of the label.

The techniques employed here do not differ significantly from the previous experiment with the non-myristoylated ARF1p. Four versions of the Myr-ARF1p peptide were synthesised (Dalton Chemical Laboratories, Toronto, Canada): one in its normal hydrogenated form, and three with single amino acid labeling. Deuterium labeling involved replacing the five hydrogen atoms around the phenylalanine ring with deuterium, each in turn at the Phe4, Phe8, and Phe12 residue positions. Peptides were incorporated into bilayers composed of DOPC:DOPG 7:3 at 3 mol% by co-dissolving in chloroform:triflouroethanol 1:1 and spraying onto a silicon slide with an artist's airbrush. This results in multilayer stacks of highly aligned bilayers.

Data were collected on the N5 spectrometer located at the Chalk River Laboratories, Canada. Typically five orders of diffraction were collected at hydrations ranging from 84% RH to 97% RH, and D_2O concentrations ranging from 8–80%. The samples were kept at a temperature of 30.0 ± 0.5 °C with a circulating water bath. Sample equilibration was determined after sequential θ–2θ scans, which showed no change in the position of the Bragg peaks. For better statistics, several data sets were averaged. Bragg peaks were fitted with Gaussian functions, and the integrated peak intensity, less the background, was taken as the measured structure factor. After correcting the data for sample geometry and absorption, the structure factors for all three labels were scaled and subtracted simultaneously. Gaussians were fit, in reciprocal space, to the difference between the labelled and unlabelled structure factors to determine the label positions, with a typical chi-squared value of 0.01.

CD samples were made by dissolving Myr-ARF1p in either a buffer, pH 7.4, of 10 mM Tris and 0.1 mM EDTA or a solution of TFE, at concentrations of 2 mg/ml. Data were taken on a Jasco J600 spectropolarimeter at the NRC's Institute for Biological Sciences, Canada. Data were averaged and background corrected. The spectra were fit with the program CDPro to determine the helical content.

3. Results and discussion

The difference in the structure factors between the deuterated and hydrogenated samples under the same conditions can be modeled as a Gaussian shaped peak in real-space, the parameters of which reveal important positional information regarding the label [22]. The first parameter to be determined is the position of the peak,

which is centered at the time-averaged center-of-mass of the phenylalanine ring (specifically its hydrogens), as measured from the center of the bilayer. The second parameter is the width of the peak, which indicates the time-averaged fluctuation amplitude of the phenylalanine ring, averaged over all of the peptides in the sample. Finally, the amplitude of the peak is simply the scattering length density of 5 deuteriums less that of 5 hydrogens. This last piece of information is used to properly scale the data.

Fig. 1 shows the positions (dotted line) of the three different labeled residues. Each label is well described by a single Gaussian (solid line), and all three labels clearly occupy only one position, situated about 16 to 18 Å from the bilayer center. The small undulations in the data stem from small errors in the structure factors and the subsequent Fourier reconstruction. Such ripples are encountered in all reconstructions of electron density or neutron scattering length, but are more pronounced in this case since we only have a few orders in the Fourier series (Fourier termination errors) when compared with a typical case in protein crystallography [24], where the system is overdetermined. The data was scaled according to the area under the peaks, a method that is self-consistent by whether or not, in the final subtraction, the unlabeled structure factor scales to the same value for each label.

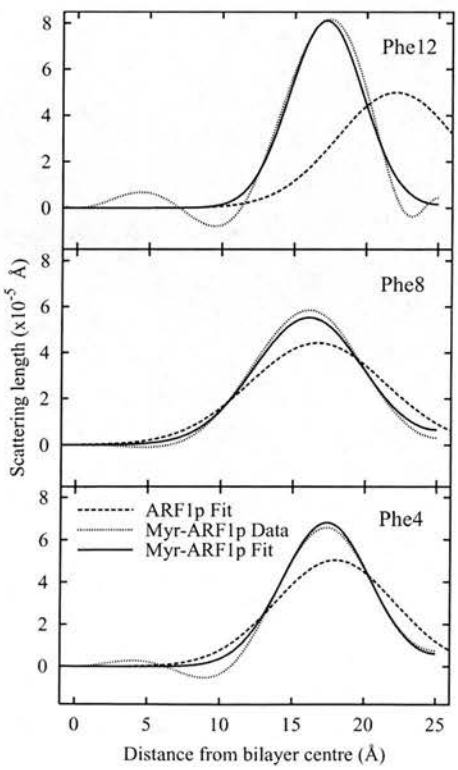

Fig. 1. The location of the deuterium labeled phenylalanines of ARF1p and Myr-ARF1p, determined from neutron diffraction. The abscissa is measured from the center of the DOPC:DOPG (7:3) bilayer, and the ordinate is the measured neutron scattering length per unit length of the label. The solid line is a Gaussian fit to the Myr-ARF1p data, shown as a dotted line. The dashed line represents the previous non-myristoylated ARF1p data for comparison [17].

Table 1
The location and standard deviation widths of the deuterium labels, determined by neutron diffraction

		Phe4	Phe8	Phe12
ARF1p	Position	17.99±0.02	16.68±0.04	22.06±0.06
	S.D.	5.83±0.03	6.64±0.04	5.88±0.08
Myr-ARF1p	Position	17.37±0.02	16.07±0.03	17.20±0.04
	S.D.	4.32±0.07	5.31±0.06	3.62±0.03

The location is measured in angstroms from the center of the bilayer. The data for ARF1p is taken from Davies et al. [17].

Included in Fig. 1, as a dashed line, are the results from the case of the non-myristoylated peptide. For Phe4 and Phe8, there is little difference in the location of the labels. Both residues are clearly in the hydrophobic/hydrophilic interface region of the lipid headgroups. In the Myr-ARF1p case, the fluctuation amplitudes are reduced, indicating that the phenylalanines are in a more constrained configuration and are undergoing somewhat less motion. The locations and standard deviation widths of the Myr-ARF1p peaks are given in Table 1, along with the results from the reference of Davies et al. The greatest difference between the myrsitoylated and non-acyl peptides is found with Phe12. For ARF1p, Phe12 stands above the headgroup region and fluctuates considerably, whereas with Myr-ARF1p, Phe12 is brought closer into the headgroups and, in comparison, is more immobile than the other measured residues.

By fitting a secondary structure to the data, we can elucidate the significance of the Phe12 difference between the myristoylated and non-acyl peptides. Here, we follow a similar method to that of Davies et al. and use circular dichroism and an atomic structure model to determine the possible modes of peptide interaction with the membrane. At least four deuterated labels would be required in order to orient a peptide secondary structural model unambiguously. One way of approaching this geometrical problem is to consider that it is possible to fit a plane triangle to any three points, but that the two opposing sides of the plane can be interchanged. The result of "flipping" the whole peptide between the two solutions can be quite dramatic to the overall orientation of the peptide relative to the membrane; the two models may be wholly unrelated, despite the fact that both have the same residues at the same depth in the bilayer. Although we are left with two mathematical alternatives, we can usually reject one on energetic and thermodynamic principles.

Before we can construct our model, we must determine its overall secondary structure using circular dichroism. Fig. 2 is the CD spectrum of Myr-ARF1p in buffer and TFE. In both polar and non-polar environments, the peptide adopts a strongly helical structure. This is in sharp contrast to ARF1p, which is predominantly a random-coil in buffer, and only partially self-folds into a helix in TFE or a lipid environment. The observation of helix promotion by myristoylation is not unexpected, such an effect has been reported in a peptide from CAMP-dependent protein kinase,

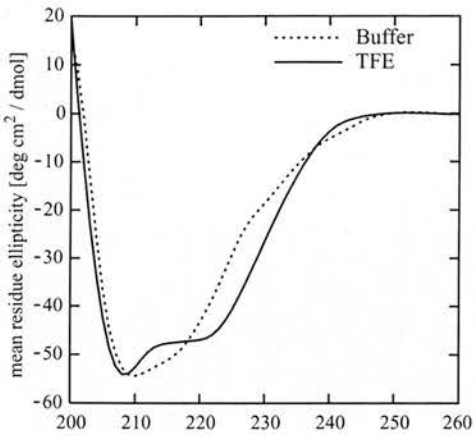

Fig. 2. Circular dichroism of Myr-ARF1p in TFE and aqueous buffer. Under both hydrophilic and hydrophobic environments, the myristoylated peptide adopts a nearly 100% α-helical structure.

though not to the same extent seen here [5]. The peptide's helical content was determined by CONTIN analysis and shows nearly 100% α-helix with little or no random coil in TFE. In buffer, the peptide is also predominantly helical, although analysis indicates that of the 80% helical content, as much as 20% of it is β-strand. The data indicates that the peptide possesses nearly complete amount of ordered secondary structure, much greater than indicated by the non-myristoylated crystal structure.

We begin with a starting model taken from a segment of the crystal structure of the full, non-myristoylated ARF1. This model has much less helical content than the CD data indicates, but its inclusion is instructive. We are not concerned with representing the myristoyl chain in the model, since we assume that it is always inserted in the same bilayer that the peptide is associated with. Fig. 3 is a diagram of the peptide, oriented with Phe labels at the positions shown in Fig. 1. In Fig. 3, only the backbone trace is shown, and the long axis of the molecule is viewed end-on. The block slab in the picture is meant to suggest the lipid bilayer headgroup region, extending between 16 and 20 Å from the center of the bilayer [22]. The water layer is above the slab and the hydrocarbon matrix below. The model sits in the headgroup region, with its long axis parallel to membrane plane. As discussed above, models A and B in Fig. 3 are mathematically optional orientations. Based on thermodynamic reasoning, we suggest that model B is incorrect, since its charged residues such as Lys14 and Lys15 are unexpectedly found buried in the center of the bilayer.

To confirm that these models have opposite hydrophobic/hydrophilic orientations, we calculate the hydrophobic moment of each model. The hydrophobic moment is taken to be the vector joining the hydrophilic and hydrophobic barycenters $\vec{\mu}$, calculated using the following relationship

$$\vec{\mu} = \frac{\sum_i H_i \vec{r}_i}{\sum_i H_i},$$

where H_i is the free energy transfer for each atom between the water and the hydrocarbon chain environments, and $\vec{r}_i$ is the atomic coordinate [25]. The sum is taken over all hydrophobic or hydrophilic atoms and has the units of Å. In Fig. 3, the hydrophobic moment is drawn as a ball-and-stick, joining the hydrophobic center of mass (in black) with the hydrophilic center of mass (in white). Although neither model has a vertically oriented moment, as one might expect for a ideal amphipathic helix, we see that in model B, the hydrophobic center is closer to the water and farther from the bilayer than the hydrophilic center. Of the two models, model A is therefore the more correct of the two.

The helical content of models A and B is much less than indicated by the CD data, so we created a second model by restricting the Φ/Ψ angles of the backbone to form a tighter α-helix. The model was then subjected to 1000 steps of energy minimization to remove bad steric contacts that might have been created. Fig. 4 shows this new model in both possible orientations. From the figure, we can see that

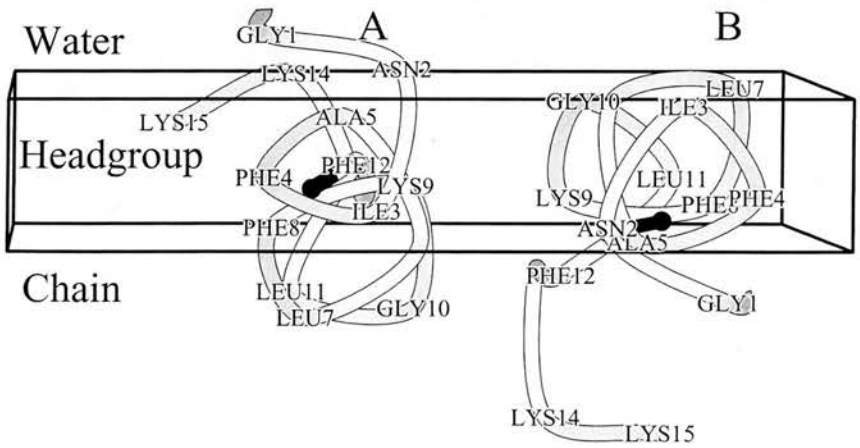

Fig. 3. The orientation of a model of Myr-ARF1p. The secondary structures of these models are derived from the crystal structure of the full ARF1 protein. Models A and B are mathematically related (see text for discussion). The slab indicates the lipid headgroup region extending from 16 to 20 Å from the bilayer center. The shading is only meant to suggest a 3D appearance. Figs. 3–5 were made with *Molscript* [26].

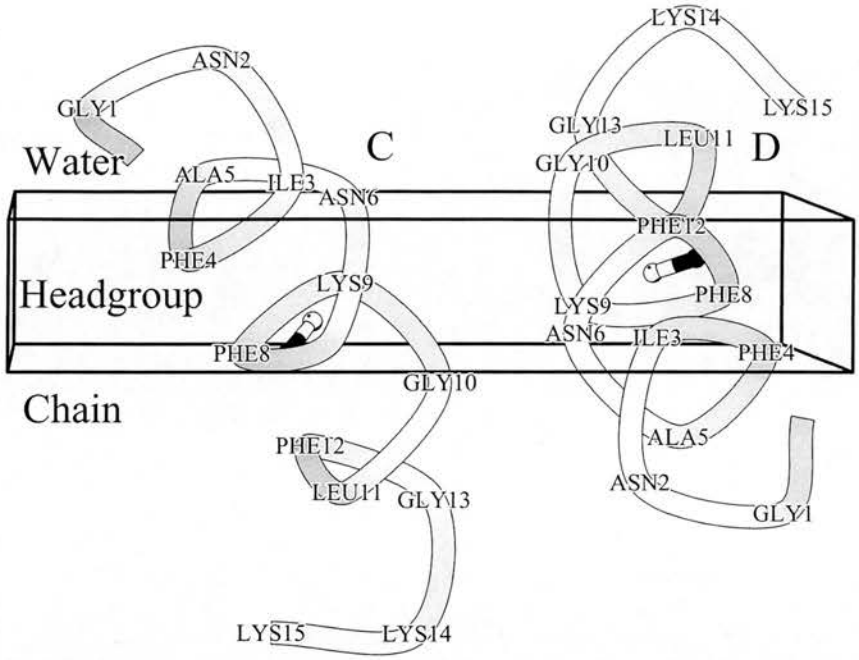

Fig. 4. The orientation of a more helical model of Myr-ARF1p. The secondary structures of these models come from increasing the helical content of models A and B. The shading is only meant to suggest a 3D appearance.

the models are unreasonably tilted out of the plane of the bilayer. The backbone atoms of models C and D were fit with a straight line to define the helical axis, which make 38° and 26° angles to the membrane plane, respectively. The tilt is primarily due to the movement of the Phe12 away from the opposite side of the molecule from Phe4 and Phe8, as seen in model A. In this configuration, Phe12 is at its greatest distance around the molecule from Phe4 and 8, making it very difficult to place all three residues at the same depth in the bilayer (ref. Fig. 1). Phe12 should ideally be on the opposite side to Phe4 and 8, as in model A, or they should all lie on the same side of the peptide.

Model E, shown in Fig. 5, is an ab initio, ideal α-helix constructed from the peptide sequence. In this arrangement, Phe12 is on the same side as Phe4 and Phe8, forming a new face of the molecule that theoretically should be expected to lie at the hydrophobic/hydrophilic interface. The peptide in this model again lies parallel to the membrane, although it "rides" higher in the headgroup region than model A. Since all three Phes are so close to each other, there is very little difference between model E and its alternative fit (not shown), unlike models A and C. The Lys15 at the C-terminus pointing toward the acyl chain region is somewhat misleading, as the full side chain snorkels up to the polar end of the lipids.

The hydrophobic moments of models C and D are perpendicular to the helical axis, indicating that the tightening of the helix is forming a new hydrophobic face. In model E, the hydrophobic moment is nearly vertical and at its maximum magnitude, as one might expect from an ideal helix with a periodic hydrophobic sequence. The difference in structure between models A and E is minor.

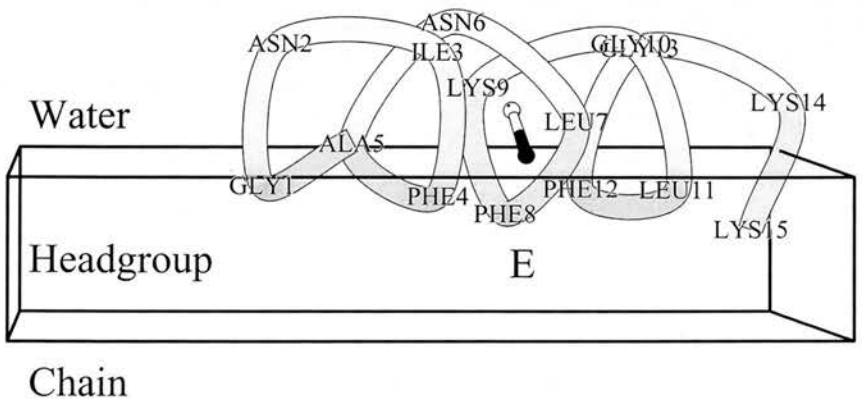

Fig. 5. The orientation of an ab initio model of Myr-ARF1p. In this case, the hydrophobic/hydrophillic centers-of-mass are at their greatest separation and alignment with the hydrophobic gradient normal to the membrane interface, which is expected from a peptide with a periodic hydrophobic sequence.

Model E therefore seems to be the best candidate for membrane associated peptide.

The data presented here show that the effect of myristoylation on ARF1 peptide is greater than previously thought. Taking into consideration our previous data, it seems that the myristoyl chain addition is a requirement for the membrane-binding domain to achieve its maximum ideal secondary structure suitable for membrane binding. The idea that the addition of myristic acid to the N-terminus can have structural effects extending further along the peptide is not unexpected. The PROSITE (PDOC00008) definition of amino acid sequence that is a candidate for modification by myristoyl CoA:protein N-myristoyl transferase (NMT) indicates that the motif extends at least 6 residues from the N-terminus. However, another analysis of a larger set of identified myristoylated proteins suggests that the motif extends as many as 17 amino acids from the N-terminal glycine [1].

The above support our observations of a greatly enhanced helix with myristoylation. Model A is a likely candidate structure for the non-myrisotylated protein; considerable helix remains, enough to maintain some membrane-binding affinity as seen in the biochemical studies. Once myristoylated, the amount of helix increases, and with it, the membrane-binding affinity and localization of certain residues at the membrane interface is also increased. Model E is not simply a better-defined helix than model A, it is also rotated along the long axis in the membrane.

ARF1 without its N-terminus can bind GTP but cannot set in motion the process of vesicle formation in vitro. Specifically, it no longer activates PLD and interferes with coatomer formation. Although it has been suggested that vesicle secretion may be linked to PLD-dependent, phosphatidic acid production [11], there is indication that the non-Myr-ARF1 competes with Myr-ARF in the process, inhibiting coat formation regardless of PLD activity [13].

The localization of the protein at the membrane interface is important, conceivably to gather together the necessary coat and packaging proteins. Jones et al. identify the two lysines 14 and 15 as necessary for PLD activation, and furthermore, substituting the ARF1 N-terminus on ARF6 greatly enhances overall ARF activity [13]. (Note that residue numbering in our case does not count the Myr as residue 1.) In that paper, the authors draw a picture of a plausible structure of membrane-bound ARF1, in which residues Lys14 and Lys15 are part of the linking domain to the rest of the protein. From inspection, this model is remarkably similar to the non-myrisoylated ARF1p model in the location of lysines and phenylalanines made by us. Here, we are suggesting that because of myristoylation, those residues are more a part of the helix, rather than the linking region, and positioned closer to the membrane headgroups. Thus, the role of Myr may be to carry out the final positioning for the activation of the ARF1 protein.

It is hoped that the data presented here will stimulate molecular dynamics simulation studies of similar membrane-binding protein domains. However, experimental data of these systems is required for the proper construction and analysis of such simulations. In this regard, the neutron diffraction data in this report is unique. The data of Fig. 1 is directly comparable to the static and time-averaged structure of a simulation, on a per-residue or per-atom group basis. Unlike other techniques, deuterium labeling does not suffer from the inherent perturbations of large molecular probes and labels. Furthermore, neutron diffraction is a reasonably direct structure determination technique and whose data does not require extensive interpretation, as can be the case with some spectroscopies. The only ambiguity with the data, is in determining which best-fit model is more probable. As we have shown, after vetting the possible protein structures with known information from other experiments one can arrive at a solution. Moreover, the location of the labeled residues, shown in Fig. 1, is accurate and unambiguous.

In conclusion, we have shown that the location of the myristoylated N-terminus of ARF1 lies flat within the headgroup region of the membrane. Using structural data and modeling, we have argued that the effect of the acyl chain modification is to increase the amount of helix in the peptide, resulting in the formation of a new hydrophobic face with increased affinity for the hydrophobic/hydrophilic interface. This implies that the role of myristoylation is to provide ARF1 with two interdependent membrane-binding domains.

References

[1] S. Maurer-Stroh, B. Eisenhaber, F. Eisenhaber, N-terminal N-myristoylation of proteins: prediction of substrate proteins from amino acid sequence, J. Mol. Biol. 317 (2002) 541–557.

[2] J.C. Amor, D.H. Harrison, R.A. Kahn, D. Ringe, Structure of the human ADP-ribosylation factor 1 complexed with GDP, Nature 372 (6507) (1994) 579–710.

[3] K.M. Jacques, Z. Nie, S. Stauffer, D.S. Hirsch, L.-X. Chen, K.T. Stanley, P.A. Randazzo, Arf1 dissociates from the clathrin adaptor GGA prior to being inactivated by Arf GTPase-activating proteins, J. Biol. Chem. 277 (49) (2002) 47235–47241.

[4] J. Menetrey, E. Macia, S. Pasqualato, M. Franco, J. Cherfils1, Structure of Arf6GDP suggests a basis for guanine nucleotide exchange factors specificity, Nat. Struct. Biol. 7 (6) (2000) 466–469.

[5] A. Tholey, R. Pipkorn, D. Bossemeyer, V.K.J. Reed, Influence of myristoylation, phosphorylation, and deamidation on the structural behavior of the N-terminus of the catalytic subunit of CAMP-dependent protein kinase, Biochemistry 40 (2001) 225–231.

[6] S. Cockcroft, G.M.H. Thomas, A. Fensome, B. Geny, E. Cunningham, I. Gout, I. Hiles, N.F. Totty, O. Troung, J.J. Hsuan, Phospholipase D: a downstream effector of ARF in granulocytes, Science 263 (1994) 523–526.

[7] S. Béraud-Dufour, S. Paris, M. Chabre, B. Antonny, Dual interaction of ADP ribosylation factor 1 with Sec7 domain and with lipid membranes during catalysis of guanine nucleotide exchange, J. Biol. Chem. 274 (53) (1999) 37629–37636.

[8] B. Antonny, S. Beraud-Dufour, P. Chardin, M. Chabre, N-terminal hydrophobic residues of the G-protein ADP-ribosylation factor-1 insert into membrane phospholipids upon GDP to GTP exchange, Biochemistry 36 (15) (1997) 4675–4684.
[9] A. Spang, ARF1 regulatory factors and COPI vesicle formation, Curr. Opin. Cell Biol. 14 (2002) 423–427.
[10] M. Franco, P. Chardin, M. Chabre, S. Paris, Myristoylation is not required for GTP-dependent binding of ADP-ribosylation factor ARF1 to phospholipids, J. Biol. Chem. 268 (3) (1993) 24531–24534.
[11] A. Fensome, E. Cunningham, S. Prosser, S.K. Tan, P. Swigart, G. Thomas, J. Hsuan, S. Cockcroft, ARF and PITP restore GTPγS-stimulated protein secretion from cytosol-depleted HL60 cells by promoting PIP_2 synthesis, J. Biol. Chem. 268 (3) (1993) 24531–24534.
[12] R.A. Kahn, P. Randazzo, T. Serafiniga, O. Weiss, C. Rulka, J. Clark, M. Amherdt, P. Roller, L. Orci, J.E. Rothrnanggn, The amino terminus of ADP-ribosylation factor (ARF) is a critical determinant of ARF activities and is a potent and specific inhibitor of protein transport, J. Biol. Chem. 267 (18) (1992) 13039–13046.
[13] D.H. Jones, B. Bax, A. Fensome, S. Cockcroft, ADP ribosylation factor 1 mutants identify a phospholipase D effector region and reveal that phospholipase D participates in lysosomal secretion but is not sufficient for recruitment of coatomer 1, Biochem. J. 341 (1999) 185–192.
[14] J. Goldberg, Structural and functional analysis of the ARF1-ARFGAP complex reveals a role for coatomer in GTP hydrolysis, Cell 96 (1999) 893–902.
[15] M.G. Roth, Snapshots of ARF1: implications for mechanisms of activation and inactivation, Cell 97 (1999) 149–152.
[16] J. Goldberg, Structural basis for activation of ARF GTPase: mechanisms of guanine nucleotide exchange and GTPMyristoyl switching, Cell 95 (1998) 237–248.
[17] S.M.A. Davies, T.A. Harroun, T. Hauss, S.M. Kelly, J.P. Bradshaw, The membrane bound N-terminal domain of human adenosine diphosphate ribosylation factor-1 (ARF1), FEBS Lett. 548 (2003) 119–124.
[18] K. Balali-Mood, T.A. Harroun, J.P. Bradshaw, Molecular dynamics simulations of a mixed DOPC/DOPG bilayer, Eur. Phys. J., E Soft Matter 12 (S01) (2003) S140–S135.
[19] K. Balali-Mood, T.A. Harroun, J.P. Bradshaw, Membrane protein simulations using experimentally determined initial conditions, submitted for publication.
[20] J.A. Losonczi, J.H. Prestegard, Nuclear magnetic resonance characterization of the myristoylated, N-terminal fragment of ADP-ribosylation factor 1 in a magnetically oriented membrane array, Biochemistry 37 (1998) 706–716.
[21] J.A. Losonczi, F. Tian, J.H. Prestegard, Nuclear magnetic resonance studies of the N-terminal fragment of adenosine diphosphate ribosylation factor 1 in micelles and bicelles: influence of N-Myristoylation, Biochemistry 39 (2000) 3804–3816.
[22] M.C. Weiner, S.H. White, Fluid bilayer structure determination by the combined use of X-ray and neutron diffraction: II. "Composition-space" refinement method, Biophys. J. 69 (1991) 174–185.
[23] J.P. Bradshaw, M.J.M. Darkes, T.A. Harroun, J. Katsaras, R.M. Epand, Oblique membrane insertion of viral fusion peptide probed by neutron diffraction, Biochemistry 39 (22) (2000) 6581–6585.
[24] M.C. Weiner, S.H. White, Fluid bilayer structure determination by the combined use of X-ray and neutron diffraction: I. Fluid bilayer models and the limits of resolution, Biophys. J. 69 (1991) 162–173.
[25] R. Brasseur, Tilted peptides: a motif for membrane destabilization (Hypothesis), Mol. Membr. Biol. 17 (2000) 31–40.
[26] P.J. Kraulis, MOLSCRIPT: a program to produce both detailed and schematic plots of protein structures, J. Appl. Crystallogr. 24 (1992) 946–950.